Towards a quantum standard for absolute pressure measurements

Pascal Gambette

HESAM UNIVERSITÉ

le cnam

ÉCOLE DOCTORALE Sciences des Métiers de l'Ingénieur
Laboratoire Commun de Métrologie LNE-Cnam

THÈSE

présentée par : **Pascal GAMBETTE**
soutenue le : **Mercredi 15 décembre 2021**

pour obtenir le grade de : **Docteur d'HESAM Université**

préparée au : **Conservatoire national des arts et métiers**

Discipline : **Milieux dilués et optique**

Spécialité : **Lasers, nanosciences et métrologie**

Towards a quantum standard for absolute pressure measurements

THÈSE dirigée par :
M. Mark PLIMMER *Maître de conférences, Cnam*
et co-encadrée par :
M. Laurent PITRE Chargé de Recherche, LNE
M. Fernando SPARASCI Ingénieur de Recherche, Cnam

Jury

M. Marc HIMBERT	Professeur, LCM LNE-Cnam, Cnam	Président
M. Roberto GAVIOSO	Chercheur, Istituto Nazionale di Ricerca Metrologica (INRiM)	Rapporteur
M. Jean-Michel DAUGAS	Ingénieur de Recherche CNRS, BioMaps, Orsay	Rapporteur
Mme Hélène BOUCHIAT	Directeur de recherche , Laboratoire de Physique des Solides CNRS, Université Paris-Saclay	Examinatrice
M. Laurent PITRE	Directeur de Recherche, LCM LNE-Cnam	Examinateur
M. Mark PLIMMER	Maître de conférences, LCM LNE-Cnam, Cnam	Directeur de thèse
Mme GAO Bo (高波)	Professeur, Technical Institute of Physics and Chemistry of the Chinese Academy of Sciences (TIPC-CAS)	Membre invité

THÈSE

Affidavit

Je soussigné, Pascal Gambette, déclare par la présente que le travail présenté dans ce manuscrit est mon propre travail, réalisé sous la direction scientifique de Mark Plimmer (directeur) et de Laurent Pitre et Fernando Sparasci (co-encadrants), dans le respect des principes d'honnêteté, d'intégrité et de responsabilité inhérents à la mission de recherche. Les travaux de recherche et la rédaction de ce manuscrit ont été réalisés dans le respect de la charte nationale de déontologie des métiers de la recherche. Ce travail n'a pas été précédemment soumis en France ou à l'étranger dans une version identique ou similaire à un organisme examinateur.

Fait à La Plaine Saint-Denis, le 13/04/2021

Signature

Affidavit

I, the undersigned, Pascal Gambette, hereby declare that the work presented in this manuscript is my own work, carried out under the scientific direction of Mark Plimmer (thesis director) and of Laurent Pitre and Fernando Sparasci (co-supervisors), in accordance with the principles of honesty, integrity and responsibility inherent to the research mission. The research work and the writing of this manuscript have been carried out in compliance with the French charter for Research Integrity. This work has not been submitted previously either in France or abroad in the same or in a similar version to any other examination body.

La Plaine Saint-Denis, date 13^{th} April 2021

Signature

Tous les instruments mentent !

*Laurent Pitre (*2017*)*

Acknowledgements

First I would like to thank Prof. Marc Himbert, Director of the LNE-Cnam Common Metrology Laboratory, for welcoming me to the laboratory.

I would also like to thank my supervisors Dr. Laurent Pitre, head of the Low Temperature Group, and Dr. Fernando Sparasci, head of the Intermediate Temperature Group, for giving me the opportunity to carry out this project within the thermometry group. Of course, I would like to thank the other present or former members of the group, namely, Véronique Barbotin and Catherine Martin, Lara Risegari, Jean-Michel Daugas, Nicola Chiodo, Mohamed Sadli and Clément Tauzin for the assistance they have been able to give me.

This project was a collaboration between several laboratories, namely the pressure division of the LNE and the "Joint Research Laboratory for Fluid Metrology Evangelista Torricelli" composed of members of LCM and INRiM. I would like to thank Pierre Otal and Djilali Bentouati from the LNE pressure division. I would also like to thank Frédéric Boineau from the LNE vacuum division for his wise reading advice, notably on the thermomolecular effect. Of course, I thank Roberto Gavioso and Daniele Madonna Ripa from the Istituto Nazionale di Ricerca Metrologica (INRiM) for their contributions and for the initial impulse they gave to the project via the manufacture of the superconducting cavity.

I thank Mr. Alexandre Vergé of Cryosud Services for the manufacture of cryostats.

I would like to express my gratitude to the visiting researchers Aleksandra Kowal from the Institute of Low Temperature and Structure Research at Wroclaw, in Poland, Pan Changzhao (潘长钊) from the Technical Institute of Physics and Chemistry (TIPC) in China, Alberto Giuliano Albo and Graziano Coppa from INRiM in Italy, Peter Pavlasek from the Slovak Institute of Metrology (SMU), for their kindness and for their collaborations.

I would like to thank Prof. Gao Bo (高波), deputy director of the TIPC-LNE Cnam joint laboratory, for her invitation to participate in the realization of an ultra-stable pressure generator in her laboratory of the Technical Institute of Physics and Chemistry (TIPC) in China. Among the members of her group I would particularly like to thank Kelly *alias* Chen Hui (陈慧), Michael *alias* Han Dongxu (韩东旭), Sam *alias* Song Yaonan (宋耀楠), John *alias* Hu Jiangfeng (胡江风), and Richard *alias* Zhang Haiyang (张海洋), for their welcome and the pleasure that I have had working with them.

I would also like to thank Chen Yanyan (陈燕燕) from TIPC for the time she devoted to me despite a very busy schedule.

Thanks also to Dr. Mike Moldover, Dr. Bobby Berg, Dr. Keith Gillis and DR. Jim Schmidt of NIST and Dr. Eric May of the University of Western Australia for their invaluable advice and encouragement.

I thank Dr. Hélène Bouchiat, research director at the *Centre National de Recherche Scientifique* (CNRS) and Member of the French Academy of Sciences, and Dr. Igor Dotsenko, lecturer at *Collège de France*, for agreeing to be part of the steering committee of the thesis and their informed advice.

I thank my supervisor Dr. Mark Plimmer, for his advice and assistance throughout this adventure.

Finally, I renew my thanks to Prof. Marc Himbert, Dr. Hélène Bouchiat, Dr. Roberto Gavioso, Dr. Jean-Michel Daugas, Dr. Mark Plimmer, Dr. Laurent Pitre and Prof. Gao Bo for having accepted to be part of the jury.

Abstract

The present dissertation describes the development of a novel absolute gas pressure standard in a range of 200 Pa to 20 kPa (0.002 atm to 0.2 atm). The method used, refractive index gas manometry, involves the determination of the refractive index of a pure noble gas (helium-4 or argon) using a microwave resonator. The refractive index is determined via the ratio of the resonant frequencies measured with the resonator under vacuum and under pressure at a constant temperature. Given the thermodynamic temperature of the gas and its refractive index, it is possible to calculate its pressure. This principle is the reciprocal of that used for refractive index gas thermometry (RIGT) in which thermodynamic temperature is extracted from the measured refractive index of gas at a known pressure. The frequency scanning pattern and fitting algorithms take advantage of earlier work in the laboratory on the determination of the Boltzmann constant prior to the 2019 redefinition of the kelvin, the SI unit of thermodynamic temperature. For helium-4, measurements were made at 5.4 K using a quasi-spherical copper resonator coated on its inner surface with a 3 μm thick layer of superconducting niobium. Superconductivity improves the quality factor Q of the resonator and thereby the frequency resolution of the system. The pressure determination benefits from the very high accuracy of the dielectric and density virial coefficients of helium-4 obtained by *ab initio* calculations. Measurements on argon were performed at a temperature of 90.4 K with an uncoated copper resonator. At this temperature, the apparatus is less demanding in terms of cryogenics than its helium counterpart and so easier to replicate.

Keywords : *Ab initio* calculation, Pressure standard, Metrology, Manometry, Thermometry, Microwave cavity, Superconductivity, Refractive index, Virial coefficient, Helium, Argon.

Résumé

Ce document décrit le développement d'un nouvel étalon de pression absolue de gaz dans dans une gamme allant de 200 Pa à 20 kPa (soit $0,002$ atm à $0,2$ atm). La méthode utilisée repose sur la mesure de l'indice de réfraction d'un gaz noble pur (hélium-4 ou argon) à l'aide d'un résonateur hyperfréquence. L'indice est déterminé par le rapport des fréquences de résonance à vide et sous pression mesurées à température constante. Connaissant la température thermodynamique du gaz et son indice de réfraction, on peut en calculer la pression. Ce principe est la réciproque de celui utilisé pour la thermométrie à gaz à indice de réfraction (RIGT) dans laquelle la température thermodynamique est déterminée à partir de la mesure de l'indice de réfraction du gaz et de sa pression maintenue constante. Le modèle de balayage de fréquence et les algorithmes d'ajustement tirent parti des travaux antérieurs du laboratoire sur la détermination de la constante de Boltzmann en vue de la redéfinition des unités du SI de 2019. Pour l'hélium-4, les mesures ont été effectuées à une température de $5,4$ K à l'aide d'un résonateur quasi-sphérique en cuivre dont la cavité est recouverte d'une couche supraconductrice de niobium d'épaisseur 3 μm. La supraconductivité permet d'améliorer le facteur de qualité Q du résonateur et par voie de conséquence la résolution en fréquence du système. La détermination de la pression bénéficie des très faibles incertitudes des coefficients du viriel des propriétés thermo-physiques de l'hélium-4 obtenue par calculs *ab initio*. Les mesures à l'argon ont été effectuées à une température de $90,4$ K avec un résonateur en cuivre (sans traitement supraconducteur). A cette température, l'expérimentation est moins exigeante en terme de cryogénie et donc plus susceptible d'être dupliquée.

Mots clés: Calculs *ab initio*, Etalon de pression, Métrologie, Manométrie, Thermométrie, Cavité hyperfréquence, Supraconductivité, Indice de réfraction, Coefficient du viriel, Hélium, Argon.

Contents

Acknowledgements **VIII**

Abstract **IX**

Résumé **XI**

Contents **XX**

List of tables **XXIV**

List of figures **XXXVIII**

Introduction **1**

1 Context and motivation **3**

1 A brief history of pressure measurement 3

2 Overview of the current context 4

3 State of the art 6

3.1 Pressure standards commonly used in national metrology laboratories 6

3.2 Examples of current Calibration and Measurement Capabilities 8

4 Photon-based standards and quantum-based standards for pressure measurement 10

4.1 Redefinition of the SI 10

4.2 *Ab initio* calculations 11

4.3 Determination of the pressure value from the refractive index measurement 11

I Helium-4 gas **15**

2 Superconducting microwave cavity **17**

1 Generalities 17

1.1 Shape 17

1.2 Dimensions 19

1.3 Estimated value of resonant frequencies 21

1.4 Advantage of superconductivity 21

2 Two applications of refractive-index measurement with a quasi-spherical resonator 22

2.1 Refractive index equation 23

2.2 Pressure measurement 23

2.3 Temperature measurement 23

3 Practical realization 24

3.1 Copper cavity 24

3.2 Superconducting cavity 26

3.3 Antennas 31

3 Cryostats **35**

1 Overview 36

2 The Cryostat Mark I (2018) 37

3 The Cryostat Mark II (2019) 40

4 The Cryostat Mark III (2020) 44

5 Estimation of the conduction heat transfer 46

4 Experimental set-up **47**

1 Overview 48

2 Instrumentation 52

2.1 Helium gas 52

2.2 Pressure generator 52

3 Software 56

3.1 Pressure and temperature regulation 56

3.2 Fitting method 58

3.3 Pressure calculation 61

4 Physical aspects 63

4.1 Skin effect 63

4.2 Influence of an external magnetic field 63

4.3 Temperature-related resonant frequency shift (thermal expansion) . . 65

4.4 Isothermal compressibility of the cavity 65

4.5 Taconis oscillation 66

4.6 Self-heating 69

4.7 Hydrostatic effect 70

4.8 Thermo-molecular effect 72

4.9 Outgassing 75

5 Results and discussion **77**

1 Resonant frequency versus temperature 77

2 Transmitted antenna power 81

3 Quality factor versus temperature 81

4 Relative frequency uncertainty 83

5 Choice of the set point for the temperature regulation of the resonator . . . 84

6 Stability under vacuum 84

7 The temperature gradient along the pressure tube 85
8 Pressure resolution 86
9 Pressure cycles 87
10 Uncertainty budget 90

II Argon gas **93**

6 Copper microwave cavity **95**
1 Generalities 95
2 Practical realisation 96
2.1 Copper cavity 96
2.2 Antennas 97

7 Cryostat for Argon gas **99**

8 Experimental set-up **103**
1 Overview 103
2 Apparatus 105
2.1 Argon gas 105
2.2 Pressure generator 105
3 Software 105
4 Physical aspects 105
4.1 Thermal expansion of the cavity 105
4.2 Isothermal compressibility of the cavity 106
4.3 Self-heating 106
4.4 Thermodynamic temperature determination 106
4.5 Hydrostatic effect 107

4.6 Thermo-molecular effect . . . 107
4.7 Outgassing . . . 109

9 Argon experiments **111**

1 Choice of the set-point for the temperature regulation of the resonator . . . 111
2 Transmitted antenna power . . . 111
3 Quality factor . . . 112
4 Impact of pre-amplifiers . . . 112
5 Stability under vacuum . . . 113
6 The temperature gradient along the pressure tube . . . 114
7 Pressure tests . . . 116
8 Uncertainty budget . . . 124

III Conclusion and perspectives **127**

10 Conclusion and perspectives **129**

References **142**

Annexes **145**

A Physical properties of helium and argon gases **145**

1 Helium gas . . . 146
1.1 Magnitude order and uncertainty table (helium) . . . 146
1.2 Refractive index (helium) . . . 147
1.3 Molar density (helium) . . . 147
1.4 Electric susceptibility (helium) . . . 148

1.5 Magnetic susceptibility (helium) 148
1.6 Relative shift of resonant frequency *versus* pressure (helium) 149
1.7 Relative shift of resonant frequency *versus* temperature (helium) . . . 149
2 Argon gas 150
2.1 Orders of magnitude and uncertainty table (argon) 150
2.2 Refractive index (argon) 151
2.3 Molar density (argon) 151
2.4 Electric susceptibility (argon) 152
2.5 Magnetic susceptibility (argon) 152
2.6 Relative resonant frequency shift *versus* pressure (argon) 153
2.7 Relative resonant frequency shift *versus* temperature (argon) 153

B Cryostat versions **155**

1 Experimental Dewar 156
2 The cryostat Mark I (2018) 157
3 The cryostat Mark II (2019) 158
4 The cryostat Mark III (2020) 159

C Instrumentation **161**

1 B-box elements 162
2 Pressure sensors 163
2.1 DIGIQUARTZ® model 745 163
3 Vector network analyser 163
4 The frequency standard 163
4.1 Rubidium oscillator 163
4.2 GPS disciplined oscillator 163
5 Ohmmeter 163

6 Current supply 164
7 Radio frequency isolator 164
8 Automatic thermometry bridge 164
9 1Ω standard resistor 1Ω 164
10 Pumping station 164

D Software **165**

1 Calculation of pressure from resonant frequency 166
1.1 Main program 166
1.2 Frequency-to-pressure subroutine 167
2 Hydrostatic correction 171
3 Spline function 174
3.1 Data organization files 175
3.2 Virial coefficients 175
3.3 Frequency to convert in pressure 175

E Analytical treatment of uncertainty **177**

1 Microwave pressure measurement 178
2 Hydrostatic correction 179
2.1 Expression of hydrostatic pressure as a function of altitude and temperature 179
2.2 Sensitivity coefficients of uncertainty 182

Detailed summary in French **183**

Résumé détaillé en français **187**

1 Introduction 187

1.1 Etat de l'art 188
1.2 Objectifs initiaux et évolution de l'étude 188
2 Principe 189
2.1 Détermination de la valeur de la pression 189
2.2 Résolution en fréquence 192
3 Materiel et méthodes 192
3.1 Résonateurs hyperfréquences 192
3.2 Antennes 194
3.3 Cryostats 194
3.4 Le montage expérimental 194
3.5 Le générateur de pression 197
4 Résultats et discussion 198
4.1 Experimentations à l'hélium 198
4.2 Expérimentations à l'argon 200
4.3 Cyles de pression de l'hélium et de l'argon 201
4.4 Budget d'incertitude provisoire de l'hélium 202
5 Conclusion 202

List of tables

1.1 Range limits of pressure standards for vacuum measurement[1]. 7

1.2 Representative Calibration and Measurement Capabilities of various national laboratories with a coverage factor of 2. Uncertainty Values are expressed with a level of confidence of 95%. The values presented in the Table come from the BIPM website [2], with the exception of that of LNE which comes from the COFRAC website [3]. 9

2.1 Estimation of eigenvalues and lowest frequencies of the triplets according the electromagnetic modes for a spherical cavity under vacuum with a radius $a = 25$ mm. 21

2.2 Characteristic values of some superconducting materials: Critical temperature T_c, critical magnetic induction B_c, London penetration depth λ_L and coherence length ξ_0 . The critical magnetic induction B_c is linked to the critical magnetic field H_c by the relation $B_c = \mu_0 H_c$, where μ_0 is the vacuum permeability [4]. 29

4.1 Temperature related frequency shift resulting from a dimensional change of the cavity and the penetration depth variation around 5.4 K. 65

4.2 Mechanical dimensions and estimation of the temperature and relative pressure at 1 kPa of the Figure 4.17 (with the stainless steel thermal conductivity fit of the reference [5]) 70

4.3 Composition of dry air, boiling point at atmospheric pressure and impact of each component at a concentration of one part per million for argon gas [6] [7]. 75

5.1 Comparison between the theory and measured resonant frequency below the critical temperature. To determine the theoretical frequencies, the diameter of the resonant cavity was first calculated from the resonant frequency measured at 9.0282 K. The theoretical frequencies at other temperatures were then deduced from this diameter by taking into account the thermal expansion of the resonator and the London penetration depth. 79

5.2 Values measured by the pressure tube thermometers with 1 kPa of helium-4 (source: He-run7). 85

5.3 Pressure resolution determination (source He-run 2). 86

5.4 Helium gas pressure measurement uncertainty budget for superconducting microwave cavity at $T = 5.4$ K. With P pressure; κ_T isothermal compressibility; T thermodynamic temperature; A_μ molar magnetic polarizability; A_ϵ molar electric polarizability; B_ϵ second dielectric virial coefficient; B_2, C_2, D_2 density virial coefficients; f_m measured frequency. Uncertainty components that are less than 20 μPa are either omitted or replaced by a dash "–". (See also Appendix A Table A.1) 90

8.1 Theoretical frequency shift coefficients resulting from thermal expansion of the cavity around 90.4K 106

8.2 Estimates of the temperatures and relative pressures at 1 kPa of the Figure 4.17 (with the stainless steel thermal conductivity fit of the reference [5]). . . 107

8.3 Flow regime for argon gas in the pressure tube of the cryostat Mark II. The mean free path values were computed with molecular collision diameter $d = 364$ pm taken from [8] 108

9.1 Comparison of the relative uncertainty in the resonant frequency with different amplifier configurations with the superconducting resonator at $T = 5.4$ K for the TM_{11} mode, VNA power: -18 dBm (*i.e.* 1.58 μW) (source He-run3). . . 112

9.2 Comparison of the relative uncertainty in the resonant frequency with different amplifier configurations with the copper resonator at $T = 90.4$ K for the TM_{11} mode, VNA power: 0 dBm (*i.e.* 1 mW) (source Ar-run7) 113

9.3 (source Ar run 7). 113

9.4 Values measured by the pressure tube thermometers 1 kPa (source: Ar-run8_27).114

9.5 Argon gas measurement uncertainty budget with the copper microwave cavity at $T = 90.4$ K. With P pressure; κ_T isothermal compressibility; T thermodynamic temperature; A_μ molar magnetic polarizability; A_ϵ molar electric polarizability; B_ϵ second dielectric virial coefficient; B_2, C_2, D_2 density virial coefficients; f_m measured frequency. (The uncertainty components that are less than 20 μ Pa are omitted or replaced by dashes. 124

A.1 Orders of magnitude and estimated uncertainties of the main physical quantities involved in determining the pressure. Uncertainty values are expressed at the 68% level of confidence. 146

A.2 Order of magnitude and estimated uncertainties of the main physical properties of argon gas involved in determining the pressure. Uncertainty values are expressed at the 68% level of confidence. 150

1 Capacités d'étalonnage et de mesure représentatives de divers laboratoires nationaux. Les incertitudes sont exprimées avec un niveau de confiance de 95%. Les valeurs présentées dans le tableau proviennent du site du BIPM [2] à l'exception de celle du LNE qui provient du site COFRAC [3] 188

2 Estimation des valeurs propres et des fréquences les plus basses des triplets selon les modes électromagnétiques pour une cavité sphérique sous vide de rayon $a = 25$ mm. 194

3 Bilan d'incertitude provisoire pour l'hélium aux pressions 200 Pa et 20 kPa mesurées à l'aide de la cavité supraconductrice à 5.4 K. Avec P pression ; κ_T compressibilité isotherme ; T temperature thermodynamique ; A_μ polarisabilité magnétique molaire ; A_ϵ polarisabilité magnétique molaire ; B_ϵ second coefficient diélectrique du viriel ; B_2, C_2, D_2 coefficients du viriel de la densité ; f_m fréquence mesurée. (Les composantes d'incertitude inférieures à 20 μPa sont omises et remplacées par le symbole "–"). 202

List of figures

1 Layout of the thesis 2

1.1 Calibration and Measurement Capability comparaison between different laboratories.Uncertainty values are expressed at the 95% confidence level [2] . Data correspond to Table 1.2 above. 9

2.1 These two circles symbolise two cross-sectional planes of the resonator. They illustrate the modification made to a sphere of radius a (1) to obtain a triaxial ellipsoid or quasi-sphere (2) 19

2.2 Simulation of the modulus of the forward transmission coefficient of a quasi-spherical copper cavity versus frequency. The degenerate frequencies of the perfect spherical cavity are split in three resonant frequencies. The cavity has a mean radius $a = 2.5$ cm and a quality factor $Q \approx 2 \times 10^4$. 20

2.3 Simulation of the forward transmission coefficient modulus of a cavity versus frequency for the TM_{11} mode of the cavity for two different quality factors $Q = 2 \times 10^4$ in blue and $Q = 4 \times 10^6$ in orange. 22

2.4 The orientation of coordinate system and local radii of the inner triaxial ellipsoid. Depth 25.000 mm, R largest radius 25.050 mm ($\epsilon_2 = -2 \times 10^{-3}$) and r smallest radius 24.950 mm ($\epsilon_1 = 2 \times 10^{-3}$). 25

2.5 A: Cross-sectional view of the hemisphere. B: Positioning of the plug on a half-sphere. (1) Antenna cable, (2) Plug, (3) Plug insertion hole, (4) Thermometer (remark: no thermometer was actually inserted in the plug during the series of tests described in this document)(drawing made by Alexandre Vergé from Cryosud Services the company by kind permission of the author). 25

2.6 Qualitative representation of the electrical resistance as a function of temperature around the transition between normal and superconducting states. At a temperature lower than the critical temperature (T_c), the electrical resistance vanishes. 26

2.7 The superconducting domain is bounded by the values of the critical field H_c, the critical density current J_c and the critical temperature T_c. 27

2.8 Magnetization curve of the two types of superconductor. The magnetization of the material M is related to the magnetic field applied H by the magnetic susceptibility χ (*i.e.* M= χH). In the superconducting state, that is for a magnetic field H lower than the critical magnetic field H_c for type I superconductors (see Figure A) or H_{c1} for type II superconductors (see Figure B) , the magnetization is equal and opposite to the magnetic field. In other words, the susceptibility $\chi = -1$ and the superconductor is a perfect diamagnetic. For the type I superconductor (see Figure A) if the magnetic field H is higher than the critical field, the magnetization abruptly decreases. For the type II superconductor (see Figure B), if the magnetic field H is higher than the 'lower' critical field H_{c1} then the magnetization gradually decreases and disappears at the 'upper' critical field H_{c2}. 28

2.9 Arrival of the superconducting cavity at the laboratory at the end of January 2018. The hemisphere is protected by a vacuum sealed hermetic plastic protective envelope. The silvery appearance of the internal surface of the hemisphere is due to the 3 μm thick layer of niobium. 31

2.10 The antennas are made from a coaxial cable of outer diameter 2.2 mm. The materials used for cable manufacturing are non-magnetic. One end of the cable is soldered to an SMA connector (shown on the right). 31

2.11 A: Plug dimensions in millimetres. B: An antenna in its plug ready to be inserted into the resonator. 32

2.12 During assembly, the end of the antenna is flush with the internal wall of the cavity. Its position is then adjusted so as to obtain the strongest possible signal on the resonances. This last operation is carried out with the help of a network analyzer. As soon as the optimal position is found, the antenna is glued into its plug 32

2.13 Installation of the antennas on the resonator: (1) Emitting antenna, (2) Receiving antenna (3) Pipe bringing a flow of helium into the cavity 33

3.1 Cryostat Mark I: (a): Cross-sectional drawing of the vacuum chamber. (1)Vacuum chamber, (2a) and (2b) Pressure equalisation plugs; (3) Superconducting quasi-spherical resonator, (4a) and (4b) antenna plugs, (5) Cernox^{TM} RTD temperature sensors, (6) Heaters, (7a) and (7b) coaxial cables, (8) Cables of temperature sensors and heaters, (9) Radiation baffles; (b): (1) Superconducting quasi-spherical resonator, (2) Cernox RTD temperature sensor, (3) Antenna, (4) Heater, (5) Thermalisation board for electrical wires 38

3.2 Cryostat Mark I: (a): Cross-sectional view of the Dewar containing the cryostat ; (b): (1) Vacuum chamber, (2) RF coaxial cables, (3) Central tube which retain the vacuum chamber, (4) Radiation baffles: During the first experiments, the copper radiation baffles were not yet available. They were later replaced by aluminium sheets mounted on polyurethane foam discs. 39

3.3 Cryostat Mark II (2019): (1) Vacuum chamber, (2) Pressure vessel, (3) Superconducting quasi-spherical resonator, (4) Heaters, (5) Cernox^{TM} RTD temperature sensors, (6) Pressure tube, (7) Platinum RTD temperature sensors, (8) Coaxial cables,(9) Cables of temperature sensors and heaters. 41

3.4 Cryostat Mark II: (1) Superconducting quasi-spherical resonator, (2) Antenna, (3) Pressure vessel lid, (4) Coaxial cables, (5) Pressure tube, (6) Vacuum chamber lid. 42

3.5 Cryostat Mark II: (a): Cross-sectional view of the Dewar with the cryostat; (b): (1) Vacuum chamber, (2a) and (2b) Coaxial cables, (3) Pressure tube, (4) Radiation baffles. 43

3.6 Overview of the pressure tube of the Cryostat Mark III (1) Vacuum jacket that thermally protects the pressure tube from liquid helium, (2) Pressure tube equipped with supports for thermometers and with copper radiation baffles, (3) Supports for thermometers with radiation baffles for the pressure tube, (4) Radiation baffles for the vacuum jacket. 44

3.7 Cryostat Mark III (version 2020) (1) Vacuum chamber, (2) Liquid nitrogen extraction line, (3) Pressure tube, (4) Thermometers and heaters wires tube, (5) Radiation baffles, (6) Cryostat lid,(7) Liquid helium level probe. The coaxial cables leading to the antennas are not shown. 45

3.8 Estimation of the ratio of power consumption by conduction heat flow for the three cryostats. 46

4.1 Schematic of the overall experiment 48

4.2 Experimental setup during run 5 (June-July 2019): (1) Turbomolecular pump backed by a dry rotary pump (2) Tube linking a turbomolecular pump to the cryostat and allowing one to evacuate gas from the vacuum chamber, (3) Computers, (4) Vector network analyser connected to the microwave resonator, (5) Rubidium frequency standard, (6) Tube linking a turbomolecular pump to the microwave resonator, (7) Tube linking the pressure generator to the vacuum chamber of the cryostat, (8) Experimental Dewar, (9) Pressure generator. . . 49

4.3 Pressure generator schematic: (1) Gas supply, (2) Regulator, (3) Manual valve, (4) Mass flow controller, (5) Valves, (6) Volumes, (7) Pressure sensor (Baratron), (8) Pressure sensor for pressure regulation (DIGIQUARTZ®), (9) Pressure sensor (DIGIQUARTZ®) used as pressure reference, (10) Mass flow controller, (11) Inlet gas valve toward the microwave resonator, (12) Part connected to the microwave resonator in the cryostat, (13) Inlet valve gas evacuation, (14) Turbomolecular vacuum pump, (15) Turbomolecular vacuum pump. 53

4.4 Simplified schematic of the B-box: (1) temperature controller, (2) Peltier modules: integrated into the air flow going around the enclosure by absorbing hot air (symbolized by red arrows) and restoring cooled air (blue arrows), (3) thermistor, (4) fans. The solid green arrows represent the links between the temperature controller, the thermistor and one of the Peltier modules. 54

4.5 Experimentation during liquid nitrogen transferring: (1) Liquid nitrogen storage dewar, (2) Experimental Dewar, (3) Temperature controller,(4) Pressure generator outlet valve allowing gas to fill the microwave resonator, (5) B-box, (6) Peltier module. 55

4.6 Temperature regulation loop schematic. 57

4.7 Area of the front panel of the LabVIEW™ control program. (A) Coefficients P and I used when the temperature lies above the set point and falls towards it, (B) Coefficients P and I used when the temperature lies below the setpoint and rises towards it, (C) Coefficients P and I used when the temperature lies above the setpoint and rises even higher, (D) Coefficients P and I used when the temperature is below the setpoint and falls even lower, (E) Coefficients P and I used when the temperature lies in the interval defined by U and L around the set point. U corresponds to a temperature interval above the setpoint and L to one below it. 57

4.8 Measured values of S_{21} around the three resonant frequencies. Each elliptic arc corresponds to a resonance the size of which increases with the quality factor. The resonances are scanned over twice. 59

4.9 Graph of measured values of S_{21} for the highest frequency peak of the triplet. 59

4.10 Graph of measured $|S_{21}|$ of the highest frequency peak of the triplet. 60

4.11 Residuals of the fit of $|S_{21}|$ for the highest frequency peak of the triplet. . . . 60

4.12 Illustration of the iterative calculation. Equation (A) gives the square of the refractive index, whose value is unknown at the start of the calculation. The left hand side represents its calculated value, the right hand side represents its measured value. The compressibility of the resonator and the resonance frequencies are known. The only unknown factor for the right-hand member is then the pressure. To solve the equation, the software proposes an *a priori* pressure value. This value is injected into the equation of state "B" which will make it possible to determine the density of the gas at the measured temperature. The density of the gas thus calculated is inserted in the equations of Clausius Mossotti (C) which make it possible to determine the relative magnetic permeability and the relative electric permittivity of the gas. The product of the two is the square of the calculated refractive index. If the equality of the two indices is not achieved, another pressure value is chosen *a priori* and the calculation repeated. The recursive process stops when the equality between the two squares of the refractive indices is achieved to the desired number of decimal places. 62

4.13 Different shielding from magnetic fields. (a): The experimental Dewar is coated outside with mu-metal strips; (b): The experimental vacuum chamber is coated inside with lead, which becomes superconducting below 7.2 K. 64

4.14 Helmholtz resonator. V: volume of the pressure vessel minus the volume of the resonator; L: length of the pressure tube; A: section of the pressure tube. . . 66

4.15 Resonant frequency of the Helmholtz resonator *versus* temperature for different lengths of the gas transport tube from $L = 0.15$ m to $L = 1.5$ m. 67

4.16 Measurement of the Taconis oscillation. The graph represents the frequency response of the $|S_{21}|$ scattering parameter for helium gas at two different pressures corresponding to the peak to peak amplitude of the Taconis oscillation. The measurement is carried out at fixed frequency. If the chosen frequency lies close to the resonant frequency (f_A), the pressure variations have little effect on the measured $|S_{21}|$ parameter (the $|S_{21}|$ difference corresponds to the segment A on the graph). On the other hand, if the chosen frequency lies close to that at half-maximum, the variations of $|S_{21}|$ (represented by the segment B) are greater. 68

4.17 Positions of thermometers in the cryostat. T_1, T_2, T_3, T_4, T_5 show the locations of the thermometers. The dimensions of the drawing are given in table 4.2 . 71

4.18 Thermomolecular correction given by Takaishi and Sensui [9] and the BIPM [10] 73

4.19 Flow regimes in the pressure tube of the Mark II cryostat. 74

4.20 Flow regimes in the pressure tube of the Mark III cryostat. 74

5.1 Variation of the transmission coefficient $|S_{21}|$ of the microwave cavity when the temperature drops below T_c, the critical temperature of the superconducting niobium inner surface. Representation of the central resonant frequency f2n of the mode TM_{12} (source: run 1). 78

5.2 Shape of the relative penetration depth $\lambda(T)$ of niobium *versus* temperature 78

5.3 Variation of the transmission coefficient $|S_{21}|$ spectrum for resonant frequency f_{2n} of the mode TM_{12} at different temperatures. Although the resonant frequency rises at lower temperatures, here peaks are aligned for clarity (*cf.* Figure 5.1) (source He-run 1). 80

5.4 Quality factors of the TM_{11} triplet resonant frequencies *versus* temperature. Emission power -28 dBm (source He-run 2). 81

5.5 Quality factors (A) Theoretical Q_i (upper curve) and measured Q (lower curve) *versus* temperature for the Mode TM_{11}. (B) Coupling Quality factor $Q_c = QQ_i/(Q_i - Q)$ deduced from curves (A) 82

5.6 Uncertainty in the frequency of the TM_{11} mode triplet components *versus* temperature. Microwave power −28 dBm. (1) Static measurement at 5.1 K. (2) Static measurement at 7.56 K (source He-run 2). 83

5.7 Relative Allan deviation of the resonant frequency with the resonator under vacuum at 5.4 K (source He-run 7). 84

5.8 Frequency shift with a 20 Pa variation of helium gas pressure at 5.1 K (source He-run 2). 86

5.9 Simultaneous evolution of the pressure to be measured, the temperature of the resonator and the resonant frequency during a pressure cycle. The mean temperature of the resonator is 5.4 K (source He-run 7). 87

5.10 Stability of the reference pressure (A) and the resonator temperature at 5.4 K (B) measured simultaneously (source He-run 7). 88

5.11 Difference between helium pressure measured via the refractive index and a reference pressure for three successive cycles (source He-run 7). 89

5.12 Relative pressure difference of three successive cycles (source He-run 7). . . . 89

5.13 Expected uncertainty propagation at 5.4 K due to the determinations of the resonance frequency (frequency) in yellow, thermodynamic temperature (Cernox AGT) in light blue, the isothermal compressibility κ_T in dark blue, the *ab initio* coefficients in grey. The red curve (all contributions) represents the square root of the quadratic sum of these elements. 91

5.14 Comparison of Calibration and Measurement Capability for pressure of different laboratories and the provisional uncertainty of this project for helium gas. Uncertainty Values are expressed with a level of confidence of 68% [2] 92

6.1 Copper cavity for argon pressure measurement. A: plug for antenna. B: the two copper hemispherical cavities of the triaxial ellipsoid resonator unassembled. 96

6.2 The helical antennas are made from a coaxial cable of outer diameter 2.2 mm. The materials used for cable manufacturing are non-magnetic. One end of the cable is soldered to an SMA connector (shown on the right). 97

6.3 The helical antenna consists of two contiguous turns (dimension: A = 2 mm, B = 1 mm, conductor diameter = 0.53 mm). 97

6.4 Antenna tuning: (a): Installation of the antennas on the resonator: (1) Transmitting antenna, (2) Receiving antenna (3) Pipe bringing a flow of helium into the cavity. ; (b): Triplet resonant frequencies measurement during antenna installation. Resonator under vacuum at room temperature (20 °C). A: Vector network analyser, B: Lower resonant frequency (8.571 670 0 GHz, −40 dBm), C: Medium resonant frequency (8.573 190 9 GHz, −28 dBm), D: Upper resonant frequency (8.573 190 9 GHz, −28 dBm), E: Isolator, F: High frequency output, G: High frequency input. 98

7.1 Cryostat Mark II (2019): (1) Vacuum chamber, (2) Pressure vessel, (3) Platinum resistance thermometer Pt25 , (4) Copper resonator, (5) Coaxial cables, (6) Temperature sensors and heater cables, (7) Platinum RTD temperature sensor Pt1000, (8) Pressure tube,(9) Six platinum RTD temperature sensors Pt100 wired in series for temperature regulation, (10) Heaters : on top of the pressure vessel 220Ω, underneath the resonator 217Ω. 100

7.2 Cryostat Mark II: (1) Platinum resistance thermometer Pt25, (2) Argon gas flow inlet tube to protect the copper cavity from oxidation, (3) Antenna in its plug, (4) Flexible stainless steel hose to convey argon gas under pressure to the copper cavity, (5) Coaxial cable, (6) Pressure vessel lid, (7) Thermalization board for the electric wires, (8) Argon gas flow outlet tube, (9) Copper resonator. 101

7.3 Cryostat Mark II: (1) Coaxial cable, (2) Pressure tube, (3) Microwave isolator, (4) Pressure vessel lid. 102

7.4 Amplifier ZX60-14012L+ from Mini-Circuits®, +11 dBm typ. output power at 1 dB compression, bandwidth: 300 kHz to 14 GHz, flatness over frequency range ±1 dB. 102

8.1 Schematic overview of experimental set-up for measurements on argon. 103

8.2 Experimental setup during run 7 (November-December 2020): (1) Resistance bridge (2) Vector network analyser connected to the microwave resonator , (3) Rubidium frequency standard, (4) Experimental Dewar, (5) Pressure generator, (6) argon gas cylinder supplying the pressure generator. 104

8.3 Flow regime in the pressure tube of the Mark II cryostat for different values of the Knudsen number K_n. 108

8.4 Flow regime in the pressure tube of the Mark III cryostat for different values of the Knudsen number K_n. 108

9.1 (source Ar run 7). 114

9.2 Stability of the pressure generator at 150 Pa. 116

9.3 Stability of the pressure generator at 20 kPa. 116

9.4 Relative Allan deviation of the pressure generated by the pressure generator at 20 kPa. The slope of $-1/2$ is consistent with white frequency noise. 117

9.5 Pressure difference between the microwave sensor and a reference sensor for four successive pressure cycles from 10 kPa to 500 Pa (source Ar-run 8). . . . 118

9.6 Relative pressure difference between the microwave sensor and a reference sensor for four pressure cycles from 10 kPa to 500 Pa (source Ar-run 8). . . 118

9.7 Relative resonant frequency measured during cycles consisting of two pressure points: vacuum and 10 kPa (source Ar-run 9). 119

9.8 Relative half-width frequency measured during cycles consisting of two pressure points: vacuum and 10 kPa (source Ar-run 9). 119

9.9 Relative values of the reference thermometer measured on cycles consisting of two pressure points: vacuum and 10 kPa. The temperature difference measured by the reference thermometer between vacuum and 10 kPa is approximately 18 mK (source Ar-run 9). 120

9.10 Pressure steps. (A) Pressure, (B)Control Temperature, (C) The reference temperature appears to follow the pressure variations, (D) Half-width, (E) Resonant frequency (source Ar-run 8). 121

9.11 Next experiment, (A) Control thermometer (Pt100) embedded in a copper tube, (B) Copper screw, (C) Stainless steel spring washer. 123

9.12 Variation with the pressure of the various contributions to the uncertainty in the pressure measurement: in purple, the temperature measurement, in dark blue the compressibility, in green the virial coefficients, in brown the compressibility, in yellow the thermal expansion and all contributions are represented by the red curve. 125

A.1 Difference between refractive index n and unity as a function of pressure at 5.4 K.147

A.2 Molar density of ^{4}He *versus* pressure at 5.4 K. 147

A.3 Electric susceptibility ($\chi_e = \epsilon_r - 1$) of ^{4}He *versus* pressure at 5.4 K. 148

A.4 *Opposite* of magnetic susceptibility ($-\chi_m = -(\mu_r - 1)$) of ^{4}He *versus* pressure at 5.4 K. 148

A.5 Relative shift of resonant frequency *versus* pressure at 5.4 K. The slope is about -18×10^{-9} Pa^{-1}. 149

A.6 Relative shift of resonant frequency of the mode TM_{11} *versus* temperature. The slope is about 641×10^{-9} K^{-1}. 149

A.7 Difference between refractive index n and unity as a function of pressure at 90.4 K. 151

A.8 Molar density of argon *versus* pressure at 90.4 K. 151

A.9 Electric susceptibility ($\chi_e = \epsilon_r - 1$) of argon *versus* pressure at 90.4 K. 152

A.10 *Negative* of magnetic susceptibility ($-\chi_m = -(\mu_r - 1)$) of argon *versus* pressure at 90.4 K. 152

A.11 Relative resonant frequency shift *versus* pressure at 90.4 K. The slope is about -8×10^{-9} Pa^{-1}. 153

A.12 Relative resonant frequency shift *versus* temperature. The slope is about 18×10^{-9} K^{-1}. 153

B.1 Experimental Dewar for all cryostat versions for helium gas with dimensions in millimetres. 156

B.2 Cryostat Mark I (2018) for superconducting resonant cavity. 157

B.3 Cryostat Mark II (2019) for superconducting resonant cavity. 158

B.4 Cryostat Mark III (2020) for superconducting resonant cavity - Simplified drawing. 159

1 Cavité supracondutrice de diamètre intérieur 50 mm (1) Demi Cavité, (2) Corps en cuivre, (3) Logement pour un thermomètre, (4) Insert pour une antenne hyperfréquence, (5) Revêtement en niobium (d'apparence argentée), (6) Résonateur hyperfréquence fermé, (7) Schéma représentant la déformation d'une sphère de rayon a pour obtenir une quasi-sphère. L'ordre de grandeur des coefficients ϵ_1 et ϵ_2 est de 10^{-3}. Cette déformation permet de distinguer les fréquences de résonance de chaque mode en les éloignant les unes des autres [11].193

2 (a) Cryostat version I, (b) Cryostat version II, (c) Plan en coupe de la chambre à vide du cryostat II, (1) Câbles coaxiaux reliant un analyser de réseau vectoriel aux antennes du résonateur hyperfréquence, (2) Vase Dewar contenant le liquide cryogénique, (3) Ecrans en cuivre réduisant les pertes thermiques par rayonnement, (4) Liquide cryogénique ,(5) Résonateur hyperfréquence, (6) Enceinte à vide, (7) Conduit convoyant le gaz vers l'enceinte de pression. (8) Ligne de vide contenant la ligne de pression, (9) Enceinte de pression en cuivre, (10) Résistances chauffantes utilisées pour la régulation en température (11) Coupe de la ligne de vide contenant la ligne de pression garnie d'écran anti-rayonnement et de thermomètres, (12) Thermomètres mesurant la température du gaz le long de la ligne de pression, (13) Thermomètres de type Cernox^{TM} RTD utilisés pour la régulation de température pour l'expérimentation à l'hélium, (14) Thermomètre à résistance de platine de type Pt25 utilisé pour la régulation de température lors de l'expérimentation à l'argon, (15) Résistance chauffante utilisée pour la régulation de température. 195

3 Schéma de principe de l'expérimentation 196

4 Montage expérimental pendant le run 5 (juin-juillet 2019): (1) Pompe turbomoléculaire avec une pompe rotative sèche, (2) Tube reliant le cryostat à une pompe turbomoléculaire et permettant d'évacuer le gaz de la chambre à vide, (3) Ordinateurs, (4) Analyseur de réseau vectoriel connecté au résonateur hyperfréquence, (5) Etalon de fréquence (Rubidium), (6) Tube reliant une seconde pompe turbomoléculaire au résonateur hyperfréquence, (7) Tube reliant le générateur de pression à l'enceinte à vide, (8) Vase Dewar, (9) Générateur de pression. 197

5 Schéma de principe du générateur de pression: (1) Alimentation en gaz, (2) Détendeur, (3) Vanne manuelle,(4) Régulateur de débit massique,(5) Vannes, (6) Volumes, (7) Capteur de pression (Baratron), (8) Capteur de pression (DIGIQUARTZ®) utilisé pour la régulation de pression, (9) Capteur de pression (DIGIQUARTZ®) utilisé comme référence, (10) régulateur de débit massique, (11) Vanne permettant d'alimenter le résonateur hyperfréquence en gaz, (12) Partie connectée à l'enceinte de pression et au résonateur hyperfréquence dans le cryostat, (13) Vanne d'évacuation du gaz, (14) Pompe turbomoléculaire, (15) Pompe turbomoléculaire. 198

6 Spectre du paramètre de transmission $|S_{21}|$ autour de la fréquence de résonance f_{12} du mode TM_{12} pour différentes valeurs de température. Les centres des résonances sont alignés pour plus de clarté (source He-run 1). 199

7 Incertitude en fréquence des composantes du triplet du mode TM_{11} en fonction de la température. Puissance micro-onde -28 dBm. (1) Mesure statique à 5.1 K.(2) Mesure statique à 7.56 K (source He-run 2). 199

8 Evolution simultanée de la pression à mesurer, de la température du résonateur et de la fréquence de résonance au cours d'un cycle de pression. La température moyenne du résonateur est égale à 5.4 K (source He-run 7). 200

9 Résultat préliminaire : différence relative entre les étalons de pression et la mesure primaire de pression obtenue avec les deux résonateurs, le supraconducteur avec de l'hélium à 5.4 K et le non supraconducteur avec de l'argon à 90.4 K 201

Introduction

The present dissertation is devoted to the development of a standard for absolute static gas pressure measurements in the range 200 Pa to 20 kPa. This standard is based on the use of a superconducting microwave cavity and quantum mechanical calculations of gas properties. For this reason it is sometimes dubbed "quantum pressure standard". A particularity of this study is that, as far as we are aware, it is the first to measure the pressure of a gas at low temperature and in this range of pressure with the help of an electromagnetic cavity in the low range of *super high frequencies* or SHF [1].

The experiments were carried out in the Low Temperature department of the thermometry laboratory of the *Laboratoire commun de métrologie LNE-Cnam* located in Saint-Denis just north of Paris. The speciality of this laboratory might seem surprising. Indeed, it would appear more natural *a priori* to develop a pressure standard in a pressure laboratory. The reason for this choice lies in the uncertainties associated with the physical quantities and the coefficients of equation 1.8. As will be shown later, temperature measurements contribute the greatest uncertainty. A thermometry laboratory was ideal for carrying out the best control of this parameter.

This study is part of an EMPIR project entitled "Towards quantum-based realizations of the pascal". This project aims to develop photon-based standards. What these standards have in common is to determine pressure via the gas density using the ideal gas law [12].

In the present project, the pressure of helium-4 gas is measured using a superconducting microwave cavity. To benefit from the superconductivity the cavity must be operated at cryogenic temperatures. The preparatory phase of this experiment consisted in designing and

[1] SHF range extends from 3 GHz to 30 GHz, which corresponds to wavelengths ranging from 10 cm to 1 cm. The wavelengths of the frequencies used during the experiment belong to the centimetre wave band.

making the superconducting cavity then the cryostat for low temperature operation (down to 5 K). The experiments consist in measuring resonant frequencies either under vacuum or at several levels of pressure in the range 200 Pa to 20 kPa.

The present dissertation retraces the experiments and summarizes the work carried out, though for clarity, subjects are presented in thematic rather than chronological order. Figure 1 shows the layout. The experiments on helium and argon are treated independently. However, in the part devoted to argon, the points of the experiment common to both gases will not be developed.

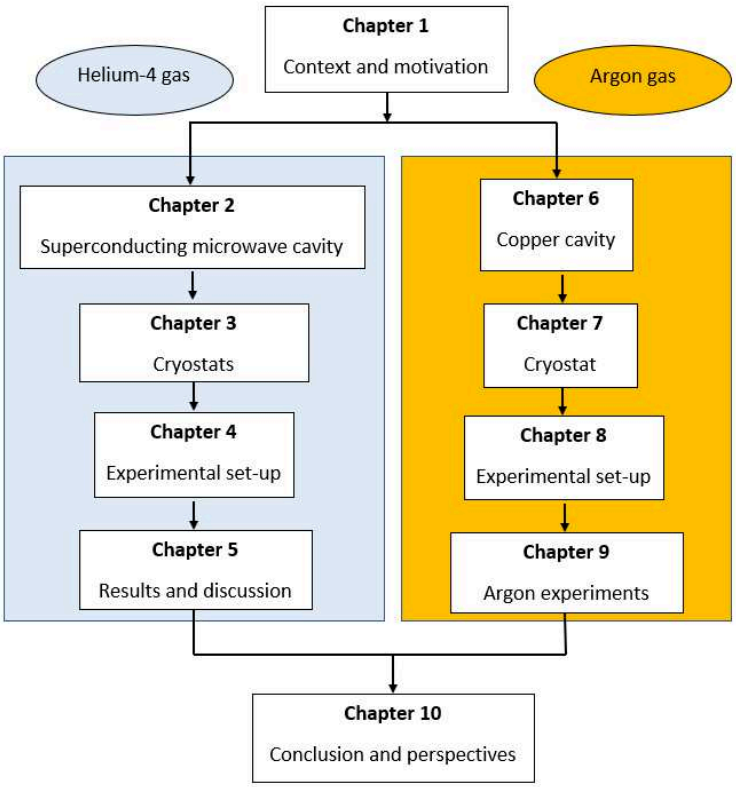

Figure 1: Layout of the thesis

Chapter 1

Context and motivation

The present dissertation is devoted to the development of a standard for absolute static gas pressure measurements in the range 200 Pa to 20 kPa. It is based on the measurement of the refractive index of either helium-4 (^{4}He) or argon (Ar) using quasi-spherical resonant microwave cavities. In the case of ^{4}He gas, the resonator is made of copper with a niobium coating. Niobium becomes superconducting when its temperature is less than 9.2 K. The cavity working temperature is 5.4 K. For Ar gas, the resonator is made entirely of copper and so is not superconducting. It was operated at a temperature of 90.4 K. The virial coefficients of the thermophysical properties of gases defined by *ab initio* quantum mechanical calculations are used to determine the pressure. For this reason the new standard is sometimes dubbed "quantum pressure standard". The aim of this chapter is to put this study into context.

1 A brief history of pressure measurement

Historically, the realization of the first absolute pressure measurement apparatus, the liquid barometer, dates from the seventeenth century. Mercury was used very early on as a manometric liquid. Its high specific gravity (13.56) allowed the size of the first instruments to be reduced and so facilitated experiments. Raffaelo Magiotti (1597-1658), Gasparo Berti (1600-1643), Evangelista Torricelli (1608-1647) and Blaise Pascal (1623-1662) are some of those who distinguished themselves in this field[13].

To honour Evangelista Torricelli and Blaise Pascal for their contributions, the scientific community has bestowed their names upon two pressure units: the torr (symbol: Torr) and the pascal (symbol: Pa) [1]. The latter (pascal) was officially introduced in 1971 during the 14^{th} *Conférence Générale des Poids et Mesures*. It belongs to the international system of units (SI) and is defined as the ratio of a force (in newton or kilogram metre per second squared) to a surface (in metre squared). The pascal is therefore a derived unit, *i.e.* it is defined from a combination of the basic SI units (in this case the kilogram, the metre and the second)[14].

We recall that atmospheric pressure lies close to 10^5 Pa. The pressure measured in the present project, from 200 Pa to 20 kPa, is thus sub-atmospheric. Its range is straddled between those of low vacuum (1×10^5 Pa to 3×10^{-3} Pa) and medium vacuum (3×10^{-3} Pa to 10^{-1} Pa). Industrial applications using these pressure ranges include, for the low vacuum range, epitaxial growth of semiconductor films and laser etching of metals, and for medium vacuum, chemical vapour deposition or ion plating [15].

2 Overview of the current context

One might wonder what motivates metrology laboratories to continue their research. Why are they striving to improve the performance of their measuring devices and why are they trying to make devices based on new principles ? The answers to these questions can be found in the needs of society as well as for scientific reasons.

Right from outset, in the seventeenth century, the mercury manometer was used with a scientific purpose. It helped highlight the importance of atmospheric pressure and played an important role in resolving the controversy over the existence of the vacuum [13]. Over time, other measurement devices were invented such as the pressure balance based on the piston-cylinder principle [16]. Meanwhile, the performance of the mercury manometer has continued to improve. It has long been used as a pressure standard by national metrology

[1] 1 Torr = $(101,325/760)$ Pa $\approx$ 133 Pa

institutes worldwide.

Over the past few years, however, mercury manometers have tended to disappear from metrology laboratories (*e.g.* for the *Laboratoire national de métrologie et d'essais (LNE)* in France at the beginning of the 2000's, and for the American *National Institute of Standards and Technology (NIST)* in 2018 [17]). This phasing out is largely due to the toxicity of mercury for both humans and the environment [18].

The decommissioning of mercury manometers is not the only reason pushing laboratories to seek alternatives [19]. In a context of economic uncertainty which characterizes the current period, it is not uncommon to see companies being bought out or disappearing altogether due to a lack of profitability, or a product line becoming discontinued overnight. Pressure standards provided by private companies, therefore, have uncertain availability and maintainability. For example, the non-rotating force-balanced piston gauge or FPG (DHI model 8601) [2] used by several laboratories as a reference is nowadays obsolete [20].

In response to these problems, companies, for strategic reasons, and researchers are led to find solutions and, in particular, explore new ways of measuring pressure. As a part of quantum-based vacuum metrology, a field to which this study is related, the measurement principle has important practical consequences. In fact, it allows devices based on this principle to materialise the pascal and therefore be directly traceable to the SI. In other words, such measurement instruments are calibration-free [21][22].

Measuring instruments based on new principles and developed by research can sometimes be transposed to industry. Still in the realm of quantum-based vacuum metrology, this was the case in 2017, of the projet led by the National Institute of Standards and Technology (NIST) and its industrial partner MKS Instruments. They aimed to adapt a quantum pressure standard to instruments intended to operate outside national laboratories, "in the real world"

[2]The FPG is a DH Instruments product. DH Instruments (DHI) was founded in 1980 before being bought out in 2007 by the Fluke Company.

(*sic*)[23].

One of the purposes of metrological research is to improve the performances of standards, in particular their accuracy. According to International Vocabulary of Metrology (VIM) [24] accuracy is defined as the "closeness of agreement between a measured quantity value and a true quantity value of a measurand". A better accuracy has the effect of making discernible physical phenomena that previously were not. This can lead to new scientific discoveries and, in the industrial domain, a better control of processes [25].

High accuracy is also important for the purpose of comparison. An unbroken chain of comparisons ensures traceability to the SI system of units. Combined with quality standards (the ISO 9000 series and ISO 17025 [26]) this traceability has improved confidence in measurements. More generally, such traceability promotes scientific and economic exchanges [1].

3 State of the art

For the pressure measurement device which is the subject of this study to be useful, its metrological performance must be comparable with that of the current standards. This section is intended to give an overview of this metrological context.

3.1 Pressure standards commonly used in national metrology laboratories

To span the range from atmospheric pressure down to ultra-high vacuum (10^5 Pa to 10^{-9} Pa) National Metrology Institutes use several types of pressure standard. The limits of their ranges are summarized in Table 1.1.

In the range covered by the present study (200 Pa to 20 kPa) the instruments currently used are liquid manometers, piston gauges (also named pressure balances) and static expansion systems. Their operating principles are as follows.

Table 1.1: Range limits of pressure standards for vacuum measurement[1].

Pressure standard type	Upper pressure limit (Pa)	Lower pressure limit (Pa)
Liquid manometer (mercury or oil)	1×10^5	1
Rotaring and non-rotating piston gauges	1×10^5	1
Static expansion systems	1×10^3	1×10^{-6}
Continuous expansion systems	1×10^{-1}	1×10^{-9}

3.1.1 Liquid manometer

A simple version of a liquid manometer consists of a U-shaped tube fixed in a vertical position. The tube contains a manometric liquid maintained in equilibrium thanks to the pressures applied at each end. One end of the U-tube is filled with a gas at the reference pressure while the other is filled with a gas at the pressure to be measured. The reference pressure may be vacuum. Any pressure difference moves the liquid in one direction or the other. The height shift Δh is proportional to the pressure difference Δp and is given by[27]:

$$\Delta h = \frac{\Delta p}{\rho\, g} \tag{1.1}$$

in which ρ is the liquid density and g is the local acceleration due to gravity.

3.1.2 Piston gauge

The sensitive element of piston balances is a vertical piston sliding in a cylinder. The pressure to be measured is applied to one of the flat surfaces of the piston and is counterbalanced by a force F applied to the other side. Given the surface area S and the force F, the value of the pressure is deduced from the relation:

$$\Delta P = \frac{F}{S}. \tag{1.2}$$

By its principle, the pressure measured by a piston balance is consistent with the definition of the unit *i.e.* a force divided by a surface area. The force F can be provided either by

masses of known values or a force balance.

3.1.3 Static expansion method

The static expansion method can be considered as an application of *Boyle*'s law [3] which stipulates that, at constant temperature, the product of a gas volume by its pressure is a constant. This method allows one to measure pressure in the range of 10^3 to 10^{-6} Pa. The gas expansion is carried out isothermally. In a first instance, the test gas is enclosed in a small volume (V_1) and its pressure (P_1) measured. A valve connecting the initial volume (V_1) to a larger, previously evacuated volume (V_2) is then opened. The gas occupies the combined volume ($V_1 + V_2$) and the pressure (P_2) can be calculated using the expression [28]:

$$P_2 = P_1 \left(\frac{V_1}{V_1 + V_2} \right). \tag{1.3}$$

Equation 1.3 shows that a knowledge of the initial volume pressure (P_1) and the volumes ratio are necessary to determine the final pressure (P_2). The pressure (P_1) is measured by instruments chosen according to the range of pressure. Resonant silicon gauges and capacitance-type diaphragm gauges are examples of frequently used instruments. The volume ratio can be determined by several methods such as calculation or by liquid filling.

3.2 Examples of current Calibration and Measurement Capabilities

A convenient way to find out the capabilities of the national metrology laboratories is to use the Calibration and Measurement Capabilities database published by the International Bureau of Weights and Measures (BIPM)[2]. Table 1.2 shows some uncertainty values of different national laboratories covering the pressure range of the present project (200 Pa to 20 kPa). The figure 1.1 shows a graph of these values. Some observations can be made:

1. The jumps in uncertainty might be caused by a change in measuring range or a change in technology of standard (for example at 15 kPa for LNE).

[3] Also known in French-speaking countries under the name of the Boyle-Mariotte law

2. For all laboratories, uncertainties increase at low pressure.

Table 1.2: Representative Calibration and Measurement Capabilities of various national laboratories with a coverage factor of 2. Uncertainty Values are expressed with a level of confidence of 95%. The values presented in the Table come from the BIPM website [2], with the exception of that of LNE which comes from the COFRAC website [3].

Country (Laboratory)	Measurand minimum value (Pa)	Measurand maximum value (Pa)	Uncertainty Value (Pa)
USA (NIST)	140	1.6×10^5	$[(6 \times 10^{-3})^2 + (5.2 \times 10^{-6}p)^2]^{1/2}$
Germany (PTB)	100	1.8×10^5	$0.06 + 6 \times 10^{-6}p$
France (LNE)	3	1.5×10^4	$0.015 + 1.6 \times 10^{-5}p$
	5×10^3	5×10^5	$0.2 + 7 \times 10^{-6}p$

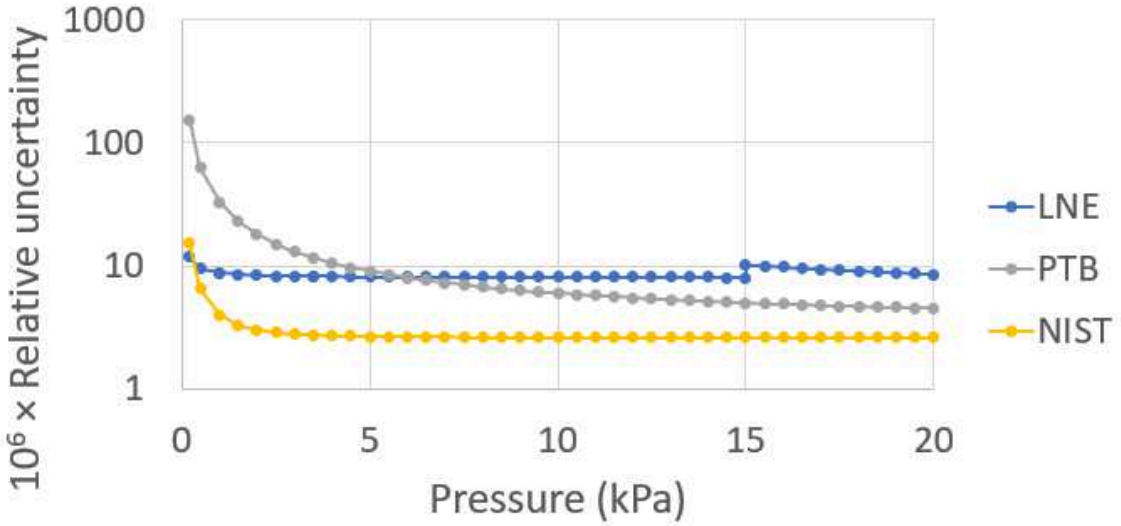

Figure 1.1: Calibration and Measurement Capability comparaison between different laboratories.Uncertainty values are expressed at the 95% confidence level [2] . Data correspond to Table 1.2 above.

4 Photon-based standards and quantum-based standards for pressure measurement

Quantum metrology allows one to measure physical quantities with high resolution and high accuracy. It uses quantum mechanics to describe physical quantities [29]. The present study can be considered as part of quantum metrology. Indeed, quantum mechanics allows one, in the form of *ab initio* calculation of the properties of the gas, to obtain the best uncertainties when determining pressure using helium.

The study of these quantum pressure standards has become interesting thanks to two factors which have contributed concurrently to improve the measurement uncertainty: gradual advances in *ab-initio* calculations of gas properties and the recent historic redefinition of the SI system of units.

4.1 Redefinition of the SI

On November 16, 2018, the 26^{th} *Conférence Générale des Poids et Mesures* endorsed the proposal made by the International Committee of Weights and Measures (CIPM) to redefine four of the seven base units of the international system (SI): the kilogram, the ampere, the mole and the kelvin[4]. These radically new definitions resulted in the fixing of the values of four physical constants: the Planck constant (h), the elementary charge (e), the Avogadro constant (N_A), and the Boltzmann constant (k). Since the implementation of these resolutions in May 2019, these constants have had the following values:

$$\begin{aligned} h &= 6.626\,070\,15 \times 10^{-34}\ \text{J.s} \\ e &= 1.602\,176\,634 \times 10^{-19}\ \text{C} \\ N_A &= 6.022\,140\,76 \times 10^{23}\ \text{mol}^{-1} \\ k &= 1.380\,649 \times 10^{-23}\ \text{J.K}^{-1} \end{aligned}$$

The uncertainties in these physical constants are zero since they have a fixed value by definition. This property leads to reduced uncertainties in the physical equations that use them, which is the case for the ideal gas law.

[4]The definitions of the other base units, second, metre and candela, were also rephrased in terms of fixed values of related constants $\Delta\nu_{Cs}$, c, and K_{cd}.

4.2 *Ab initio* calculations

"*Ab initio* calculation" is one of the methods used in computational chemistry to calculate molecular properties. As the method is based on quantum mechanics it is sometimes designated by the expression "*Ab initio* quantum chemistry method". "*Ab initio*" means "from first principles" or "from the beginning". This Latin locution indicates that the input data used are values of physical constants [30].

In practice, the determination of the thermophysical properties of helium gas from its physical constants is carried out in two calculational steps. The first uses quantum mechanics to calculate, *ab initio*, the inter-atomic potential energy $\varphi(r)$ for two atoms separated by a distance r. The second step uses quantum-statistical mechanics and the kinetic theory of gases to determine the thermophysical properties from the potential energy $\varphi(r)$. These calculations are very demanding in terms of computer time and memory but allow ultimately one to obtain the most accurate values for gaseous helium at low density [31].

4.3 Determination of the pressure value from the refractive index measurement

Pressure is a mechanical concept usually defined as the applied force per unit surface area ($\mathrm{N.m^{-2}}$). According to this definition, pressure sensors are generally based on the measurement of the effects caused by the pressure on a surface. The principle used to measure the pressure in the present study is different and is based on the equation of state of a gas. The pressure of an ideal gas can be expressed as

$$p = \rho_N kT \tag{1.4}$$

where ρ_N is the number density (number of molecules N per unit volume), k the Boltzmann constant and T the thermodynamic temperature. It is also possible to express the pressure as a function of the molar density ρ_m ($\mathrm{mol.m^{-3}}$):

$$p = \rho_m RT \tag{1.5}$$

where

$$\rho_N = \rho_m N_A \tag{1.6}$$

and

$$R = kN_A \tag{1.7}$$

where R is the ideal gas constant (8.314 462 618 153 24 J K^{-1} mol^{-1})[5] and N_A is the Avogadro constant. To describe real gases, expression (1.5) is modified to:

$$p = \rho_m RT(1 + B(T)\rho_m + C(T)\rho_m^2 + ...). \tag{1.8}$$

where *B(T)*, *C(T)* are the molar density *virial* coefficients. These coefficients can be measured experimentally or determined by *ab initio* calculations. For multi-electron atoms such as argon ($Z = 18$) or neon ($Z = 10$), the determination of *virial* coefficients by experimental means gives the lowest uncertainties [32]. For helium, however, the determination of *virial* coefficients by *ab initio* calculations has now become more accurate than that by experiment [33].

The refractive index of the gas can be deduced from the molar density by the Clausius-Mossotti equations for electric permittivity and magnetic permeability:

$$\frac{\varepsilon_r - 1}{\varepsilon_r + 2} = \rho_m A_\varepsilon(1 + B_\varepsilon(T)\rho_m + C_\varepsilon(T)\rho_m^2 + ...). \tag{1.9}$$

$$\frac{\mu_r - 1}{\mu_r + 2} = \rho_m A_\mu(1 + ...). \tag{1.10}$$

[5]The ideal gas constant has an exact value since it is equal to the product of the Avogadro and Boltzmann constants which themselves were fixed with exact values (cf. section 4.1).

where A_ϵ and A_μ the molar polarizabilities (in $\mathrm{m}^3.\mathrm{mol}^{-1}$) associated with the relative electric permittivity ε_r and the relative magnetic permeability μ_r. The coefficients $B_\epsilon(T)$ and $C_\varepsilon(T)$ are the dielectric virial coefficients. Finally, using the relative electric permittivity ε_r and the relative magnetic permeability μ_r, one can express the square of the refractive index n defined as

$$n^2 = \varepsilon_r \mu_r. \tag{1.11}$$

In conclusion, gas pressures can be deduced from refractive index measurements. In the optical domain, accurate measurements are made using Fabry Perot cavities [34]. In the present study the measurement is made in the microwave frequency domain using a quasi-spherical resonator cavity. Physical properties of helium and argon gases are given in Appendix A.

Part I

Helium-4 gas

Chapter 2

Superconducting microwave cavity

This chapter describes the central element of the pressure standard, a low-temperature gas refractometer based on a microwave cavity.

1 Generalities

1.1 Shape

A priori, the shape of the electromagnetic cavity should have no influence on the measurement principle. In fact, if it is true that the measurement is possible whatever the cavity, its shape nevertheless influences the quality of the measurement via the resolution.

Intuitively and from a spectral point of view, the narrower the bandwidth, the easier it would appear to measure the resonance frequency accurately. Indeed, the frequency resolution in the presence of white noise can be expressed by the following relation [35]

$$\frac{\Delta f}{f} = \frac{1}{A}\frac{1}{Q}\frac{1}{(SNR)}\sqrt{\frac{\tau}{t}} \tag{2.1}$$

where A is a dimensionless constant of order unity, Q the quality factor of the cavity, SNR the signal-to-noise ratio, τ the single measurement time and t the integration time. This relation shows that the higher the quality factor, the better the resolution.

Very generally, the quality factor of a resonant cavity characterized by an inner volume V of surface S can be roughly approximated by the expression [36]

$$Q \cong \frac{2}{\delta}\frac{V}{S} \tag{2.2}$$

where

$$\delta = \sqrt{\frac{1}{\pi \mu_0 \sigma f}} \tag{2.3}$$

is the skin depth, μ_0 the magnetic permeability of the vacuum, σ the electrical conductivity of the cavity walls and f the frequency of the electromagnetic wave. Equation 2.2 shows that to obtain the greatest quality factor, the volume V to surface S ratio must be maximized. The shape that maximizes this ratio is a sphere.

For a 'perfectly' spherical cavity without loss, the electromagnetic field eigenfrequencies are given by [37]

$$f_{ln}^{\varsigma} = \frac{1}{\sqrt{\mu\varepsilon}}\left(\frac{\xi_{ln}^{\varsigma}}{2\pi a}\right) \tag{2.4}$$

where l,n are integers which identify the eigenfrequency f_{ln}^{ς} , ς specifies the modes TM or TE[1], ε is the electric permittivity and μ is the magnetic permeability, ξ_{ln}^{ς} is an eigenvalue determined by the boundary conditions and a is the radius of the cavity. The electromagnetic modes are $(2l+1)$-fold degenerate multiplets (identical resonant frequencies)[2]. The lowest degenerate frequency number per mode is for $l = 1$, which corresponds to a frequency triplet.

In practice, the deviations of the manufactured cavity from a perfect sphere do not make it possible to distinguish all the components of the triplet. This makes it difficult to determine

[1]The transverse electric (TE) (resp. transverse magnetic (TM)) modes have their electric (resp. magnetic) field in the plane perpendicular to the radiation's propagation direction. They are defined from a spherical coordinate frame whose origin is at the centre of the spherical cavity.

[2]This contrasts with spherical cavities used in acoustic applications where radial acoustic modes are non-degenerate [11].

resonance frequencies accurately and can increase their relative uncertainties to a few times 10^{-6}, or even more [38]. It is possible to split these frequencies by deforming the spherical cavity slightly. This is achieved in spherical triaxially ellipsoidal cavities often called quasi-spherical cavities. The four quarters of a 'perfect' sphere are joined by cylinder thickness of $2\varepsilon_1 a$ and $2\varepsilon_2 a$ (see Fig 2.1). The order of magnitude of ϵ_1 and ϵ_2 is 10^{-3}. With such a small deformation of the sphere one can still predict accurately characteristics such as the resonance frequencies or the half-widths of the microwave modes [37].

As mentioned previously, the eigenfrequencies of equation 2.4 have $(2l+1)$-fold degenerate solutions with $l \geq 1$. For the TM_{11}, TE_{11}, TM_{12} and TE_{12} modes, the spectra are composed of frequency triplets. The geometric deformation of the quasi-spherical cavity causes a splitting of the triplets into distinguishable frequencies [11] (see Fig 2.2).

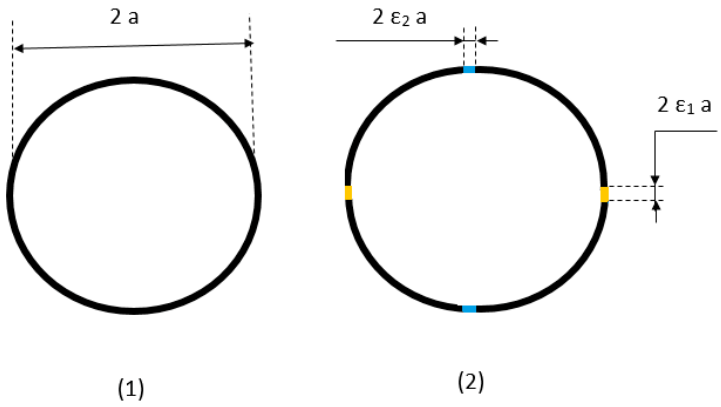

Figure 2.1: These two circles symbolise two cross-sectional planes of the resonator. They illustrate the modification made to a sphere of radius a (1) to obtain a triaxial ellipsoid or quasi-sphere (2)

1.2 Dimensions

The shape of a quasi-spherical resonator allows one to retain the benefit of the large quality factor and while splitting the degenerate microwave triplets of each mode into distinct frequencies in a stable and predictable way [11]. The frequency of the electromagnetic wave corresponding to a given mode is related to the size of the resonator. The triaxial ellipsoid for

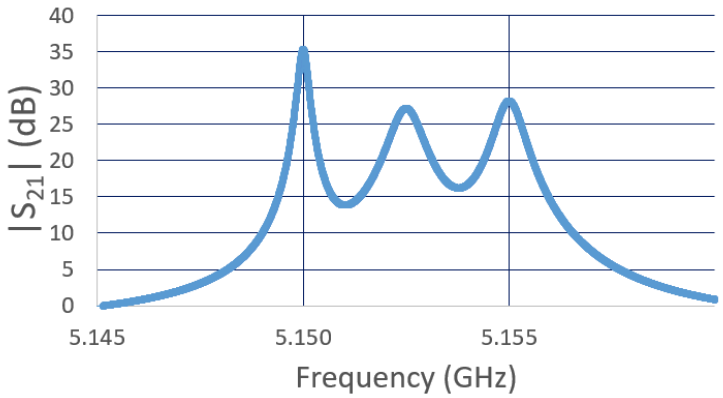

Figure 2.2: Simulation of the modulus of the forward transmission coefficient of a quasi-spherical copper cavity versus frequency. The degenerate frequencies of the perfect spherical cavity are split in three resonant frequencies. The cavity has a mean radius $a = 2.5$ cm and a quality factor $Q \approx 2 \times 10^4$.

a cavity of eccentricities ϵ_1 and ϵ_2 is described by the following equation:

$$\frac{x^2}{(1+\varepsilon_2)^2} + y^2 + \frac{z^2}{(1+\varepsilon_1)^2} = \frac{a^2}{(1+\varepsilon_1)^2(1+\varepsilon_2)^2}. \tag{2.5}$$

As previously mentioned, the values of ε_1 and ε_2 are small ($\pm$ 0.002) which leads to differences of $\pm$ 50 μm for radii of 25 mm.

To take into account the perturbations caused by the aspherical shape, electromagnetic transducers, pressure equalization openings, and the finite electrical conductivity of the wall, the measured electromagnetic resonance frequencies f_{ln}^{ς} have to be corrected with a term $\Delta f_{ln}^{\varsigma}$ evaluated by modelling the electromagnetic field. The equivalent radius a_{eq} of a spherical resonator filled with helium at a static pressure p and temperature T is given by:

$$a_{ln}^{\sigma} = \frac{c}{2\pi\sqrt{\mu_r \varepsilon_r}} \frac{\xi_{ln}^{\varsigma}}{< f_{ln}^{\sigma} + \Delta f_{ln}^{\varsigma} >} \tag{2.6}$$

where c is the speed of light in vacuum (299 792 458 ms^{-1}), ε_r is the relative electrical permittivity, μ_r its relative magnetic permeability and ξ_{ln}^{ς} is an eigenvalue. The angle brackets (around the frequencies) denote an average over the triplet components. Using this equation it is possible to calculate the radius a_{ln}^{ς} of the equivalent sphere by measuring the resonance

frequencies of a given triplet.

1.3 Estimated value of resonant frequencies

From a practical point of view, it is useful to be able to estimate the value of the resonance frequencies from the radius a of the cavity. If one considers the quasi-spherical cavity to be spherical with a perfectly conducting surface, equation 2.4 can be written for a cavity under vacuum [37] as

$$f_{ln}^{S} = \frac{c\,\xi_{ln}^{S}}{2\pi a} \tag{2.7}$$

where f_{ln}^{S} are the eigenfrequencies and ξ_{ln}^{S} is a eigenvalue. Table 2.1 shows the eigenvalues and average frequencies of the lowest-frequency triplets calculated for $a = 25$ mm.

Table 2.1: Estimation of eigenvalues and lowest frequencies of the triplets according the electromagnetic modes for a spherical cavity under vacuum with a radius $a = 25$ mm.

Mode	ξ_{ln}^{S}	f_{ln}^{S} (GHz)
TM_{11}	2.743 707 2	5.24
TE_{11}	4.493 409 4	8.58
TM_{12}	6.116 764 2	11.67
TE_{12}	7.725 251 8	14.74

1.4 Advantage of superconductivity

In previous experiments carried out on quasi-spherical copper microwave cavities, the quality factors achieved were of the order of $Q = 2 \times 10^4$. However, as equation 2.1 shows, the resolution of the frequency measurement is inversely proportional to the quality factor Q. To increase Q, the solution adopted was to use a superconducting cavity. Such kinds of resonators can display very high quality factors Q factors, greater than 10^{10} [39]. Figure 2.3 shows the simulation of a triplet with quality factors of 2×10^4 and 4×10^6. The narrowness of the resonance curve is manifest.

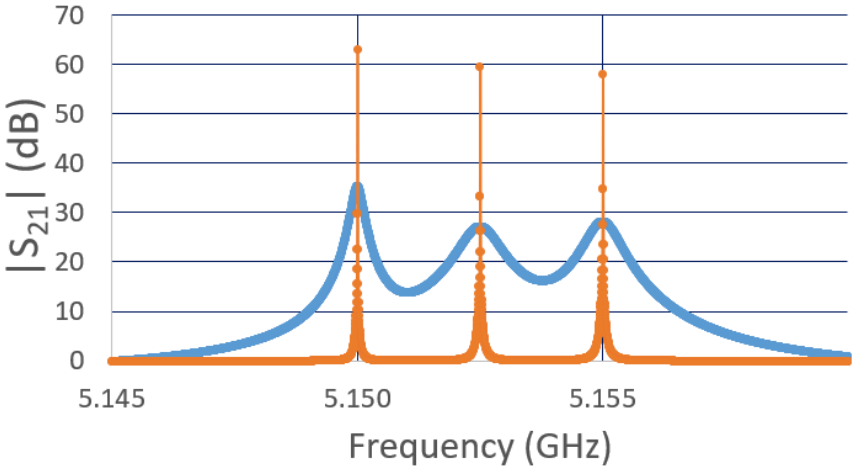

Figure 2.3: Simulation of the forward transmission coefficient modulus of a cavity versus frequency for the TM_{11} mode of the cavity for two different quality factors $Q = 2 \times 10^4$ in blue and $Q = 4 \times 10^6$ in orange.

2 Two applications of refractive-index measurement with a quasi-spherical resonator

The pressure measurement is based on the measurement of the refractive index of a gas by the quasi-spherical resonant cavity. From a general point of view, the refractive index of the gas is a function of its temperature and its pressure. Consequently, a refractive index measurement has two possible complementary uses:

- if the thermodynamic temperature is known, the measurement of the refractive index makes it possible to deduce the gas pressure;
- if the pressure is known, the measurement of the refractive index yields the gas temperature.

The first case corresponds to the project described in the present dissertation while the second has been jointly developed by Technical Institute of Physics and Chemistry of the Chinese Academy of Sciences (TIPC-CAS) in China and Laboratoire national de métrologie et d'essais-Conservatoire national des arts et métiers (LNE-Cnam) in France [35]. The latter represents the current state of art of thermometry for the temperature range from 5 K to 24.5 K, albeit without recourse to a superconducting cavity.

2.1 Refractive index equation

The refractive index n is the ratio of electromagnetic wave speed in a medium (here a gas) to that in vacuum. If ϵ_r is the relative electrical permittivity and μ_r is the relative magnetic permeability, the square of the refractive index is given by equation 1.11. The square of the refractive index measured by the quasi-spherical resonator is given by [37]:

$$n^2 = \epsilon_r(p,T)\mu_r(p,T) = \left[\frac{< f_{ln}^{em} + \Delta f_{ln}^{em} >_0 \, [1 + \kappa_T(p/3)]}{< f_{ln}^{em} + \Delta f_{ln}^{em} >}\right]^2 \tag{2.8}$$

where $< f_{ln}^{em} + \Delta f_{ln}^{em} >_0$ denotes the mean value of the triplet frequency measured under vacuum, $< f_{ln}^{em} + \Delta f_{ln}^{em} >$ that with a gas-filled resonator and κ_T is the isothermal compressibility of the resonator. At the low temperatures where the present microwave resonator is used, the order of magnitude of $\kappa_T(p/3)$ is very small compared to 1 in the pressure range studied (with $\kappa_T \approx \ 7 \times 10^{-12}$ Pa^{-1}) [40].

2.2 Pressure measurement

The permittivity ϵ_r and permeability μ_r of a gas of molar density ρ can be expressed by Clausius-Mossotti equations (*cf.* 1.9 and 1.10). The molar density ρ can also be developed as a virial expansion as a function of pressure p and temperature T:

$$\rho(p,T) = \frac{p}{RT[1 + B_2(T)\rho + C_2(T)\rho^2 + D_2(T)\rho^3 + ...]}. \tag{2.9}$$

where $B_2(T)$, $C_2(T)$ and $D_2(T)$ are density virial coefficients describing the behavior of a real gas. After measuring the resonant frequencies in vacuum and under pressure, one can combine equations 1.9, 1.10 and 2.9 with equation 2.8 to determine the pressure via an iterative calculation (see Chapter 4 for details).

2.3 Temperature measurement

A single-pressure refractive index gas thermometer was built in China in 2018 and has been used to measure thermodynamic temperature in the range of 5 K to 26 K [41]. To

do this, the gas refractive index is measured at two different temperatures, one of them a reference (*e.g.* a fixed point of ITS-90) the other the temperature to be determined. The ratio of refractive indices is given by

$$\frac{n(T,p)}{n(T_{ref},p)} = \frac{\frac{<f_{ln}^{em}+\Delta f_{ln}^{em}>_{(T,0)}[1+\kappa_T(p/3)]}{<f_{ln}^{em}+\Delta f_{ln}^{em}>_{(T,p)}}}{\frac{<f_{ln}^{em}+\Delta f_{ln}^{em}>_{(T_{ref},0)}[1+\kappa_T(p/3)]}{<f_{ln}^{em}+\Delta f_{ln}^{em}>_{(T_{ref},p)}}}. \tag{2.10}$$

The resonant frequencies $<f_{ln}^{em} + \Delta f_{ln}^{em}>$ are measured under pressure and under vacuum at the reference temperature T_{ref} and at the unknown one T. The value of the latter temperature is then determined by iterative calculation using equations 2.10, 1.9, 1.10 and 2.9.

The thermometer in the Franco-Chinese experiment uses a quasi-spherical resonator made from copper [42]. As in the pressure measurement apparatus described here, the gas used is ^{4}He. Although the SPRIGT pressure generator is similar in principle to that used at LNE-Cnam, it is somewhat more refined [43] [44].

3 Practical realization

The superconducting cavity was made in several stages. The elements that make up the quasi-spherical resonator (*i.e.* the two hemispherical shells and the inserts) were first machined from copper. In a second step, a niobium deposit was applied to the inner surfaces. Finally, the closed cavity was assembled in the laboratory by taking care to reduce the contact time with the ambient air to avoid the oxidation of niobium.

3.1 Copper cavity

The values of the quasi-spherical shape coefficients used to manufacture the copper resonator are $\epsilon_1 = 2 \times 10^{-3}$ and $\epsilon_2 = -2 \times 10^{-3}$ (Fig. 2.4) .

In practice, a quasi-spherical cavity is formed of two identical hemispheres of copper (Fig. 2.5) joined together. Four conical plugs (Fig. 2.11) are inserted into the quasi-sphere: two of

them allow the passage of the HF transmitting and receiving antennas. The other two make it possible to have equal pressure between the outside of the resonator and the inside so as to limit mechanical stresses.

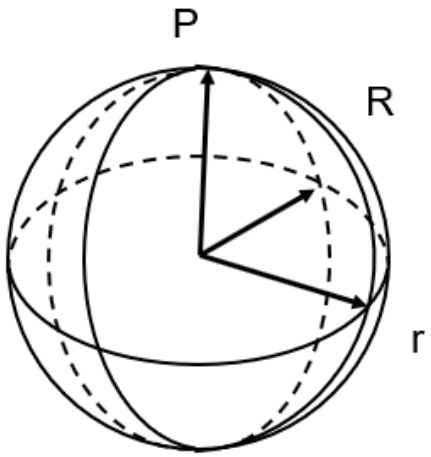

Figure 2.4: The orientation of coordinate system and local radii of the inner triaxial ellipsoid. Depth 25.000 mm, R largest radius 25.050 mm ($\epsilon_2 = -2 \times 10^{-3}$) and r smallest radius 24.950 mm ($\epsilon_1 = 2 \times 10^{-3}$).

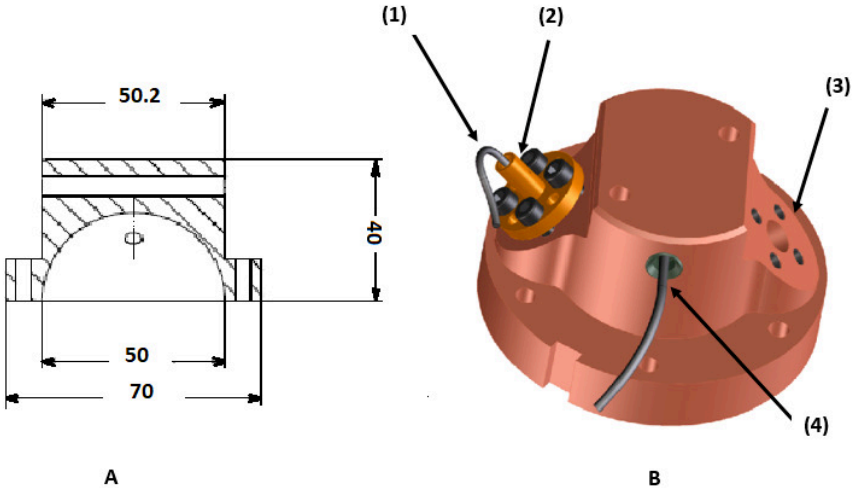

Figure 2.5: A: Cross-sectional view of the hemisphere. B: Positioning of the plug on a half-sphere. (1) Antenna cable, (2) Plug, (3) Plug insertion hole, (4) Thermometer (remark: no thermometer was actually inserted in the plug during the series of tests described in this document)(drawing made by Alexandre Vergé from Cryosud Services the company by kind permission of the author).

3.2 Superconducting cavity

This section gives a historical overview with some basics elements about superconductivity. The practical realization of the superconducting cavity is then approached.

3.2.1 A brief introduction to superconductivity

Superconductivity was fortuitously discovered in 1911 by Heike Kamerlingh Onnes and his team at Leiden University, in the course of a systematic study of the electrical conductivity of metals at low temperatures [45]. During a measurement consisting in gradually lowering the temperature of a sample of mercury, the operator was surprised to find that below a particular temperature called afterwards the critical temperature and equal to $T_c = 4.15$ K, the electrical resistivity of the sample abruptly disappeared (see Figure 2.6) [46] [47]. The continuation of the study showed that other materials had this property like lead ($T_c = 7.2$ K) or niobium ($T_c = 9.2$ K). It was also established that it was possible to remove the superconducting effect if the density of electrical current through it exceeds a critical value (J_c) [48].

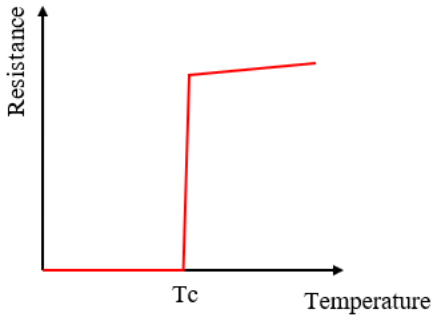

Figure 2.6: Qualitative representation of the electrical resistance as a function of temperature around the transition between normal and superconducting states. At a temperature lower than the critical temperature (T_c), the electrical resistance vanishes.

It was in 1933 that Walther Meissner and Robert Ochsenfeld demonstrated that superconductors expel external magnetic fields acting like a perfect diamagnetic with an internal magnetic field equal to zero [49]. Moreover, if the external magnetic field exceeds a so-called critical field value (H_c), the material loses its superconducting properties and becomes normal. The critical field, the critical current density and the critical temperature allow one to define a domain of existence of superconductivity as illustrated by Figure 2.7.

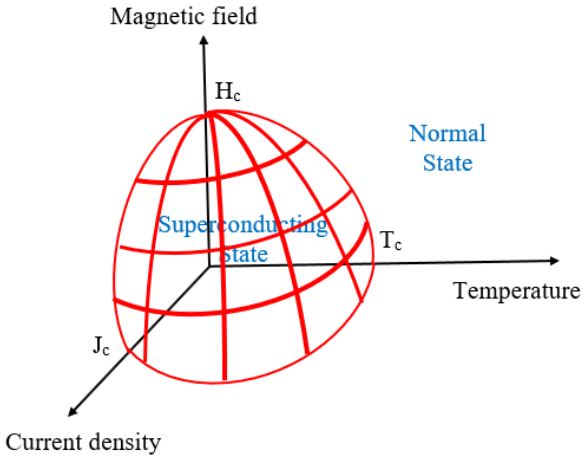

Figure 2.7: The superconducting domain is bounded by the values of the critical field H_c, the critical density current J_c and the critical temperature T_c.

The behavior of superconductors with respect to an external magnetic field has led to a distinction between two types of materials.

- Type I superconductors abruptly lose their superconductivity once the critical field H_c is reached (see Figure 2.8 (A)). These materials are pure metals like lead.
- Type II superconductors exhibit a gradual disappearance of superconductivity from a so-called 'lower' critical field H_{c1} to disappear completely beyond a so-called 'upper' critical field H_{c2} (see Figure 2.8 (B)). Most Type II superconductors are alloys and compounds. Although niobium is a pure metal, it is also a Type II superconductor[3].

For many years, all known superconducting materials had critical temperatures below 24 K. During the 1980s, a new family of superconducting materials, the cuprates, was explored. Some of them were found to have a critical temperature above that of boiling liquid nitrogen (77 K). Since then the search for a high temperature superconductor with increasingly high critical temperatures has not stopped. In 2020 a critical temperature of about 288 K (15 °C) was reported for carbonaceous sulphur hydride under high pressure (about 267 GPa) [50].

The theoretical understanding of superconductivity has gone through several stages. The first phenomenological model dates from 1933 and is due to Fritz and Heinz London who by a

[3]The other two pure metal type II superconductors are vanadium and technetium.

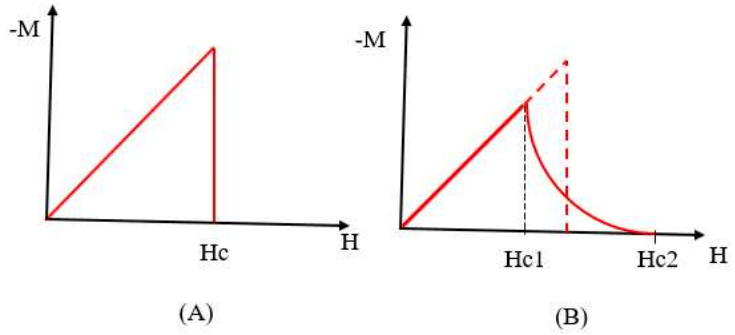

Figure 2.8: Magnetization curve of the two types of superconductor. The magnetization of the material M is related to the magnetic field applied H by the magnetic susceptibility χ (*i.e.* M= χH). In the superconducting state, that is for a magnetic field H lower than the critical magnetic field H_c for type I superconductors (see Figure A) or H_{c1} for type II superconductors (see Figure B) , the magnetization is equal and opposite to the magnetic field. In other words, the susceptibility $\chi = -1$ and the superconductor is a perfect diamagnetic. For the type I superconductor (see Figure A) if the magnetic field H is higher than the critical field, the magnetization abruptly decreases. For the type II superconductor (see Figure B), if the magnetic field H is higher than the 'lower' critical field H_{c1} then the magnetization gradually decreases and disappears at the 'upper' critical field H_{c2}.

set of equations were able to describe the diamagnetism observed by Meissner and Ochsenfeld [49]. They showed that the magnetic field decreases from the surface of the superconductor exponentially following equation 2.11.

$$B(x) = B_0 e^{\frac{-x}{\lambda_L(T)}} \tag{2.11}$$

where $B(x)$ is the magnetic induction at the distance x between the surface of the superconductor and the point considered, B_0 is the magnetic induction on the surface of the superconductor, and $\lambda_L(T)$ called the London penetration depth. This characteristic length depends on the temperature.

In 1934, Gorter and Casimir developed a thermodynamic model [51] in which the transition to the superconducting state is considered to be a phase change. Their model is based on the existence of two fluids, one superconducting and the other normal, with respective densities $n_s(T)$ and $n_n(T)$, the total electron density being the sum of the two ($n(T) = n_s(T) + n_n(T)$). At a temperature of 0 K, all electrons are superconducting while above the critical temperature

T_c all electrons are normal. Within the material, the superconducting electron density is uniform and equal to n_{s-in}. From the surface of the material, the density of superconducting electron evolves exponentially from 0 to n_{s-in} according to equation 2.12.

$$n_s(x) = n_{s-in}(1 - e^{\frac{-x}{\xi(T)}}) \tag{2.12}$$

where $\xi(T)$ is the coherence length. This characteristic quantity depends on the temperature. London penetration depth and coherence length give a way to distinguish the two types of superconductor:

- for type I superconductors:

$$\frac{\lambda}{\xi} < \frac{1}{\sqrt{2}} \tag{2.13}$$

- for type II superconductors:

$$\frac{\lambda}{\xi} > \frac{1}{\sqrt{2}}. \tag{2.14}$$

Other phenomenological models were subsequently developed such as that of Vitaly Ginsburg and Lev Landau in 1950 [52]. However it was only in 1957 that a microscopic theory was published by John Bardeen, Leon Cooper and John Robert Schieffer known as the BCS theory [53]. Even so this last theory does not explain the behavior of all superconductors. Just like the research on new superconducting materials which strives to find ever higher values of critical field, critical current density, and critical temperature, theoretical research is still active. Table 2.2 gives some characteristic values for the materials used during this study.

Table 2.2: Characteristic values of some superconducting materials: Critical temperature T_c, critical magnetic induction B_c, London penetration depth λ_L and coherence length ξ_0 . The critical magnetic induction B_c is linked to the critical magnetic field H_c by the relation $B_c = \mu_0 H_c$, where μ_0 is the vacuum permeability [4].

Material	$T_c[K]$	B_c [mT]	λ_L [nm]	ξ_0 [nm]
Pb	7.196	80.3	37	83
Nb	9.250	194.4	39	38

3.2.2 Practical aspects of the superconducting cavity

Ideally, for the present application, the superconducting material should be chosen so that the system can operate at a temperature below half of its critical temperature. Indeed, below this temperature, the characteristics of the superconductor (*e.g.* the surface resistance) are more stable as a function of the temperature [54]. For practical reasons, niobium was chosen. The resonator is made of copper with a niobium coating of mean thickness 3 μm. The interest of a niobium coating on copper compared with bulk niobium lies in better thermal conductivity for the same mechanical strength as well as a lower sensitivity to external magnetic fields [55].

The cavity, although designed in France, was manufactured in Italy under the supervision of our colleagues from INRiM. The copper cavity was machined by the company DG-Technology in Turin. The deposition of a superconducting niobium film on 12 conical plugs and two copper hemispheres were carried out by the Italian National Inter-university Consortium of Materials Science and Technology (INSTM).

The deposition of the niobium coating was carried out in several steps. First, the parts (hemisphere and conical plugs) were chemically treated to polish the surface and improve the quality of the niobium deposit. A chemical polishing process called SUBU5 removed a material thickness between 5 and 10 μm. This thickness was determined by weighing before and after the chemical process. The niobium film was then deposited by magnetron sputtering at temperatures below 350 °C so as not to modify the mechanical properties of the copper substrate. The final activity report of INSTM states the thickness of the film is between 2 and 4 μm (see Fig. 2.9). Note that the thickness of the niobium coating is much greater than its coherence length (see table 2.2). From this point of view, the niobium coating can therefore be considered as a bulk superconductor.

In the presence of air, an oxide layer forms naturally on the niobium coating. This phenomenon increases the surface resistance of the cavity, thereby reducing its quality factor. [56]. To slow the formation of this oxide layer, the resonator is either maintained in a vacuum enclosure, or, during its installation in the cryostat, preserved from the ambient air by a constant flow of helium blown through the cavity. It is possible to remove the oxide layer by baking the resonator at a temperature of 100 to 150 °C under ultra-high vacuum ($< 10^{-5}$ Pa)

Figure 2.9: Arrival of the superconducting cavity at the laboratory at the end of January 2018. The hemisphere is protected by a vacuum sealed hermetic plastic protective envelope. The silvery appearance of the internal surface of the hemisphere is due to the 3 μm thick layer of niobium.

[57]. The latter process has not yet been used with the present superconducting cavity.

3.3 Antennas

The resonator is equiped with two antennas, one for emission, the other for reception. It should be noted however that because the dipole is symmetrical this designation is arbitrary.

From a practical point of view, the antennas are made from a non-magnetic coaxial cable (Fig. 2.10). The non-magnetic aspect is required so as not to perturb the superconducting effect. When the antennas are placed in the resonator, their position in the plugs is adjusted using a vector network analyzer so as to obtain the best coupling (see Figures 2.11, 2.12 and 2.13).

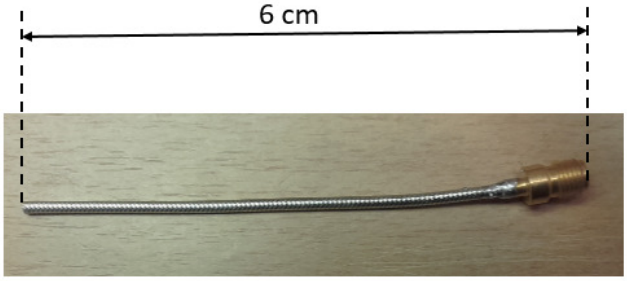

Figure 2.10: The antennas are made from a coaxial cable of outer diameter 2.2 mm. The materials used for cable manufacturing are non-magnetic. One end of the cable is soldered to an SMA connector (shown on the right).

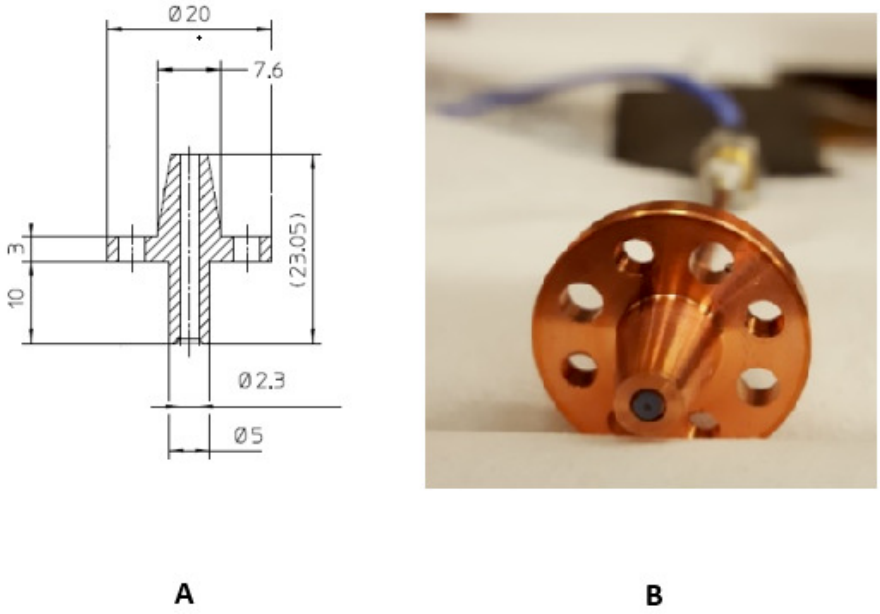

Figure 2.11: A: Plug dimensions in millimetres. B: An antenna in its plug ready to be inserted into the resonator.

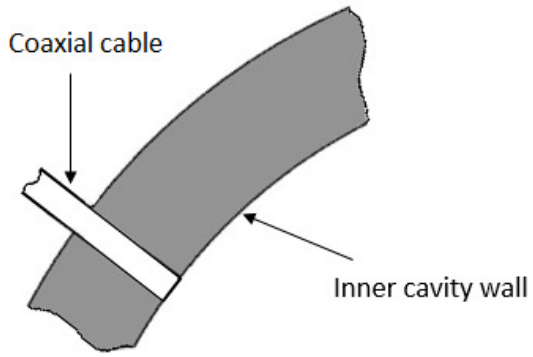

Figure 2.12: During assembly, the end of the antenna is flush with the internal wall of the cavity. Its position is then adjusted so as to obtain the strongest possible signal on the resonances. This last operation is carried out with the help of a network analyzer. As soon as the optimal position is found, the antenna is glued into its plug

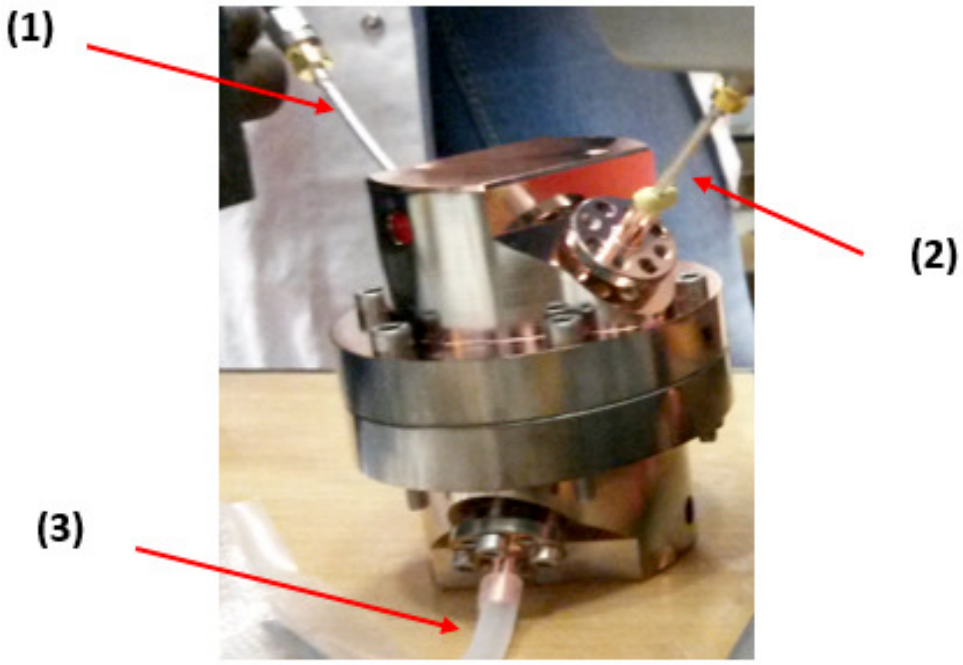

Figure 2.13: Installation of the antennas on the resonator: (1) Emitting antenna, (2) Receiving antenna (3) Pipe bringing a flow of helium into the cavity .

Chapter 3

Cryostats

Niobium becomes superconducting when cooled below its critical temperature (9.2 K). This means one needs to use a cryostat. There are basically two ways to cool a system to cryogenic temperature [58], sometimes called the “wet” and the “dry” methods.

The ”dry method” uses machines called cryocoolers that produce cold using a working gas. This gas follows a specific thermodynamic cycle composed of successive compressions and expansions. Cryocoolers are relatively convenient to use but their mechanism usually generates temperature oscillations on the chilled part. However, they allow for uninterrupted operations over several months.

The “wet method” uses a bath of cryogenic fluid in which the system is immersed. This method allows one to reach a temperature down to around 77 K with liquid nitrogen (N_2) or 4.2 K with liquid helium (^{4}He) at atmospheric pressure. From an experimental point of view, the use of cryogenic fluids needs requires more attention than a cryocooler. Indeed, the evaporation of cooling liquids means frequent refills are needed to maintain operation. Moreover, the high price and shortages of liquid helium have the negative effect of limiting the duration of the experiments.

To reach a temperature of 4.2 K from room temperature, the cryostat is first cooled with liquid nitrogen. Once the temperature reaches 77 K, the liquid nitrogen is then evacuated and replaced by liquid helium. To improve heat transfer, a small amount of helium gas is placed in the vacuum chamber of the cryostat at room temperature. This exchange gas is removed when the temperature of the resonator is about 15 K.

1 Overview

For practical reasons, the wet cooling method was chosen. Chronologically, three versions of cryostat were used.

The first version (2018), Mark I , allowed us to validate the measurement principle. It allowed us to check that the resonant cavity worked correctly. It also allowed us in particular to observe the transition of the niobium coating to the superconducting state and to measure the frequency resolution of the system.

The second version (2019), Mark II, was a modification of the first cryostat to make it possible to check the behaviour of the system under pressure. A tube transporting helium gas to the resonator was added. This was thermally isolated from the liquid helium bath by a vacuum jacket. Thermometers were installed along the tube delivering the helium gas to allow correction of hydrostatic pressure effects. Moreover, a pressure vessel was added to homogenize the temperature of the gas in the resonator.

Nevertheless, the Mark II cryostat was not intended for pressure measurements. In particular, the diameter of the tube transporting the helium gas to the resonant cavity was not designed to reduce the effects of thermal transpiration. As a suitable modification of the cryostat Mark II proved too difficult to implement, a further cryostat version (2020), Mark III, was designed based on experience obtained with the two previous versions. The sizes of all of them were chosen to fit inside the same existing test Dewar.

This chapter describes all three in turn.

2 The Cryostat Mark I (2018)

The first cryostat was designed in late 2017 and manufactured and assembled in early 2018. As its purpose was to validate the operation of the superconducting cavity and the measurement principle, its design was relatively simple (see Appendix B Fig. B.2).

The resonator is hung from a copper platform inside the vacuum chamber (Fig. 3.1a). The two plugs on the lower part of the resonator guarantee equal pressure between the inside and outside of the cavity. The two plugs in the upper half of the resonator bear the RF antennas. They are connected to coaxial cables that exit the vacuum chamber, pass through liquid helium and exit outside the Dewar (Fig. 3.1a). A central tube holds the vacuum chamber. It allows one either to pump out the resonator or inject helium gas into it. It also allows the passage of the electrical wires of the two heaters and the two Cernox^{TM} RTD temperature sensors. One heater and Cernox^{TM} sensor are fixed to the upper part of the resonator. The other heater and Cernox^{TM} sensor are attached to the copper platform from which the resonator is suspended.

•The external reservoir (Dewar)

The external reservoir is a cylindrical cryogenic storage Dewar of external height 1437 mm and diameter 286 mm. Its internal depth is 1355 mm and internal diameter 140 mm. At 366 mm from the top, there is an enlargement of the internal cavity over a length of 293 mm with a diameter of 200 mm.The capacity of the Dewar is around 20 L. The internal vacuum of the Dewar was regularly pumped out before experiments to prevent the effects of possible leakage.

•Thermal radiation protection shields

The cryostat was equipped with two sets of thermal radiation shields consisting of five copper disks with a central hole and a cut-out for passing wires or tubes. The first series was located in the upper part of the cryostat and surrounded the central tube. The second series was inside the central tube. Figure 3.2 shows a drawing of the cryostat in the Dewar as well as a photograph of the cryostat. At the time the photograph was taken, the copper radiation baffles were not yet available and were replaced temporarily by aluminium sheets mounted on polyurethane foam discs.

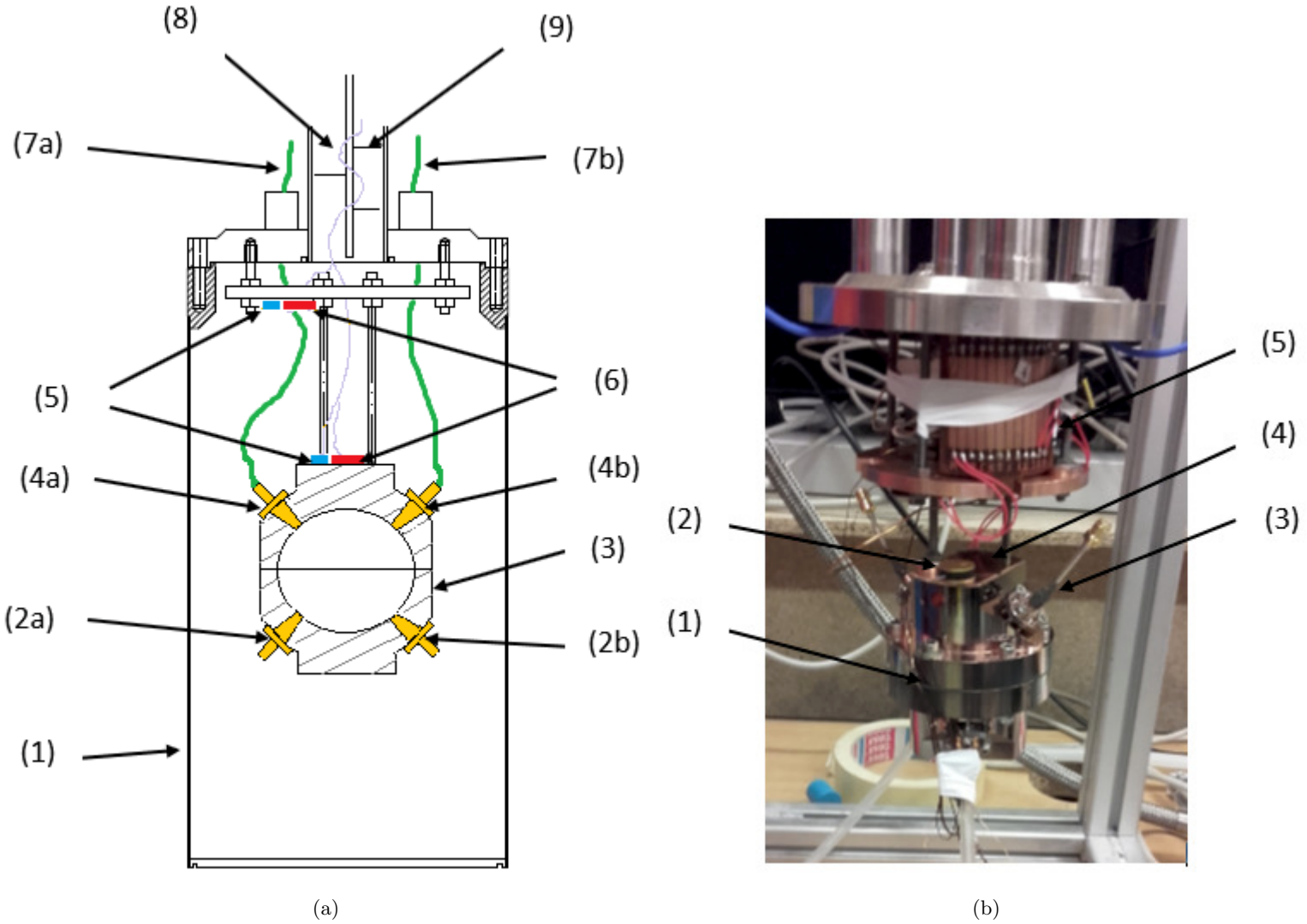

(a) (b)

Figure 3.1: Cryostat Mark I: (a): Cross-sectional drawing of the vacuum chamber. (1)Vacuum chamber, (2a) and (2b) Pressure equalisation plugs; (3) Superconducting quasi-spherical resonator, (4a) and (4b) antenna plugs, (5) Cernox^{TM} RTD temperature sensors, (6) Heaters, (7a) and (7b) coaxial cables, (8) Cables of temperature sensors and heaters, (9) Radiation baffles; (b): (1) Superconducting quasi-spherical resonator, (2) Cernox RTD temperature sensor, (3) Antenna, (4) Heater, (5) Thermalisation board for electrical wires

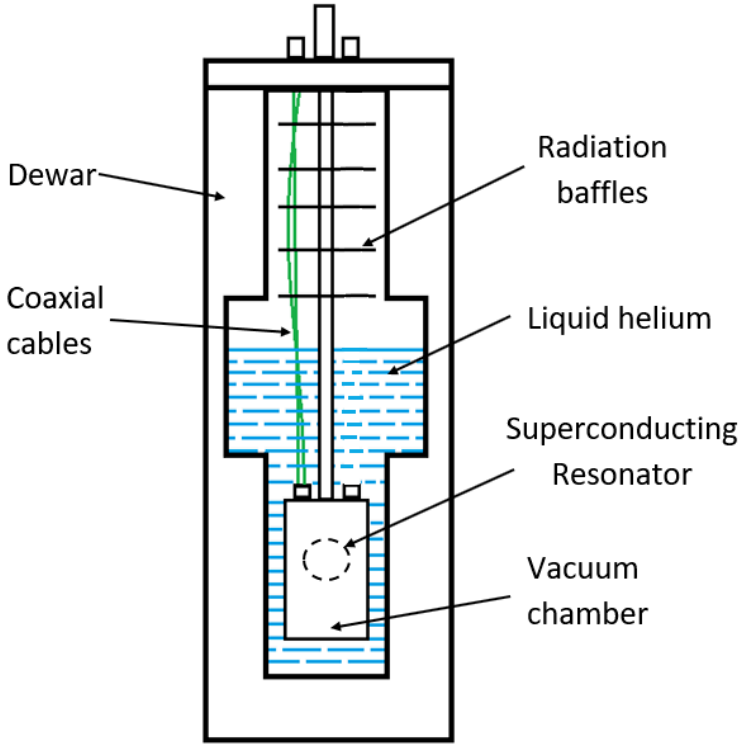

(a)

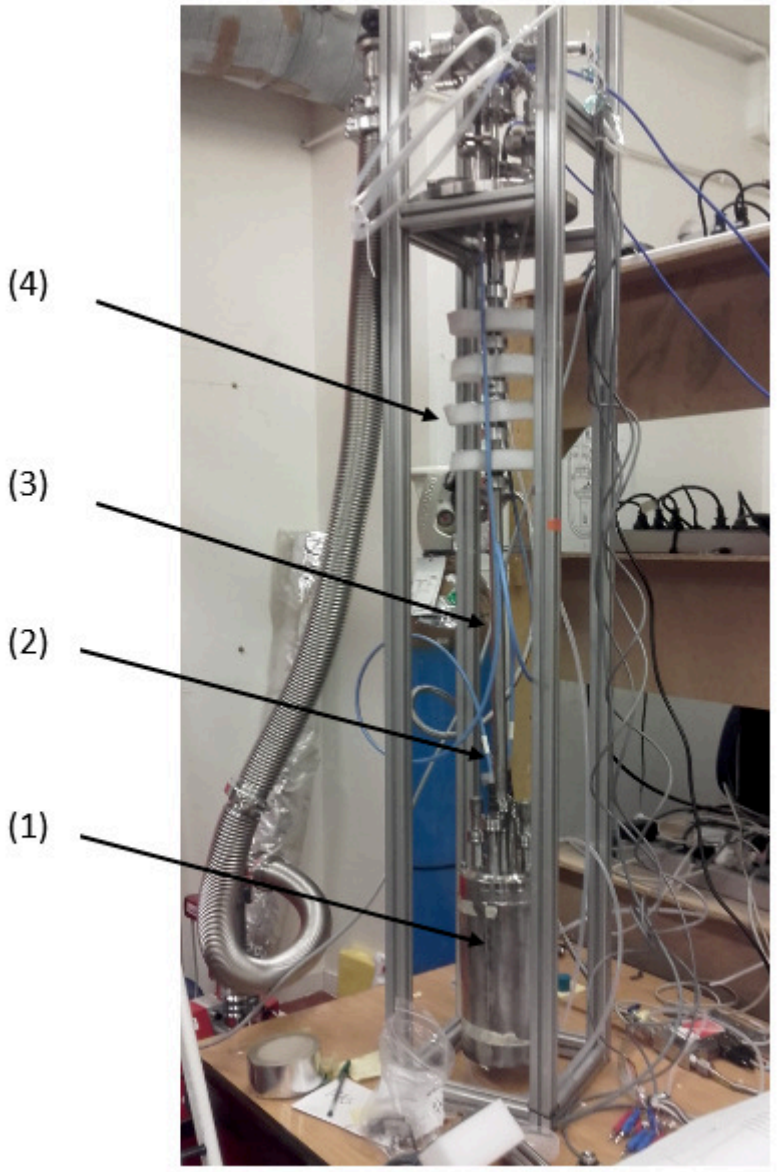

(b)

Figure 3.2: Cryostat Mark I: (a): Cross-sectional view of the Dewar containing the cryostat ; (b): (1) Vacuum chamber, (2) RF coaxial cables, (3) Central tube which retain the vacuum chamber, (4) Radiation baffles: During the first experiments, the copper radiation baffles were not yet available. They were later replaced by aluminium sheets mounted on polyurethane foam discs.

3 The Cryostat Mark II (2019)

With the cryostat Mark I, the only way to fill the resonator with helium gas was *via* the central tube. As this tube is immersed directly in liquid helium (T = 4.2 K), the gas temperature could not be controlled. To remedy this problem, in the cryostat Mark II (2019), a new tube was installed to transport helium gas from the pressure generator into the pressure vessel. This tube is protected from the liquid helium bath by another tube of larger diameter maintained under vacuum. Since a knowledge of the temperature profile is required to calculate the hydrostatic pressure correction, five platinum resistance thermometers were fixed at intervals along the pressure tube .

To homogenize the temperature of the helium gas the microwave resonator is placed in a copper pressure vessel. For temperature monitoring and regulation, a Cernox^{TM} RTD temperature sensor and a heater were fixed on the pressure vessel lid and on the microwave resonator.

The installation of the insulated pressure tube initially proved to be problematic. In a first version, several mechanical elements of the pressure tube were held together by gluing. During the first pressure tests, a leak was detected. When it was repaired, another one appeared. It then became clear that the tube had to be remade but this time with welded elements.

Figures 3.3, 3.4, 3.5a and 3.5b show the cryostat version Mark II.

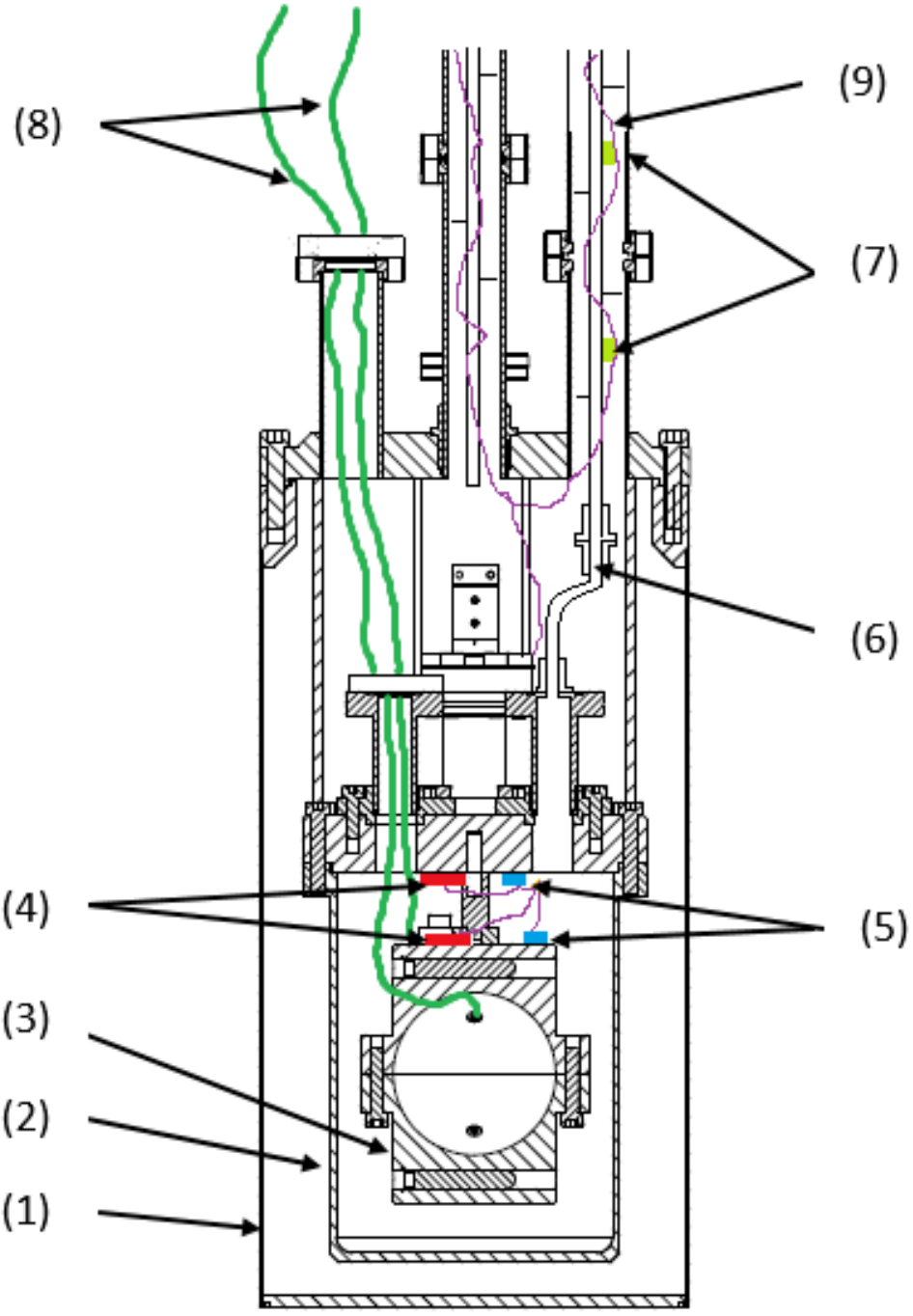

Figure 3.3: Cryostat Mark II (2019): (1) Vacuum chamber, (2) Pressure vessel, (3) Superconducting quasi-spherical resonator, (4) Heaters, (5) Cernox^{TM} RTD temperature sensors, (6) Pressure tube, (7) Platinum RTD temperature sensors, (8) Coaxial cables,(9) Cables of temperature sensors and heaters.

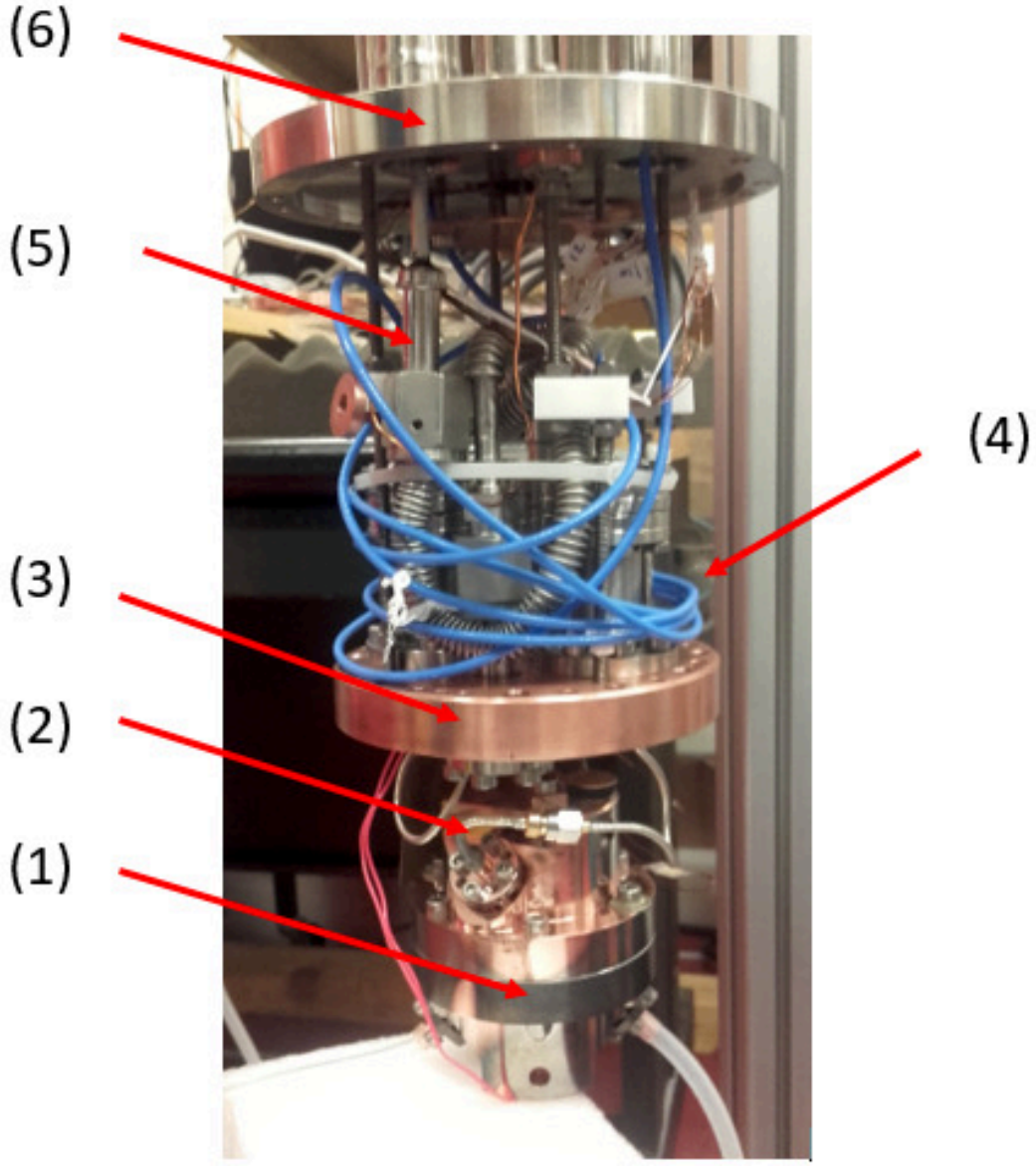

Figure 3.4: Cryostat Mark II: (1) Superconducting quasi-spherical resonator, (2) Antenna, (3) Pressure vessel lid, (4) Coaxial cables, (5) Pressure tube, (6) Vacuum chamber lid.

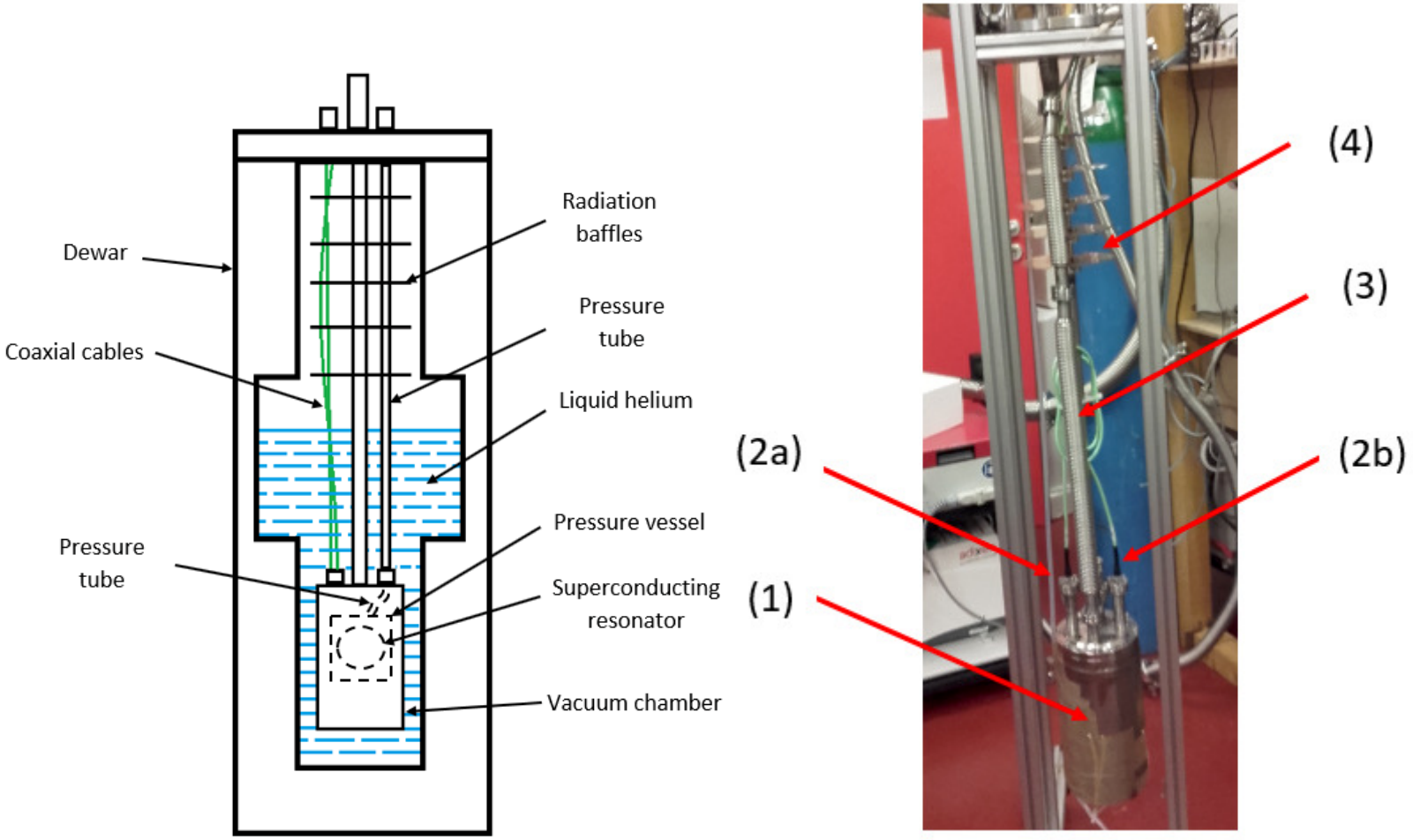

(a) (b)

Figure 3.5: Cryostat Mark II: (a): Cross-sectional view of the Dewar with the cryostat; (b): (1) Vacuum chamber, (2a) and (2b) Coaxial cables, (3) Pressure tube, (4) Radiation baffles.

Experiments carried out with the cryostat Mark II revealed the thermomolecular correction formula recommended by the Guide to the realization of ITS-90 was unexpectedly inadequate [10] 4.8. The thermomolecular effect, also called thermal transpiration, is the appearance of a pressure difference in the pressure tube caused by the difference in temperature of the gas outside the cryostat and in the resonator [8]. This pressure difference is related both to the mean free path of the gas and the dimensions of the pressure tube.

4 The Cryostat Mark III (2020)

A simple way to reduce the thermomolecular effect revealed with the cryostat Mark II is to increase the diameter of the pressure tube. The installation of a larger diameter pressure tube in the cryostat Mark II was considered infeasible, so it was decided to make a third version with a larger diameter pressure tube. The inner diameter was increased from 3 mm to 19 mm (see Figures 3.6 and 3.7).

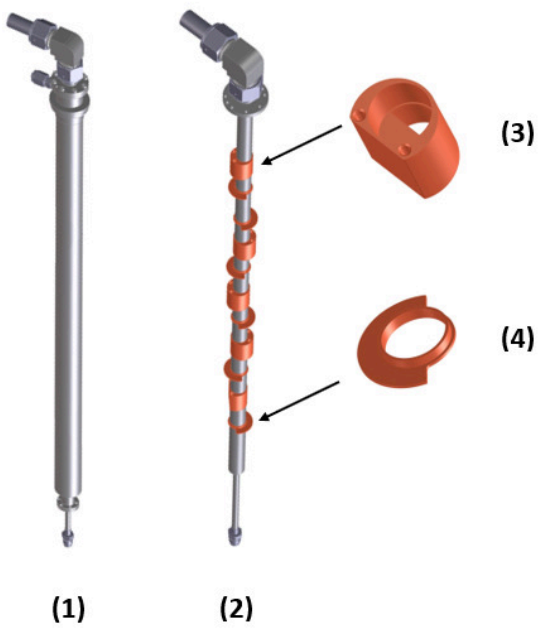

Figure 3.6: Overview of the pressure tube of the Cryostat Mark III (1) Vacuum jacket that thermally protects the pressure tube from liquid helium, (2) Pressure tube equipped with supports for thermometers and with copper radiation baffles, (3) Supports for thermometers with radiation baffles for the pressure tube, (4) Radiation baffles for the vacuum jacket.

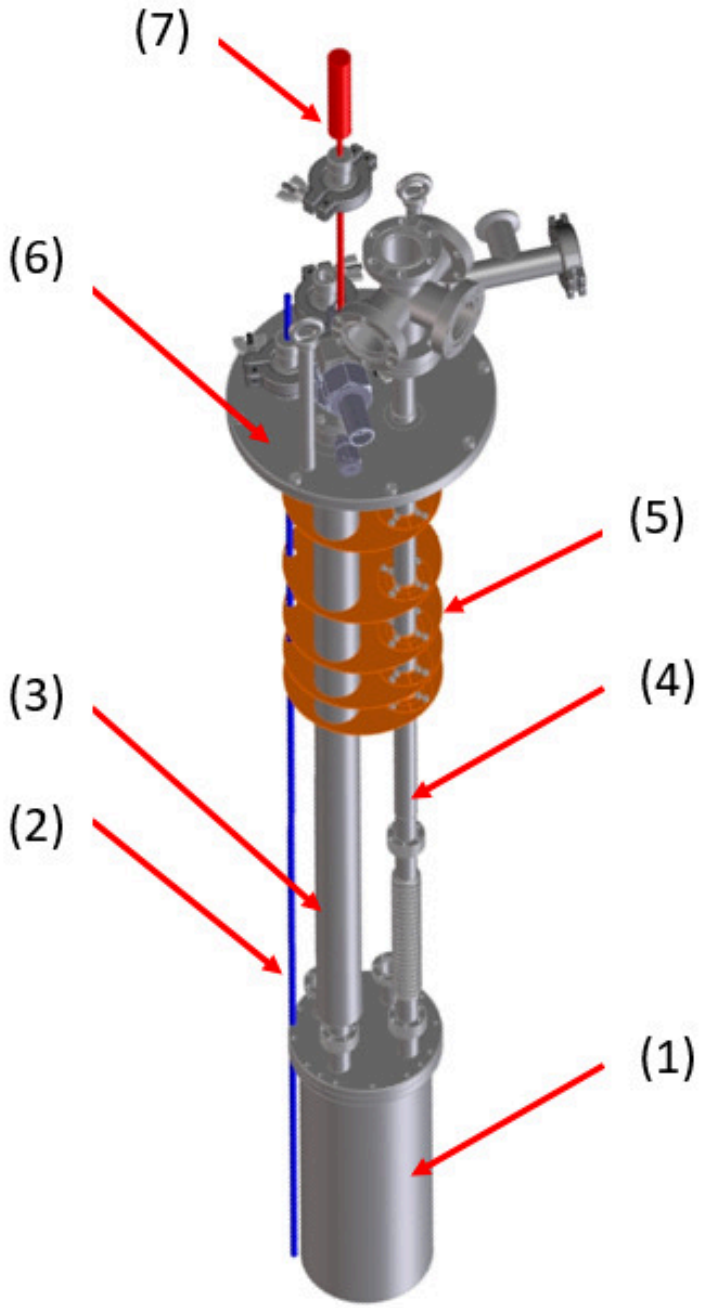

Figure 3.7: Cryostat Mark III (version 2020) (1) Vacuum chamber, (2) Liquid nitrogen extraction line, (3) Pressure tube, (4) Thermometers and heaters wires tube, (5) Radiation baffles, (6) Cryostat lid,(7) Liquid helium level probe. The coaxial cables leading to the antennas are not shown.

5 Estimation of the conduction heat transfer

The modifications of the cryostat affect heat transfer. They relate essentially to the pumping tube for the vacuum chamber, the pressure tube and its the vacuum jacket. These tubes are subjected to a temperature gradient ranging from room temperature to approximately that of liquid helium. For a rod of section A and length L the conduction heat flow is given by

$$\dot{Q} = \frac{A}{L} \int_{T_1}^{T_2} \lambda(T) dT \tag{3.1}$$

where T_1 and T_2 are the temperatures at the ends of the bar and $\lambda(T)$ is its thermal conductivity. The tubes used in the cryostat are made from stainless steel (type 304). For which the average thermal conductivity between 4 K to 300 K is $\lambda_{300K-4K} = 3.06$ kW.m^{-1} [58]. By considering an identical height of liquid helium for the cryostat versions, and the different sections of the tubes, it is possible to compare the different conduction heat flows. Special care was taken in the design of the Mark III cryostat to reduce the heat conduction loss compared to that of the Mark II, as Figure 3.8 shows.

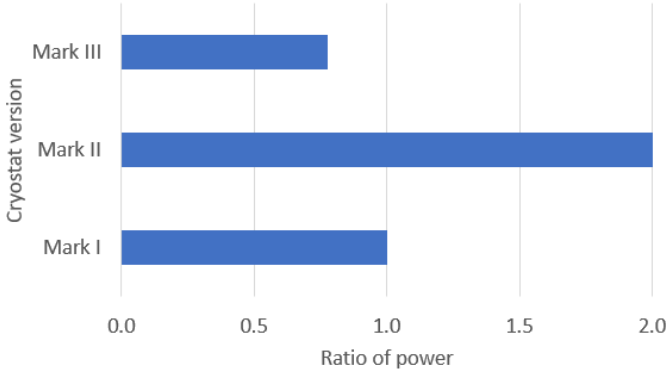

Figure 3.8: Estimation of the ratio of power consumption by conduction heat flow for the three cryostats.

Chapter 4

Experimental set-up

This chapter is devoted to the description of the experimental set-up as well as the presentation of expected physical phenomena. After an overview of the experimental set-up, its various elements are described in detail. The description of the instrumentation is completed in Appendix C. The following section describes the main software used, more details of which can be found in Appendix D. The chapter ends with an inventory of the main physical effects related to the experiment and affecting the pressure measurement.

Initially, at the beginning of 2018, the experiment shared its instrumentation with that of an already existing experiment. Later, in the spring of 2019, it was installed in another room with its own instrumentation, which greatly facilitated day-to-day running.

1 Overview

A simplified schematic of the experiment is shown in Figure 4.1 while Figure 4.2 shows a photograph of it.

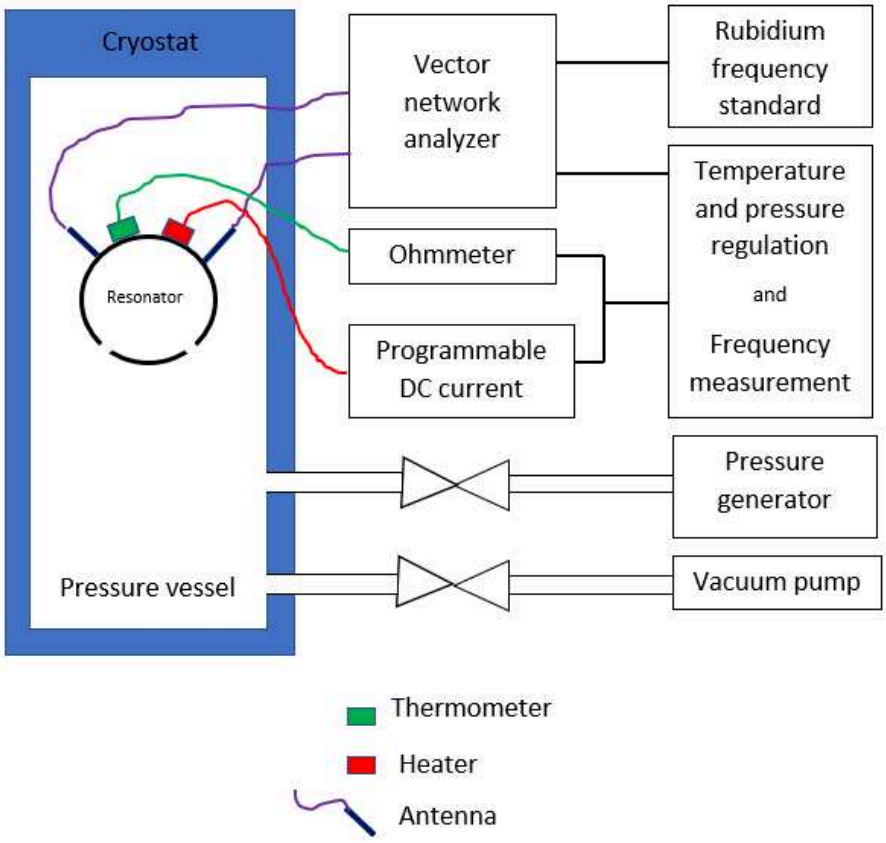

Figure 4.1: Schematic of the overall experiment

To prevent the oxidation of niobium, the cavity of the superconducting resonator is either maintained under vacuum or under helium pressure. The pressure vessel containing the resonator is always maintained under vacuum using a turbomolecular pump. The resonator, equipped with its two microwave antennas, a thermometer and a heater. The emitting and receiving microwave antennas are connected to a vector network analyzer. This is connected via a GPIB link to a computer on which software has been developed to measure the spectrum around the resonant frequencies of the resonator in a given mode. The computer that controls

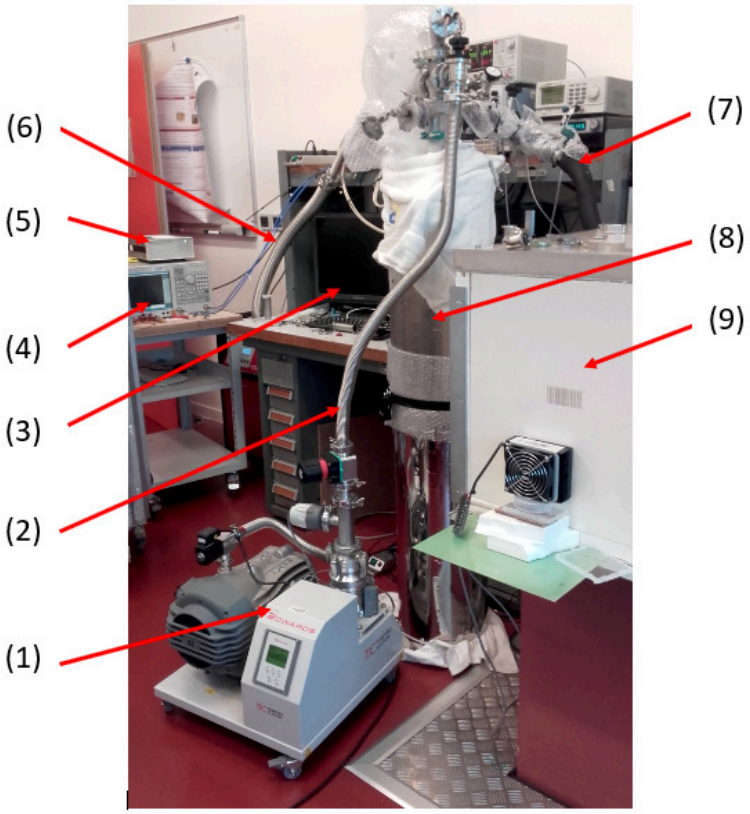

Figure 4.2: Experimental setup during run 5 (June-July 2019): (1) Turbomolecular pump backed by a dry rotary pump (2) Tube linking a turbomolecular pump to the cryostat and allowing one to evacuate gas from the vacuum chamber, (3) Computers, (4) Vector network analyser connected to the microwave resonator, (5) Rubidium frequency standard, (6) Tube linking a turbomolecular pump to the microwave resonator, (7) Tube linking the pressure generator to the vacuum chamber of the cryostat, (8) Experimental Dewar, (9) Pressure generator.

the experiment is also connected *via* a GPIB interface to an ohmmeter enabling the value of the thermometer to be measured and to a current source supplying the heater. The heater is only activated in the temperature regulation phase. To simplify the schematic of figure 4.1, a certain number of elements have been omitted. Three pressure measuring devices are connected to the pressure part of the resonator. The pressure circuit is described later in the present document (*cf.* 2.2). Five thermometers measuring the temperature of the pressure tube in the cryostat are also connected to ohmmeters whose values are read by the computer that controls the experiment. At the start of the experiment, the resonator is cooled down from room temperature to its operating temperature.

- Temperature drop

Since the cryostat containing the resonator is designed to operate with a cryogenic liquid, the working temperature is reached in two stages. The first step is to fill the Dewar containing the cryostat with liquid nitrogen, which allows the system to reach a temperature of 77 K. In a second step, the liquid nitrogen is replaced by liquid helium. This operation is delicate because if there is liquid any nitrogen left in the Dewar, it solidifies on contact with liquid helium and increases consumption of the latter. To avoid this drawback and to ensure that no liquid nitrogen remains, the Dewar is first pressurized with nitrogen gas a little above atmospheric pressure. The liquid nitrogen is thus evacuated by an open pipe rising from the bottom of the Dewar and leading to the outside. Once this has been done, the temperature of the cryostat gradually rises. Once it has reached 100 K, the liquid helium is then poured into the Dewar. To accelerate the drop in temperature, a small amount of helium gas (typically 1 cm^3 at atmospheric pressure) is introduced into the cavity separating the pressure vessel and the vacuum chamber to create a thermal link between the helium bath and the pressure vessel. Once the temperature reaches 20 K, the exchange gas is evacuated by a turbomolecular pump to remove the thermal link between the pressure vessel and the vacuum chamber which is at the temperature of liquid helium, which has the effect of slowing the drop in temperature. The temperature of the cryostat then continues to fall slowly to the temperature of liquid helium (4.2 K). To maintain the cold inside the cryostat while compensating for the evaporation of liquid helium, the Dewar must be refilled from time to time. When the cryostat is fully thermalized, the helium must be refilled every 24 hours to maintain a working temperature of 5.4 K at the location of the resonator. When the temperature of liquid helium is reached and after the ten hours taken for the cryostat to thermalize, the temperature of the resonator can be adjusted using the heater.

- Temperature regulation

The temperature control loop consists of a thermometer and a heater placed on (or near) the resonator and Proportional Integral (PI) control software, the principle of which is described in section 3.1.

- Measurement principle

The measurement can start as soon as the temperature is steady enough (standard deviation less than 50 μK). First, the resonance frequency is measured under vacuum (about 10 μPa). This value is memorized by the computer so that the values of the pressures to be measured can be calculated. The valve connecting the resonator to the turbomolecular pump is then closed. The opening of the pressure generator outlet valve allows gas to enter the resonator through openings provided for this purpose. The fact there is an identical gas pressure inside and outside the resonator reduces the mechanical stresses on the walls of the cavity. After stabilization of the pressure and the temperature of the gas, a new measurement of the resonant frequency can be carried out. At this level, values of resonance can be corrected for thermal expansion. This correction is determined from the measurement of the resonance frequency as a function of the resonator temperature under vacuum. The measured temperature must also be corrected for the offset caused by thermometer self-heating. Knowing the temperature and the resonant frequencies of the cavity with and without gas, we determine the value of the pressure by iterative calculation using the *ab initio* virial coefficients of helium (see 3.3). It only remains for us to correct the calculated pressure for hydrostatic pressure and, if necessary, thermal transpiration effect to determine the pressure at the inlet of the cryostat.

2 Instrumentation

2.1 Helium gas

The helium gas must be highly pure because the measurement principle is based on its characteristics. The chosen gas supplier guarantees the purity of the helium gas to be greater or equal to $99,9999$ % mol with a proportion of (in $\times 10^{-6}$ mol): $H_2O \leq 0.5$, $O_2 \leq 0.1$, $C_nH_m \leq 0.1$, CO≤ 0.1, $CO_2 \leq 0.1$, $H_2 \leq 0.1$.

2.2 Pressure generator

The pressure generator, the principle of which is shown in figure 4.3, is protected from variations of room temperature by a thermal chamber nicknamed the 'B-box'[1]. The gas is supplied by a pressure cylinder at a pressure of 200 bar. A regulator connected to the cylinder reduces this pressure to a level close to atmospheric pressure. The gas passes through the pressure generator through two mass flow controllers, before being extracted from the pressure circuit by a vacuum pump. Two volumes located on either side of the inlet mass flow controller helps to stabilize the pressure and smooth out pressure spikes. The inlet mass flow is set to a fixed value. The output mass flow controller acts as an actuator for pressure regulation. The regulation feedback consists of a resonant quartz pressure sensor (Paros Scientific DIGIQUARTZ® model 745), the output mass flow and regulation software. The control software is the same as that described in section 1.

- Temperature stabilized enclosure: the B-box

Tests have shown that the pressure generator is sensitive to temperature variations. The construction of a suitable climatic enclosure was undertaken to alleviate this effect.

The purpose of this enclosure is not to have a uniform temperature within it but rather to isolate the pressure generator from the outside world. One can tolerate therefore temperature disparities within the B-box provided they are only weakly dependent on variations in room temperature. Tests have shown that for a variation of 1°C in ambient temperature, the

[1] B stands for Bobby (Berg), a guest researcher from the National Institute of Standards and Technology (NIST), who suggested we use it to stabilize the temperature of the experimental apparatus [59].

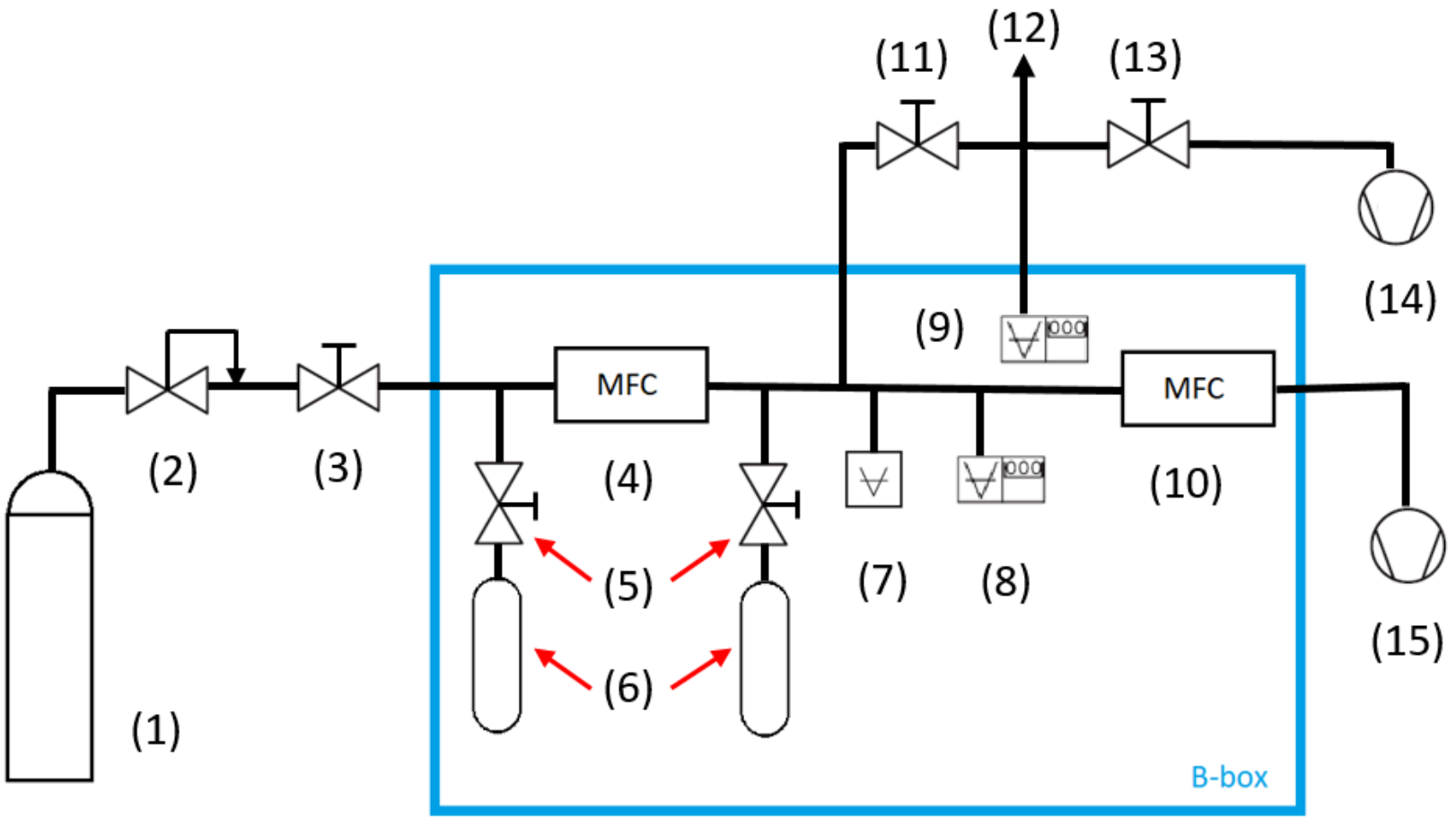

Figure 4.3: Pressure generator schematic: (1) Gas supply, (2) Regulator, (3) Manual valve, (4) Mass flow controller, (5) Valves, (6) Volumes, (7) Pressure sensor (Baratron), (8) Pressure sensor for pressure regulation (DIGIQUARTZ®), (9) Pressure sensor (DIGIQUARTZ®) used as pressure reference, (10) Mass flow controller, (11) Inlet gas valve toward the microwave resonator, (12) Part connected to the microwave resonator in the cryostat, (13) Inlet valve gas evacuation, (14) Turbomolecular vacuum pump, (15) Turbomolecular vacuum pump.

variation in internal temperature is less than 0.05°C.

The B-box consists of an extruded polystyrene box (length 130 cm, width 100 cm, height 100 cm) in which the pressure generator is installed. To control its internal temperature, convection is created using fans. The air flow passes through radiators mounted on Peltier modules (for reference see Appendix C). A temperature controller located outside the B-box measures the temperature of the air flow using a sensor and adjusts its value via one of the Peltier modules (see 4.4).

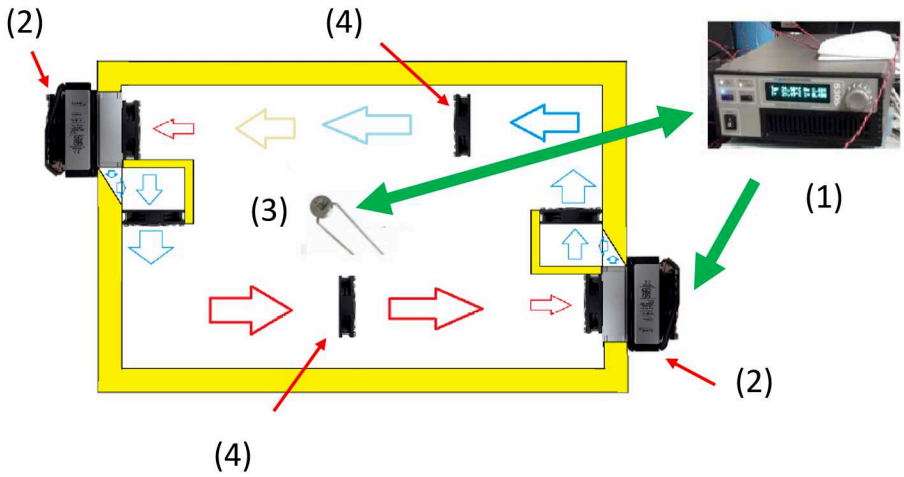

Figure 4.4: Simplified schematic of the B-box: (1) temperature controller, (2) Peltier modules: integrated into the air flow going around the enclosure by absorbing hot air (symbolized by red arrows) and restoring cooled air (blue arrows), (3) thermistor, (4) fans. The solid green arrows represent the links between the temperature controller, the thermistor and one of the Peltier modules.

Figure 4.5 shows a photograph of the experiment during a transfer of liquid nitrogen. The B-box appears in the foreground on the right.

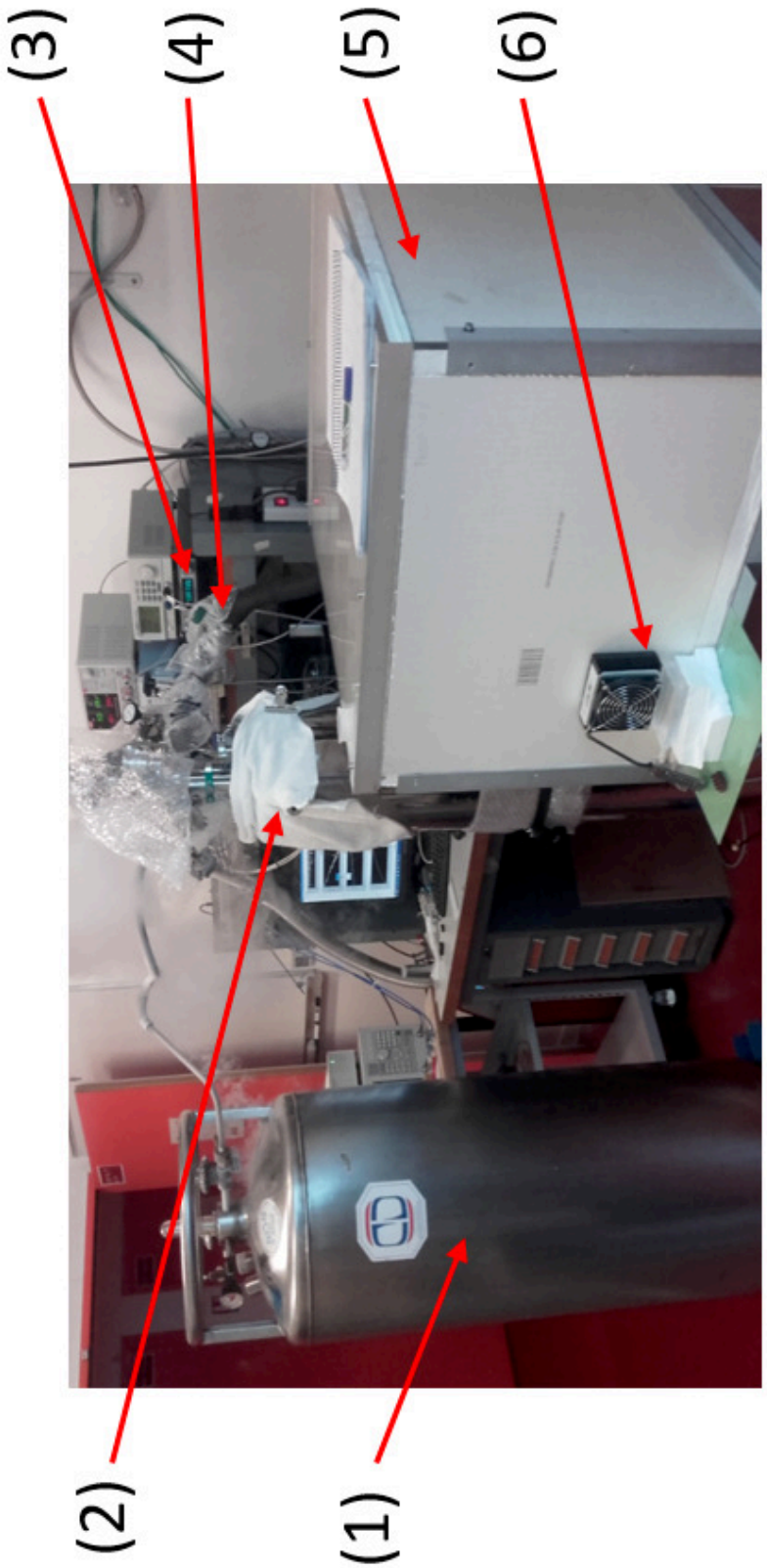

Figure 4.5: Experimentation during liquid nitrogen transferring: (1) Liquid nitrogen storage dewar, (2) Experimental Dewar, (3) Temperature controller,(4) Pressure generator outlet valve allowing gas to fill the microwave resonator, (5) B-box, (6) Peltier module.

3 Software

3.1 Pressure and temperature regulation

This control software, based on the proportional-integral (PI) control algorithm, was first developed with LabVIEW^{TM} (a visual programming language from National Instruments) by Laurent Pitre in 1997 for temperature regulation between 1 K and 30 mK. With a classic PI controller [60] shown with its regulation loop in Figure 4.6, the proportional action P creates a proportional command of a gain K_P to the error *e(t)* while the integral action I creates a proportional command of a gain K_I at the integral of the error *e(t)*. These two actions are combined while their gains K_P and K_I are kept constant. In the present experiment, within a definable interval U (upper value) and L (lower value) around the set point, the PI regulation is traditional. Generally, this interval is chosen so that it corresponds to the tolerated temperature fluctuation. Outside this interval, the coefficients are defined as a function of the position and the direction of temperature change relative to the set point. In all, five pairs of coefficients P and I are used to regulate the temperature:

1. one for when the temperature lies above the set point and falls towards it,
2. one for when it lies below the set point and rises towards it,
3. one for when the temperature lies above the set point and rises even higher,
4. one for when it lies below the set point and falls even lower,
5. one for a defined interval around the set point.

Figure 4.7 shows the area of the front panel for entering proportional and integral coefficients extracted from the front panel of the program. During the experiment, these coefficients are adjusted manually.

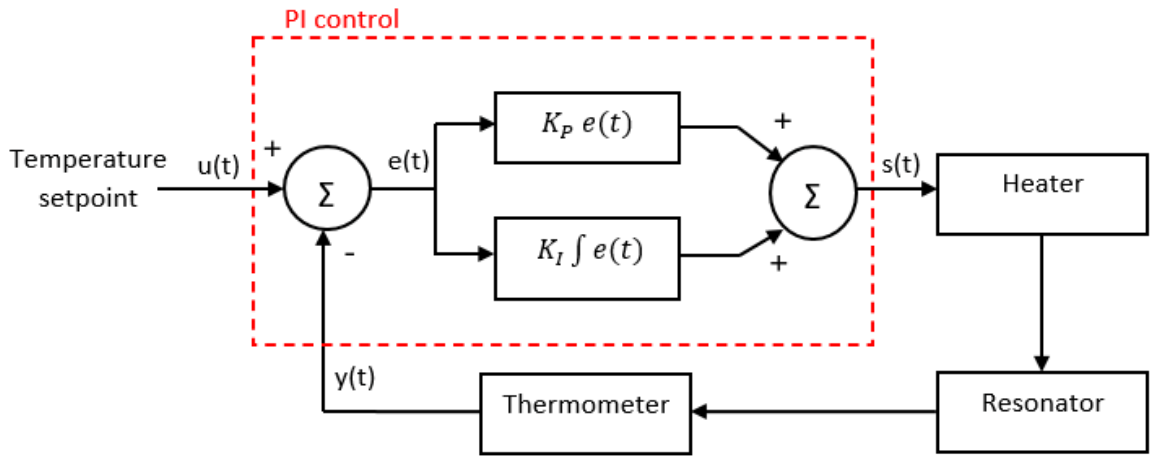

Figure 4.6: Temperature regulation loop schematic.

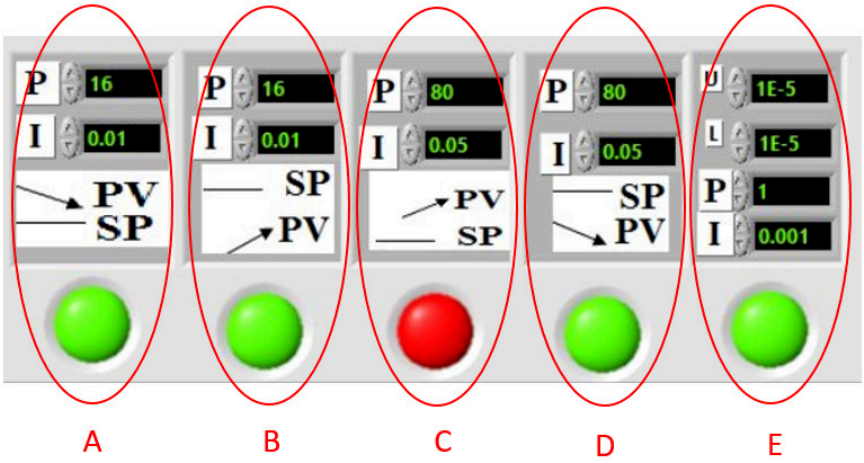

Figure 4.7: Area of the front panel of the LabVIEW^{TM} control program. (A) Coefficients P and I used when the temperature lies above the set point and falls towards it, (B) Coefficients P and I used when the temperature lies below the setpoint and rises towards it, (C) Coefficients P and I used when the temperature lies above the setpoint and rises even higher, (D) Coefficients P and I used when the temperature is below the setpoint and falls even lower, (E) Coefficients P and I used when the temperature lies in the interval defined by U and L around the set point. U corresponds to a temperature interval above the setpoint and L to one below it.

In addition to the variable P and I coefficients depending on the position and the direction of variation of the quantity to be regulated with respect to the setpoint, there is a 'step' function. This function allows one to strengthen the corrective action outside the area defined by U and L when the signal moves away from the setpoint, by adding an adjustable pulse to the actuator control.

Three operating zones can thus be defined. The first corresponds to the interval defined by U and L around the set point. The second lies close to the previous limit and corresponds to the area where the pulses created by the 'step' function have an influence. The third zone lies beyond the second one.

3.2 Fitting method

The vector network analyzer measures the scattering parameter S_{21} of the microwave resonator. This parameter, complex number, is measured in a frequency range ($\approx$ 20 MHz) comprising the triplet of the mode studied but the measurement points are concentrated around the resonant frequencies so as to be able to characterize them as well as possible. The data thus collected are then fitted by a suitable function to determine the resonant frequencies and half-widths of the triplet. The fit is calculated by a program in LabVIEW^{TM} written by May *et al.* [37]. It implements the Levenberg-Marquardt method, an iterative algorithm for solving non-linear least-squares problems [61]. The model function used for the fitting is [37]:

$$S_{21}(f) = \frac{A_p f}{f^2 - (f_{lnp}^{\varsigma} + i g_{lnp}^{\varsigma})^2} + B + C(f - f_{lnp}^{\varsigma}) + D(f - f_{lnp}^{\varsigma})^2 \tag{4.1}$$

where A_p, B, C and D are complex constants, f_{lnp}^{ς} the resonant frequencies and g_{lnp}^{ς} the half-widths of the triplet components. From experimental data (source He-run7), Figure 4.8 shows the S_{21} values around the three resonant frequencies. Figures 4.9 and 4.10 show the values of S_{21} for the highest frequency peak. Figure 4.11 shows the residuals of the S_{21} fit.

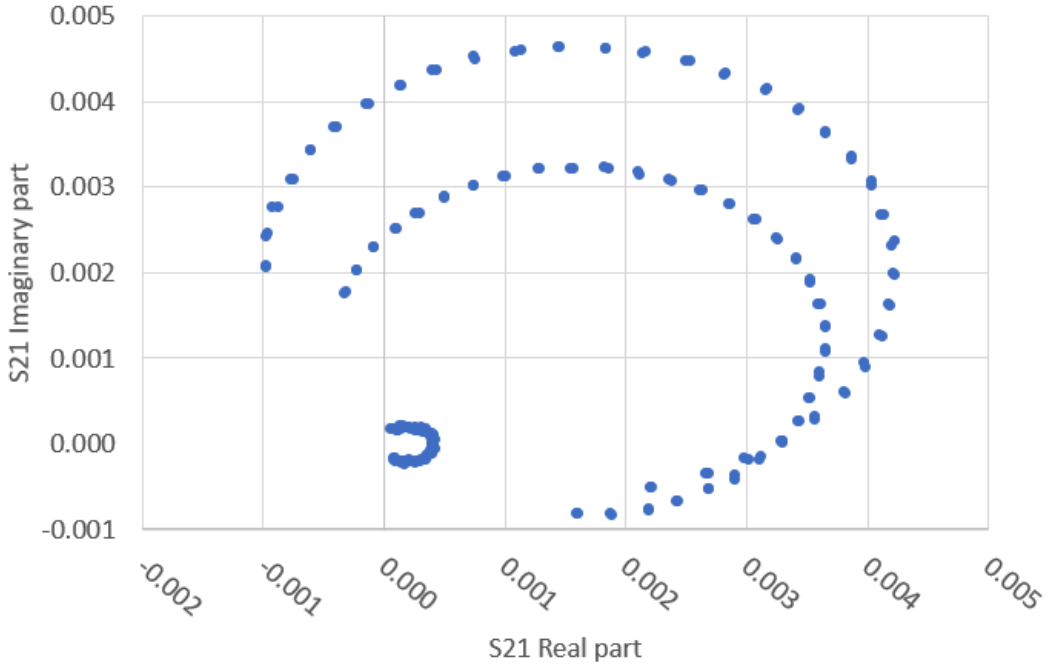

Figure 4.8: Measured values of S_{21} around the three resonant frequencies. Each elliptic arc corresponds to a resonance the size of which increases with the quality factor. The resonances are scanned over twice.

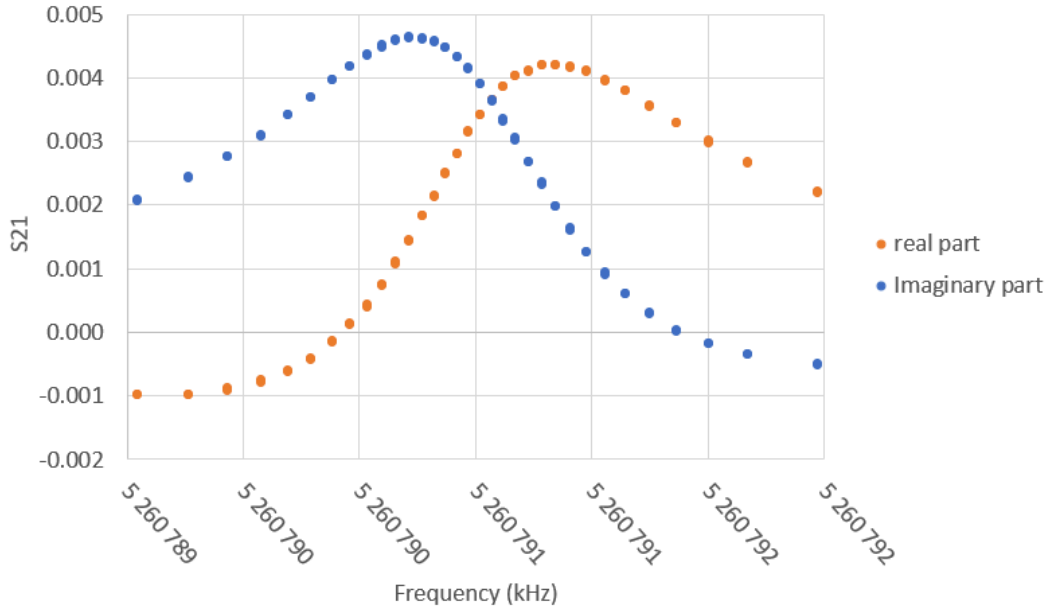

Figure 4.9: Graph of measured values of S_{21} for the highest frequency peak of the triplet.

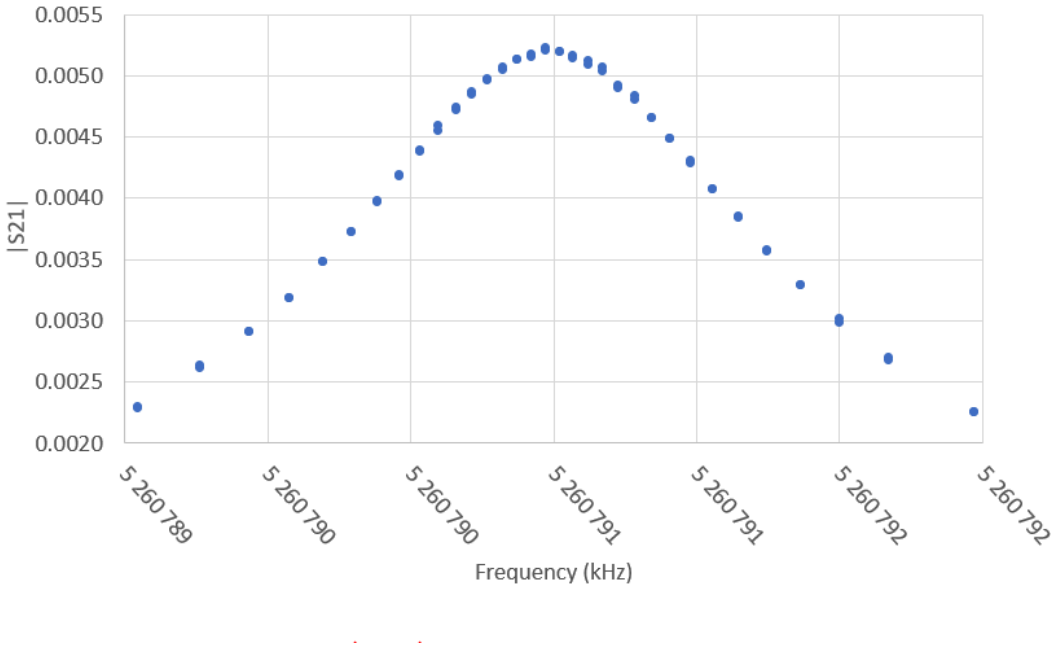

Figure 4.10: Graph of measured $|S_{21}|$ of the highest frequency peak of the triplet.

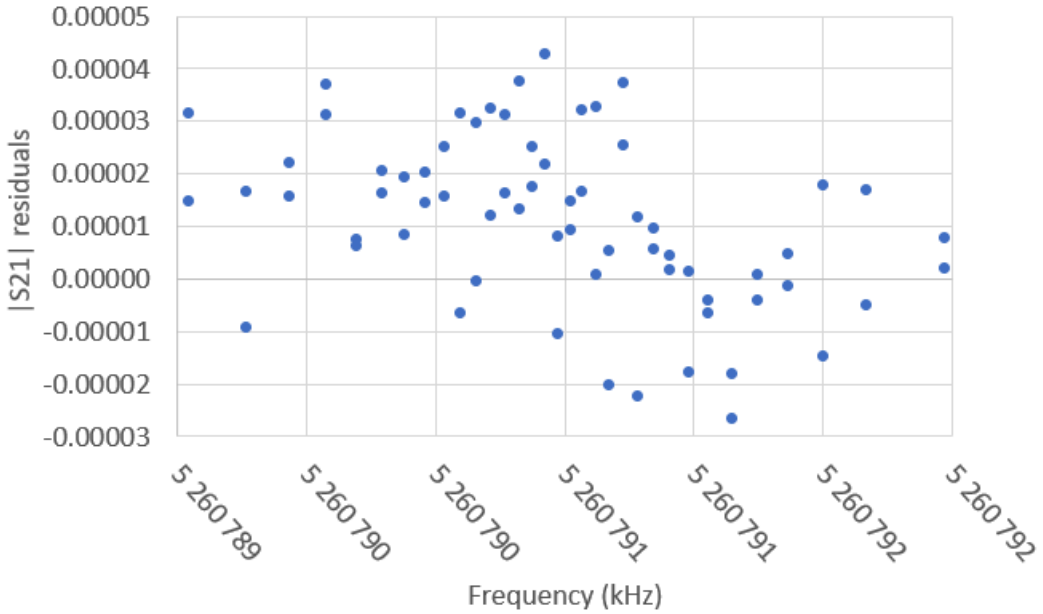

Figure 4.11: Residuals of the fit of $|S_{21}|$ for the highest frequency peak of the triplet.

3.3 Pressure calculation

The pressure calculation can begin from the moment the gas temperature, the vacuum and pressure resonance frequencies are known. The calculation algorithm is an iterative loop using three physical equations (Fig 4.12). The first expresses the square of the refractive index of the gas as a function of the resonance frequencies and the pressure. A second equation or equation of state allows one to calculate the molar density of the gas from its pressure and temperature. The last equation includes the two Clausius-Mossotti equations allowing one to calculate the relative magnetic permeability μ_r and the relative electric permittivity ε_r of the gas from its molar density. The product $\varepsilon_r \mu_r$ gives the square of the refractive index of the gas. The virial coefficients of the equation of state and of the Clausius-Mossotti equations can be taken either from experimental measurements elsewhere or theoretical calculations [33]. In the case of helium, they are calculated *ab initio*, which makes it possible to obtain the lowest uncertainties.

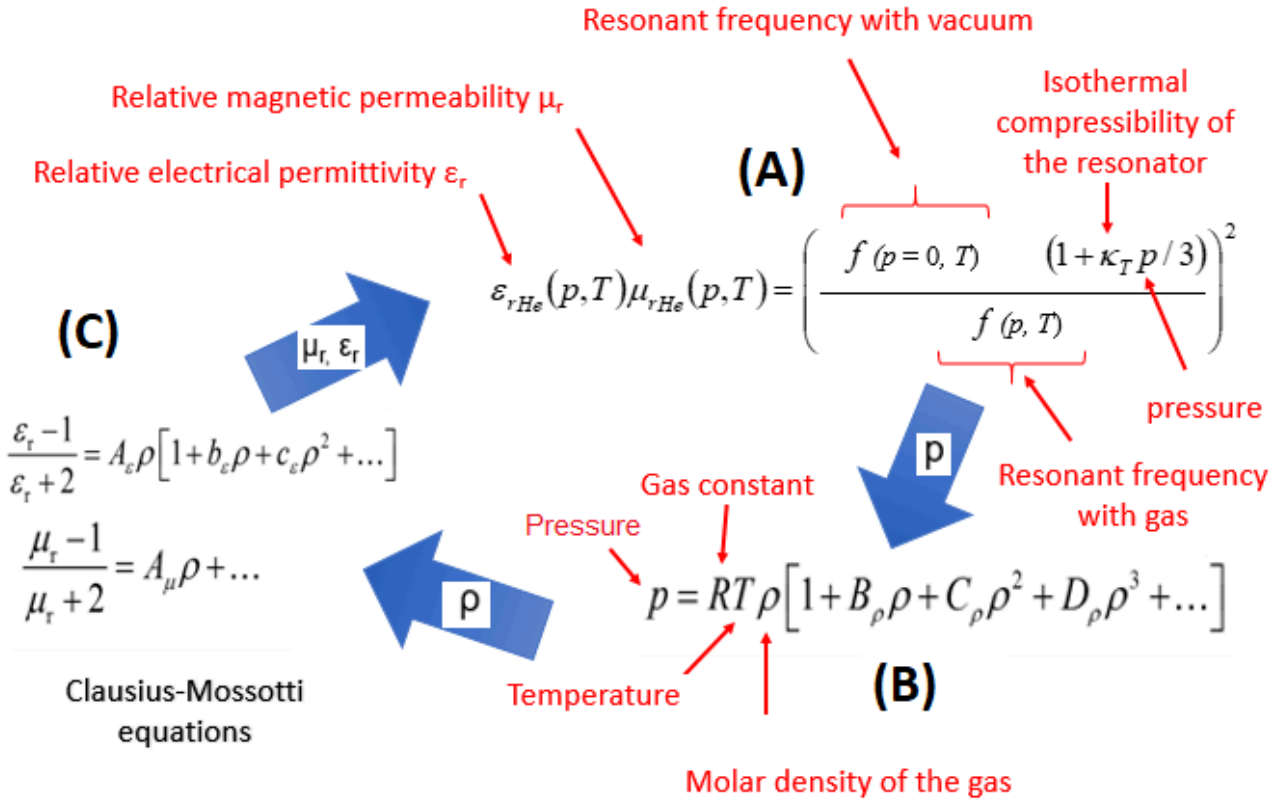

Figure 4.12: Illustration of the iterative calculation. Equation (A) gives the square of the refractive index, whose value is unknown at the start of the calculation. The left hand side represents its calculated value, the right hand side represents its measured value. The compressibility of the resonator and the resonance frequencies are known. The only unknown factor for the right-hand member is then the pressure. To solve the equation, the software proposes an *a priori* pressure value. This value is injected into the equation of state "B" which will make it possible to determine the density of the gas at the measured temperature. The density of the gas thus calculated is inserted in the equations of Clausius Mossotti (C) which make it possible to determine the relative magnetic permeability and the relative electric permittivity of the gas. The product of the two is the square of the calculated refractive index. If the equality of the two indices is not achieved, another pressure value is chosen *a priori* and the calculation repeated. The recursive process stops when the equality between the two squares of the refractive indices is achieved to the desired number of decimal places.

4 Physical aspects

In this section we review the physical phenomena that can affect the pressure measurement. The physical phenomena discussed in this section are the skin effect, external magnetic fields, thermal expansion, isothermal compressibility, the possible Taconis oscillation, self-heating, the hydrostatic effect, thermo-molecular effect and outgassing.

4.1 Skin effect

The high frequency electromagnetic wave penetrates into the cavity wall up to a depth given for a normal conductor at room temperature by equation 2.3 and for a superconductor conductor by equation 5.1. This penetration results in a decrease of the measured frequency. This effect is taken into account by the addition of a frequency correction term Δf_{ln}^{σ} in equations 2.6 and 2.8, the value of which is equal to the measured half-width of the resonance frequency [37].

4.2 Influence of an external magnetic field

In order to verify the influence of an external magnetic field on the resonant frequency, the system was tested first without then with anti-magnetic shielding. The shielding consists on the one hand of the external covering of the Dewar by mu-metal strips Figure 4.13a and on the other hand in the papering of the internal part of the vacuum chamber with lead strips Figure 4.13b.

Mu-metal (a nickel–iron soft ferromagnetic alloy with very high permeability) is commonly used to protect sensitive electronic components against static or low frequency magnetic fields. The superconducting transition temperature of lead is 7.2 K. When the experimental vacuum chamber is immersed in liquid helium (4.2 K) the lead strips glued onto its inner wall become superconducting and therefore diamagnetic.

In practice, a comparison of the signals with or without a protective shield showed no noticeable difference. All tests were carried out with a neodymium-iron-boron permanent magnet (with a degree of magnetization N35, the remanent induction corresponds to ≈ 1 T). The magnet had the shape of a cylinder 6 mm in diameter and 6 mm in length. The comparison

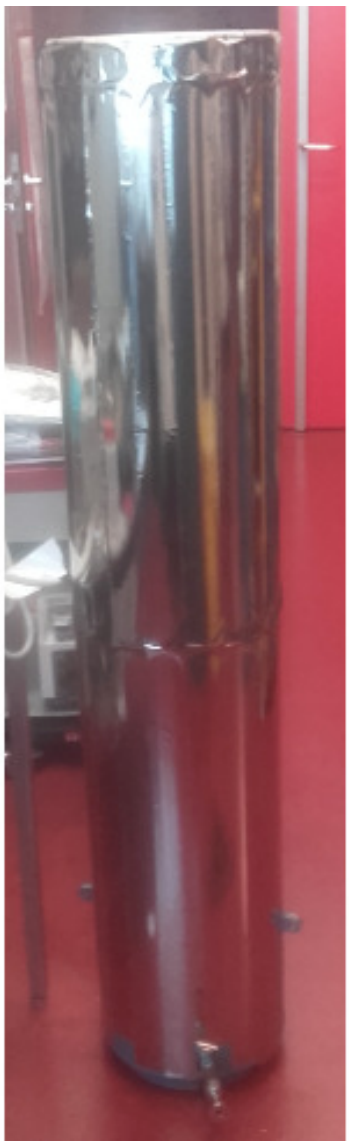

(a) Mu-metal

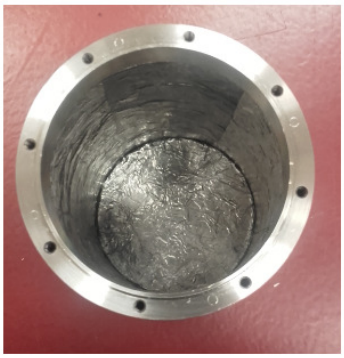

(b) Lead

Figure 4.13: Different shielding from magnetic fields. (a): The experimental Dewar is coated outside with mu-metal strips; (b): The experimental vacuum chamber is coated inside with lead, which becomes superconducting below 7.2 K.

of the resonant frequencies in the presence and absence of the magnet when it was moved around the Dewar showed no noticeable effects.

4.3 Temperature-related resonant frequency shift (thermal expansion)

Any change in temperature of the resonator modifies in its dimensions and therefore its resonance frequencies. The deformation of a copper cavity can be estimated from its thermal expansion coefficient [40]. We believe it reasonable to suppose the niobium coating follows the expansion and contraction of copper surface to which it adheres. From 293 K (room temperature) to 4 K the initial radius of 25 mm of the copper cavity is reduced by 81 μm (*i.e.* -0.324 % of its initial value).

However, the temperature not only affects the dimensions of the cavity but also the penetration depth of the electromagnetic wave, given by equation 5.1. Table 4.1 shows the calculated temperature coefficient of frequency shift taking into account the penetration depth around 5.4 K.

Table 4.1: Temperature related frequency shift resulting from a dimensional change of the cavity and the penetration depth variation around 5.4 K.

Mode	Temperature coefficient of frequency shift (Hz K^{-1})
TM_{11}	$-306(47)$
TE_{11}	$-501(77)$
TM_{12}	$-682(105)$
TE_{12}	$-862(132)$

4.4 Isothermal compressibility of the cavity

Data for the isothermal compressibility of copper can be found in the literature [62] [40]. At the temperatures explored in the present work its order of magnitude is very small ($\approx 7 \times 10^{-12}$ Pa^{-1}). At 1 kPa, the experimental uncertainty in the frequency is less than 2 Hz and the frequency shift caused by compressibility is of the order of 12 Hz. So, if the compressibility uncertainty is known to within 0.1 % (see [63]), it becomes negligible compared with the experimental uncertainty.

4.5 Taconis oscillation

The gas conveyed by a tube towards the resonator, passes from ambient temperature to a cryogenic one. The pressure difference can create thermoacoustic oscillations in the tube. This phenomenon is also called Taconis oscillation, named after the eponymous author of an article which describes it [64]. Not only can these oscillations be detected by the pressure sensor, they also create a thermal link between the environment at cryogenic temperature and the outside world. If the amplitude of the oscillation is difficult to assess, its frequency must correspond to the resonant frequency of the resonator formed by the pressure tube and the pressure vessel. Indeed, to a first approximation, the pressure tube and the pressure vessel can be considered to form a Helmholtz resonator [65] (see Figure 4.14).

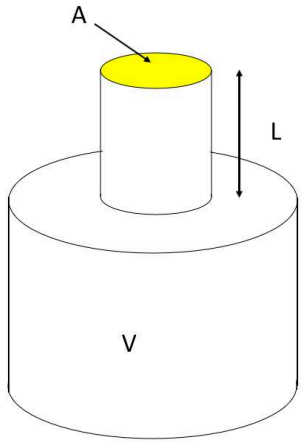

Figure 4.14: Helmholtz resonator. V: volume of the pressure vessel minus the volume of the resonator; L: length of the pressure tube; A: section of the pressure tube.

The frequency of the resonator is given by

$$f_0 = \frac{v}{2\pi}\sqrt{\frac{A}{VL}} \tag{4.2}$$

where A is the cross-sectional area of the tube, L its length, V the volume of the cavity and the speed of sound v is given by

$$v = \sqrt{\frac{\gamma RT}{M}}. \tag{4.3}$$

Here γ is the ratio of the specific heat at constant pressure to the specific heat at constant volume, R is the universal gas constant, M the molecular mass of the gas, and T is the temperature of the cold section. Figure 4.15 shows the resonant frequency of the resonator as a function of temperature for different lengths of tube. Taking into account the experimental parameters, the thermoacoustic oscillation frequency should lie close to 2 Hz.

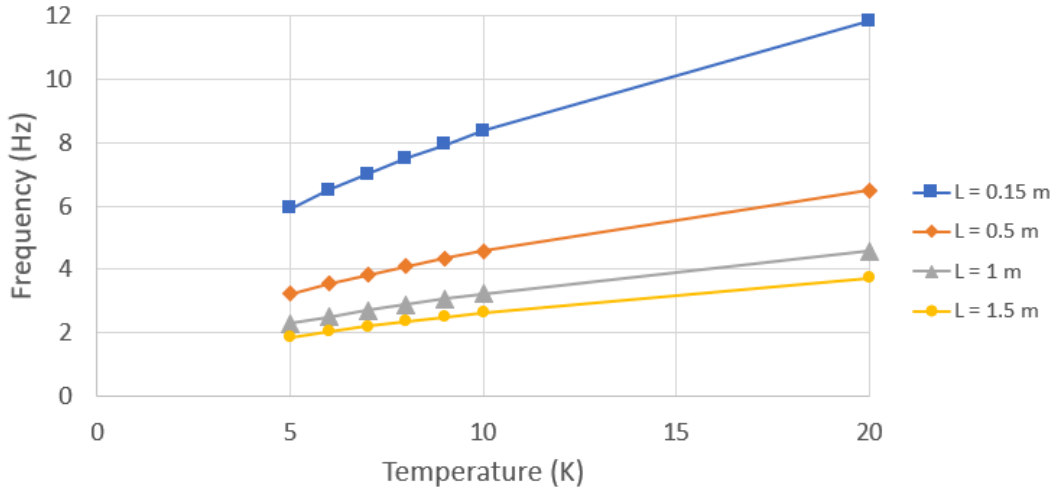

Figure 4.15: Resonant frequency of the Helmholtz resonator *versus* temperature for different lengths of the gas transport tube from $L = 0.15$ m to $L = 1.5$ m.

The method used to detect the Taconis a possible oscillation is to measure the $|S_{21}|$ scattering parameter at a fixed frequency. This frequency is chosen close to the half-height amplitude of a resonant frequency in order to facilitate the detection. Indeed this position allows having a great variation of $|S_{21}|$ as illustrated in Figure 4.16.

In the present experiment, however, no such oscillation was detected. This might because, as discussed by Rott [66], the length and temperature ratios of the hot and cold sections of the tubing lie beyond the region of allowed parameters for the phenomenon to occur.

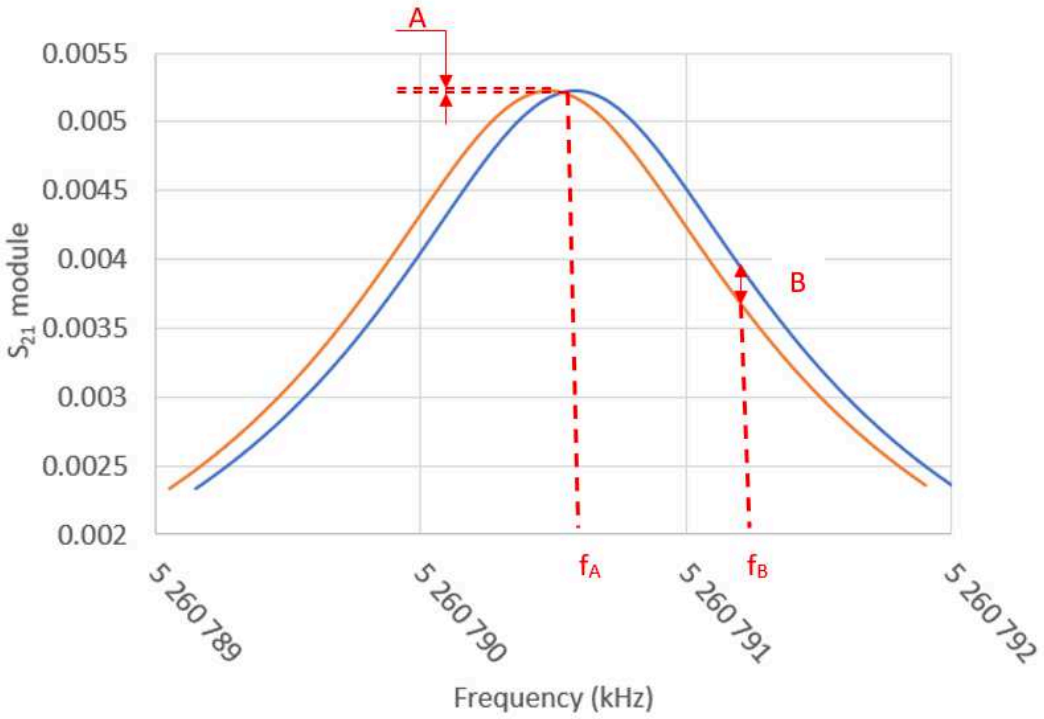

Figure 4.16: Measurement of the Taconis oscillation. The graph represents the frequency response of the $|S_{21}|$ scattering parameter for helium gas at two different pressures corresponding to the peak to peak amplitude of the Taconis oscillation. The measurement is carried out at fixed frequency. If the chosen frequency lies close to the resonant frequency (f_A), the pressure variations have little effect on the measured $|S_{21}|$ parameter (the $|S_{21}|$ difference corresponds to the segment A on the graph). On the other hand, if the chosen frequency lies close to that at half-maximum, the variations of $|S_{21}|$ (represented by the segment B) are greater.

4.6 Self-heating

The temperature of the cryostat is measured with resistance thermometers. They can be platinum, rhodium-iron or Cernox™ thermometers. The currents used to measure their values cause a bias by increasing their temperatures (self-heating effect).

During experiments the self-heating was not accurately measured but just estimated. The range of the Keithley multimeter used to measure the resistance of the thermometer was modified so that the latter is supplied with a current (96 μA) considered as having no thermal effect compared with the usual measurement current (960 μA). This method made it possible to estimate the self-heating of the thermometer at 17.5 mK.

4.7 Hydrostatic effect

The gas to measure is subjected to gravitational attraction. The pressure variation Δp between two heights h_1 and h_2 is given by

$$\Delta p = \int_{h_1}^{h_2} dp = \int_{h_1}^{h_2} \rho \; g \; dh \tag{4.4}$$

where g is the acceleration due to gravity, ρ is the density of gas. The density of the gas being itself a function of the temperature T, the preceding equation can be written in the form

$$\Delta p = g \left[\int_{h_1}^{h_2} \rho \; dh + (h_2 - h_1) \int_{T_1}^{T_2} \frac{\partial \rho}{\partial T} \; dT \right] \tag{4.5}$$

where T_1 and T_2 are the respective temperatures at the altitudes h_1 and h_2.

It follows that to determine the hydrostatic pressure difference, one must measure not only the height differences of the gas but also the temperature gradients [67].

Figure 4.17 shows the dimensions of the cryostat and the positions of the thermometers along the pressure tube. The two Tables 4.2 give the dimensions and locations of thermometers defined in Figure 4.17 and an estimate of the temperature and the relative variation of pressure due to the hydrostatic effect along the pressure tube.

Table 4.2: Mechanical dimensions and estimation of the temperature and relative pressure at 1 kPa of the Figure 4.17 (with the stainless steel thermal conductivity fit of the reference [5])

Dimension	Value (mm)
A	206.6 (0.1)
B	1261 (0.1)
C	50.5 (0.1)
D	100.2 (0.1)
E	283.1 (0.1)
F	260.8 (0.1)
G	249.8 (0.1)

Position	Temperature (K)	Relative pressure deviation at 1 kPa (%)
Room	300	+0.00 (0.00)
T5	238	+0.14 (0.04)
T4	228	+0.17 (0.09)
T3	207	+0.22 (0.15)
T2	140	+0.41 (0.22)
T1	59	+0.74 (0.34)
Cavity	5.4	+2.1 (0.9)

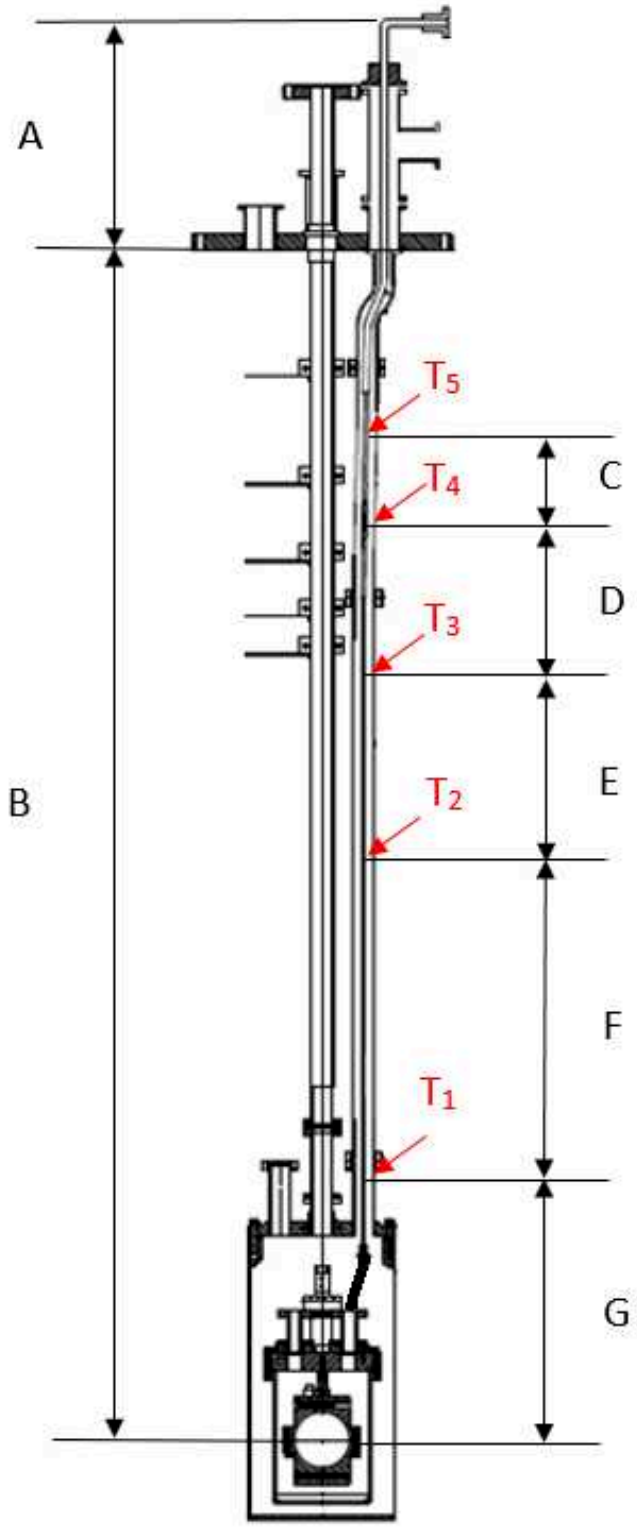

Figure 4.17: Positions of thermometers in the cryostat. T_1, T_2, T_3, T_4, T_5 show the locations of the thermometers. The dimensions of the drawing are given in table 4.2

4.8 Thermo-molecular effect

The thermo-molecular effect, also called thermal transpiration, occurs when a rarefied gas (*i.e.* in the molecular flow regime) having a uniform pressure is subjected to a temperature gradient. A difference of pressure then arises between the warm and the cold parts of the gas. It originates from the movement of molecules going from a higher density to a lower density region, namely from the colder to the warmer part of the gas [68]. This movement stops once the probabilities of molecules moving in one direction or the other equalize.

The molecular regime occurs when the mean free path of the gas molecules is larger than the system dimension. In the cryostat, the 'system' corresponds to the tube transporting the gas to the resonator. The relevant dimension is its inner diameter. The warm end is at room temperature while the cold end is at a cryogenic temperature. In steady-state and in the molecular regime, the kinetic theory of gases relates temperatures and the pressures at the cold and warm points by the Knudsen equation [8]

$$\frac{P_c}{P_w} = \sqrt{\frac{T_c}{T_w}} \tag{4.6}$$

where P_w and T_w are the temperature and the pressure at the warm end and P_c and T_c are the temperature and the pressure at the cold end. However, this equation does not account for the gas behaviour from the molecular regime to the continuum regime. To make the Knudsen equation more general, several semi-empirical equations have been developed [69]. Figure 4.18 shows the calculation of some models found in the literature for the Mark II cryostat pressure tube. For low pressure, there is clearly a dispersion between the models. It is useful to specify to which flow regime the gas belongs, given that the thermo-molecular effect is more likely to be present at higher temperature because the gas is less dense (*cf.* equation 2.9). The Knudsen number K_n defines the boudary between the different flow regimes. It is defined as the ratio of the molecular mean free path l to a characteristic length D:

$$K_n = \frac{l}{D} \tag{4.7}$$

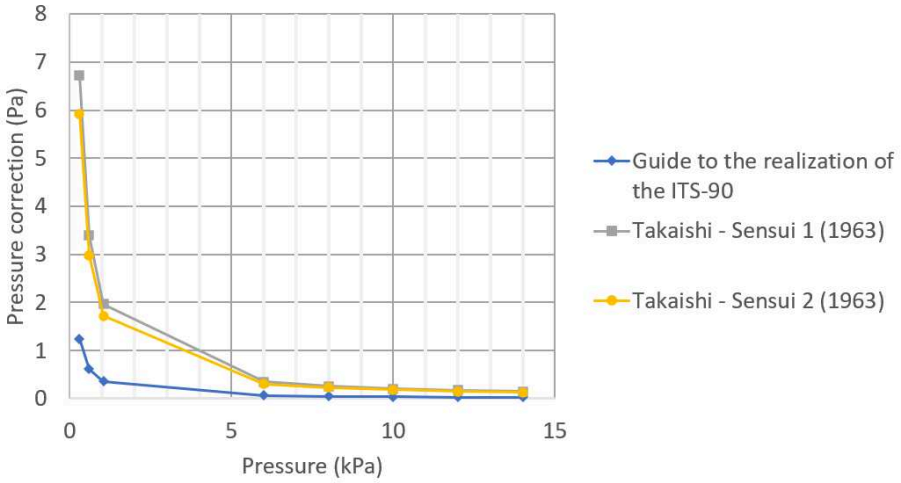

Figure 4.18: Thermomolecular correction given by Takaishi and Sensui [9] and the BIPM [10]

Here, the characteristic size is the inner diameter of the pressure tube. The inner diameter of the pressure tube of the Mark II cryostat is 3 mm and that of the Mark III cryostat 19 mm. The mean free path of the gas is given by [70]

$$l = \frac{kT}{\sqrt{2}\pi d^2 p} \tag{4.8}$$

where k is Boltzmann's constant, T the thermodynamic temperature, d the diameter of the colliding molecule and p the pressure of the gas. The flow regimes are traditionally classed as follows [71]:

$K_n < 0.01$	Continuum or viscous regime
$0.01 < K_n < 0.1$	Slip regime
$0.1 < K_n < 10$	Transitional regime
$10 < K_n$	Free molecular regime

Figures 4.19 and 4.20 plotted drawn using equations 4.7 and 4.8 so as to show the boundaries between the different regimes for the cryostats Marks II and III. The pressure tube temperature varies approximately from 5 K to 300 K. For a pressure of 100 Pa, the gas flow of cryostat Mark II is in the slip regime from 50 K to 300 K while that of cryostat Mark III approaches the slip regime only ounce temperatures approach 300 K.

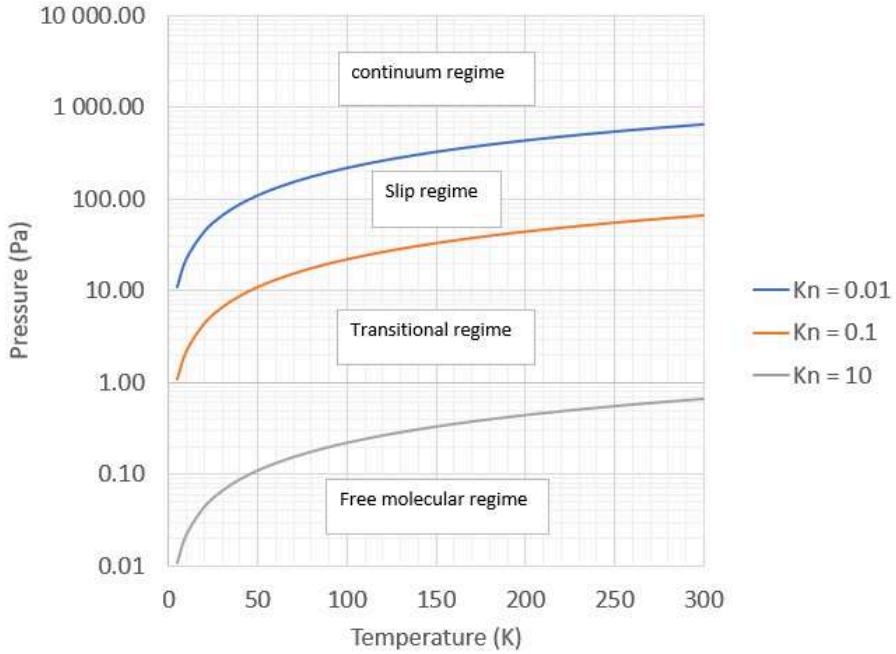

Figure 4.19: Flow regimes in the pressure tube of the Mark II cryostat.

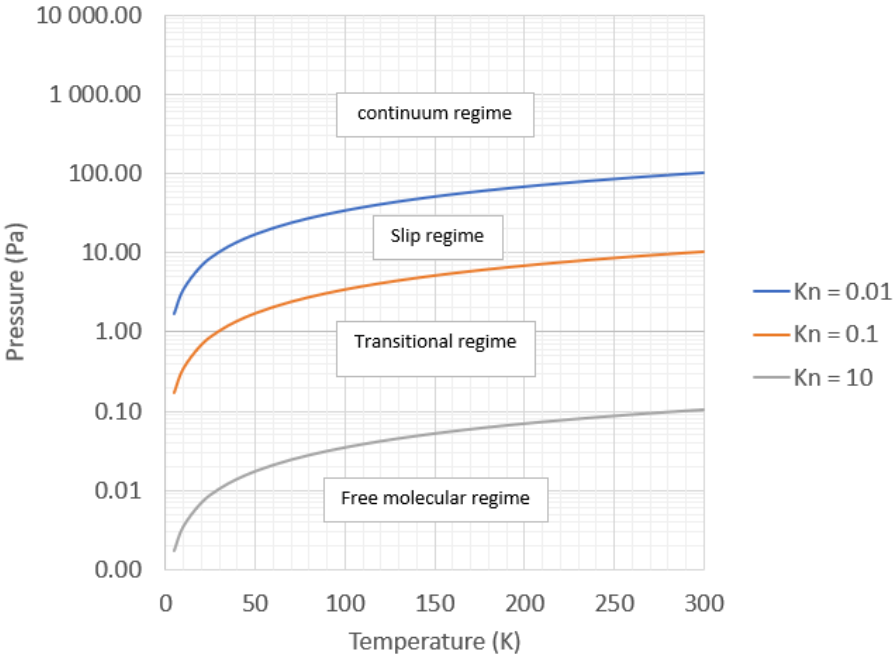

Figure 4.20: Flow regimes in the pressure tube of the Mark III cryostat.

4.9 Outgassing

Outgassing corresponds to a supply of molecules from materials or from the walls in contact with the gas to be measured. These molecules in the gaseous state may have been previously trapped in cavities (e.g. in screw housings) or deposited on the walls superficially or more deeply by absorption. Outgassing can create a bias on the pressure measurement by changing the chemical composition of the gas. The main pollutant is the air which is in contact with the cryostat surfaces when it is opened. Table 4.3 gives the composition of dry air as well as the different boiling points of its components.

Table 4.3: Composition of dry air, boiling point at atmospheric pressure and impact of each component at a concentration of one part per million for argon gas [6] [7].

Dry air components	Volume ratio (%)	Atmospheric pressure boiling point (K)	Effect on argon gas pressure of an impurity concentration of one part per million at 1 kPa and 90.4 K
Nitrogen (N_2)	78.08	77.4	-0.06×10^{-6}
Oxygen (O_2)	20.95	90.2	0.06×10^{-6}
Argon (Ar)	0.934	87.3	–
Carbon dioxide (CO_2)[1]	0.041	194.7	–
Neon (Ne)	0.001818	27.2	0.76×10^{-6}
Helium (He)	0.000524	4.2	0.87×10^{-6}
Methane (CH_4)	0.000179	111.7	–
Krypton (Kr)	0.0001	119.8	–
Hydrogen (H_2)	0.00005	20.3	0.52×10^{-6}
Xenon (Xe)	0.000009	165.1	–

[1] At 1 atm solid CO_2 sublimes

The water vapour (H_2O) contained in the humid air, which can reach a few percent per volume at room temperature, is entirely in solid form in the pressure range 200 Pa to 20 kPa and at temperatures below 200 K [72]. At a temperature close 5.4 K, the air component molecules, apart from helium, are no longer in the gaseous state and are bonded on the walls by cryo-condensation. It follows that the measurement of the pressure for helium is unperturbed by the presence of other gas molecules.

Regarding the pressure measurement with argon, the last column of the Table presents the impact on the measurement of each air molecule still in gaseous form at a temperature of 90.4 K. It appears that for a proportion of one part per million of concentration, the presence of impurety in the argon gas has little influence on the result of the measurement.

To reduce outgassing and before each experiment, the parts in contact with the gas remain more than two days under a vacuum created by a turbo-molecular pump.

Chapter 5

Results and discussion

This chapter presents different results obtained during the experiments. The effect of superconductivity on the resonant frequency and on the quality factor is discussed first. The choices of transmitted microwave power and operating temperature are then justified. The measurements concern in particular the relative uncertainty in frequency, the stability of the resonant frequency under vacuum, the pressure resolution, the quality factor, and the temperature gradient of the pressure tube. The behavior of the system subjected to pressure cycles is studied. Finally, a first uncertainty budget is proposed. Each time the cryostat is cooled down from room temperature to cryogenic temperature, the recording of measurements carried out is denoted by the word 'run' followed by a chronological number (e.g. run1).

1 Resonant frequency versus temperature

Fig.5.1 shows the measured transmission coefficient $\mid S_{21} \mid$ of the central resonant frequency f2n of the mode TM_{12} as a function of temperature when the temperature drops below the critical temperature of superconducting niobium.

The resonant frequency depends on the temperature. This behaviour can be explained by considering the London penetration depth $\lambda(T)$ of the superconducting material [73]. Its expression is given by

$$\lambda(T) = \frac{\lambda_0}{\sqrt{1 - (\frac{T}{T_c})^4}}. \tag{5.1}$$

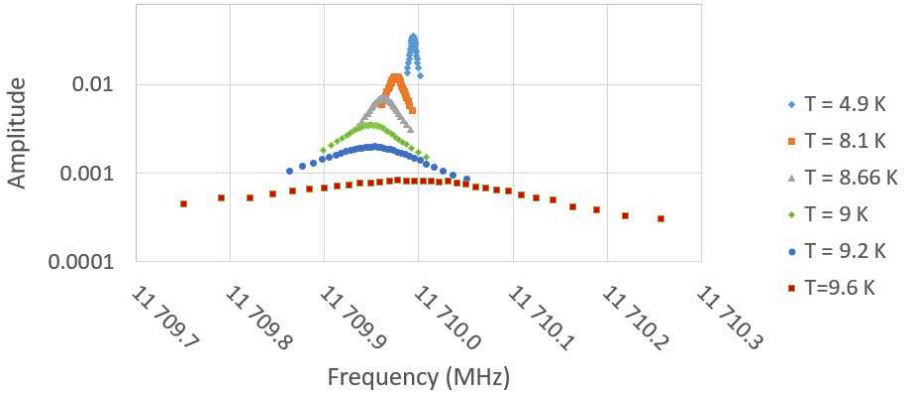

Figure 5.1: Variation of the transmission coefficient $|S_{21}|$ of the microwave cavity when the temperature drops below T_c, the critical temperature of the superconducting niobium inner surface. Representation of the central resonant frequency f2n of the mode TM_{12} (source: run 1).

where λ_0 is the penetration depth at absolute zero, T is the temperature considered and T_c the critical temperature of the superconducting material. Figure 5.2 represents the shape of the curve for niobium ($\lambda_0 = 39$ nm [74]). The graph shows that the value of the penetration depth becomes almost constant for $T \ll T_c$.

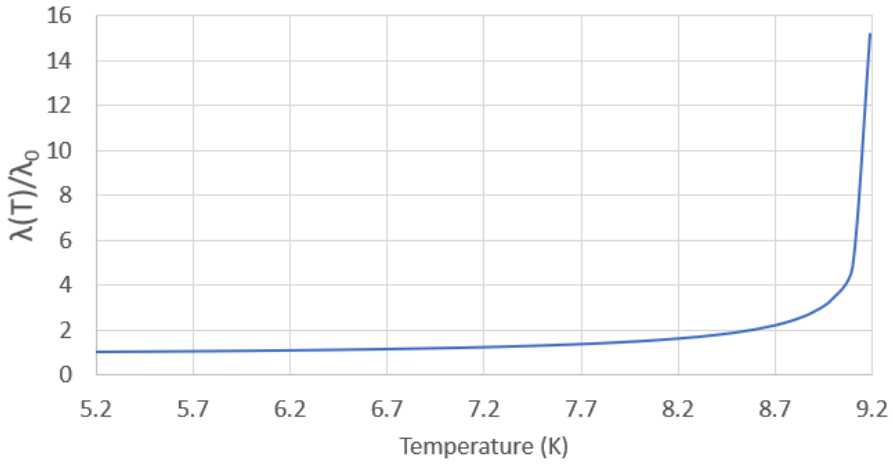

Figure 5.2: Shape of the relative penetration depth $\lambda(T)$ of niobium *versus* temperature

By interpreting the penetration length as being the depth of penetration of the electromagnetic wave in the superconducting material, one can express the resonant frequency of the spherical cavity as a function of temperature. The lowest resonant frequency of the triplet can be deduced from equation 2.7 and its eigenvalue ξ_{11}^{TM} given in Table 2.1. The resonant

frequency is then given by

$$f_{11}^{TM} = \frac{c\ \xi_{11}^{TM}}{2\pi(a+\lambda(T))} = \frac{c\ \xi_{11}^{TM}}{2\pi\left(a + \frac{\lambda_0}{\sqrt{1-(\frac{T}{T_c})^4}}\right)} \tag{5.2}$$

where c is the speed of light in vacuum and a the radius of the cavity. A comparison between the calculated and measured resonant frequencies is given in Table 5.1.

Table 5.1: Comparison between the theory and measured resonant frequency below the critical temperature. To determine the theoretical frequencies, the diameter of the resonant cavity was first calculated from the resonant frequency measured at 9.0282 K. The theoretical frequencies at other temperatures were then deduced from this diameter by taking into account the thermal expansion of the resonator and the London penetration depth.

Temperature (K) (K)	Measured resonant frequency (Hz) (Hz)	$\frac{f_{Theo} - f_{Meas}}{f_{Meas}}$ ($\times 10^6$)
9.0282	11 697 968 105 (3109)	0
8.6596	11 698 016 320 (6195)	−1.69(26)
8.1005	11 698 046 018 (9926)	−1.64(32)
4.9148	11 698 079 370 (2722)	−2.01(62)

Given the fact that the calculations were made with the approximation of a perfectly spherical cavity and that the measurements of the resonant frequency were carried out with a non-optimized temperature regulation, the small deviations between the measured and theoretical values of the Table 5.1 tend to confirm the agreement between the theory and the observed values.

Figure 5.3 shows the spectrum of $|\ S_{21}\ |$ for different temperatures when the resonant frequencies are aligned. Compared with the value for 9.6 K, the amplitude increases by almost two orders of magnitude when the temperature is lowered by a factor of about two.

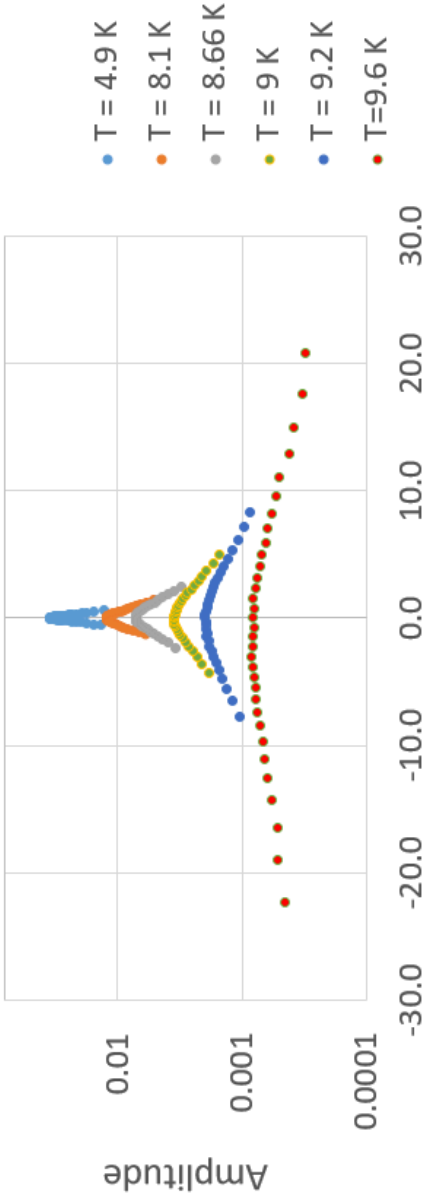

Figure 5.3: Variation of the transmission coefficient | S_{21} | spectrum for resonant frequency f_{2n} of the mode TM_{12} at different temperatures. Although the resonant frequency rises at lower temperatures, here peaks are aligned for clarity (*cf.* Figure 5.1) (source He-run 1).

2 Transmitted antenna power

After several tests the transmitted power was adjusted to minimize its effect on the resonator temperature without deteriorating the signal-to-noise ratio. The value retained was -28 dBm which corresponds to 1.6 μW.

3 Quality factor versus temperature

Figure 5.4 shows the quality factors Q_{f1n}, Q_{f2n} and Q_{f3n} of the TM_{11} triplet resonant frequencies as a function of the temperature. The symbols f1n, f2n and f3n correspond to resonant frequencies classed in ascending order with respective half-widths g1n, g2n and g3n. It is clear that the quality factors increase when the temperature is lowered and tend to become constant at low temperature. Consequently, the choice of a low operating temperature makes it possible to obtain a better relative uncertainty in the resonant frequency (*cf.* equation 2.1) as well as a better stability thereof.

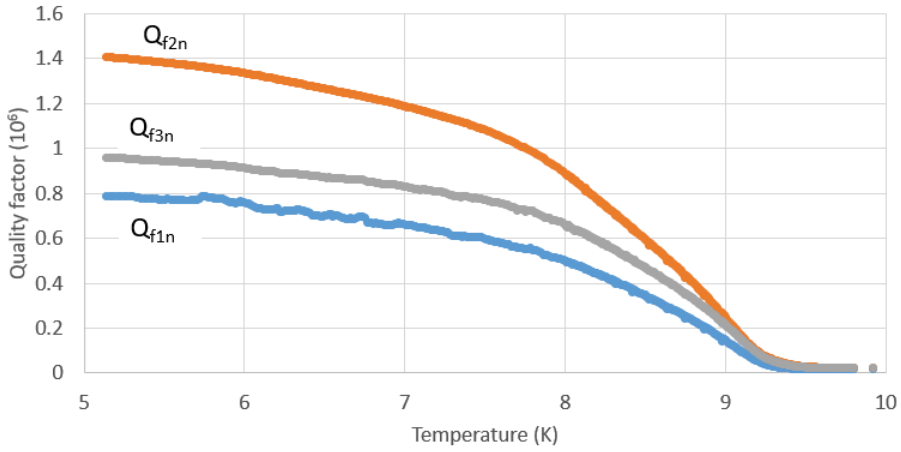

Figure 5.4: Quality factors of the TM_{11} triplet resonant frequencies *versus* temperature. Emission power -28 dBm (source He-run 2).

Subsequently, the antennas used in Figure 5.4 were replaced with new ones tuned with looser coupling (*i.e.* the position of the antennas are more distant than the previous ones from the centre of the cavity). The quality coefficient thus increased from around 1.4 million to 3.8 million at a temperature of 5.4 K (source He-run7).

From a theoretical point of view, and assuming that the London penetration length for superconducting material corresponds to the skin depth for a normal conductor for the microwave frequencies range used in this experiment [75], the half-width of the TM_{ln} mode is given by [37]

$$g_{ln}^{TM} = f_{ln}^{TM} \frac{\lambda(T)}{2a} \left(\frac{(\xi_{ln}^{TM})^2}{(\xi_{ln}^{TM})^2 - l(l+1)} \right) \tag{5.3}$$

where l,n are integers which identify the eigenfrequency f_{ln}^{TM} , ξ_{ln}^{TM} an eigenvalue of the mode TM and a the radius of the cavity. From 5.3, one can express the quality factor of the same mode given by[1]

$$Q_{ln}^{TM} = \frac{f_{ln}^{TM}}{2 * g_{ln}^{TM}} = a \frac{\sqrt{1 - (\frac{T}{T_c})^4}}{\lambda_0} \left(\frac{(\xi_{ln}^{TM})^2 - l(l+1)}{(\xi_{ln}^{TM})^2} \right). \tag{5.4}$$

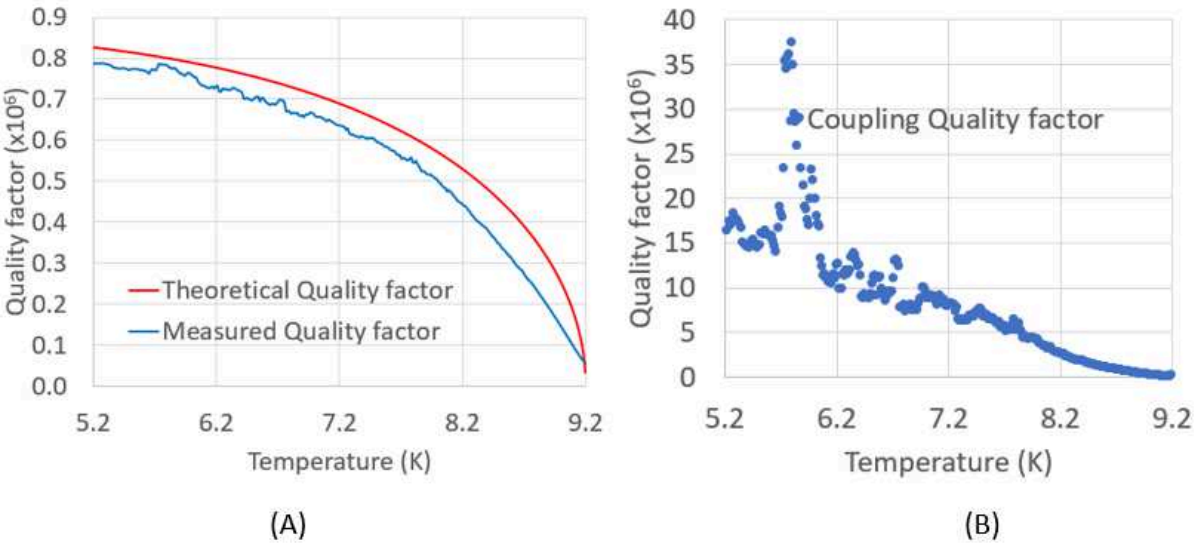

Figure 5.5: Quality factors (A) Theoretical Q_i (upper curve) and measured Q (lower curve) *versus* temperature for the Mode TM_{11}. (B) Coupling Quality factor $Q_c = QQ_i/(Q_i - Q)$ deduced from curves (A)

[1]Here, the effect of surface impedance, a function of the London penetration length, is implicit (see for instance H. Padamsee [76] page 86).

Figure 5.5 (A) shows the theoretical and measured quality factors for the lowest frequency of the TM_{11} triplet. The measured quality factor Q, also called the global quality factor, is composed of an internal quality factor Q_i, specific to the resonant cavity, and a coupling quality factor Q_c, related to the action of circuits outside the cavity. They are linked by the relation

$$\frac{1}{Q} = \frac{1}{Q_i} + \frac{1}{Q_c}. \tag{5.5}$$

Figure 5.5 (B) shows the coupling quality factor Q_c deduced from Figure 5.5 (A) and equation 5.5. There are also other ways to measure the different quality factors [77] [78] but none were used here.

4 Relative frequency uncertainty

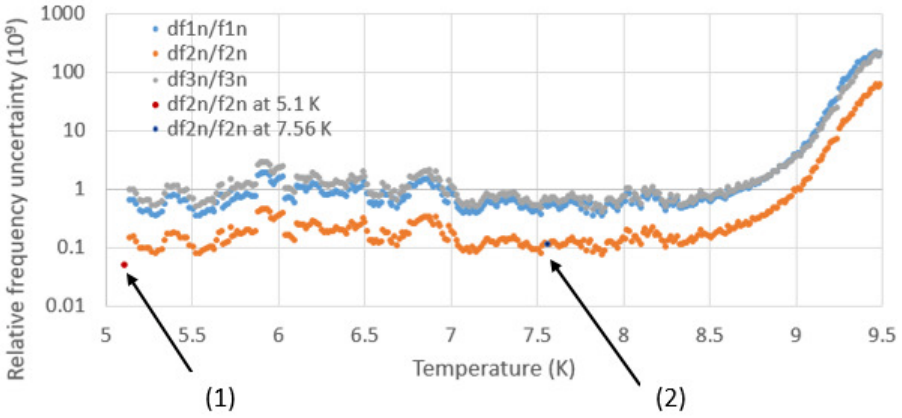

Figure 5.6: Uncertainty in the frequency of the TM_{11} mode triplet components *versus* temperature. Microwave power −28 dBm. (1) Static measurement at 5.1 K. (2) Static measurement at 7.56 K (source He-run 2).

Figure 5.6 shows the relative uncertainty of the three resonance frequencies for the mode TM_{11} as a function of the temperature. This measurement was carried out dynamically. The highest resonant frequency f3n yields the lowest uncertainty. The points marked (1) and (2) correspond to static measurements of the relative uncertainty of the frequency f3n at the

respective temperatures of 5.1 K and 7.56 K. It is clear that the lowest uncertainty is obtained at the lowest temperature.

5 Choice of the set point for the temperature regulation of the resonator

After finding that the best uncertainty was obtained at low temperatures (see section 4), we performed several tests at different temperatures from 4.7 K to 6.0 K after which the set point temperature was fixed at 5.4 K in all subsequent experiments. This temperature was a good compromise between the reduction of the quality factor at higher temperatures and the risk of the appearance of precondensation phenomena at lower temperatures [79].

6 Stability under vacuum

The stability of the resonant frequency was measured under vacuum at a temperature of 5.4 K. Figure 5.7 shows the relative Allan deviation of the measurements, which reaches 0.1×10^{-9} after 10 min of integration time.

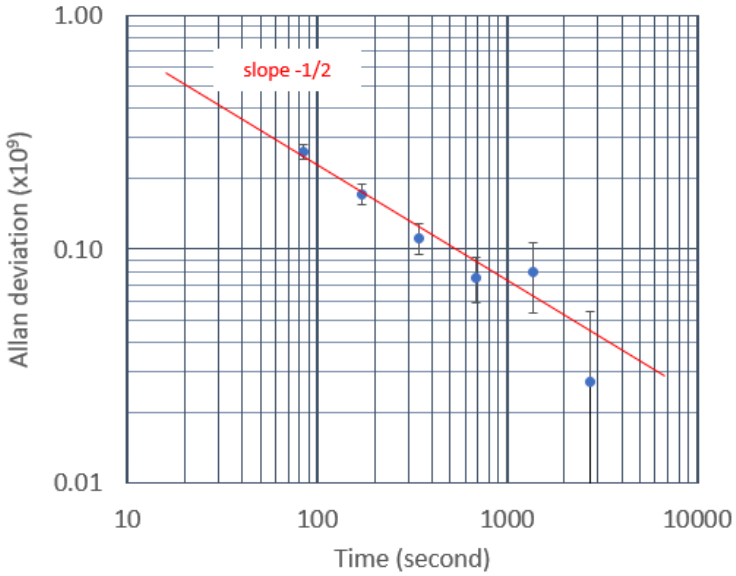

Figure 5.7: Relative Allan deviation of the resonant frequency with the resonator under vacuum at 5.4 K (source He-run 7).

7 The temperature gradient along the pressure tube

The temperatures measured at different points along the pressure tube turned out to be different from those estimated (*cf.* 4.2). Table 5.2 shows their values for a pressure of 1 kPa.

Table 5.2: Values measured by the pressure tube thermometers with 1 kPa of helium-4 (source: He-run7).

Position	Temperature (K)
Room	297.3
T_5	71.45
T_4	59.33
T_3	39.58
T_2	21.09
T_1	20.38
Cavity	5.40

A comparison of tables 4.2 and 5.2 shows that the mere consideration of thermal conductivity of the stainless steel tube is not sufficient to describe the temperature variation along the pressure tube. The estimate used to calculate the values of 4.2 did not take into account the thermal conductivity of the gas nor the radiative heat transfer from the hotter pressure tube to the colder vacuum jacket at 4.2 K. As the thermal conductivity of helium gas (0.07 W m^{-1} K^{-1} at 100 K) is much lower than that of stainless steel (9 W m^{-1} K^{-1} at 100 K), it can therefore be neglected [7]. Consequently, only heat transfer by radiation due to the large temperature difference between liquid helium and the pressure tube must be taken into account to improve the model [58].

According to the standard IEC 60751:2008, the platinum temperature sensors of the pressure tube can be used down to a temperature as low as 73.15 K (−200 C°) but no lower. However, we considered it was also possible to use the values measured by the sensors at positions T_5 and T_4 because, from experience, their sensitivity remains constant down to about 60 K and the lowest temperature is very close to this value [80]. The readings of sensors at the positions T_1, T_2, and T_3 were not be taken into account for the calculation of the hydrostatic pressure correction.

8 Pressure resolution

The pressure resolution was estimated during the first tests. In the initial state, the resonator was under vacuum and at a temperature of 5.1 K. A helium pressure of 20 Pa was applied to it for about 45 min. Finally, at the end of this time, the gas was pumped out to restore the resonator to the initial state. Figure 5.8 shows the evolution of the resonant frequency during the test. The pressure variation of 20 Pa changes the resonant frequency by 2.5 KHz. This made it possible to estimate the adjustment resolution of the resonant frequency to 3 mPa by rounding upwards. Table 5.3 summarizes results of the calculation.

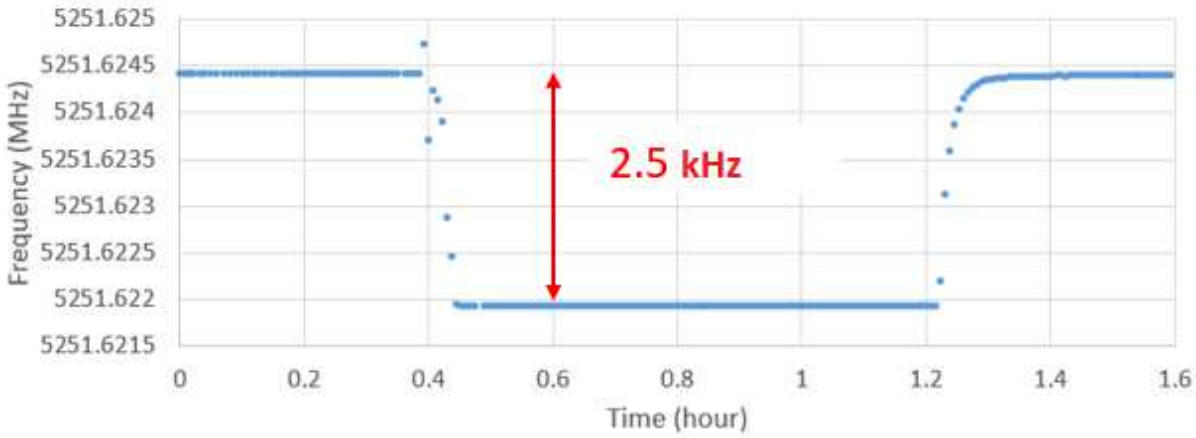

Figure 5.8: Frequency shift with a 20 Pa variation of helium gas pressure at 5.1 K (source He-run 2).

Table 5.3: Pressure resolution determination (source He-run 2).

Comment	Symbol	Unit	Value
Pressure variation applied	ΔP	Pa	20
Frequency variation resulting	Δf	Hz	2500
Pressure applied to frequency resulting ratio	ΔP \ Δf	Pa Hz^{-1}	0.008
Resonant frequency fit resolution	df2n	Hz	0.2698
Measured pressure resolution	(ΔP \ Δf) $\times$ df2n	Pa	0.0022

9 Pressure cycles

To evaluate the system in the measuring range, a series of pressure steps was applied between 20 kPa and 500 Pa. The pressure values were set and the measurements carried out automatically by a program written with LabVIEW^{TM} software. The measurement took about four hours. Figure 5.9 shows a typical pressure cycle. Temperature spikes occur each time the pressure is changed.

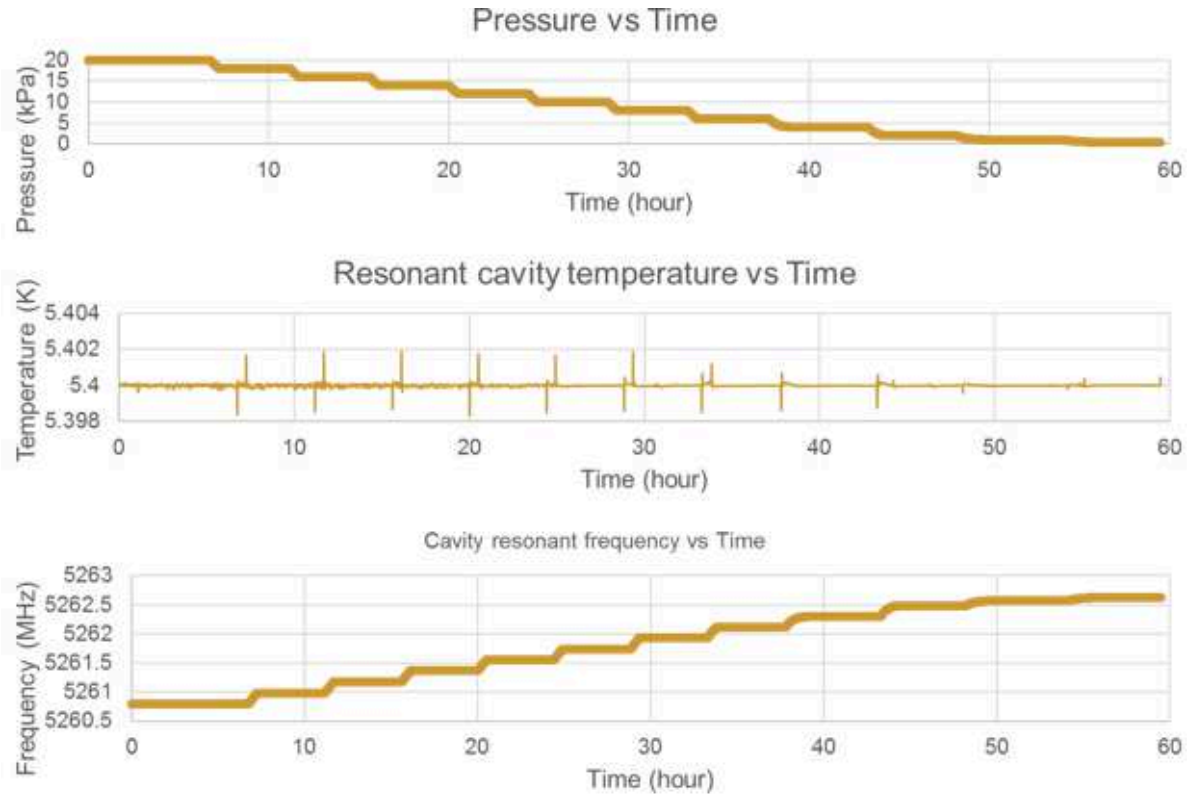

Figure 5.9: Simultaneous evolution of the pressure to be measured, the temperature of the resonator and the resonant frequency during a pressure cycle. The mean temperature of the resonator is 5.4 K (source He-run 7).

The figure 5.10 shows the stability of the reference pressure around 20 kPa and the resonator temperature at 5.4 K measured simultaneously over several hours.

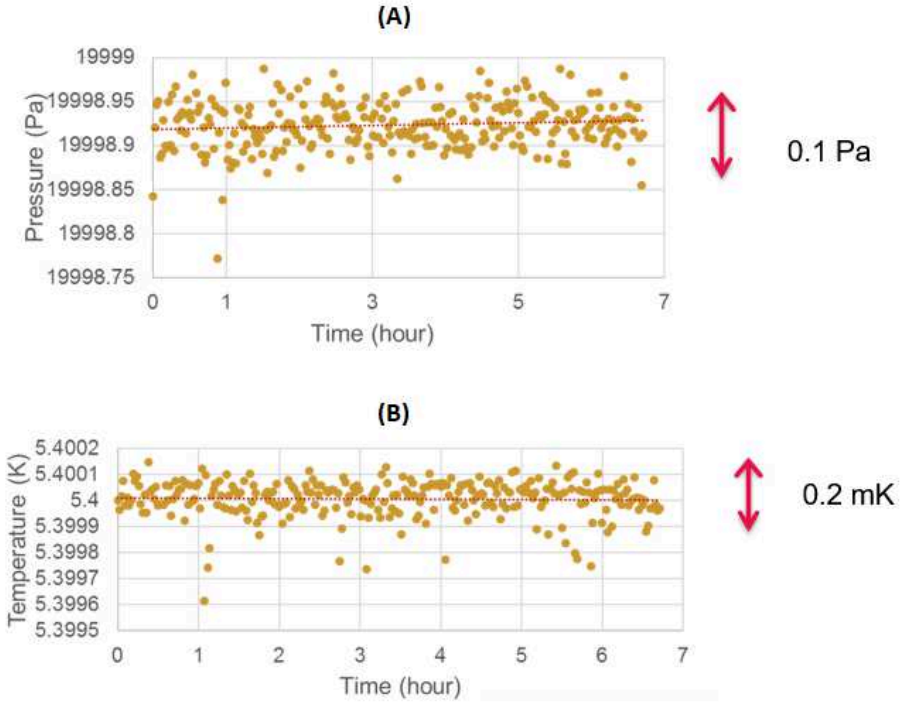

Figure 5.10: Stability of the reference pressure (A) and the resonator temperature at 5.4 K (B) measured simultaneously (source He-run 7).

Figures 5.11 and 5.12 show respectively the absolute and relative pressure differences between the sensor under study and a reference sensor over three cycles. The pressure cycles were carried out successively and are identified in the figures by the numbers 1, 2 and 3. All the corrections described in Chapter 4 were made to calculate the pressure measured using the superconducting resonator. For the thermo-molecular effect, the correction recommended by the guide to the realisation of the ITS-90 was used [10].

In Figure 5.11, the pressure drifts but seems to become more stable with successive cycles. This drift may be due either to the sensor used in the pressure regulation loop, or to the reference sensor or to the microwave sensor, or to any combination of the three. The start of stabilization in the third cycle indicates the need to perform several pressure ageing cycles before making measurements with the microwave sensor.

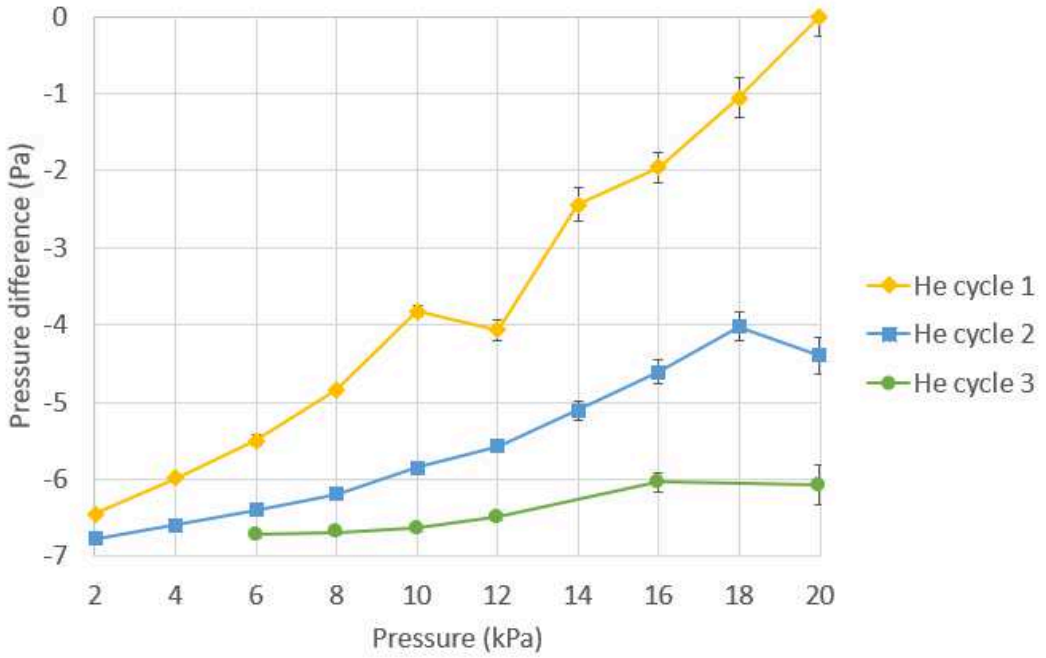

Figure 5.11: Difference between helium pressure measured via the refractive index and a reference pressure for three successive cycles (source He-run 7).

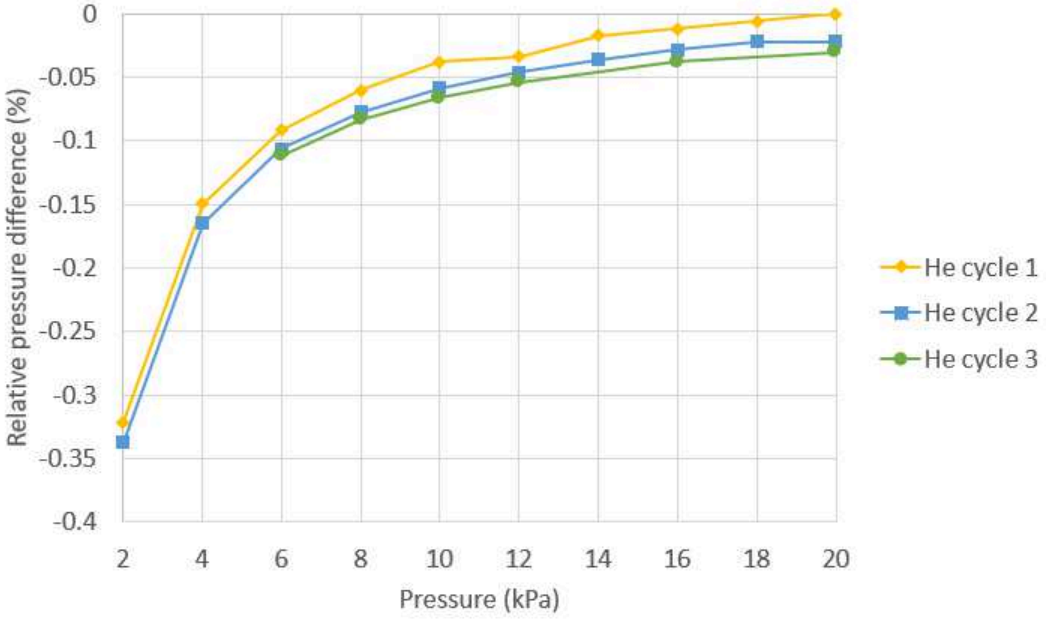

Figure 5.12: Relative pressure difference of three successive cycles (source He-run 7).

10 Uncertainty budget

Table 5.4 shows a provisional uncertainty budget for two pressure values 200 Pa and 20 kPa, the superconducting resonator being at a temperature of 5.4 K. Figure 5.13 illustrates the propagation of uncertainties between 200 Pa and 20 kPa. It appears that the predominant uncertainty comes from the temperature measurement. For comparison, Figure 5.14 shows the global provisional uncertainty of the present study among the Calibration and Measurement Capabilities of different laboratories presented in section 3.2. An analytical treatment of uncertainty is developed in Appendix E.

Table 5.4: Helium gas pressure measurement uncertainty budget for superconducting microwave cavity at $T = 5.4$ K. With P pressure; κ_T isothermal compressibility; T thermodynamic temperature; A_μ molar magnetic polarizability; A_ϵ molar electric polarizability; B_ϵ second dielectric virial coefficient; B_2, C_2, D_2 density virial coefficients; f_m measured frequency. Uncertainty components that are less than 20 μPa are either omitted or replaced by a dash "–". (See also Appendix A Table A.1)

Working pressure Uncertainty unit	200 Pa (mPa)	20 kPa (mPa)
P uncertainty components, Type B		
κ_T	0.028	2.5
T calibration	3.9	545
Gas impurities	–	–
A_μ [62]	0.065	6.4
A_ϵ [62]	0.039	3.7
B_ϵ [62]	0.018	3.7
B_ρ [81]	0.005	47
C_ρ [81]	–	4
D_ρ [81]	–	0.6
P uncertainty components, Type A		
T regulation	1.2	252
f_m measurement and corrections	0.89	0.84
P combined uncertainty	4.18	602

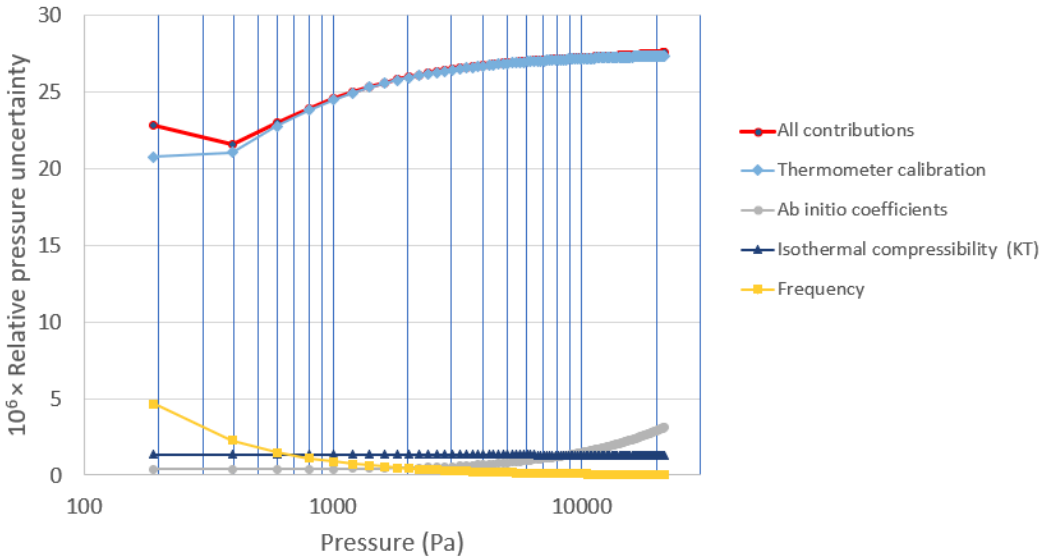

Figure 5.13: Expected uncertainty propagation at 5.4 K due to the determinations of the resonance frequency (frequency) in yellow, thermodynamic temperature (Cernox AGT) in light blue, the isothermal compressibility κ_T in dark blue, the *ab initio* coefficients in grey. The red curve (all contributions) represents the square root of the quadratic sum of these elements.

The thermometer used is a Cernox^{TM} RTD temperature sensor calibrated by the manufacturer. Constant offset increase observed during pressure cycles. However a constant offset in the temperature calibration cannot account for the increased pressure measurement deviation observed at low pressure.

Once the measurement deviation observed at low pressure has been corrected, it will be possible to reduce the uncertainties to 10 ppm in the temperature measurement by using a rhodium-iron resistance thermometer calibrated against an acoustic gas thermometer.

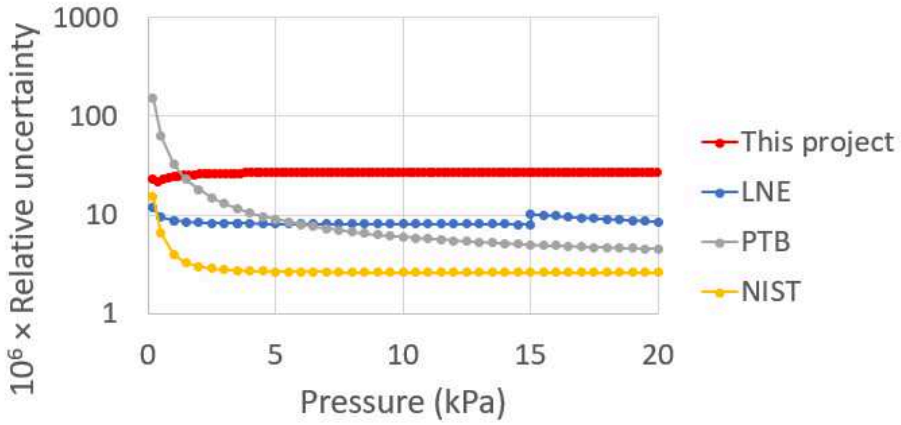

Figure 5.14: Comparison of Calibration and Measurement Capability for pressure of different laboratories and the provisional uncertainty of this project for helium gas. Uncertainty Values are expressed with a level of confidence of 68% [2] .

Part II

Argon gas

Chapter 6

Copper microwave cavity

1 Generalities

The use of the present measurement method with other gases than helium seems natural. Argon is a possible choice because its *ab initio* coefficients are known [82] [83] and some works are in progress to improve their uncertainties[12]. Argon boiling point is 87.3 K. The temperature is too high for the niobium coating of the microwave resonator to be in the superconducting state (T_c = 9.2 K). There are several superconducting materials with a transition temperature higher than the argon boiling point temperature: for example the compound Y-Ba-Cu-O whose transition temperature is 93 K [84]. However, before embarking on the manufacture of a new cavity, simpler solutions should be explored.

Originally, the choice of using a superconducting cavity was made for helium because it provides a large quality factor and thereby improves the frequency resolution (*cf.* equation 2.1). However, another way to improve the frequency resolution is to increase the signal-to-noise ratio of the received microwave signal by using a pre-amplifier [85]. A test carried out on the superconducting cavity showed the correct operation of this method and the hope of obtaining interesting measurement uncertainties for argon with a copper cavity.

The time interval required for the manufacture of the Mark III cryostat made it possible to carry out the experiments with argon using the Mark II cryostat.

2 Practical realisation

The resonator used for this experimentation was manufactured in China under the supervision of Prof. Gao Bo from the Technical Institute of Physics and Chemistry. The assembly of the resonator, the manufacture of the antennas and their adaptation in the cavity were carried out in France at the LNE-Cnam Common Metrology Laboratory.

2.1 Copper cavity

The resonator shown figure 6.1 used for the experiment is a triaxially ellipsoidal copper cavity. It was made with the same plans used to fabricate the superconducting cavity describe in chapter 2. The mass of a copper hemisphere is 0.545(1) kg.

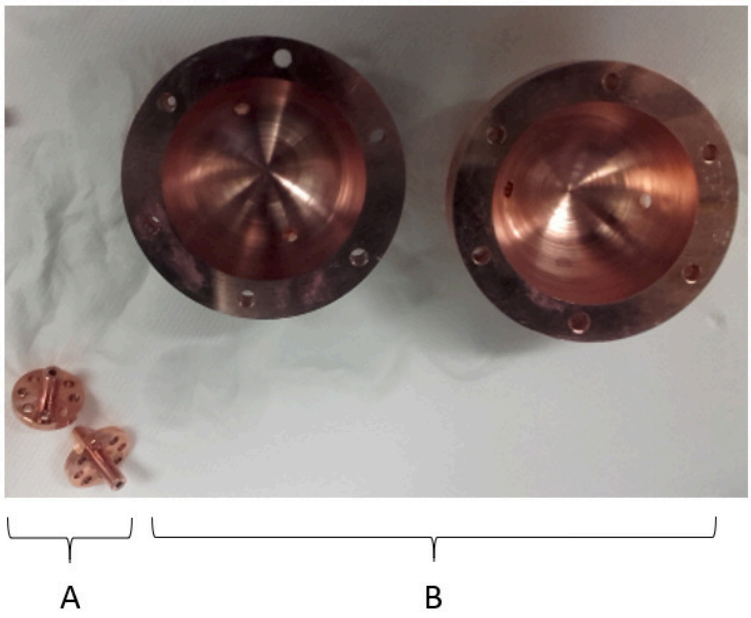

Figure 6.1: Copper cavity for argon pressure measurement. A: plug for antenna. B: the two copper hemispherical cavities of the triaxial ellipsoid resonator unassembled.

After cleaning of the various copper parts and assembling the hemispheres fitted with their plugs, the resonator cavity was subjected to a continuous flow of gaseous argon to limit the formation of an oxide layer on its inner surface.

2.2 Antennas

Two helical antennas were used for the argon experiments. Although more difficult to make than wire antennas like the one used with the superconducting cavity, they nevertheless make it possible to excite the lowest order magnetic mode (TM_{11}) and the lowest order electric mode (TE_{11}) of the resonator (see table 2.1).

Figure 6.2 shows a helical antenna ready to be inserted into its plug. Figure 6.3 shows a drawing of the helical part. Figure 6.4 shows the resonator and the vector network analyser during the positioning of the antennas. The antennas do not protrude into the cavity but are flush with the internal wall. They are rotated and translated to optimize the resolution and amplitudes of the three resonant frequencies of the mode. Once the best position and angle have been found the antennas are glued in place with Loctite® Stycast 2850FT adhesive.

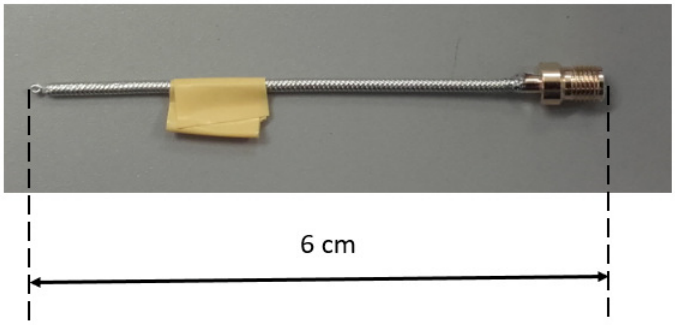

Figure 6.2: The helical antennas are made from a coaxial cable of outer diameter 2.2 mm. The materials used for cable manufacturing are non-magnetic. One end of the cable is soldered to an SMA connector (shown on the right).

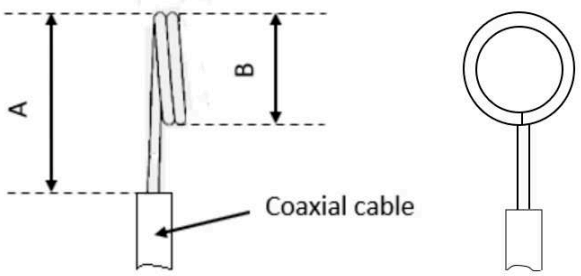

Figure 6.3: The helical antenna consists of two contiguous turns (dimension: A = 2 mm, B = 1 mm, conductor diameter = 0.53 mm).

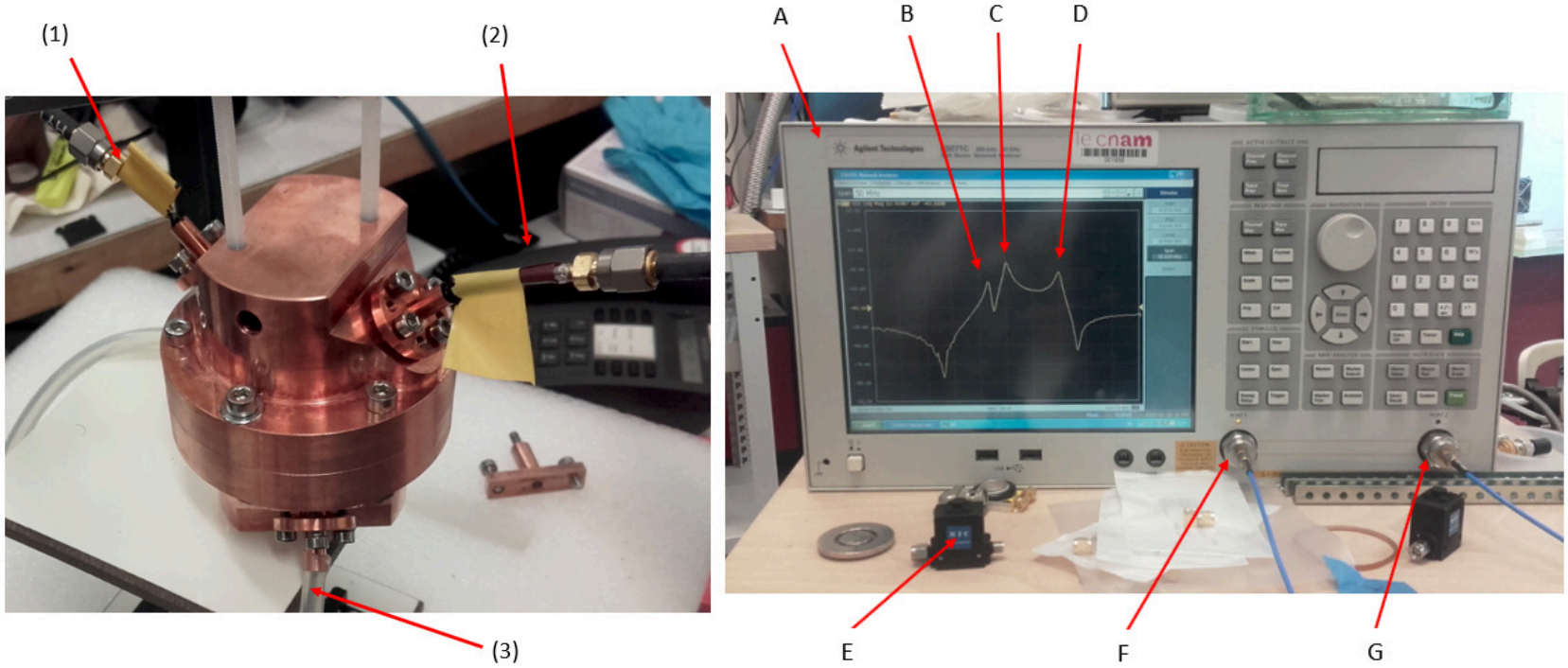

(a) (b)

Figure 6.4: Antenna tuning: (a): Installation of the antennas on the resonator: (1) Transmitting antenna, (2) Receiving antenna (3) Pipe bringing a flow of helium into the cavity. ; (b): Triplet resonant frequencies measurement during antenna installation. Resonator under vacuum at room temperature (20 °C). A: Vector network analyser, B: Lower resonant frequency (8.571 670 0 GHz, −40 dBm), C: Medium resonant frequency (8.573 190 9 GHz, −28 dBm), D: Upper resonant frequency (8.573 190 9 GHz, −28 dBm), E: Isolator, F: High frequency output, G: High frequency input.

Chapter 7

Cryostat for Argon gas

The cryostat used for the argon gas experiments is the same as the one used for helium (*i.e.* the Mark II version). Nevertheless, some adaptations were made to do it.

- The resonant cavity is made only of copper (see chapter 6).
- The thermometers which measure the temperature of the resonator are of the platinum resistance type. The thermometer which ensures the temperature regulation of the resonator consists of six Pt100 mounted in series. They are glued all around the resonator using Loctite® Stycast 2850FT. The reference thermometer is a Pt25 housed within the resonator (see Figures 7.1 and 7.2).
- The Pt1000 thermometers measuring the pressure tube temperature gradient were not replaced. Indeed, their temperatures cannot fall below their operating limit ($\approx -200°C$) because the coldest temperature of the cryostat is that of liquid nitrogen ($\approx -196°C$).
- The antennas are helical type in order to allow us to excite both the TM and TE modes (see chapter 6).
- Microwave isolators were placed at the radio frequency inlet and outlet of the pressure vessel to carry out tests at higher power and protect the vector network analyzer from the effects of impedance mismatch (see Figure 7.3).
- Amplifiers were mounted at the output of the cryostat in order to verify their effects on the measurement uncertainty (see Figure 7.4).

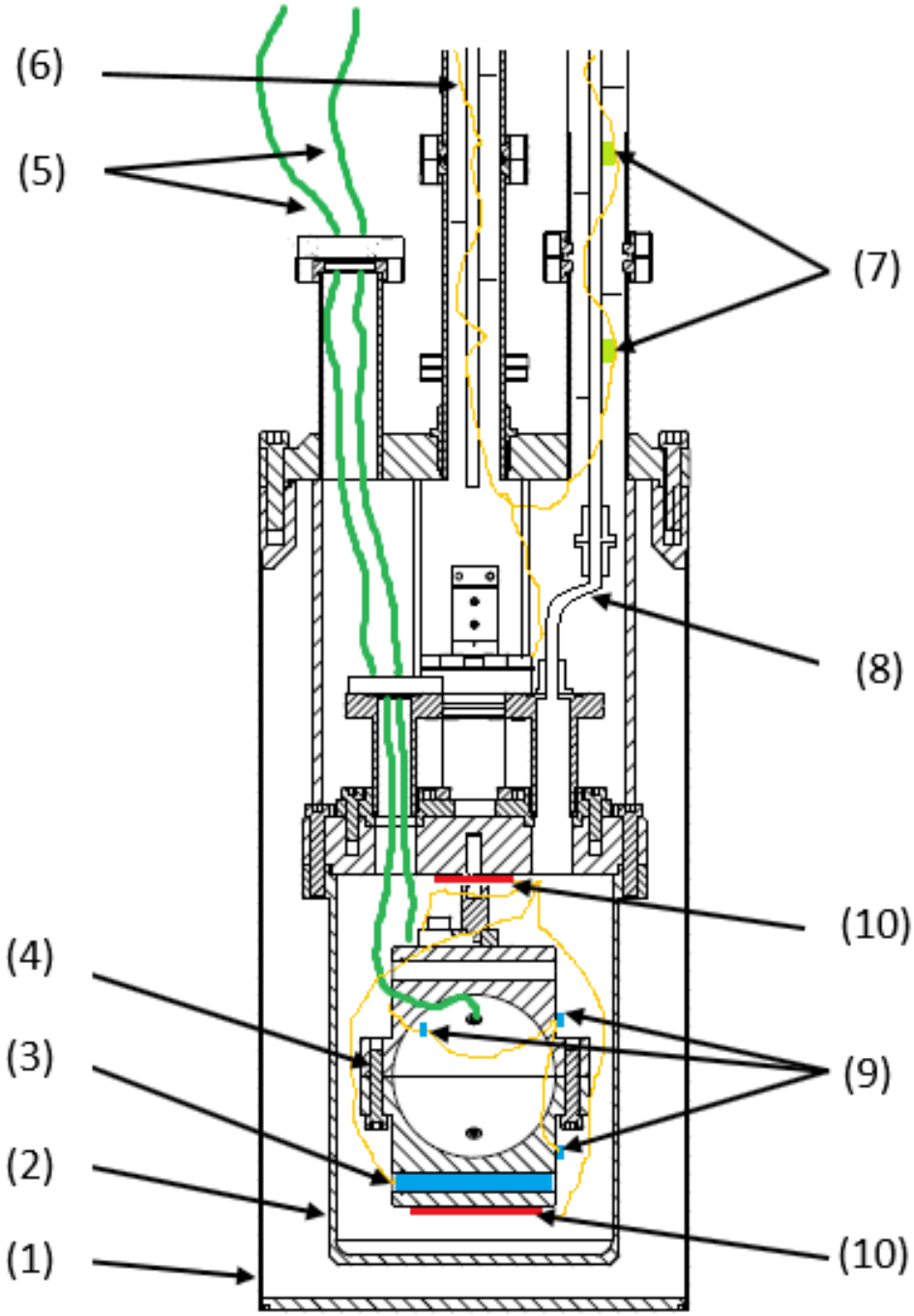

Figure 7.1: Cryostat Mark II (2019): (1) Vacuum chamber, (2) Pressure vessel, (3) Platinum resistance thermometer Pt25 , (4) Copper resonator, (5) Coaxial cables, (6) Temperature sensors and heater cables, (7) Platinum RTD temperature sensor Pt1000, (8) Pressure tube,(9) Six platinum RTD temperature sensors Pt100 wired in series for temperature regulation, (10) Heaters : on top of the pressure vessel 220Ω, underneath the resonator 217Ω.

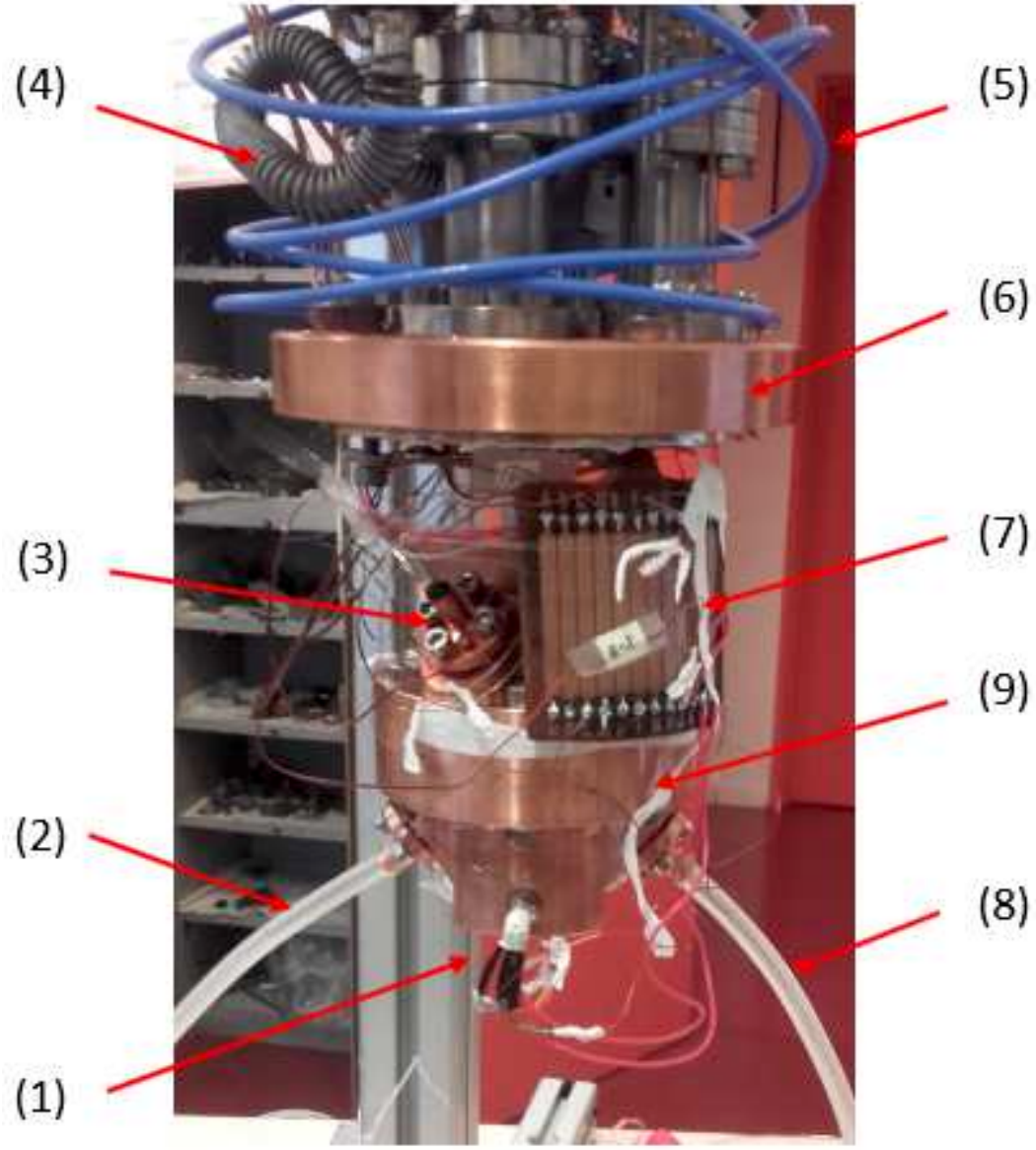

Figure 7.2: Cryostat Mark II: (1) Platinum resistance thermometer Pt25, (2) Argon gas flow inlet tube to protect the copper cavity from oxidation, (3) Antenna in its plug, (4) Flexible stainless steel hose to convey argon gas under pressure to the copper cavity, (5) Coaxial cable, (6) Pressure vessel lid, (7) Thermalization board for the electric wires, (8) Argon gas flow outlet tube, (9) Copper resonator.

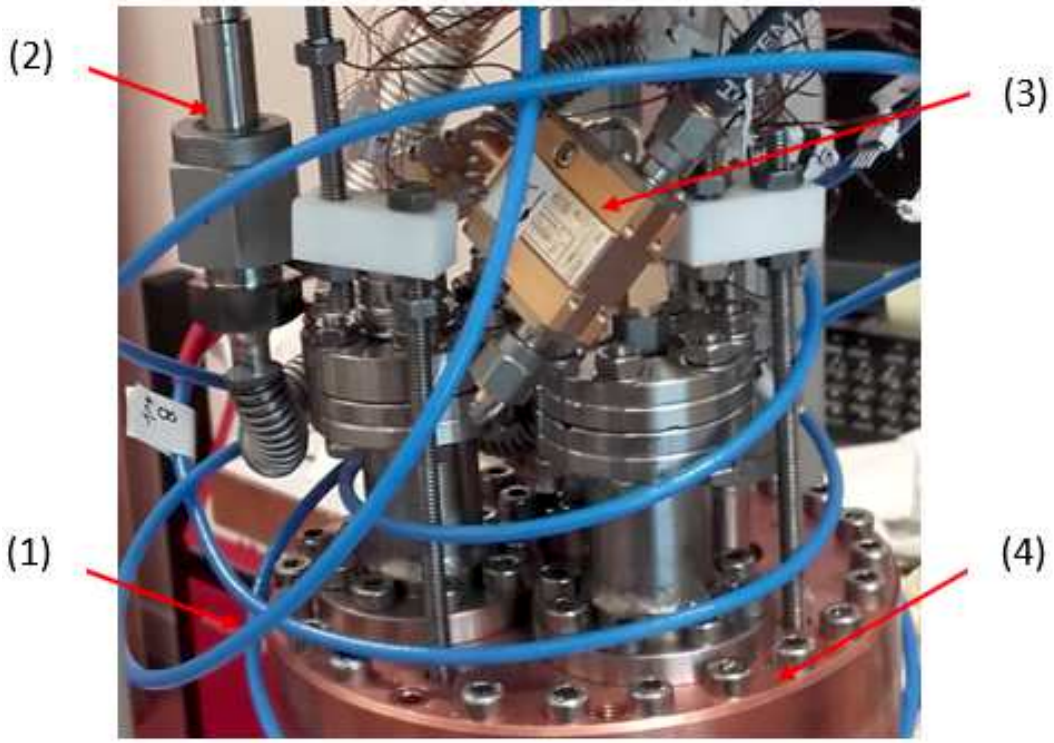

Figure 7.3: Cryostat Mark II: (1) Coaxial cable, (2) Pressure tube, (3) Microwave isolator, (4) Pressure vessel lid.

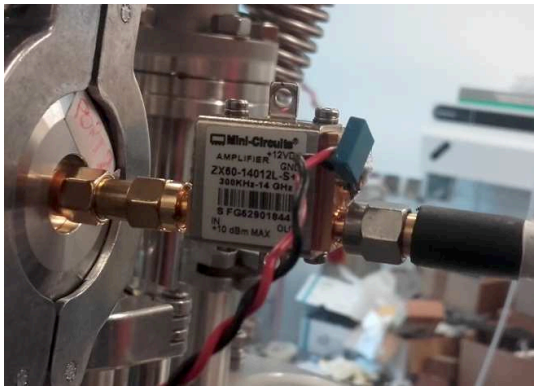

Figure 7.4: Amplifier ZX60-14012L+ from Mini-Circuits®, +11 dBm typ. output power at 1 dB compression, bandwidth: 300 kHz to 14 GHz, flatness over frequency range ±1 dB.

Chapter 8

Experimental set-up

1 Overview

The experimental set-up shown in Figure 8.1 is very similar to that used for helium (see Figure 4.1). Several measuring devices were however replaced to improve the overall performance.

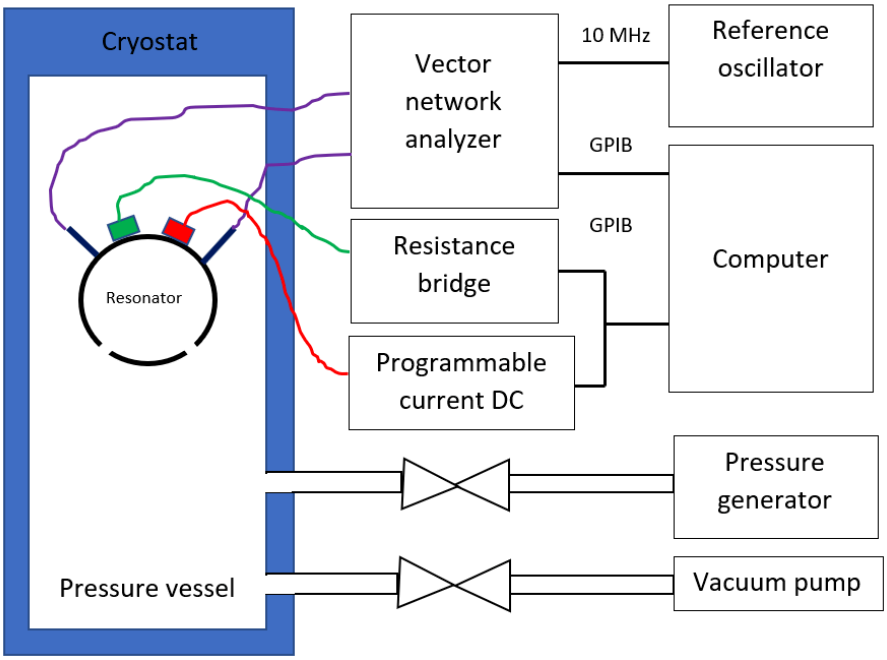

Figure 8.1: Schematic overview of experimental set-up for measurements on argon.

The resonator temperature is now measured by a platinum resistance thermometer (of 25Ω) connected to an MI6010T automated resistance bridge. The stability in the temperature measurement was thus improved by a factor of 1.3 compared to when the Keithley 2002 multimeter was used.

The reference oscillator which initially was a rubidium oscillator was replaced by a global positioning system (GPS) disciplined oscillator (FS740) and a rubidium time base. The latter, while having the same short-term stability as the rubidium reference (1×10^{-12}) , improves long-term stability (1×10^{-13}). Experiments with argon gas can indeed last several weeks.

The figure 8.2 shows a photograph of the experiment. At the time of its taking, the reference oscillator was still a rubidium frequency standard.

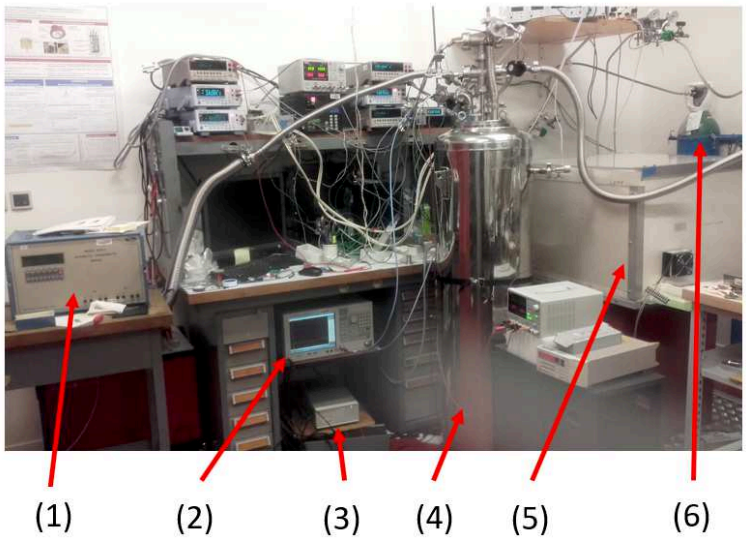

Figure 8.2: Experimental setup during run 7 (November-December 2020): (1) Resistance bridge (2) Vector network analyser connected to the microwave resonator , (3) Rubidium frequency standard, (4) Experimental Dewar, (5) Pressure generator, (6) argon gas cylinder supplying the pressure generator.

2 Apparatus

2.1 Argon gas

As was the case for helium, the level of purity for argon gas must be high because the measurement principle is based on its characteristics. The chosen gas supplier guarantees the purity of the argon gas greater or equal to $99,9999$ % mol with a proportion of (in $\times 10^{-6}$ mol): $H_2O \leq 0.5$, $O_2 \leq 0.1$, $C_nH_m \leq 0.1$, $CO \leq 0.1$, $CO_2 \leq 0.1$, $H_2 \leq 0.1$.

2.2 Pressure generator

Apart from the source gas used which is argon, the pressure generator is identical to that for helium (see chapter 4 section 2.2).

3 Software

The most part of LabVIEW^{TM} VI[1] already used for helium were reused for argon (*cf.* chapter 4 section 3). The regulation coefficients for temperature and pressure were adapted to the new environment. To improve the fitting resolution, only one resonance was followed. Argon virial coefficients were used to calculate the pressure.

4 Physical aspects

4.1 Thermal expansion of the cavity

The deformation of a copper cavity due to its temperature variations can be estimated from its thermal expansion coefficient [40]. From 293 K (room temperature) to 77 K the initial radius of 25 mm of the copper cavity is reduced by 76 μm (*i.e.* -0.302 % of its initial value). Table 8.1 presents the theoretical values of thermal coefficient expansion relating the resonator temperature to the resonant frequency around 90.4 K.

[1]The Virtual Instruments (vi) of LabVIEW^{TM} software are user interfaces that contain the code for a particular application.

Table 8.1: Theoretical frequency shift coefficients resulting from thermal expansion of the cavity around 90.4K .

Mode	Thermal expansion coefficient(Hz K^{-1})
TM_{11}	−49943(735)
TE_{11}	−81792(1203)
TM_{12}	−111342(1638)
TE_{12}	−140621(2069)

The skin effect can be neglected with respect to the dimensional variation. Indeed, when the temperature is increased from 77 K to 90.4 K, the radius of the cavity varies by 3.2 μm and the variation in skin depth is less than a tenth of a nanometer for all modes. The measured thermal expansion is equal to −49962(139) Hz K^{-1} (source: Ar-run8). Its value is consistent with the theoretical one.

4.2 Isothermal compressibility of the cavity

As for a temperature of 5.4 K (see chapter 4 section 4.4) the isothermal compressibility of copper at 90 K is of the order of $\approx 7 \times 10^{-12}$ Pa^{-1}.

4.3 Self-heating

The temperature rise due to self-heating was measured with the MI6010T automated resistance bridge. It is equal to 269(73)μK.

4.4 Thermodynamic temperature determination

The temperature used to calculate the pressure is the thermodynamic temperature while that given by the platinum resistance thermometer corresponds to the International Temperature Scale of 1990 [10]. Consequently, the temperature once measured with the ITS-90 scale is then converted into the thermodynamic scale using the expression [86]:

$$T = T_{90} + \Delta T \tag{8.1}$$

where T is the thermodynamic temperature (in kelvin), T_{90} is the ITS-90 temperature (in kelvin) and the temperature deviation ΔT is given in mK by:

$$\Delta T = T - T_{90} = \sum_{i=0}^{7} b_i * \log_{10}\left[\left(\frac{T_{90}}{273.16 \times 10^3}\right)\right]^{i+1} \tag{8.2}$$

with the following values for the b_i coefficients :

$$\begin{array}{lll} b_0 = 4.42457 \times 10^1 & b_1 = -1.76311 \times 10^2 & b_2 = -1.53985 \times 10^3 \\ b_3 = -3.63685 \times 10^3 & b_4 = -4.19898 \times 10^3 & b_5 = -2.61319 \times 10^3 \\ b_6 = -8.41922 \times 10^2 & b_7 = -1.10322 \times 10^2 & \end{array}$$

A new equation is expected to be released soon.

4.5 Hydrostatic effect

The location of the thermometers along the pressure tube is the same as that used for helium (see chapter 4 4.7). Table 8.2 shows the evaluation carried out for argon gas. These values are given only as an indication because the experiments with helium showed that the model used to calculate them (*i.e.* by taking into account only the conductivity of the pressure tube) did not make it possible to predict accurately the measured temperatures.

Table 8.2: Estimates of the temperatures and relative pressures at 1 kPa of the Figure 4.17 (with the stainless steel thermal conductivity fit of the reference [5]).

Position	Temperature (K)	Relative pressure deviation at 1 kPa (%)
Room	300	+0.00 (0.00)
$\mathbf{T}_5$	247.41	+0.14 (0.04)
$\mathbf{T}_4$	239.02	+0.16 (0.09)
$\mathbf{T}_3$	222.36	+0.21 (0.14)
$\mathbf{T}_2$	175.3	+0.38 (0.20)
$\mathbf{T}_1$	131.92	+0.58 (0.28)
Cavity	90.4	+0.86 (0.39)

4.6 Thermo-molecular effect

Table 8.3 shows the flow regimes in the cryostat Mark II. For the same temperature and pressure conditions as Table 8.3, the flow in the cryostat Mark III is always in the continuum regime (see 8.4). According to Figures 4.19 and 8.3 of the Mark II cryostat, compared to helium, argon is somewhat less likely to exhibit a thermo-molecular effect. For example, at a

Table 8.3: Flow regime for argon gas in the pressure tube of the cryostat Mark II. The mean free path values were computed with molecular collision diameter $d = 364$ pm taken from [8]

Pressure (Pa)	Temperature (K)	Mean free path (μm)	Knudsen number	Flow regime
200	300	35.2	0.012	Slip
400	300	17.6	0.006	Continuum
600	300	11.7	0.011	Continuum
800	300	88.0	0.003	Continuum

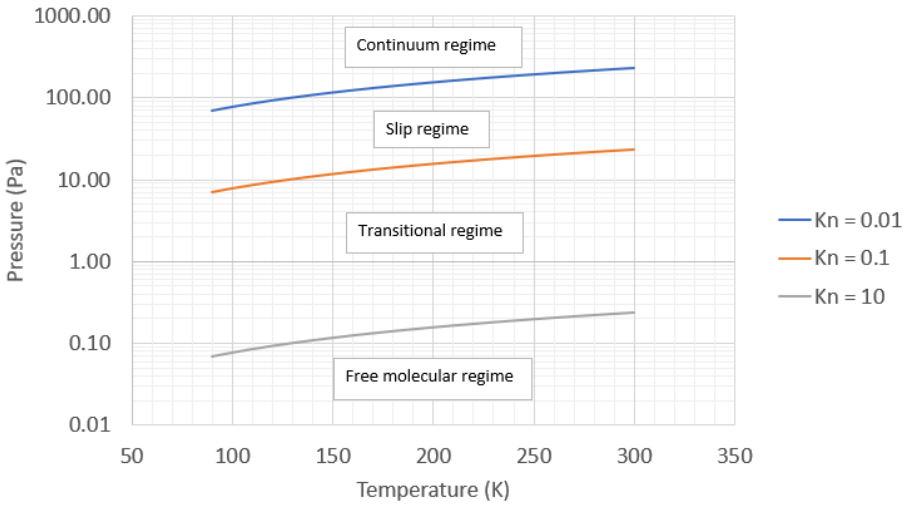

Figure 8.3: Flow regime in the pressure tube of the Mark II cryostat for different values of the Knudsen number K_n.

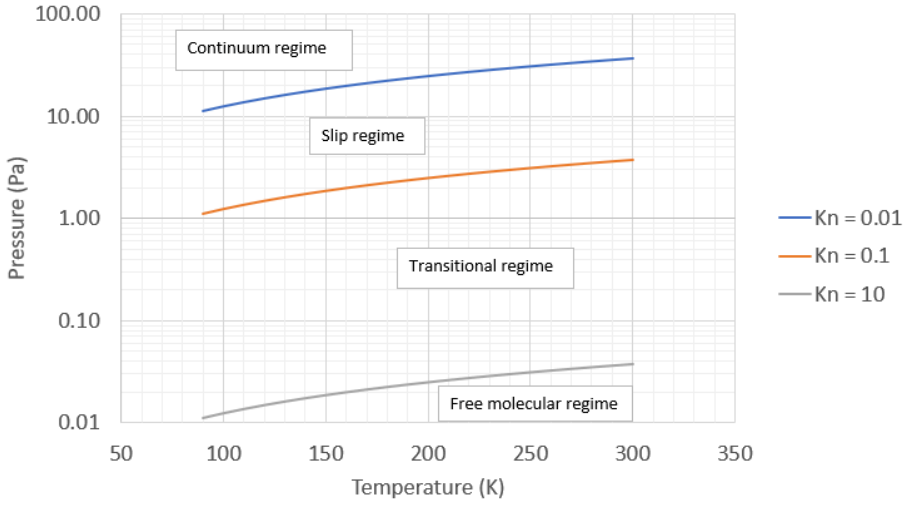

Figure 8.4: Flow regime in the pressure tube of the Mark III cryostat for different values of the Knudsen number K_n.

pressure of 100 Pa and a temperature of 100 K, flow in argon is in continuous mode and in helium in slip mode.

4.7 Outgassing

This influence factor is addressed in chapter 4 (see 4.9).

Chapter 9

Argon experiments

This chapter is devoted to the experimental results obtained during the argon gas pressure measurement sessions. *A priori*, the measure of argon pressure appeared not to present any difficulty after the 'know-how' and knowledge acquired during experiments with helium. The cryostat (Mark II) used for argon was the same as for helium except for the microwave resonator and its thermometers. In addition, the measurements would be facilitated by the longer time between two fillings with cryogenic fluid (between 24 and 48 hours for liquid helium versus over a week for liquid nitrogen). However, as described below, the argon experiment turned out to be far more challenging than expected.

1 Choice of the set-point for the temperature regulation of the resonator

During the experiments, the temperature of the resonator was set at 90.4 K. This temperature allows the argon not only to remain in the gaseous state (it becomes a liquid at this temperature for a pressure greater than or equal to 138 870 Pa) but also avoids any liquid condensation problems.

2 Transmitted antenna power

As for helium experiments, several tests were performed (see section 2). The transmitted power was adjusted to minimize its effect on the resonator temperature without deteriorating the signal-to-noise ratio. The value retained is -20 dBm (*i.e.* 0.01 mW).

3 Quality factor

The quality factor measured with the bare copper resonator is of the order of 26 000 *i.e.* 146 times lower than that measured with the superconducting resonator used for helium (see chapter 5 section 3). To offset this deficit to a certain extent compared to the helium experiment, pre-amplifiers were used to increase the signal-to-noise ratio and thereby the frequency resolution.

4 Impact of pre-amplifiers

Pressure is determined from refractive index measured via the ratio of resonant frequencies. The resonant frequencies are extracted from fits of transmission coefficient $\mid S_{21} \mid$ spectra. Yang *et al.* [85] have shown that the fitting uncertainty can be reduced by inserting two amplifiers (Mini-Circuits model ZX60-14012L) in the microwave circuit. These amplifiers were located close to the cryostat on the cable which links it to the vector network analyzer network receiver.

A first test was carried out with the microwave resonator under vacuum. Table 9.1 summarizes the results. The gain in uncertainty with a single amplifier was 1.6 while the addition of a second amplifier had little impact.

Table 9.1: Comparison of the relative uncertainty in the resonant frequency with different amplifier configurations with the superconducting resonator at $T = 5.4$ K for the TM_{11} mode, VNA power: -18 dBm (*i.e.* 1.58 μW) (source He-run3).

Number of amplifiers	$\frac{\Delta f}{f}$ ($\times 10^9$)	Gain in uncertainty
Without	0.0771	1.0
1	0.0497	1.6
2	0.0447	1.7

A second test was carried out with the copper cavity under vacuum. The result is presented Table 9.2. The gains in uncertainty are identical to those of Table 9.1.

Table 9.2: Comparison of the relative uncertainty in the resonant frequency with different amplifier configurations with the copper resonator at $T = 90.4$ K for the TM_{11} mode, VNA power: 0 dBm (*i.e.* 1 mW) (source Ar-run7) .

Number of amplifiers	$\frac{\Delta f}{f}$ ($\times 10^9$)	Gain in uncertainty
Without	0.80	1.0
1	0.51	1.6
2	0.47	1.7

It should be noted that the gain measured of the fitting resonant frequency uncertainty is lower than that found by Inseok Yang *et al.* They measured a gain of 7.2 (see Table 2 of [85]) *versus* 1.7 for the present experiment (see Tables 9.1 and 9.2).

The two amplifiers were left connected for the next measurements. They were placed in the thermal chamber of the pressure generator in order to ensure their thermal stabilization.

5 Stability under vacuum

The stability of the resonant frequency was measured under vacuum at a temperature of 90.4 K. Figure 9.1 and Table 9.3 show the Allan deviation. The frequency noise increased about ninefold compared with the helium experiment (see section 6). Theoretically, thermal noise varies as the square of the temperature. So between the temperatures of 5.4 K and 90.4 K, it should have increased by a factor of about 4 (square root of the temperature ratio).

Table 9.3: (source Ar run 7).

τ (s)	Allan Deviation the relative resonant frequency ($\times 10^{-9}$)	Standard deviation ($\times 10^{-9}$)
120	1.81	0.07
240	1.30	0.08
480	0.89	0.07
960	0.60	0.07
1920	0.52	0.09
3840	0.36	0.13
7680	0.22	0.13
15 360	0.09	0.09

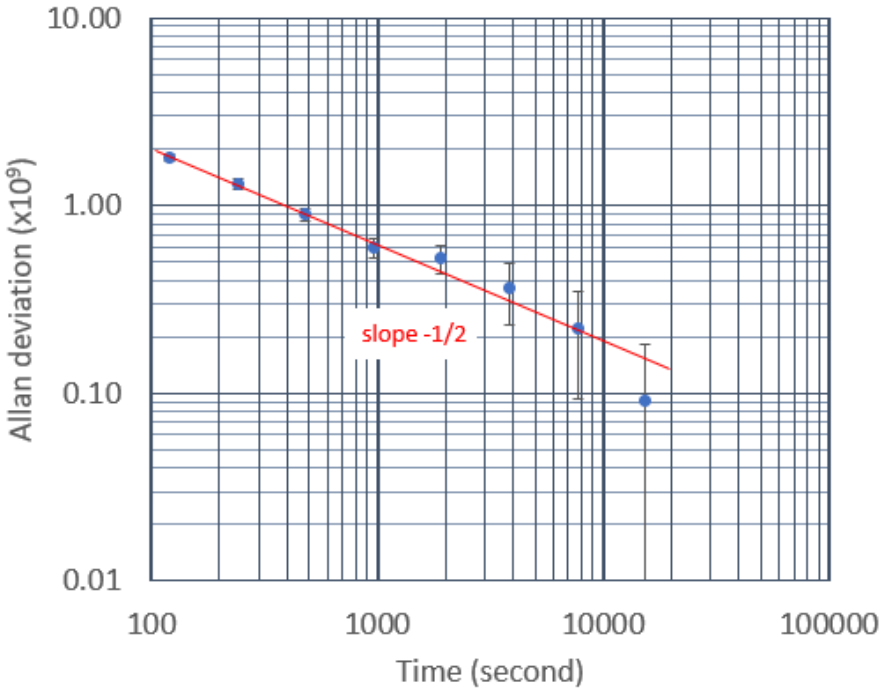

Figure 9.1: (source Ar run 7).

6 The temperature gradient along the pressure tube

As expected, the measured temperatures turned out to be different from those estimated (see Table 8.2). Table 9.4 shows the temperature measured by the pressure tube thermometer for a pressure of 1 kPa.

Table 9.4: Values measured by the pressure tube thermometers 1 kPa (source: Ar-run8_27).

Position	Temperature (K)
Room	301.87
$\mathbf{T}_5$	189.82
$\mathbf{T}_4$	170.68
$\mathbf{T}_3$	143.08
$\mathbf{T}_2$	100.62
$\mathbf{T}_1$	82.40
Cavity	90.40

The thermometer T_1 measures a lower temperature (82.40 K) than that of the resonator (90.40 K). If the temperature of T_1 is correct, it points to a non-monotonic distribution

of the temperature along the pressure tube between the outside of the cryostat and the resonator that could be the cause of gas turbulence which would produce an increase in measurement uncertainty. This fact could not be observed during the helium experiment because the temperature indicated by the sensors lay outside their specified operating range (see section 7). The thermometers along the pressure tube were not calibrated before the experiment. It is therefore possible that the measured value of T1 does not correspond to the actual temperature. To check that the thermometer T1 was behaving correctly, an electrical test was first performed which did not show any problem. A second check was carried out by increasing the gas pressure in order to achieve a change of state of the latter. The liquefaction point of argon gas at a temperature of 90.4 K corresponds to a pressure of 138 870 Pa (*cf.* [87]). A pressure of 138 778 Pa with a cavity temperature of 90.485 K was reached without the gas liquefying. The thermometer T1 measured a temperature of 84.2 K which corresponds to a liquefaction pressure of 72 078 Pa (*cf.* [87]). This result shows that the thermometer T1 indicated an incorrect value and that the real temperature distribution is in fact monotonic. Consequently, the T_1 value was no longer taken into account for the calculation of the hydrostatic pressure correction.

7 Pressure tests

Figure 9.3 shows the stability of the pressure generated over several hours. At 150 Pa the pressure is stable to better than 0.01 Pa while at 20 kPa it is stable to better than 0.1 Pa. The slope of $-1/2$ of the Allan deviation Fig 9.4 indicates the presence of white frequency noise for more than an hour.

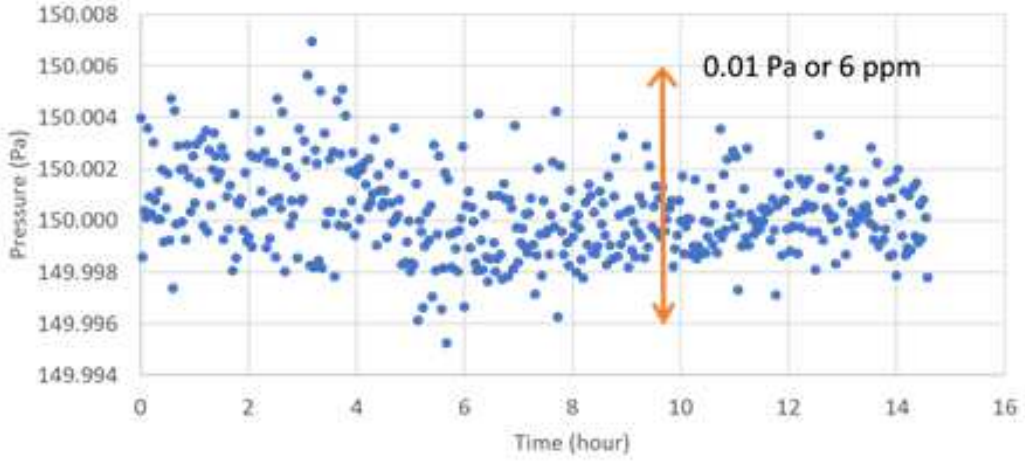

Figure 9.2: Stability of the pressure generator at 150 Pa.

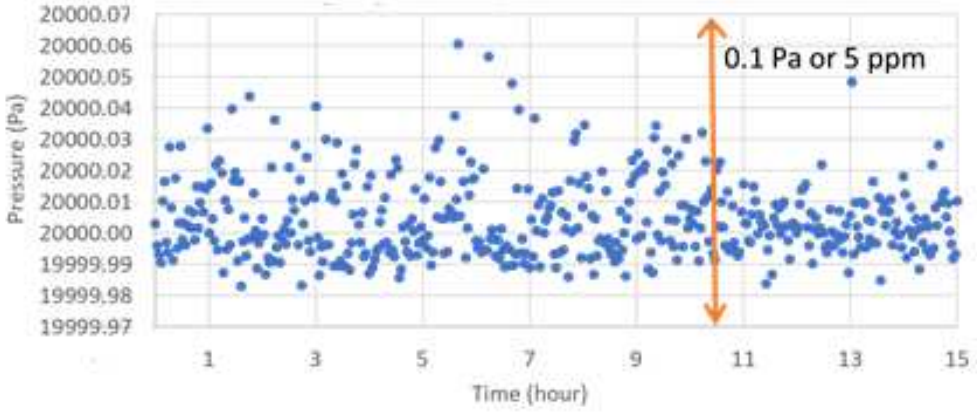

Figure 9.3: Stability of the pressure generator at 20 kPa.

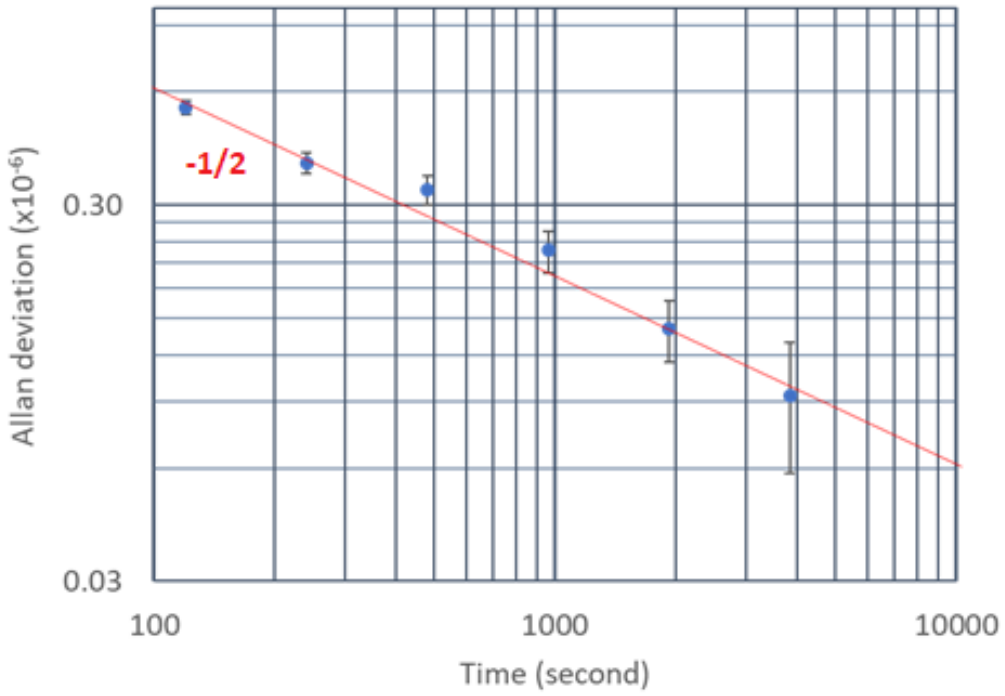

Figure 9.4: Relative Allan deviation of the pressure generated by the pressure generator at 20 kPa. The slope of $-1/2$ is consistent with white frequency noise.

Figures 9.5 and 9.6 show the pressure difference and the relative pressure difference between the microwave sensor and the reference standard for four successive pressure cycles between 10 kPa and 500 Pa. For the first three cycles a quadratic background was used for the frequency fitting and for the fourth a linear [1]. As for the experiment with helium, there appears a variable deviation depending on the pressure but this time repeating of the cycles does not tend to stabilize pressure.

Figure 9.7 shows the resonance frequency for repeated jumps between two pressure points: the first under vacuum (obtained with a turbo-molecular pump), the second at 10 kPa. The resonant frequency is unstable.

Figure 9.8 shows the half-width during the same test on two pressure points. It should be constant, but instead it moves without tending to stabilize.

[1] *C.f.* equation 4.1, in the equation, the polynomial complex coefficients for the background are B, C and D

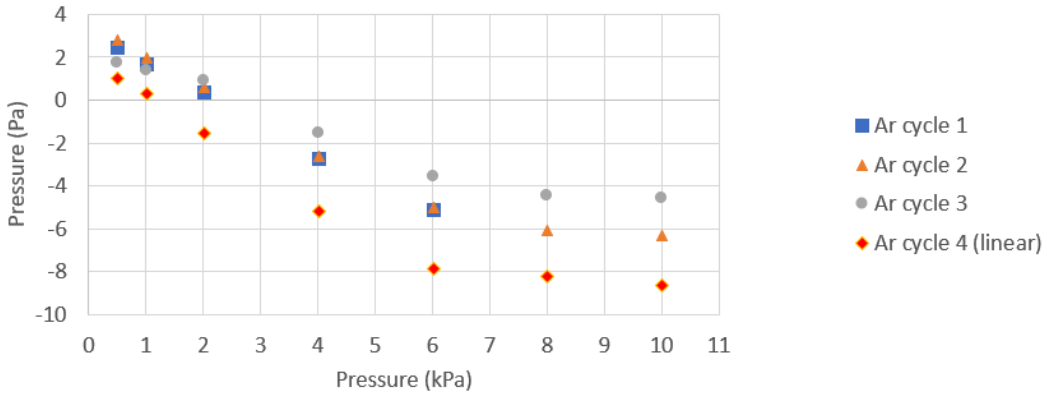

Figure 9.5: Pressure difference between the microwave sensor and a reference sensor for four successive pressure cycles from 10 kPa to 500 Pa (source Ar-run 8).

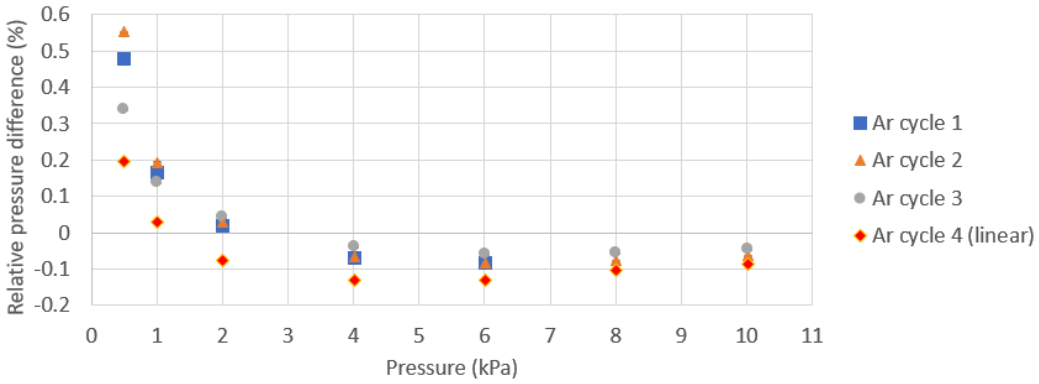

Figure 9.6: Relative pressure difference between the microwave sensor and a reference sensor for four pressure cycles from 10 kPa to 500 Pa (source Ar-run 8).

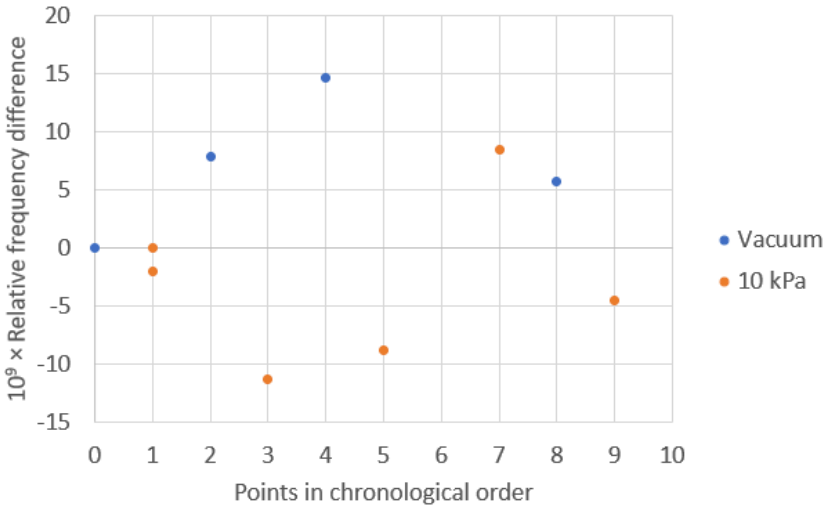

Figure 9.7: Relative resonant frequency measured during cycles consisting of two pressure points: vacuum and 10 kPa (source Ar-run 9).

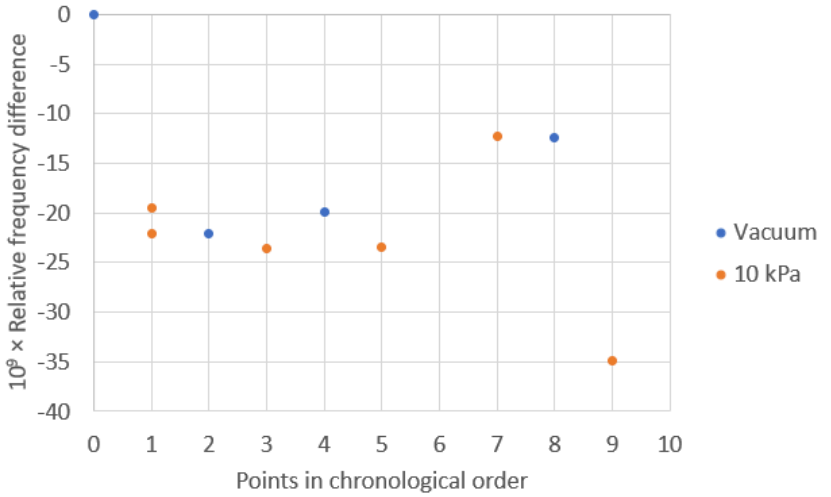

Figure 9.8: Relative half-width frequency measured during cycles consisting of two pressure points: vacuum and 10 kPa (source Ar-run 9).

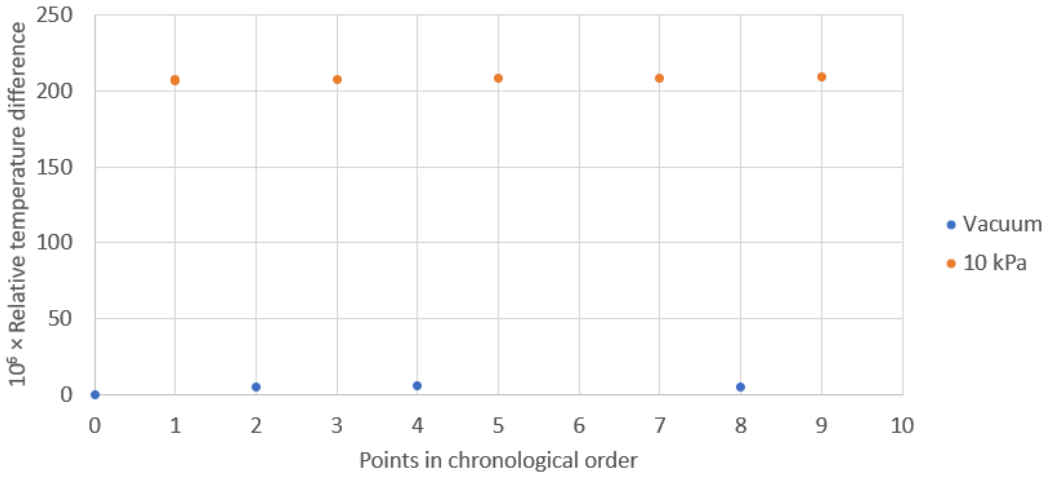

Figure 9.9: Relative values of the reference thermometer measured on cycles consisting of two pressure points: vacuum and 10 kPa. The temperature difference measured by the reference thermometer between vacuum and 10 kPa is approximately 18 mK (source Ar-run 9).

Figure 9.9 shows the temperature measured by the reference thermometer during the alternating pressure test (vacuum and 10 kPa). It should be constant whatever the pressure because the reference thermometer is fixed to the copper resonator near the regulation thermometer. However, the measurements show a difference of about 18 mK between vacuum and 10 kPa.

A new test was performed by changing the conductive heat transfer caused by temperature regulation. The heaters inside the pressure vessel were disconnected and new ones were fixed on the outer walls of the pressure vessel. The test of the two pressure points gave the same result as before.

Figure 9.10 shows another example of the problems encountered. Several pressure levels around 4 kPa are applied to the device. The temperature measured by the reference thermometer clearly shows a pressure dependence. At the same time, the half-width of the resonant frequency drops for no apparent reason. In fact, a few hours earlier, during a liquid nitrogen transfer, it had increased sharply. The half-width tends to return to its initial value.

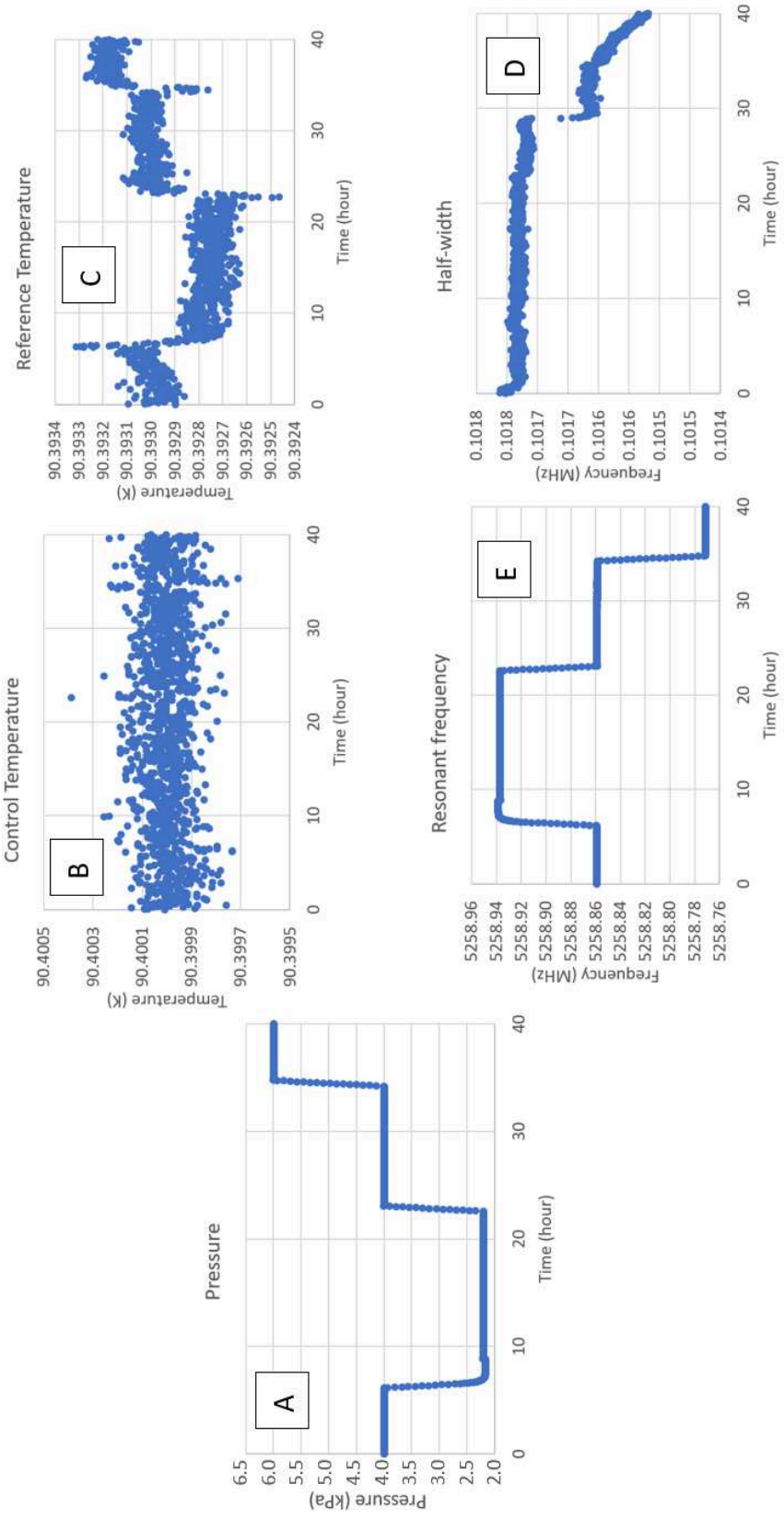

Figure 9.10: Pressure steps. (A) Pressure, (B)Control Temperature, (C) The reference temperature appears to follow the pressure variations, (D) Half-width, (E) Resonant frequency (source Ar-run 8).

These experiments highlighted three problems: variable half-width, a temperature difference between the regulation and resonator thermometers, and frequency instability.

The frequency instability is probably caused by the first two problems. The variation in the half-width might come from a variation in the volume of the cavity. The antennas can move. The two hemispheres that make up the resonator can also move relative to each other. To verify the first hypothesis, new antennas were made. Tests carried out with them showed that the half-width continued to vary. The problem with thermometers could come from their dependence on the pressure or from the movement of the two hemispheres constituting the resonator.

Figure 9.11 shows the solutions implemented to remedy these problems. To protect them from pressure variations, the Pt100 sensors constituting the regulation thermometer were placed in copper tubes and are held in place by adhesive (Loctite® Stycast 2850FT). These tubes are then held onto the resonator by a screw nut system, the copper of the tubes being in contact with the body of the resonator. Three stainless steel bolts holding the two hemispheres of the resonator were replaced by three copper screws so as to have the same coefficient of thermal expansion as the resonator. A stainless steel spring washer was also added to strengthen the contact of the two hemispheres at low temperatures.

This new system should make it possible to remedy the problems encountered and improve the quality of the measurements.

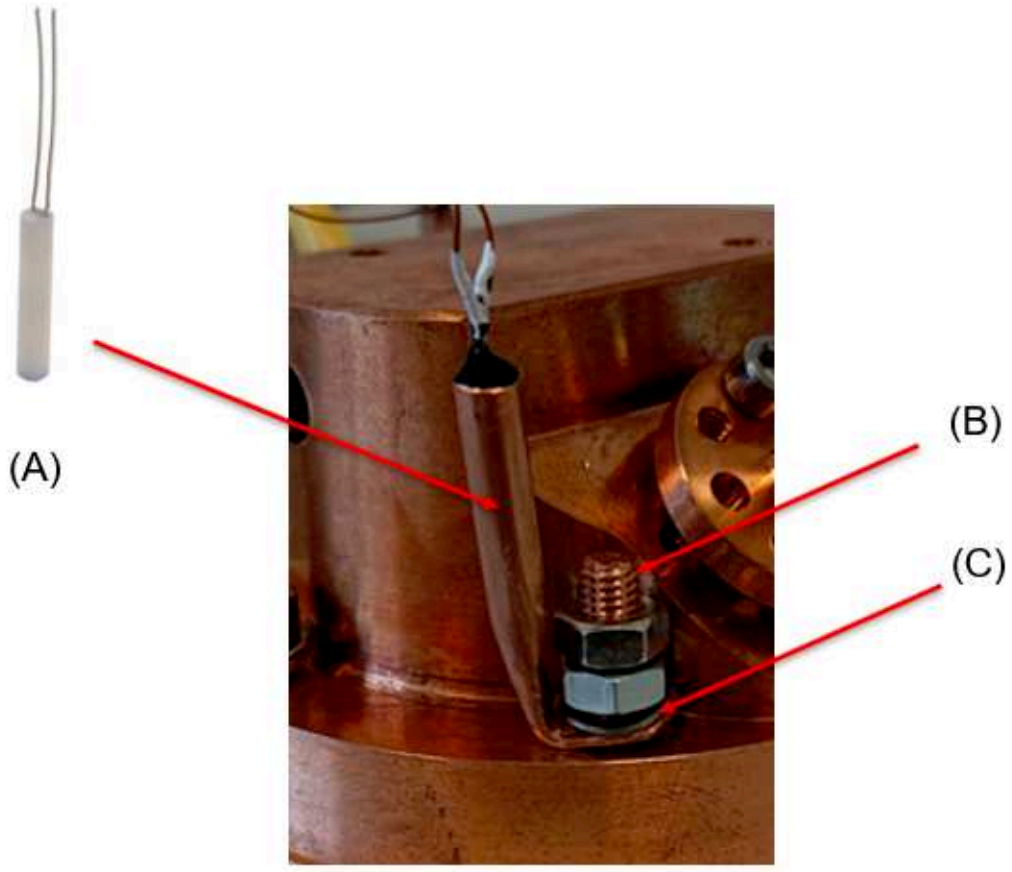

Figure 9.11: Next experiment, (A) Control thermometer (Pt100) embedded in a copper tube, (B) Copper screw, (C) Stainless steel spring washer.

8 Uncertainty budget

It is possible to establish a first uncertainty budget by assuming the stability problems mentioned above to have been solved. Table 9.5 shows a provisional uncertainty budget for pressures of 200 Pa and 20 kPa, the resonator being at a temperature of 90.4 K. Figure 9.12 illustrates the propagation of uncertainties between 200 Pa and 20 kPa. Unlike helium experiments at 5 K, the thermal expansion is no longer negligible and temperature fluctuations give rise to a type-A contribution. In addition, the second density virial coefficient B_ρ is no longer negligible at 20 kPa.

Table 9.5: Argon gas measurement uncertainty budget with the copper microwave cavity at $T = 90.4$ K. With P pressure; κ_T isothermal compressibility; T thermodynamic temperature; A_μ molar magnetic polarizability; A_ϵ molar electric polarizability; B_ϵ second dielectric virial coefficient; B_2, C_2, D_2 density virial coefficients; f_m measured frequency. (The uncertainty components that are less than 20 μ Pa are omitted or replaced by dashes.

Working pressure Uncertainty unit	200 Pa (mPa)	20 kPa (mPa)
P uncertainty components, Type B		
Isothermal compressibility κ_T	0.6	56.1
Gas impurities	–	–
A_μ [88]	–	2.9
A_ϵ [32]	0.47	48
B_ϵ [89]	–	10.9
B_ρ [82]	–	354
C_ρ [83]	–	–
D_ρ [83]	–	–
P uncertainty components, Type A		
Thermal expansion	121	119
f_m measurement and half-with correction	115	114
Temperature calibration, Type B	0.2	22.4
Temperature measurement, Type A	0.1	9.6
Temperature conversion in the thermodynamic scale, Type B[86]	2.5	246
P combined uncertainty	167	467

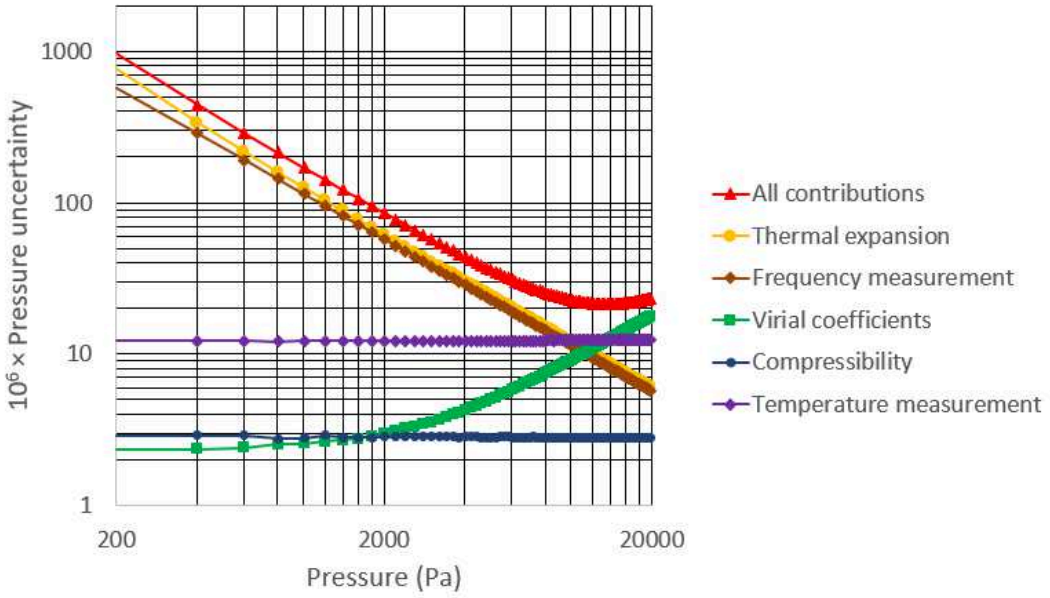

Figure 9.12: Variation with the pressure of the various contributions to the uncertainty in the pressure measurement: in purple, the temperature measurement, in dark blue the compressibility, in green the virial coefficients, in brown the compressibility, in yellow the thermal expansion and all contributions are represented by the red curve.

Part III

Conclusion and perspectives

Chapter 10

Conclusion and perspectives

This thesis has described the development of a novel absolute pressure standard for the range 200 Pa to 20 kPa. The aim is to provide better calibration and measurement capabilities in this range than those currently available using piston balances. In the present work, pressure is measured via refractive index gas manometry using either helium-4 or argon gas. The refractive index is measured using microwave resonance (from 5.0 GHz to 11.7 GHz) with a quasi-spherical niobium-coated copper resonator and takes advantage of over a decade of work in the same group to measure the Boltzmann constant using these gases. Since the refractive index is a function of both temperature and pressure, if the former is measured using a calibrated thermometer, one can extract the pressure. The complementary technique refractive index gas thermometry (RIGT) whereby refractive index measurements at a known pressure are used to determine a temperature, is already well established. The current project has benefited from RIGT studies by our sister group at the Laboratory of Cryogenics, Technical Institute of Physics and Chemistry, Chinese Academy of Sciences (TIPC CAS).

The major part of the thesis has dealt with a novel device which uses a superconducting niobium coated copper cavity to measure the refractive index of helium-4 around $T = 5.4$ K, a temperature below the superconducting transition temperature of niobium (9.2 K) but above the helium-4 liquefaction point. The use of helium-4 is also attractive in that the dielectric and density virial corrections to account for non ideal gas behaviour can be calculated *ab initio* with an accuracy surpassing that of experiments [33].

Work on helium involved the development successively of three cryostats: one for proof of principle, the second for the study of behaviour under pressure and the third incorporating improvements based on experience gained with previous cryostats (*e.g.* larger diameter pressure tubing to minimize the thermomolecular effect, wider range thermometers to calculate the hydrostatic correction). If most of the goals have been achieved, a comparison with a calibrated pressure standard remains to be performed.

During an inevitable hiatus in the experiment related to the building of the third cryostat, the initial project was expanded to include an analogous measurement with argon. Here a copper resonator was used at 90 K. While no superconducting coating was employed, a gain in signal-to-noise (SNR) and hence frequency resolution was expected via the use of pre-amplifiers. Thus far, the effect of these has been disappointing (the fitting resonant frequency uncertainty reduction was only 1.7 versus the 7 expected). Although the virial coefficients of this gas come from experimental data, and the experiments lack the novelty of the superconducting cavity used for helium, the apparatus is less demanding in terms of cryogenics (liquid nitrogen alone suffices). This would make it more likely to be copied or adapted by other standards laboratories. At the time of writing, reproducible results with argon have not been forthcoming. The cause is suspected to be of technical origin, possibly related to the sealing of the microwave resonator and work is in progress to solve the problem. Since both experiments use cryogen-filled cryostats, progress has often been dogged by the unavailability of liquid nitrogen or liquid helium for logistical reasons. The continuity and comfort of measurements would be improved considerably via the use of a cryogen-free cryostat cooled with a pulse-tube cryocooler. This would make the measurement easier. Thermal oscillations generated by the cryocooler can be minimized according to Pan *et al.* [90].

Finally, this study on a novel instrument follows the current trend in metrology of basing the working principle of measuring devices on fundamental constants. The recent redefinition of the SI system of units via the fixing of values of fundamental or physical constants contributes to this evolution.

References

References

[1] Jousten K. Traceability to SI units for vacuum measurement in industrial applications. *Measurement*, 45(10):2420–2425, December 2012.

[2] BIPM. Database of Calibration and Measurement Capabilities – CMCs. `https://www.bipm.org/kcdb/`. Consulted in June 2021.

[3] COFRAC. Database of calibration and measurement capabilities. `https://tools.cofrac.fr/annexes/sect2/2-37.pdf/`. Consulted in June 2021.

[4] Mangin P. and Kahn R. *Matériaux supraconducteurs*. EDP Sciences, 2017.

[5] *Cryogenic material properties database - Cryocoolers 11*. Springer, 2002.

[6] Williams D. R. NASA Space Science Data Coordinated Archive. `https://nssdc.gsfc.nasa.gov/planetary/factsheet/earthfact.html`. Consulted in June 2021.

[7] *CRC Handbook of Chemistry and Physics*. CRC Press, 97th edition, 2017.

[8] Kennard E. H. *Kinetic Theory of Gases, with an Introduction to Statistical Mechanics*. McGraw-Hill, 1938.

[9] Takaishi T. and Sensui Y. Thermal transpiration effect of hydrogen, rare gases and methane. *Transactions of the Faraday Society*, 59:2503–2514, 1963.

[10] BIPM. Guide to the realization to the ITS-90 - interpoling constant-volume gas thermometry. `https://www.bipm.org/utils/common/pdf/ITS-90/Guide-ITS-90-GasThermometry-2015.pdf`, 2015.

[11] Mehl J. B., Moldover M. R., and Pitre L. Designing quasi-spherical resonators for acoustic thermometry. *Metrologia*, 41(4):295–304, June 2004.

[12] EMPIR. Towards quantum-based realisations of the pascal. https://www.ptb.de/empir2019/quantumpascal/home/. Website of the EU-project 18SIB04 'QuantumPascal'.

[13] Mazauric S. *Gassendi, Pascal et la querelle du vide*. Presses Universitaires de France, 1998.

[14] BIPM. The international system of units (SI) 9th edition. https://www.bipm.org/utils/common/pdf/si-brochure/SI-Brochure-9.pdf, 2019.

[15] O'Hanlon J. F. *A User's Guide to Vacuum Technology*. Wiley-Interscience, 3rd edition, 2003.

[16] Dadson R. S., Peggs G. N., and Lewis S. L. *The Pressure balance: theory and practice*. Her Majesty's Stationery Office, 1982.

[17] Corey P. No Longer Under Pressure: NIST Dismantles Giant Mercury Manometer. https://www.nist.gov/news-events/news/2019/06/no-longer-under-pressure-nist-dismantles-giant-mercury-manometer, June 2019.

[18] World Health Organization. Mercury and health. https://www.who.int/news-room/fact-sheets/detail/mercury-and-health, March 2017.

[19] Gibney E. Pressure's 400-year-old measurement techniques get an upgrade. *Nature*, 570(7762):424–426, 2019.

[20] Fluke. Fluke calibration discontinued and obsolete products. https://us.flukecal.com/products/obsolete-products. Fluke calibration website consulted in July 2021.

[21] Hendricks J. Quantum for pressure. *Nature Physics*, 14(1):100, 2018.

[22] Scherschligt J., Fedchak J. A., Ahmed Z., Barker D. S., Douglass K., Eckel S., Hanson E., Hendricks J., Klimov N., Purdy T., Ricker J., Singh R., and Stone J. Quantum-based vacuum metrology at the National Institute of Standards and Technology. *J. Vac. Sci. and Techn.*, 36(4):040801, 2018.

[23] NIST. NIST industry partner aim to develop quantum pascal standard into real-world device. https://www.nist.gov/news-events/news/2017/09/nist-industry-partner-aim-develop-quantum-pascal-standard-real-world-device, September 2017.

[24] BIPM. International vocabulary of metrology – basic and general concepts and associated terms (VIM). https://www.bipm.org/utils/common/documents/jcgm/JCGM_200_2012.pdf, 2012. 3rd Edition.

[25] Jousten K. Vacuum metrology and its impact on research and industry. *Vakuum in Forschung und Praxis*, 31(4):16–22, 2019.

[26] ISO. International Organization for Standardization website. https://www.iso.org/. Consulted in July 2021.

[27] Bennett S. J., Clapham P. B., Daborn J. E., and Simpson D. I. Laser interferometry applied to mercury surfaces. *J. Phys. E: Sci. Instrum.*, 8(1):5–7, January 1975.

[28] Poulter K. F. The calibration of vacuum gauges. *J. Phys. E: Sci. Instrum.*, 10(2):112–125, 1977.

[29] Nawrocki W. *Introduction to Quantum Metrology: The Revised SI System and Quantum Standards*. Springer, 2019.

[30] Levine I. *Quantum Chemistry*. Pearson Education, 2000.

[31] Hurly J. J. and Moldover M. R. *Ab initio* Values of the Thermophysical Properties of Helium as Standards. *Journal of Research of the National Institute of Standards and Technology*, 105(5):667–688, 2000.

[32] Gaiser C. and Fellmuth B. Polarizability of helium, neon, and argon: New perspectives for gas metrology. *Phys. Rev. Lett.*, 120(12):123203, 2018.

[33] Rourke P. M. C. Perspective on the refractive-index gas thermometry data landscape. *Journal of Physical and Chemical Reference Data*, 50(3):033104, 2021.

[34] Silvestri Z., Bentouati D., Otal P., and Wallerand J.-P. Towards an improved helium-based refractometer for pressure measurements. *ACTA IMEKO*, 9(5):305–309, December 2020.

[35] Gao B., Pitre L., Luo E. C., Plimmer M. D., Lin P., Zhang J. T., Feng X. J.and Chen Y. Y., and Sparasci F. Feasibility of primary thermometry using refractive index measurements at a single pressure. *Measurement*, 103:258–262, 2017.

[36] Hill David A. *Electromagnetic fileds in cavities: deterministic and statistical theories*. John Wiley and Sons, 2009.

[37] May E.F., Pitre L., Mehl J. B., Moldover M. R., and Schmidt J. W. Quasi-spherical cavity resonators for metrology based on the relative dielectric permittivity of gases. *Review of Scientific Instruments*, 75:3307–3317, 2004.

[38] Moldover M. R., Boyes S. J, Meyer Ch. W., and Goodwin A. R. H. Thermodynamic temperatures of the triple points of mercury and gallium and in the interval 217 K to 303 K. *Journal of Research of the National Institute of Standards and Technology*, 104(1):11, 1999.

[39] Stein S.R. and Turneaure J.P. Superconducting resonators: High stability oscillators and applications to fundamental physics and metrology. In *AIP Conference Proceedings*, volume 44, pages 192–213. American Institute of Physics, 1978.

[40] Simon N.J., Drexler E.S., and Reed R.P. *Properties of Copper and Copper Alloys at Cryogenic Temperatures*, volume 177 of *NIST Monograph*. National Institute of Standards and Technology, 1992.

[41] Zhang H.Y., Gao B., Liu W.J., Pan C.Z., Han D.X., Plimmer M., Luo E.C., and Pitre L. Resonance frequency measurement with accuracy and stability at the 10^{-12} level in a copper microwave cavity below 26 K by experimental optimization. *Measurement Science and Technology*, 31(7):075011, 2020.

[42] Zhang H.Y., Liu W.J., Gao B., Chen Y.Y., Pan C.Z., Song Y.N., Chen H., Han D.X., Hu J.F, Luo E.C., and Pitre L. A high-stability quasi-spherical resonator in SPRIGT for microwave frequency measurement at low temperatures. *Sci. Bull.*, 64:286–8, 2019.

[43] Han D.X., Gao B., Chen H., Gambette P., Zhang H.Y., Pan Ch.zh., Song Y.N., Liu W.J., Hu J.F., Yu B., Yingwen L., Luo E.C., and Pitre L. Ultra-stable pressure is realized for Chinese single pressure refractive index gas thermometry in the range 30–90 kPa. *Sci. Bull.*, 63:1601–3, 2018.

[44] Gao B., Chen H., Han D.X., Gambette P., Zhang H.Y., Pan C.Z., Liu Y.W., Yu B., Luo E.C., Plimmer M., and Pitre L. Realization of ppm level pressure stability for primary thermometry using a primary piston gauge. *Measurement*, 160:107807, 2020.

[45] Van Delft D. and Kes P. The discovery of superconductivity. *Physics Today*, 63(9):38–43, 2010.

[46] Kammerlingh Onnes H. Further experiments with liquid helium. On the change of electric resistance of pure metals at very low temperature etc. IV. The resistance of pure mercury at helium temperatures. *Communications of the Physical Laboratory of the University of Leiden*, (120b):3–5, 1911.

[47] Matricon J. and Waysand G. *La guerre du froid: une histoire de la supraconductivité*. Seuil, 1994.

[48] Ginzburg V. L. Superconductivity: the day before yesterday, yesterday, today, tomorrow. *Advances in Physical Science*, 170(6):619–630, 2000.

[49] Meissner W. and Ochsenfeld R. Ein neuer Effekt bei Eintritt der Supraleitfähigkeit. *Naturwissenschaften*, 21(44):787–788, 1933.

[50] Snider E., Dasenbrock-Gammon N., McBride R., Debessai M., Vindana H., Vencatasamy K., Lawler K. V., Salamat A., and Dias R. P. Room-temperature superconductivity in a carbonaceous sulfur hydride. *Nature*, 586:373–377, 2020.

[51] Gorter C. J. and Casimir H. On supraconductivity I. *Physica*, 1(1-6):306–320, 1934.

[52] Landau L. D. and Ginzburg V. L. On the theory of superconductivity. *Zh. Eksp. Teor. Fiz.*, 20:1064, 1950.

[53] Bardeen J., Cooper L. N., and Schrieffer J. R. Theory of superconductivity. *Physical Review*, (5):1175, 1957.

[54] Buschow K.H.J. *Concise Encyclopedia of Magnetic and Superconducting Materials*. Elsevier, 2005.

[55] Langner J., Catani L., Cianchi A., Mirowski R., Lorkiewicz J., Proch D., Russo R., Sadowski M.J., Strzyzewski P., Tazzari S., and Witkowskia J. Thin superconducting niobium-coatings for RF accelerator cavities. In *Photonics Applications in Industry and Research IV*, volume 5948, page 594809. International Society for Optics and Photonics, 2005.

[56] Palmer F. Surface resistance of superconductors–Examples from Nb - O Systems. Technical report, Proceedings of the Third Workshop on RF Superconductivity, Argonne National Laboratory, Illinois, USA, 1988.

[57] Ciovati G. Effect of low-temperature baking on the radio-frequency properties of niobium superconducting cavities for particle accelerators. *Journal of Applied Physics*, 96(3):1591–1600, 2004.

[58] Ekin J. *Experimental techniques for low-temperature measurements: cryostat design, material properties and superconductor critical-current testing*. Oxford University Press, 2006.

[59] Berg R. F., Gooding T., and Vest R. E. Constant pressure primary flow standard for gas flows from 0.01 cm^3/min to 100 cm^3/min (0.007–74 μmol/s). *Flow Measurement and Instrumentation*, 35:84–91, 2014.

[60] Visioli A. *Practical PID control*. Springer Science & Business Media, 2006.

[61] Strutz T. *Data Fitting and Uncertainty, A practical introduction to weighted least squares and beyond*. Vieweg Teubner, 2010.

[62] Schmidt J.W., Gavioso R.M., May E.F., and Moldover M.R. Polarizability of helium and gas metrology. *Physical Review Letters*, 98(25):254504, 2007.

[63] Gaiser C. and Fellmuth B. Method for extrapolating the compressibility data of solids from room to lower temperatures. *Physica Status Solidi*, 253(8):1549–1556, 2016.

[64] Taconis K. W., Beenakker J. J. M., Nier A. O. C., and Aldrich L. T. Measurements concerning the vapour-liquid equilibrum of solutions of He3 in He4 below 2.19 K. *Physica*, 15(8-9):1949, 1949.

[65] Yoshida S., Ravikumar K.V., Williamson J., Papavasiliou N., and Frederking T.H.K. Thermoacoustic Taconis oscillations in helium-4 liquid level sensors. In Haruyama T., Mitsui T., and Yamafuji, editors, *Proceedings of the Sixteenth International Cryogenic Engineering Conference/International Cryogenic Materials Conference*, pages 657–660. Elsevier Science Ltd, 1997. Kitakyushu, Japan, 20th-24th May 1996.

[66] Rott N. Thermoacoustics. In *Advances in Applied Mechanics*, volume 20, pages 135–175. Elsevier, 1980.

[67] Pan C. Z., Chen H., Han D.X., Zhang H.Y, Plimmer M., Imbraguglio D., Luo E.C., Gao B., and Pitre L. Numerical and Experimental Study of the Hydrostatic Pressure Correction in Gas Thermometry: A Case in the SPRIGT. *International Journal of Thermophysics*, 41(8):1–17, 2020.

[68] Rojas C. M., Graur I., Perrier P., and Meolans J. G. Thermal transpiration flow: A circular cross-section microtube submitted to a temperature gradient. *Physics of Fluids*, 23(3):031702, 2011.

[69] Pavese F. and Beciet G. M. M. *Modern Gas-Based Temperature and Pressure Measurements*. Springer Science & Business Media, 2012.

[70] Hirschfelder J. O., Curtiss Ch. F., Bird R. B., and Mayer M. G. *Molecular theory of gases and liquids*, volume 165. Wiley New York, 1964.

[71] Shen C. *Rarefied Gas Dynamics: Fundamentals, Simulations and Micro Flows*. Springer Science & Business Media, 2006.

[72] Chaplin M. F. Structure and properties of water in its various states. *Encyclopedia of Water: Science, Technology, and Society*, pages 1–19, 2019.

[73] Mangin Ph. and Kahn R. *Superconductivity: an introduction*. Springer, 2016.

[74] Maxfield B. W. and M^{c}Lean W.L. Superconducting penetration depth of niobium. *Physical Review*, 139(5A):A1515, 1965.

[75] Szeftel J., Sandeau N., and Khater A. Study of the skin effect in superconducting materials. *Physics Letters A*, 381(17):1525–1528, 2017.

[76] Padamsee H. *RF Superconductivity Science, Technology and Applications*. Wiley Online Library, 2009.

[77] McRae C. R. H., Wang H. z., J. S. Gao, Vissers M. R., Brecht T., Dunsworth A., Pappas D. P., and Mutus J. Materials loss measurements using superconducting microwave resonators. *Review of Scientific Instruments*, 91(9):091101, 2020.

[78] Leong K. and Mazierska J. Precise measurements of the Q factor of dielectric resonators in the transmission mode-accounting for noise, crosstalk, delay of uncalibrated lines, coupling loss, and coupling reactance. *IEEE Transactions on Microwave Theory and Techniques*, 50(9):2115–2127, 2002.

[79] Mehl J. B. and Moldover M. R. Precondensation phenomena in acoustic measurements. *The Journal of Chemical Physics*, 77(1):455–465, 1982.

[80] Ramalingam R., Boguhn D., Fillinger H., Schlachter S.I., and Süßer M. Study of robust thin film Pt-1000 temperature sensors for cryogenic process control applications. In *AIP Conference Proceedings*, volume 1573, pages 126–131. American Institute of Physics, 2014.

[81] Shaul K. R. S., Schultz A. J., and Kofke D. A. Path-integral Mayer-sampling calculations of the quantum Boltzmann contribution to virial coefficients of Helium-4. *J. Chem. Phys.*, 137(18):184101, November 2012.

[82] Moldover M. R., Gavioso R. M., Mehl J. B., Pitre L., de Podesta M., and Zhang J. T. Acoustic gas thermometry. *Metrologia*, 51(1):R1–R19, 2014.

[83] Wiebke J., Pahl E., and Schwerdtfeger P. Sensitivity of the thermal and acoustic virial coefficients of argon to the argon interaction potential. *The Journal of Chemical Physics*, 137(6):064702, 2012.

[84] Wu M.K., Ashburn J. R., Torng C.J., Hor P. H., Meng R. L., Gao L., Huang Z. J., Wang Y.Q., and Chu C.W. Superconductivity at 93 K in a new mixed-phase Y-Ba-Cu-O compound system at ambient pressure. *Physical Review Letters*, 58(9):908, 1987.

[85] Yang I., Underwood R., and de Podesta M. Investigating the adequacy of a low-cost vector network analyser for microwave measurements in quasispherical resonators. *Measurement Science and Technology*, 29(7):075013, 2018.

[86] Fischer J., de Podesta M., Hill K.D., Moldover M., Pitre L., Rusby R., Steur P., Tamura O., White R., and Wolber L. Present estimates of the differences between thermodynamic temperatures and the ITS-90. *International Journal of Thermophysics*, 32(1):12–25, 2011.

[87] Lemmon E. W., Huber M. L., and McLinden M. O. NIST Standard Reference Database 23: Reference Fluid Thermodynamic and Transport Properties - REFPROP, version 7.0, 2002.

[88] Barter C., Meisenheimer R.G., and Stevenson D.P. Diamagnetic susceptibilities of simple hydrocarbons and volatile hydrides. *The Journal of Physical Chemistry*, 64(9):1312–1316, 1960.

[89] Garberoglio G. and Harvey A. H. Path-integral calculation of the second dielectric and refractivity virial coefficients of helium, neon, and argon. *J. Res. Natl. Inst. Stand. Technol.*, 125:125022, 2020.

[90] Pan C. Z., Gao B., Song Y.N., Zhang H.Y., Han D.X, Hu J.F., Liu W.J., Chen H., Plimmer M., Sparasci F., Luo E.C., and Pitre L. Active suppression of temperature oscillation from a pulse-tube cryocooler in a cryogen-free cryostat: Part 1. Simulation modeling from thermal response characteristics. *Cryogenics*, 109:103097, 2020.

[91] Pitre L., Moldover M. R., and Tew W. L. Acoustic thermometry: new results from 273 K to 77 K and progress towards 4 K. *Metrologia*, 43(1):142–62, 2006.

[92] BIPM, IEC, IFCC, ILAC, ISO, IUPAC, IUPAP, and OIML. Evaluation of measurement data — Guide to the expression of uncertainty in measurement (GUM). `https://www.bipm.org`, 2008.

[93] Rourke P. M. C., Gaiser C., Gao B., Ripa D. M., Moldover M. R., Pitre L., and Underwood R. J. Refractive-index gas thermometry. *Metrologia*, 56(3):032001, 2019.

[94] Julien L., Nez F., Thomas M., Espel P., Ziane D., Pinot P., Piquemal F., Cladé P., Guellati-Khélifa S., Djordjevic S., Poirier W., Schopfer F., Thévenot O., Pitre L., and Sadli M. Le nouveau système international d'unités - le kilogramme, l'ampère, la mole et le kelvin redéfinis. *Reflets de la Physique*, (62):11–11, 2019. `https://doi.org/10.1051/refdp/201962011`.

[95] Jousten K., Hendricks J., Barker D., Douglas K., Eckel S., Egan P., Fedchak J., Flügge J., Gaiser C., Olson D., Ricker J., Rubin T., Sabuga W., Scherschligt J., Schöde R., Sterr U., Stone J., and Strouse G. Perspectives for a new realization of the pascal by optical methods. *Metrologia*, 54(6):s146, 2017.

[96] Harrington R. F. *Time-harmonic electromagnetic fields*. John Wiley and Sons, 2001.

Appendices

Appendix A

Physical properties of helium and argon gases

This appendix gives an overview of the orders of magnitude the physical quantities relevant to this project.

1 Helium gas

1.1 Magnitude order and uncertainty table (helium)

The table A.1 gathers together the orders of magnitude and estimated uncertainties of the main physical properties of helium gas involved in determining the pressure. The Cernox type thermometer used to measure the temperature of the sphere is assumed to have been calibrated with an Acoustic Gas Thermometer (AGT). The uncertainty in the temperature regulation was measured during the experiments. Values of the thermophysical virial coefficients B_2, C_2 and D_2 vary with temperature.

Table A.1: Orders of magnitude and estimated uncertainties of the main physical quantities involved in determining the pressure. Uncertainty values are expressed at the 68% level of confidence.

Variable	Symbol	Unit	Value	Law	Comments
Temperature regulation	T_{reg}	K	5.4	Gaussian	Experimental
	s_{Treg}	K	7×10^{-7}		
Cernox calibration	U_{Tcal}	K	0.15×10^{-3}	Gaussian	See [91]
Isothermal compressibility	κ_T	Pa^{-1}	7.0423×10^{-12}	Gaussian	See [62] and [40]
	s_{Treg}	Pa^{-1}	7.04×10^{-14}		
Molar magnetic polarizability	A_μ	$\mathrm{m}^3\ \mathrm{mol}^{-1}$	-8.03×10^{-12}	Gaussian	See [62]
	$s_{A\mu}$	$\mathrm{m}^3\ \mathrm{mol}^{-1}$	1.7×10^{-13}		
Molar electric polarizability	A_ϵ	$\mathrm{m}^3\ \mathrm{mol}^{-1}$	$5.172\,541\,9 \times 10^{-7}$	Gaussian	See [62]
	$s_{A\epsilon}$	$\mathrm{m}^3\ \mathrm{mol}^{-1}$	1×10^{-13}		
Second dielectric virial coefficient	B_ϵ	$\mathrm{m}^3\ \mathrm{mol}^{-1}$	-9.8×10^{-8}	Gaussian	See [62]
	$s_{B\epsilon}$	$\mathrm{m}^3\ \mathrm{mol}^{-1}$	4×10^{-9}		
Second molar density virial coefficient	B_2	$\mathrm{m}^3\ \mathrm{mol}^{-1}$	$\simeq -56.784 \times 10^{-6}$	Gaussian	See [81]
	s_{B2}	$\mathrm{m}^3\ \mathrm{mol}^{-1}$	5×10^{-9}		
Third molar density virial coefficient	C_2	$\mathrm{m}^6\ \mathrm{mol}^{-2}$	$\simeq 920.7 \times 10^{-12}$	Gaussian	See [81]
	s_{C2}	$\mathrm{m}^6\ \mathrm{mol}^{-2}$	0.9×10^{-12}		
Fourth molar density virial coefficient	D_2	$\mathrm{m}^9\ \mathrm{mol}^{-3}$	$\simeq 16\,100 \times 10^{-18}$	Gaussian	See [81]
	s_{D2}	$\mathrm{m}^9\ \mathrm{mol}^{-3}$	300×10^{-18}		
Electromagnetic wave frequency (pressure)	f	Hz	$\simeq 5.26 \times 10^9$	Uniform	Resolution 1 Hz
	s_f	Hz	0.289		
Electromagnetic wave frequency (vacuum)	f_{vacuum}	Hz	$\simeq 5.26 \times 10^9$	Uniform	Resolution 1 Hz
	$s_{fvacuum}$	Hz	0.289		

1.2 Refractive index (helium)

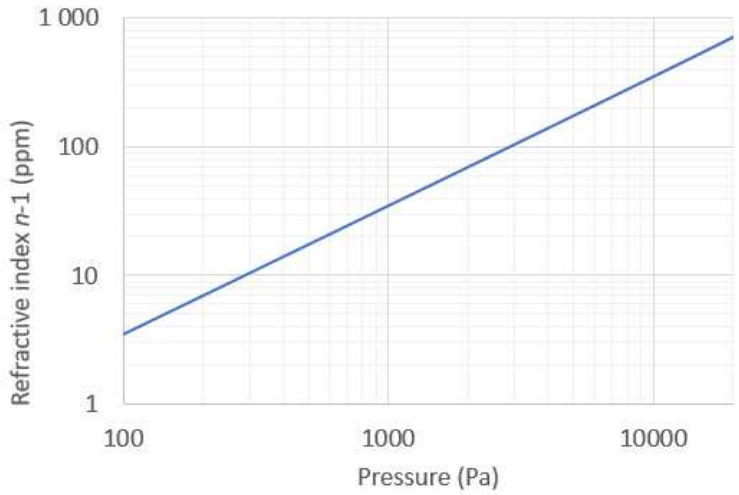

Figure A.1: Difference between refractive index n and unity as a function of pressure at 5.4 K.

1.3 Molar density (helium)

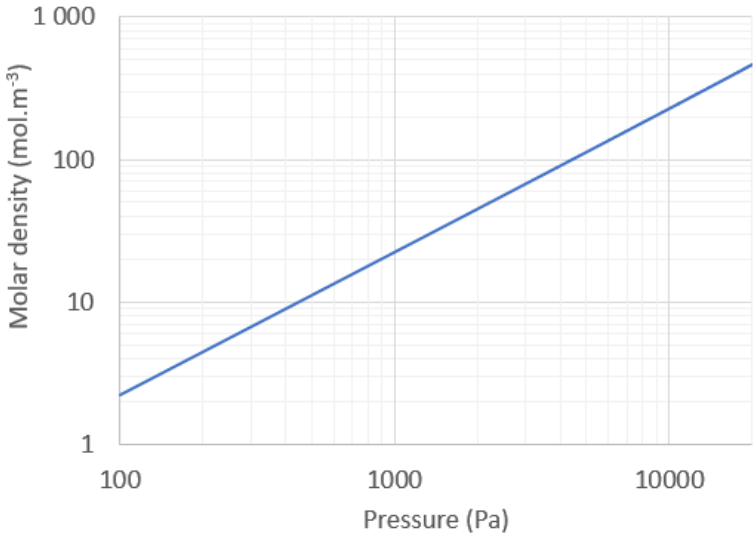

Figure A.2: Molar density of ^{4}He *versus* pressure at 5.4 K.

1.4 Electric susceptibility (helium)

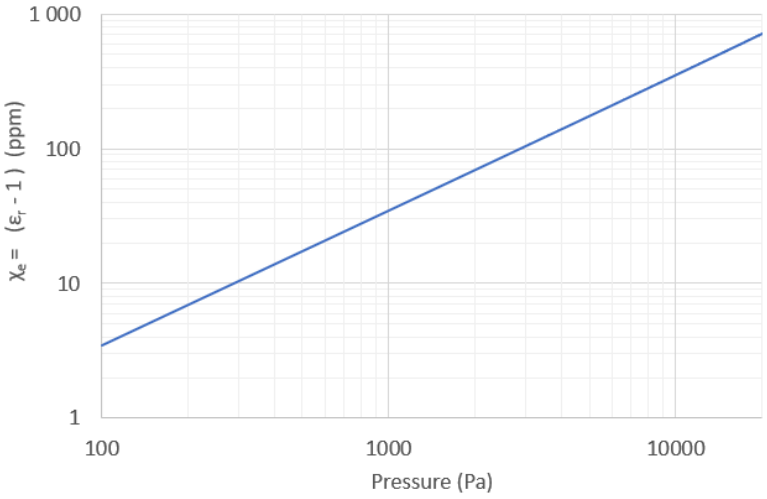

Figure A.3: Electric susceptibility ($\chi_e = \epsilon_r - 1$) of ^{4}He *versus* pressure at 5.4 K.

1.5 Magnetic susceptibility (helium)

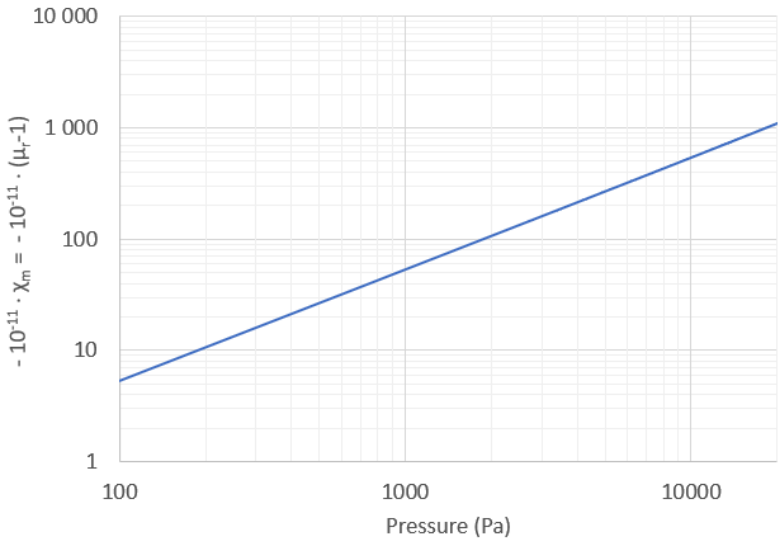

Figure A.4: *Opposite* of magnetic susceptibility ($-\chi_m = -(\mu_r - 1)$) of ^{4}He *versus* pressure at 5.4 K.

1.6 Relative shift of resonant frequency *versus* pressure (helium)

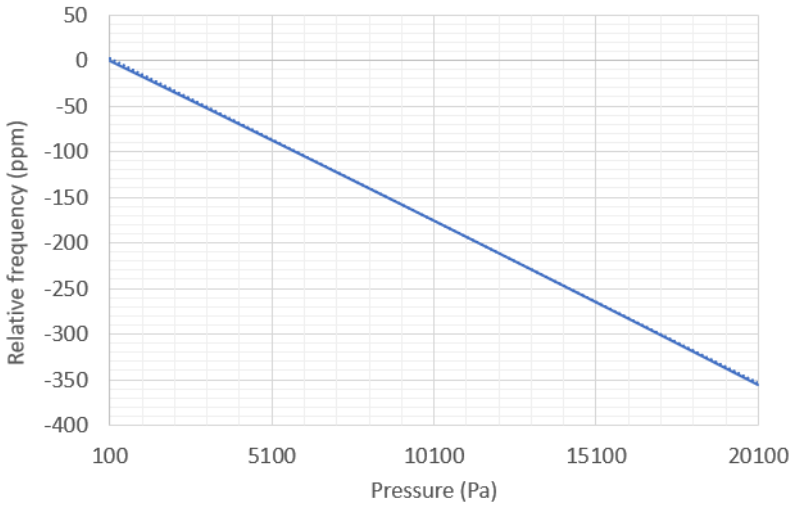

Figure A.5: Relative shift of resonant frequency *versus* pressure at 5.4 K. The slope is about -18×10^{-9} Pa^{-1}.

1.7 Relative shift of resonant frequency *versus* temperature (helium)

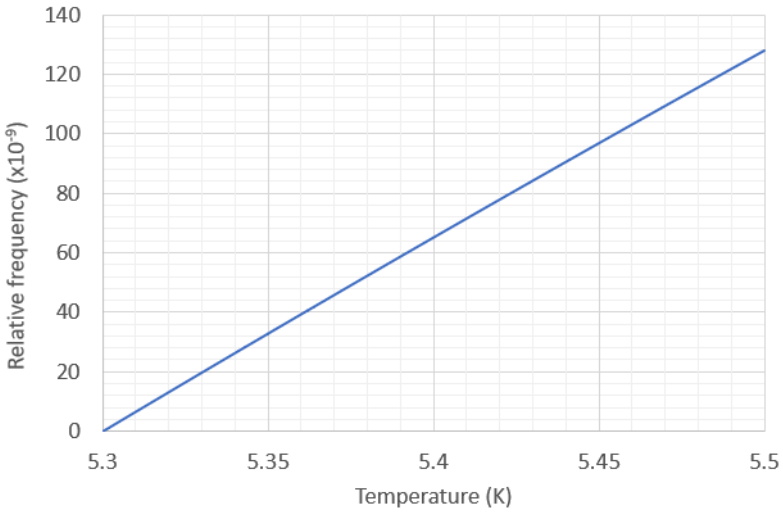

Figure A.6: Relative shift of resonant frequency of the mode TM_{11} *versus* temperature. The slope is about 641×10^{-9} K^{-1}.

2 Argon gas

2.1 Orders of magnitude and uncertainty table (argon)

Table A.2: Order of magnitude and estimated uncertainties of the main physical properties of argon gas involved in determining the pressure. Uncertainty values are expressed at the 68% level of confidence.

Variable	Symbol	Unit	Value	Law	Comments
Temperature regulation	T_{reg}	K	90.4	Gaussian	Experimental
	s_{Treg}	K	8×10^{-4}		
PRT[1]calibration	U_{Tcal}	K		Gaussian	Internal calibration
Isothermal compressibility	κ_T	Pa^{-1}	7×10^{-12}	Gaussian	See [63]
	s_{Treg}	Pa^{-1}	0.7×10^{-12}		
Molar magnetic polarizability	A_μ	$\mathrm{m}^3\ \mathrm{mol}^{-1}$	-8.09×10^{-11}	Gaussian	See [82]
	$s_{A\mu}$	$\mathrm{m}^3\ \mathrm{mol}^{-1}$	6×10^{-13}		
Molar electric polarizability	A_ϵ	$\mathrm{m}^3\ \mathrm{mol}^{-1}$	$4.142\,03 \times 10^{-6}$	Gaussian	See [82]
	$s_{A\epsilon}$	$\mathrm{m}^3\ \mathrm{mol}^{-1}$	15×10^{-11}		
Second dielectric virial coefficient	B_ϵ	$\mathrm{m}^3\ \mathrm{mol}^{-1}$	0.52×10^{-6}	Gaussian	See [82]
	$s_{B\epsilon}$	$\mathrm{m}^3\ \mathrm{mol}^{-1}$	–		
Second molar density virial coefficient	B_2	$\mathrm{m}^3\ \mathrm{mol}^{-1}$	$\simeq -221.282 \times 10^{-6}$	Gaussian	See [82]
	s_{B2}	$\mathrm{m}^3\ \mathrm{mol}^{-1}$	0.655×10^{-6}		
Third molar density virial coefficient	$C2$	$\mathrm{m}^6\ \mathrm{mol}^{-2}$	$\simeq -7109.79 \times 10^{-6}$	Gaussian	See [83]
	s_{C2}	$\mathrm{m}^6\ \mathrm{mol}^{-2}$	–		
Fourth molar density virial coefficient	D_2	$\mathrm{m}^9\ \mathrm{mol}^{-3}$	$\simeq -3\,650\,781.02 \times 10^{-18}$	Gaussian	See [83]
	s_{D2}	$\mathrm{m}^9\ \mathrm{mol}^{-3}$	–		
Electromagnetic wave frequency (pressure)	f	Hz	$\simeq 5.26 \times 10^9$	Uniform	Resolution 1 Hz
	s_f	Hz	5		
Electromagnetic wave frequency (vacuum)	f_{vacuum}	Hz	$\simeq 5.26 \times 10^9$	Uniform	Resolution 1 Hz
	$s_{fvacuum}$	Hz	5		

[1] Platinum resistance thermometer (ref. $B397$)

2.2 Refractive index (argon)

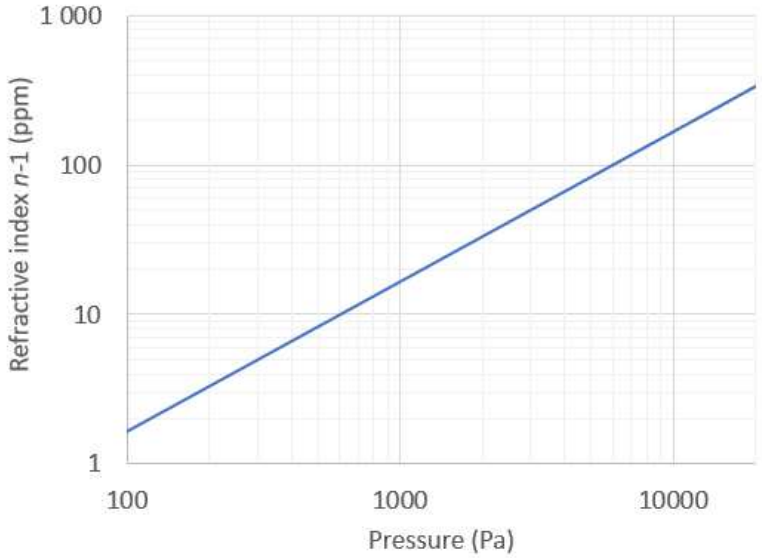

Figure A.7: Difference between refractive index n and unity as a function of pressure at 90.4 K.

2.3 Molar density (argon)

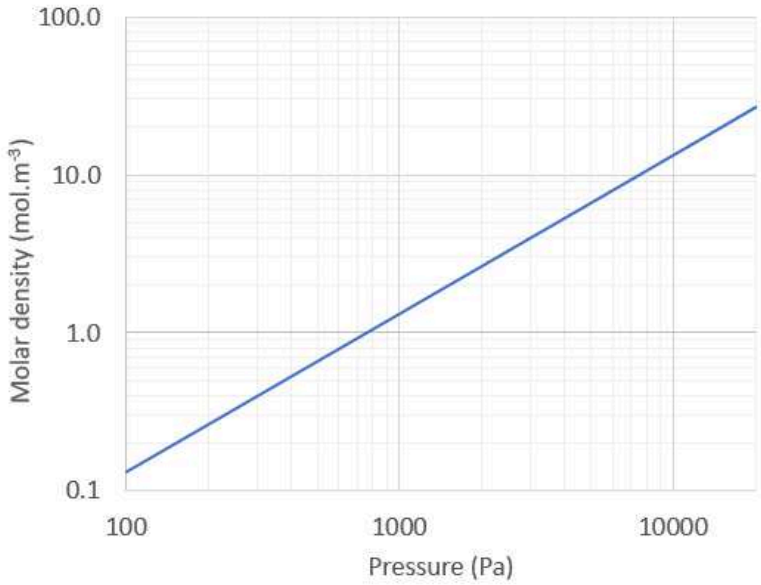

Figure A.8: Molar density of argon *versus* pressure at 90.4 K.

2.4 Electric susceptibility (argon)

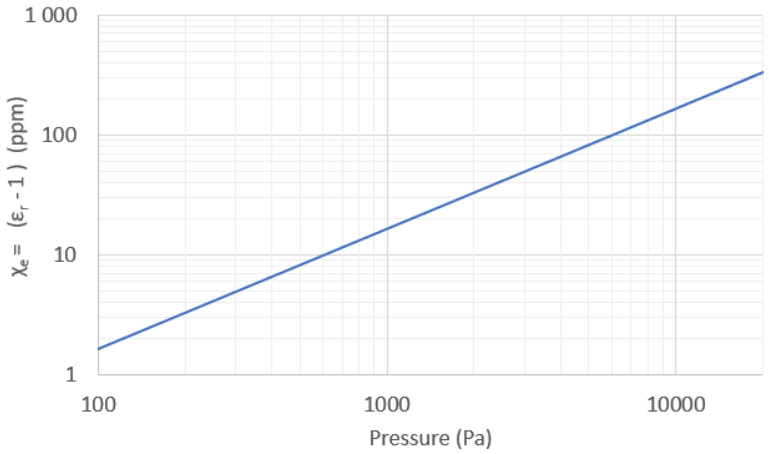

Figure A.9: Electric susceptibility ($\chi_e = \epsilon_r - 1$) of argon *versus* pressure at 90.4 K.

2.5 Magnetic susceptibility (argon)

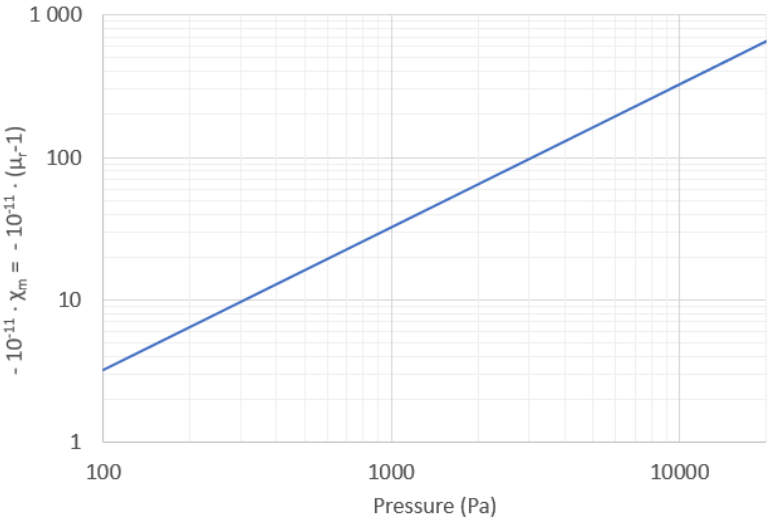

Figure A.10: *Negative* of magnetic susceptibility ($-\chi_m = -(\mu_r - 1)$) of argon *versus* pressure at 90.4 K.

2.6 Relative resonant frequency shift *versus* pressure (argon)

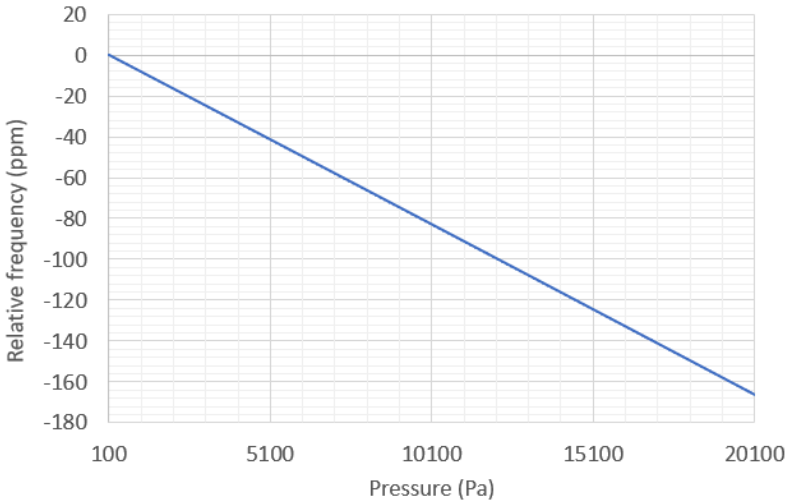

Figure A.11: Relative resonant frequency shift *versus* pressure at 90.4 K. The slope is about -8×10^{-9} Pa^{-1}.

2.7 Relative resonant frequency shift *versus* temperature (argon)

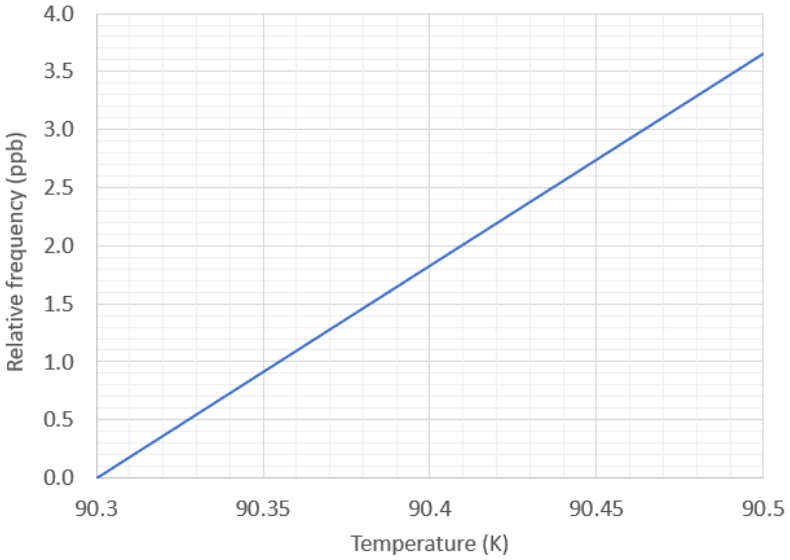

Figure A.12: Relative resonant frequency shift *versus* temperature. The slope is about 18×10^{-9} K^{-1}.

Appendix B

Cryostat versions

This appendix gives an overview, as a sectional plan, of the experimental Dewar and of the three versions of the cryostat used during the experiments.

1 Experimental Dewar

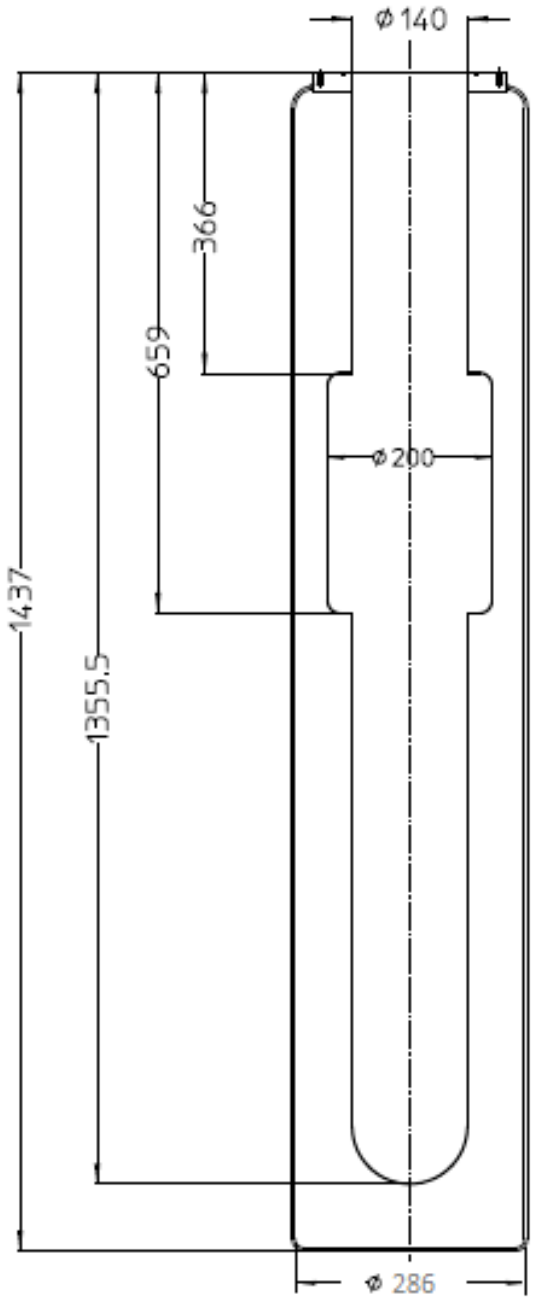

Figure B.1: Experimental Dewar for all cryostat versions for helium gas with dimensions in millimetres.

2 The cryostat Mark I (2018)

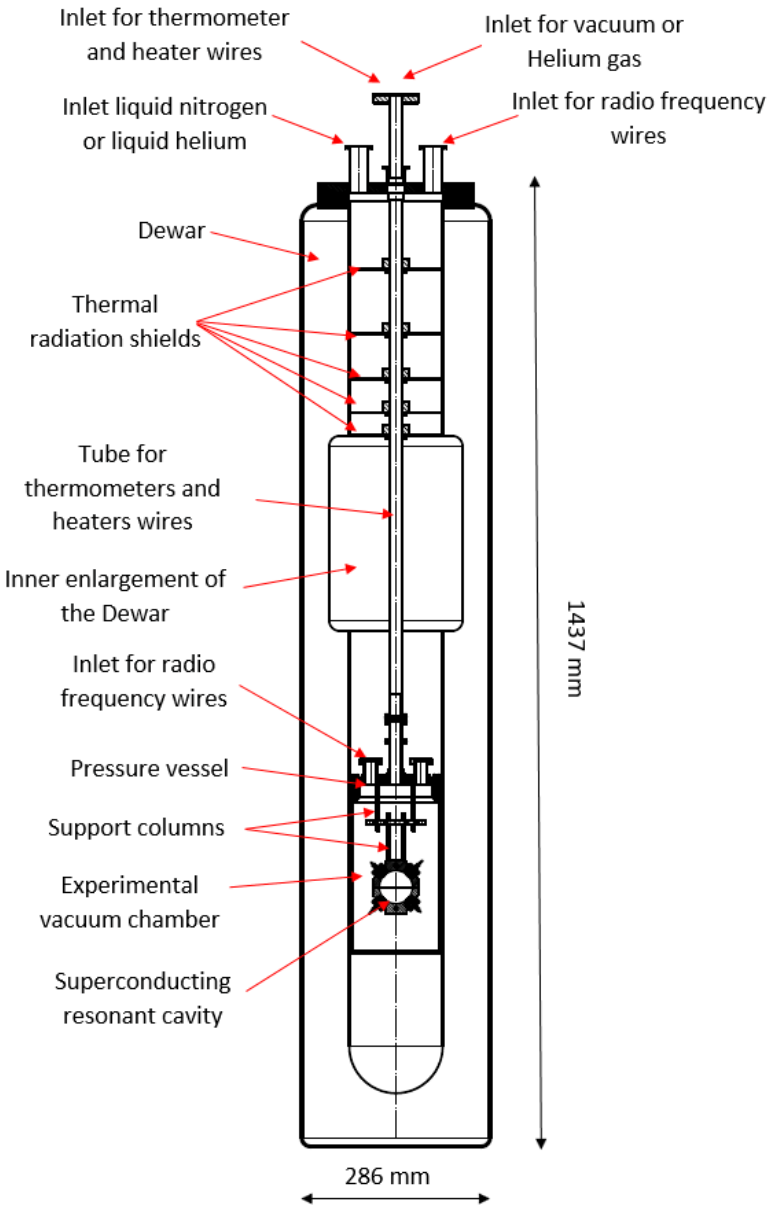

Figure B.2: Cryostat Mark I (2018) for superconducting resonant cavity.

3 The cryostat Mark II (2019)

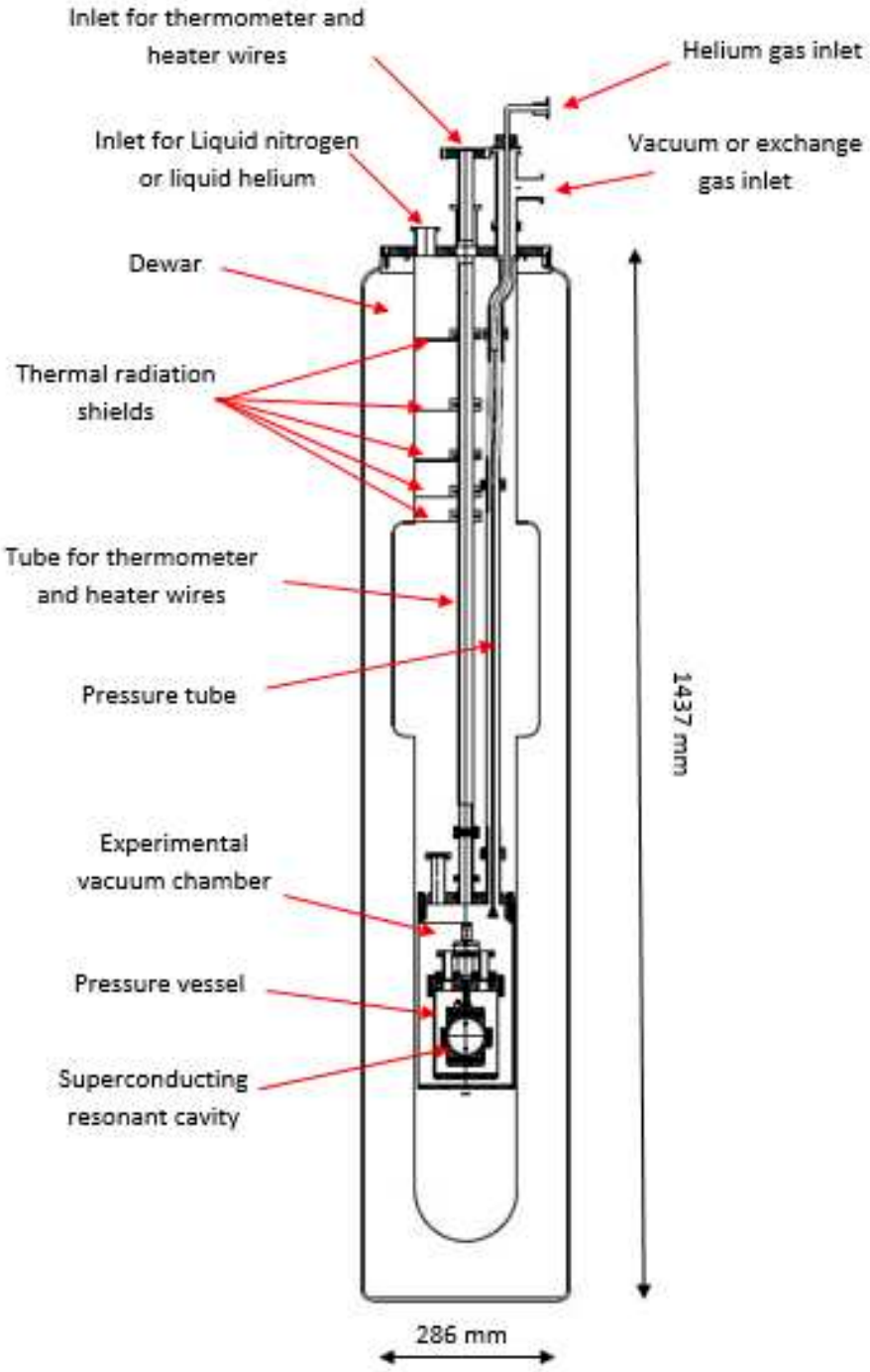

Figure B.3: Cryostat Mark II (2019) for superconducting resonant cavity.

4 The cryostat Mark III (2020)

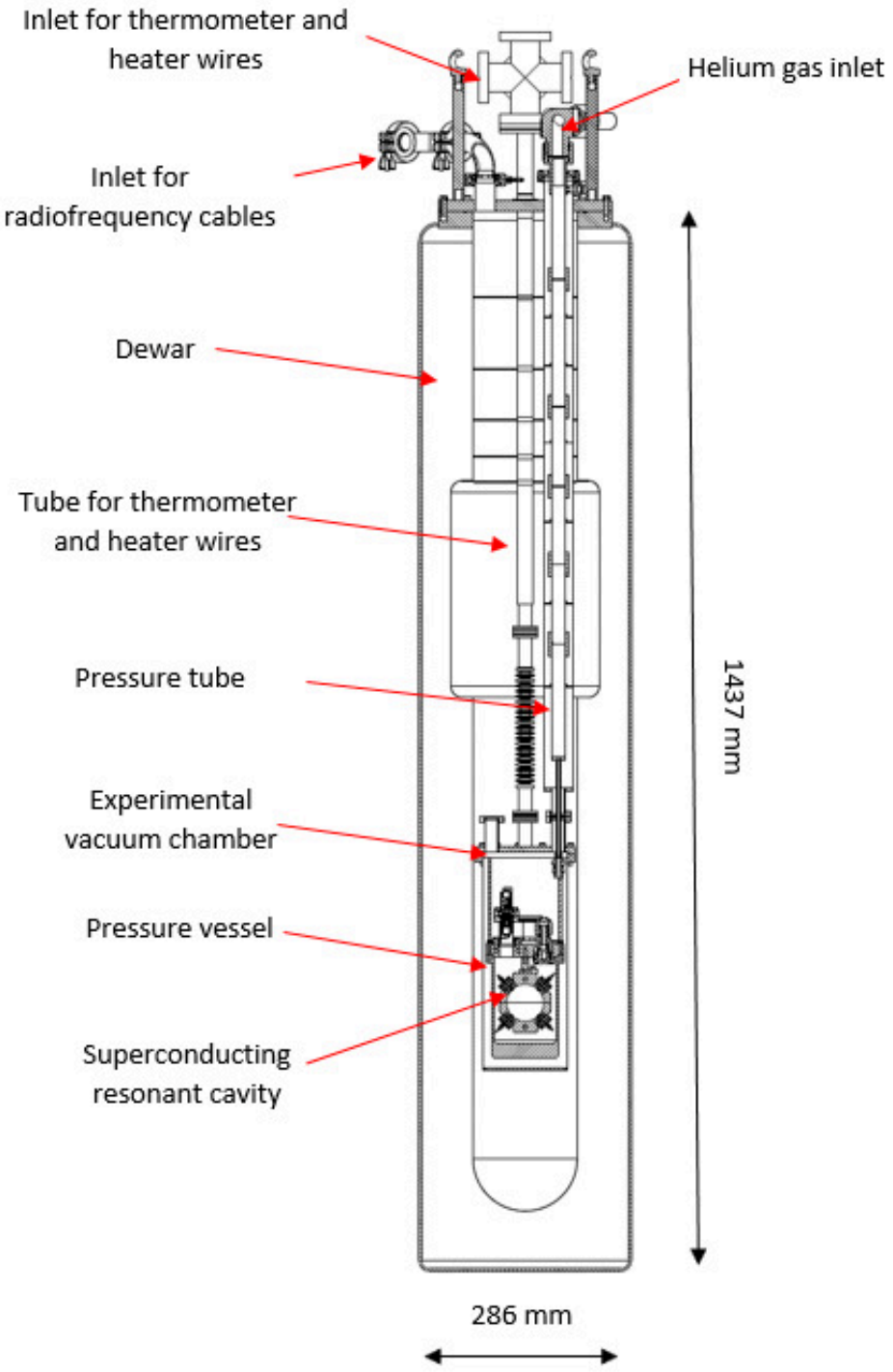

Figure B.4: Cryostat Mark III (2020) for superconducting resonant cavity - Simplified drawing.

Appendix C

Instrumentation

This appendix gives information about the main instruments and assorted apparatus used during the experiments.

1 B-box elements

The 'B-box' contains by the following elements:

Temperature controller: Arroyo Instruments 5305

Thermoelectric assembly (Peltier module): Laird $AA-034-12-22-00-00$

Fans: sleeve bearing 12 VDC, 0.17 A

Thermistor: 10 kΩ, Negative temperature coefficient (NTC), 2 %

Panels: extruded polystyrene (3 cm thick)

The parameters used for the Arroyo Instruments 5305 controller during the tests are the following:

$$
\begin{aligned}
&Mode = Tmode\\
&Mount = UserDefined\\
&ILim = 3.00A\\
&Gain = PID\\
&PIDP = 30.0000\\
&PIDI = 0.0030\\
&PIDD = 0.0000\\
&Sensor = 100uATherm\\
&T-LowLim = 10.0C\\
&T-HighLim = 40.0C\\
&R-LowLim = 5.00kOhm\\
&R-LowLim = 20.00kOhm\\
&Toltime = 5.0sec\\
&Toltemp = 0.10C\\
&H/Cmode = Heat/Cool\\
&ExtFan = Fast\\
&ExtFanMode = On\\
&CableR = 0.0000Ohm
\end{aligned}
$$

2 Pressure sensors

2.1 DIGIQUARTZ® model 745

The resonant quartz pressure sensor DIGIQUARTZ® model 745 is a product of the American company, Paros Scientific. Two of these devices are used in the experimentation: one in the pressure regulation loop, the other to measure the pressure at the inlet valve of the cryostat. Both are used in nano-resolution mode.

In standard mode, the DIGIQUARTZ® Model 745 has, a typical resolution of 0.0001% (1 ppm) of full scale and an uncertainty of 0.008% (80 ppm) of full scale. This uncertainty is relative to a primary standard and includes resolution, hysteresis and repeatability.

The nano-resolution mode is initialized by the XM command. The method chosen is that of the infinite impulse response filter. To select the latter, the command XM = 1 is transmitted from the computer to the pressure sensor. The same goes for selecting the resolution of 1.6 ppb (command IA = 11) or 1.1 mPa and the integration time of one second (command PI = 1000).

3 Vector network analyser

The vector network analyser is an Agilent E5071C 300 KHz-200GHz ENA Series (SN:MY46105805)

4 The frequency standard

4.1 Rubidium oscillator

Rubidium frequency standard is a Stanford Research Systems model FS725 (SN:121623).

4.2 GPS disciplined oscillator

GPS disciplined oscillator time and frequency system is an acalbfi model FS740 with a rubidium timebase model FS740/OPT2

5 Ohmmeter

- Keithley 2002 multimeter (SN:4019194).

- Keithley 2007 multimeter (SN:0916442).

6 Current supply

- DC current source: Yokogawa GS210-7-F (SN:91N612708)
- DC current source: Yokogawa GS210-7-F (SN:91UC27928)
- DC current source: Yokogawa GS210-7-F (SN:91T61402)
- DC current source: Yokogawa GS210-7-F (SN:91T61708)

7 Radio frequency isolator

Two isolators from Low Noise Factory AB company model $LNF - ISC4_12A4 - 12$ GHz.

8 Automatic thermometry bridge

Measurements international limited (mmi) Model 6010T (SN:1041005)

9 1Ω standard resistor 1Ω

Tinsley London Type 5685A (SN:7003/01)

10 Pumping station

Combined pumping station including turbopump and backing pump: Pfeiffer-vacuum HiCube 80 Pro, DN 63 CF-F, ACP 15. Vacuum gauge Pfeiffer Pirani/Cold Cathode PKR-361 FullRange® gauge.

Appendix D

Software

This appendix gives an overview of the software used to calculate and correct physical quantities. These programs are written in Python. They are neither optimized for size nor for speed of convergence.

1 Calculation of pressure from resonant frequency

1.1 Main program

```
"""
Created on Sat Jun 29 12:04:02 2019
@author: gambette
"""
import numpy as np
from B_spline import B_spline
from Frequencytopressure import Frequencytopressure
import matplotlib.pyplot as plt
import os

# get current directory
#import os and get current directory
from os import getcwd
rep_cour = getcwd()

# change directory to current directory
from os import chdir
chdir(rep_cour)

def read_DATA_IN(file):


    data={}
    data["Press_Pa"],data["Freq_Hz"],data["Temp_K"] = np.loadtxt(file,comments=
    '#', unpack=True)
    return data

#cycle 1
DATA_IN_file = "DATA_IN_cycle1_1000Pa.txt"

dT= -0.0348 # thermometer self-heating

fg_vacuum = 5262668489.84253 # (Hz)vacuum frequency

T_vacuum = 5.40017427608463 # (K) sphere temperature during frequency vacuum
measurement

Slope_f_T = -2024.52691648249 # (Hz/K) slope of the temperature correction
```

```
data_p = read_DATA_IN(DATA_IN_file) # read data

press = np.zeros(len(data_p["Freq_Hz"]))


for nv in range(0,len(data_p["Freq_Hz"])−1):
    B2 = B_spline (data_p["Temp_K"][nv]+dT,"B_Shaul.csv")   cm^3 mol^-1
    C2 = B_spline (data_p["Temp_K"][nv]+dT,"C_Shaul.csv")   cm^6 mol^-1
    D2 = B_spline (data_p["Temp_K"][nv]+dT,"D_Shaul.csv")   # (cm^9 mol^-1)
    B2 = B2 * 10 * *(−6)                                    (m^3 mol^-1)
    C2 = C2 * 10 * *(−12)                                   (m^6 mol^-1)
    D2 = D2 * 10 * *(−18)                                   # (m^9 mol^-1)

    press[nv] = Frequencytopressure(data_p["Freq_Hz"][nv]-Slope_f_T*
    data_p["Temp_K"][nv]+ Slope_f_T*T_vacuum,
    data_p["Temp_K"][nv]+dT, fg_vacuum, B2, C2, D2)

print('Calculated pressure (Pa) :')


for nv in range(0,len(data_p["Freq_Hz"])-1):
    print(press[nv])
```

1.2 Frequency-to-pressure subroutine

```
"""
Created on Fri Dec 14 18:10:58 2018
@author: gambette
"""


#import os and get current directory
from os import getcwd
rep_cour = getcwd()

# change directory to current directory
from os import chdir
chdir(rep_cour)
```

```
import numpy as np
# decimal configuration
from decimal import *
getcontext().prec = 25

def Frequencytopressure(fg, T, fg_vacuum, B, C, D):
press_h = np.float64(10 * 1e5)
press_l = np.float64(1e - 7)
press = (press_h + press_l)/2
long = 100000 mat = np.zeros((long,3),dtype='float64')
afpress = np.zeros(long)
afh2 = np.zeros(long)
afepsmu = np.zeros(long)
afeps = np.zeros(long)
afmu = np.zeros(long)
afrho = np.zeros(long)
j = 0

while True:
    # compressibility
    k = 7.04233595 * 10 * *(-12)
    # Gas density calculation from the virial expression of the pressure
    p = R.T.rho.[1 + B.rho + C.rho^2 + D.rho^3]
    # R is the molar gas constant (Jmol - 1K^-1)
    R= 8.3144621
    # pressure calculation
    rho_l = np.float64(1e - 7)
    rho_h = np.float64(100000)
    index_rho= 0
    i = np.float64(10)
    i_test = 10.0
    while abs(i_test) > 10 * *(-11):
        rho_r = (rho_h + rho_l)/2
        pp = R * T * rho_r * (1.0 + B * rho_r + C * rho_r * *2 + D * rho_r * *3)
        p = R * T * rho_l * (1.0 + B * rho_l + C * rho_l * *2 + D * rho_l * *3)
        i = (p - press) * (pp - press)
        i_test = (rho_h - rho_l)/rho_r
        if i <= 0 :
            rho_l = rho_l
            rho_h = rho_r
        else:
            rho_l = rho_r
            rho_h = rho_h
        rho = rho_h
        index_rho = index_rho + 1
```

```
#
    # magnetic permeability calculation
    # mur-1/mur+2 = Am.rho
    Am = −0.00000803 ∗ 10 ∗ ∗(−6)
    mu_ref = Am ∗ rho
    mu_l = np.float64(0)
    mu_h = np.float64(4)
    mu = mu_h
    index_mu = 0
    i = np.float64(10)
    i_test = 10.0
    while abs(i_test) > 10 ∗ ∗(−12):
        mu_r = (mu_h + mu_l)/2
        i = (((mu_l − 1)/(mu_l + 2)) − mu_ref)
            ∗(((mu_r − 1)/(mu_r + 2)) − mu_ref)
        i_test = (mu_h − mu_l)/mu_r
        if i <= 0:
            mu_l = mu_l
            mu_h = mu_r
        else:
            mu_l = mu_r
            mu_h = mu_h
        mu = mu_h
        index_mu = index_mu + 1
    # electric permittivity calculation
    #er − 1/μer + 2 = Ae.rho.(1 + Be.rho + Ce.rho^2)
    Ae = np.float64(0.51725419 ∗ 10 ∗ ∗(−6))
    Be = np.float64(−9.8 ∗ 10 ∗ ∗(−8))
    eps_ref = Ae ∗ rho ∗ (1.0 + Be ∗ rho)
    eps_l = np.float64(0)
    eps_h = np.float64(4)
    eps = eps_h
    index_eps = 0
    i = np.float64(10)
    i_test = 10.0
    whileabs(i_test) > 10 ∗ ∗(−12):
        eps_r = (eps_h + eps_l)/2
        i = (((eps_l − 1)/(eps_l + 2)) − eps_ref)
            ∗(((eps_r − 1)/(eps_r + 2)) − eps_ref)
        i_test = (eps_h − eps_l)/eps_r
        ifi <= 0 :
            eps_l = eps_l
            eps_h = eps_r
```

```
#
        else:
            eps_l = eps_r
            eps_h = eps_h
        eps = eps_h
        index_eps = index_eps + 1
    h = fg_vacuum * (1 + k * press/3.0)/fg
    h2 = h**2
    epsmu = eps * mu
    h = epsmu - h2
    mat[j,0] = press
    mat[j,1] = h2
    mat[j,2] = epsmu
    afpress[j] = press
    afh2[j] = h2
    afepsmu[j] = epsmu
    afeps[j] = eps
    afmu[j] = np.float64(mu)
    afrho[j] = rho
    if abs(epsmu - h2) > 10**(-12):
        j = j + 1
        if(epsmu - h2) < 0:
            press_l = press
            press = (press_h + press_l)/2
        else:
            press_h = press
            press = (press_h + press_l)/2
    else:
        press_final = press
        break
    nless1 = epsmu - 1
return (press_final)
```

2 Hydrostatic correction

```
# """
Created on Sun Oct 18 16:19:57 2020
@author: gambette
"""

#import numpy as np
from B_spline import B_spline
from Frequencytopressure_Ar_v1 import Frequencytopressure_Ar_v1
import matplotlib.pyplot as plt
import os

#import os and get current directory
from os import getcwd
rep_cour = getcwd()
print (rep_cour)
# change directory to current directory
from os import chdir
chdir(rep_cour)


def moyenne(tableau):
    return sum(tableau, 0.0) / len(tableau)
def moyenne_2(tableau):
    return sum(tableau, 0.0) / (len(tableau)-1)
def variance(tableau):
    m=moyenne(tableau)
    returnmoyenne_2([(x - m) * *2forxintableau])
def ecartype(tableau):
    returnvariance(tableau) * *0.5


#########
# Gas density determination
def density(press,T):
    R = 8.3144621
# molar mass M = 4.002602 g/mol for He and M = 39.948 g/mol for Ar
    M = 4.002602
# (with R in J mol^-1 K^-1)
    B2 = B_spline (T,"B_Shaul.csv")
# (with B2 cm^3 mol^-1 )
    C2 = B_spline (T,"C_Shaul.csv")
# (with C2 cm^6 mol^-1 )
```

```
#
    D2 = B_spline (T,"D_Shaul.csv")
# (with D2 cm^9 mol^-1 )
#
    B =#B2 * 10**(-6)
# (with B2 m^3 mol^-1 )
    C = C2 * 10**(-12)
# (with C2 m^6 mol^-1 )
    D =#D2 * 10**(-18)
# (with D2 m^9 mol^-1 )
    rho_l = np.float64(0.01)
    rho_h = np.float64(100)
    i = np.float64(10)
    i_test = 10.0
    while abs(i_test) > 10**(-11):
        rho_r = (rho_h + rho_l)/2
        pp = R* T * rho_r*(1.0 + B * rho_r + C * rho_r**2 + D * rho_r**3)
        p = R* T * rho_l*(1.0 + B * rho_l + C * rho_l**2 + D * rho_l**3)
        i = (p - press)*(pp - press)
        i_test = (rho_h - rho_l)/rho_r
        if i<=0:
            rho_l = rho_l
            rho_h = rho_r
        else:
            rho_l = rho_r
            rho_h = rho_h
    rho = rho_h
    return M * rho \ 1000


#######
# pressure variation up
def dPress_up (T_height_min, T_height_max, Press, h, n):
    g = 9.80938101
    dh = h /n
    dT=(T_height_max - T_height_min)/n
    P=Press
    for i in range(1, n+1):
        T = T_height_min + (i-1) * dT;
        rho_up = density(P,T)
        P=P-rho_up * g * dh
    return P
```

```
#
# Tcavity <L0> T1 <L1> T2 <L2> T3 <L3> T4 <L4> T5 <L5> Troom <Lout>
Troom

# distance
Lout = 0.2066
L5 = 0.31638;
L4=0.0505;
L3=0.1002;
L2=0.2831;
L1=0.261;
L0=0.24979;

# Temperature
Troom = 300;
T5 = 226.084;
T4 = 214.286;
T3 = 190.876;
T2 = 124.736;
T1 = 63.758;
Tcavity = 5.4;

# pressure
Pcavity=1000;

# Computation
P1=dPress_up( Tcavity,T1,Pcavity,L0,100)
P2=dPress_up( T1,T2,P1,L1,100)
P3=dPress_up( T2,T3,P2,L2,100)
P4=dPress_up( T3,T4,P3,L3,100)
P5=dPress_up( T4,T5,P4,L4,100)
Proom_L=dPress_up( T5,Troom,P5,L5,50)
Proom_H=dPress_up( Troom,Troom,Proom_L,L5,50)

# Display results
print(Proom_H)
print(Proom_L)
print(P5)
print(P4)
print(P3)
print(P2)
print(P1)
```

3 Spline function

```
# -*- coding: utf-8 -*-
"""
Spline interpolation from the Scipy library
"""

import matplotlib.pyplot as plt
from scipy import interpolate
import numpy as np
import csv

#import os and get current directory
from os import getcwd
rep_cour = getcwd()

# change directory to current directory
from os import chdir
chdir(rep_cour)


def B_spline(Temperature,file_coef):
    Temperature_node=[]
    B_node=[]
    datafile = open(file_coef, "r")
    test=csv.reader(datafile)
    for row in test:
        Temperature_node.append(float(row[0]))
        B_node.append(float(row[1]))
    datafile.close()
# Interpolant
    tck = interpolate.splrep(Temperature_node,B_node,s=0)
    y = interpolate.splev(Temperature,tck,der=0)
    return y
```

3.1 Data organization files

3.2 Virial coefficients

In the box below is shown an extract of the file "B_Shaul.csv" as an example. The first column represents the thermodynamic temperature in kelvin. The second column represents the coefficient B in $cm^3\ mol^{-1}$ (values taken from reference [81]).

2.6	−141.50
2.8	−129.89
3	−119.827
3.25	−109.075
3.5	−99.883
3.75	−91.938
4	−85.022

3.3 Frequency to convert in pressure

The box below is an extract from the "DATA_IN_cycle1 _1000Pa" measurement file. The first column represents the pressure measured by a reference sensor. The second column represents the resonant frequency. The third column corresponds to the temperature of the microwave resonator.

#Press_Pa	#Freq_Hz	#Temp_K
996.832437	5262577017	5.400012216
996.829572	5262577019	5.399990374
996.830884	5262577017	5.400019497
996.833821	5262577019	5.399983094
996.837299	5262577021	5.399994015
996.841426	5262577018	5.400030418
996.841592	5262577017	5.400001295

Appendix E

Analytical treatment of uncertainty

The pressure measurement performed in the present study can be separated into two distinct parts: the pressure measurement by microwave resonance and the hydrostatic pressure correction. This appendix presents an analytical treatment of the uncertainty for both. The uncertainty assessment for the former was presented in Table 5.4 for helium and in Table 9.5 for argon. These estimates were carried out by iteration via the algorithm presented in chapter 4 section 3.3 using a numerical method recommended by the 'Guide for the Expression of Uncertainty in Measurement' (GUM) for the case of uncorrelated input quantities (see chapter 5.1.3 of the GUM [92]). This iterative method has the advantage of minimizing the approximations used. The second part of the measurement concerns the hydrostatic correction.

1 Microwave pressure measurement

The literal expression for the uncertainty sensitivity coefficients can be deduced from the pressure. The first two terms of the power series expansion for the pressure are given by [93]

$$P = \frac{RT}{(A_\varepsilon + A_\mu) - \frac{2\kappa_T}{9}RT}\left\{ \left[\frac{\left(\frac{f_m(0)}{f_m(P)-\alpha(T-T_0)}\right)^2 - 1}{\left(\frac{f_m(0)}{f_m(P)-\alpha(T-T_0)}\right)^2 + 2}\right] + \left[\frac{\left(\frac{f_m(0)}{f_m(P)-\alpha(T-T_0)}\right)^2 - 1}{\left(\frac{f_m(0)}{f_m(P)-\alpha(T-T_0)}\right)^2 + 2}\right]^2 \frac{\left(B_\rho - \frac{B_\varepsilon + A_\varepsilon^2}{A_\varepsilon + A_\mu} + \frac{2}{9}\kappa_T RT\left(1 + \frac{B_\rho}{A_\varepsilon + A_\varepsilon}\right)\right)}{(A_\varepsilon + A_\mu) - \frac{2}{9}\kappa_T RT} \right\} \tag{E.1}$$

where R is the molar gas constant, T the thermodynamic temperature of the gas and T_0 the thermodynamic temperature of the resonator under vacuum. The coefficient κ_T is the isothermal compressibility of the resonator, α the thermal expansion (temperature related resonant frequency shift), $f_m(0)$ the resonant frequency measured under vacuum, $f_m(P)$ that measured with gas. The variables A_ε and A_μ denote respectively the molar electric and magnetic polarizabilities of the gas, B_ρ the second density virial coefficient and B_ε the second dielectric virial coefficient. If one assumes the input quantities are uncorrelated, the combined variance $u^2(P)$ (square of the combined standard uncertainty $u(P)$) can be found in the GUM [92]

$$\begin{aligned} u^2(P) = &\left(\frac{\partial P}{\partial T}\right)^2 u^2(T) + \left(\frac{\partial P}{\partial T_0}\right)^2 u^2(T_0) + \left(\frac{\partial P}{\partial \kappa_T}\right)^2 u^2(\kappa_T) + \left(\frac{\partial P}{\partial \alpha}\right)^2 u^2(\alpha) \\ &+ \left(\frac{\partial P}{\partial f_m(0)}\right)^2 u^2(f_m(0)) + \left(\frac{\partial P}{\partial f_m(P)}\right)^2 u^2(f_m(P)) + \left(\frac{\partial P}{\partial B_\rho}\right)^2 u^2(B_\rho) \\ &+ \left(\frac{\partial P}{\partial A_\varepsilon}\right)^2 u^2(A_\varepsilon) + \left(\frac{\partial P}{\partial B_\varepsilon}\right)^2 u^2(B_\varepsilon) + \left(\frac{\partial P}{\partial A_\mu}\right)^2 u^2(A_\mu). \end{aligned} \tag{E.2}$$

The partial derivatives of equation E.2 are the sensitivity coefficients which can be easily calculated using computer algebra software. By way of example, the following expression

represents the equation E.1 in the syntax of the free software *Maxima*

$$\begin{aligned} p : (R*T/((Ae+Am)-(2*k*R*T/9)))*((f0/(fp-a*(T-T0)))^2-1) \\ /((f0/(fp-a*(T-T0)))^2+2)+(((f0/(fp-a*(T-T0)))^2-1)^2 \\ /((f0/(fp-a*(T-T0)))^2+2)^2*(B-((Be+Ae^2)/(Ae+Am)) \\ +(2*k*R*T/9)*(1+B/(Ae+Am)))/(Ae+Am-2*k*R*T/9)); \end{aligned} \tag{E.3}$$

The sensitivity coefficient of the thermodynamic temperature of the gas can be calculated with the following syntax

$$diff(p, T, 1); \tag{E.4}$$

2 Hydrostatic correction

In this section a formulation of the hydrostatic pressure will be presented taking into account not only the difference in altitude but also the variations in gas density due to the temperature gradient [67]. Thereafter, the uncertainty sensitivity coefficients will be deduced from it.

2.1 Expression of hydrostatic pressure as a function of altitude and temperature

If P_0 is the pressure measured at the level of the microwave resonator, the pressure P in the pressure tube at an altitude L above it is given by

$$P = P_0 - \Delta P \quad = P_0 - gLM\rho \tag{E.5}$$

where ΔP is the hydrostatic pressure, g the acceleration due to gravity, M the molar mass of the gas molecules and ρ the molar gas density. As the gas is at low pressure (20 kPa to 200 Pa), it is possible to consider only the first two terms of the virial expansion of the gas molar density, whereby the pressure at the thermodynamic temperature T is given by

$$P = RT\rho(1 + B_\rho\rho). \tag{E.6}$$

It is convenient to rewrite equation E.6 as a quadratic equation for the density.

$$\rho^2 + \frac{\rho}{B_\rho} - \frac{P}{B_\rho RT} = 0. \tag{E.7}$$

The solutions of the quadratic equation E.7 are

$$\rho = \frac{-1 \pm \sqrt{\frac{4B_\rho P}{RT} - 1}}{2B_\rho}. \tag{E.8}$$

The two roots are positive because B_ρ is negative (*cf.* table A.1 for helium and Table A.2 for argon). Quantitatively however, for helium gas at 100 Pa and 5.4 K, for instance, the first root is $\rho \approx 2.23$ mol m^{-3} while the second root is $\rho \approx 17608$ mol m^{-3}. The same calculation carried out without taking into account the correction due to B_ρ gives a density equal to $\rho \approx 2.23$ mol m^{-3}. This result corresponds, in the first decimal places, to that of the first root and is far removed from the second. The latter must therefore be discarded. It follows that appropriate expression for the density is

$$\rho = \frac{-1 + \sqrt{\frac{4B_\rho P}{RT} - 1}}{2B_\rho}. \tag{E.9}$$

The expression for the hydrostatic pressure is thus

$$\Delta P = MgL\frac{-1 + \sqrt{\frac{4B_\rho P}{RT} - 1}}{2B_\rho}. \tag{E.10}$$

Let dL represent a small variation in altitude such that the sum of N variations in altitude is $L = NdL$. The hydrostatic pressure on a difference in altitude L can be decomposed as

$$\begin{aligned}
\Delta P_1 &= MgdL\frac{-1+\sqrt{\frac{4B_\rho(T_1)P_0}{RT_1}-1}}{2B_\rho(T_1)} \\
\Delta P_2 &= MgdL\frac{-1+\sqrt{\frac{4B_\rho(T_2)P_1}{RT_2}-1}}{2B_\rho(T_2)} \\
\Delta P_3 &= MgdL\frac{-1+\sqrt{\frac{4B_\rho(T_3)P_2}{RT_3}-1}}{2B_\rho(T_3)} \\
&... \\
\Delta P_N &= MgdL\frac{-1+\sqrt{\frac{4B_\rho(T_N)P_{N-1}}{RT_N}-1}}{2B_\rho(T_N)},
\end{aligned} \tag{E.11}$$

the total pressure variation being given by

$$\Delta P = \sum_{n=1}^{N}\Delta P_n \quad = \sum_{n=1}^{N} Mg\frac{L}{N}\frac{-1+\sqrt{\frac{4B_\rho(T_n)P_{n-1}}{RT_n}-1}}{2B_\rho(T_n)}. \tag{E.12}$$

For a difference of altitude L_i (where $i \geq 1$ is an integer), if T_{i-1} and P_{i-1} correspond respectively to the temperature and pressure at the lower altitude and T_i corresponds to the temperature at the higher altitude, the hydrostatic pressure is given by

$$\Delta P_i = \sum_{n=1}^{N_i} Mg\frac{L_i}{N_i}\frac{-1+\sqrt{\frac{4B_\rho(T_{i-1}+n\frac{T_i-T_{i-1}}{N_i})P_{i,n-1}}{R(T_{i-1}+n\frac{T_i-T_{i-1}}{N_i})}-1}}{2B_\rho(T_{i-1}+n\frac{T_i-T_{i-1}}{N_i})}. \tag{E.13}$$

For J altitude differences L_i the temperatures of which T_{i-1} at the bottom and T_i at the top are known (*i.e.* measured by thermometers), the hydrostatic pressure is given by

$$\Delta P = \sum_{i=1}^{J}\sum_{n=1}^{N_i} Mg\frac{L_i}{N_i}\frac{-1+\sqrt{\dfrac{4B_\rho(T_{i-1}+n\dfrac{T_i-T_{i-1}}{N_i})P_{i,n-1}}{R(T_{i-1}+n\dfrac{T_i-T_{i-1}}{N_i})}-1}}{2B_\rho(T_{i-1}+n\dfrac{T_i-T_{i-1}}{N_i})}. \tag{E.14}$$

Equation E.14 can also be expressed as follows:

$$\Delta P = \sum_{i=1}^{J}\sum_{n=1}^{N_i} Mg\frac{L_i}{N_i}\frac{-1+\sqrt{\dfrac{4B_\rho(\tau_{i,n})P_{i,n-1}}{R(\tau_{i,n})}-1}}{2B_\rho(\tau_{i,n})} \tag{E.15}$$

where

$$\tau_{i,n} = T_{i-1} + n\frac{T_i - T_{i-1}}{N_i}. \tag{E.16}$$

2.2 Sensitivity coefficients of uncertainty

If one assumes the input quantities in equation E.15 are uncorrelated, the combined variance $u^2(\Delta P)$ is given by

$$\begin{aligned} u^2(\Delta P) = \sum_{i=1}^{J}\sum_{n=1}^{N_i}\Bigg(&\left(\frac{\partial \Delta P}{\partial M}\right)^2 u^2(M) + \left(\frac{\partial \Delta P}{\partial g}\right)^2 u^2(g) + \left(\frac{\partial \Delta P}{\partial B_\rho}\right)^2 u^2(B_\rho(\tau_{i,n})) \\ &+ \left(\frac{\partial \Delta P}{\partial P_{i,n-1}}\right)^2 u^2(P_{i,n-1}) + \left(\frac{\partial \Delta P}{\partial L_i}\right)^2 u^2(L_i) + \left(\frac{\partial \Delta P}{\partial T_{i,n}}\right)^2 u^2(T_{i,n})\Bigg) \end{aligned} \tag{E.17}$$

where the corresponding sensitivity coefficients for each uncertainty are given by

$$
\begin{aligned}
\left(\frac{\partial P}{\partial M}\right) &= g\frac{L_i}{N_i}\frac{-1+\sqrt{\dfrac{4B_\rho(\tau_{i,n})P_{n-1}}{R\tau_{i,n}}-1}}{2B_{\rho(\tau_{i,n})}\tau_{i,n}} \\
\left(\frac{\partial P}{\partial g}\right) &= M\frac{L_i}{N_i}\frac{-1+\sqrt{\dfrac{4B_\rho(\tau_{i,n})P_{n-1}}{R\tau_{i,n}}-1}}{2B_\rho(\tau_{i,n})\tau_{i,n}} \\
\left(\frac{\partial P}{\partial B_\rho}\right) &= Mg\frac{L_i}{N_i}\left(\frac{P_{n-1}}{B_\rho(\tau_{i,n})R\tau_{i,n}^2\sqrt{\dfrac{4B_\rho(\tau_{i,n})P_{n-1}}{R\tau_{i,n}}-1}}-\frac{-1+\sqrt{\dfrac{4B_\rho(\tau_{i,n})P_{n-1}}{R\tau_{i,n}}-1}}{2B_\rho(\tau_{i,n})^2\tau_{i,n}}\right) \\
\left(\frac{\partial P}{\partial P_{i,n-1}}\right) &= Mg\frac{L_i}{N_i}\frac{1}{R\tau_{i,n}^2\sqrt{\dfrac{4B_\rho(\tau_{i,n})P_{n-1}}{R\tau_{i,n}}-1}} \\
\left(\frac{\partial P}{\partial L_i}\right) &= \frac{Mg}{N_i}\left(\frac{-1+\sqrt{\dfrac{4B_\rho(\tau_{i,n})P_{\tau_{i,n}}}{R\tau_{i,n}}-1}}{2B_\rho(\tau_{i,n})\tau_{i,n}}\right) \\
\left(\frac{\partial P}{\partial T_{i,n}}\right) &= -Mg\frac{L_i}{N_i}\left(\frac{P_{n-1}}{R\tau_{i,n}^3\sqrt{\dfrac{4B_\rho(\tau_{i,n})P_{n-1}}{R\tau_{i,n}}-1}}+\frac{-1+\sqrt{\dfrac{4B_\rho(\tau_{i,n})P_{n-1}}{R\tau_{i,n}}-1}}{2B_\rho(\tau_{i,n})\tau_{i,n}^2}\right).
\end{aligned}
\tag{E.18}
$$

Here P_0 and T_0 denote respectively the pressure and temperature of the gas in the resonator, J the number of thermometers along the pressure tube, N_i the number of elementary altitude segments between two thermometers considered to perform the calculation, M the molar mass, g the acceleration due to gravity and B_ρ the second molar density virial coefficient of the gas, which depends on the temperature.

Detailed summary in French

Résumé détaillé en français

1 Introduction

Les progrès sur l'incertitude des coefficients du viriel des propriétés thermo-physiques des gaz, obtenus grâce aux calculs *ab initio*, ainsi que l'attribution de valeurs numériques exactes aux constantes d'Avogadro et de Boltzmann lors de la 26^e conférence générale des poids et mesures, mise en application le 20 mai 2019 [94], ont favorisé le développement d'étalons de mesure de pression quantique. Leurs caractéristiques métrologiques prometteuses pourraient non seulement réduire l'incertitude des étalons primaires de pression absolue dans la gamme 1 Pa à 100 kPa [34], mais encore elles pourraient devenir une solution au remplacement des manomètres à colonne de mercure dont la toxicité conduit les laboratoires de métrologie à s'en séparer peu à peu [21].

Tout en suivant cette tendance, l'étalon de pression étudié ici s'en distingue néanmoins dans le sens où, à notre connaissance, il est le premier à mesurer la pression d'un gaz au moyen d'une cavité électromagnétique fonctionnant à une température cryogénique dans la gamme supra-haute fréquence (SHF)[1]. Son principe est cependant similaire à celui d'autres étalons quantiques actuellement développés dans le domaine optique [95]: L'indice de réfraction du gaz est d'abord mesuré à température constante. Sa valeur est ensuite comparée à un indice de réfraction théorique dont la valeur est ajustée en faisant varier sa pression. L'égalité des deux indices est obtenue pour la valeur de pression recherchée.

Cette étude fait partie du projet EMPIR, Quantum Pascal 18SIB04, intitulé « Vers des réalisations quantiques du pascal »[12]. Sa réalisation permet la collaboration de différents laboratoires, à savoir la division pression du Laboratoire National de métrologie et d'Essais

[1] La gamme SHF s'étend de 3 GHz à 30 GHz et correspond à des longueurs d'onde allant de 10 cm à 1 cm.

(LNE) en France et le « laboratoire commun de recherche en métrologie des fluides Evangelista Torricelli » composé de membres du Laboratoire Commun de Métrologie LNE-Cnam (LCM) en France et de l'Istituto Nazionale di Ricerca Metrologica (INRiM) en Italie.

1.1 Etat de l'art

Le Tableau 1 résume les capacités d'étalonnage et de mesure de quelques grands laboratoires nationaux dans des gammes de pression qui recouvrent celle de la présente étude.

Table 1: Capacités d'étalonnage et de mesure représentatives de divers laboratoires nationaux. Les incertitudes sont exprimées avec un niveau de confiance de 95%. Les valeurs présentées dans le tableau proviennent du site du BIPM [2] à l'exception de celle du LNE qui provient du site COFRAC [3]

Pays (Laboratoire)	Measurand minimum valeur (Pa)	Measurand maximum valeur (Pa)	Incertitude(Pa)
USA (NIST)	140	160×10^3	$[(6 \times 10^{-3})^2 + (5.2 \times 10^{-6} p)^2]^{1/2}$
Allemagne (PTB)	100	1.8×10^5	$0.06 + 6 \times 10^{-6} p$
France (LNE)	3	1.5×10^4	$0.015 + 1.6 \times 10^{-5} p$
	5×10^3	5×10^5	$0.2 + 7 \times 10^{-6} p$

1.2 Objectifs initiaux et évolution de l'étude

Ce projet consiste à réaliser un étalon de pression absolue pour l'hélium-4 gazeux dans la gamme 200 Pa à 20 kPa. Cet étalon utilise une cavité résonante hyperfréquence supraconductrice en cuivre munie d'un revêtement en niobium. Pour permettre au niobium d'être à l'état supraconducteur, la cavité est placée dans un cryostat fonctionnant à une température inférieure à sa température critique (9.2 K). L'étude consiste dans un premier temps à concevoir et réaliser une cavité hyperfréquence supraconductrice ainsi qu'un cryostat refroidi à l'hélium liquide destiné à la recevoir, puis à valider le principe de la mesure en vérifiant sa faisabilité pratique et en caractérisant l'étalon métrologiquement.

Un premier cryostat (version I) est réalisé pour l'étude de la faisabilité dans lequel la cavité hyperfréquence est simplement protégée du liquide cryogénique par une enceinte à vide. Le bon fonctionnement de la cavité supraconductrice est constaté et une première mesure de pression de faible exactitude est effectuée. Pour améliorer les mesures, une nouvelle version de

cryostat est réalisée (version II). Cette version est, en fait, une modification de la précédente dans laquelle une chambre de pression est ajoutée pour uniformiser la température du gaz. Ce dernier est acheminé par une ligne de pression indépendante, munie de thermomètres permettant d'effectuer une correction hydrostatique. Les résultats des mesures réalisées font notamment apparaître en basse pression des déviations qui sont attribuées à l'effet thermomoléculaire. Selon les dimensions du système par rapport au libre parcours moyen des molécules du gaz, cet effet peut produire une pression parasite sous l'action d'une différence de température. Il existe plusieurs formules semi-empiriques qui décrivent cet effet selon le gaz employé et la nature des parois mais il n'existe pas de "théorie générale" applicable à toutes les spécificités expérimentales [69]. La prise en compte de ces résultats conduit à la fabrication d'un nouveau cryostat (version III).

Pour bénéficier d'un autre point de vue sur l'étalon et vérifier l'action de l'effet thermomoléculaire sur un autre gaz, pendant le temps de construction du cryostat version III, le cryostat II est aménagé pour fonctionner avec de l'argon. Le point de liquéfaction de l'argon (≈ 87 K) permet l'emploi de l'azote liquide comme liquide cryogénique. L'azote liquide présente plusieurs avantages. Il est plus facile à manipuler et moins cher que l'hélium liquide. Comme sa chaleur lattente est d'environ dix fois supérieure à celle de l'hélium (199.2 kJ.kg^{-1} contre 20.15 kJ.kg^{-1} [58]), il en résulte que l'azote liquide a une vitesse d'évaporation plus lente dans les mêmes conditions. Ceci permet d'augmenter le temps d'expérimentation entre deux renouvellements de liquide cryogénique. A la température de l'argon gazeux, le niobium n'est pas supraconducteur, les expérimentations ont donc été réalisées avec un autre résonateur hyperfréquence en cuivre de mêmes dimensions que le précédent.

2 Principe

2.1 Détermination de la valeur de la pression

La pression est un concept mécanique traditionnellement définie comme une force appliquée par unité de surface (N.m^{-2}). Selon cette définition, les capteurs de pression sont généralement basés sur la mesure des effets provoqués par la pression sur une surface. Le principe utilisé dans la présente étude repose, quant à lui, sur l'équation d'état d'un gaz. La pression p d'un

gaz parfait peut être exprimée sous la forme :

$$p = \rho_N kT \tag{19}$$

où ρ_N est la densité numérique (nombre de molécules N par volume), k est la constante de Boltzmann ($1.380\,649 \times 10^{-23}$ JK^{-1}) et T la température thermodynamique (en kelvin). Il est également possible d'exprimer la pression en fonction de la densité molaire ρ_m (mol.m^{-3}) :

$$p = \rho_m RT \tag{20}$$

avec

$$\rho_N = \rho_m N_A \tag{21}$$

et

$$R = N_A k \tag{22}$$

où N_A est la constante d'Avogadro ($6.022\,140\,76 \times 10^{23}$ mol^{-1}) et R est la constante des gaz parfaits ($8.314\,462\,618\,153\,24$ JK^{-1} mol^{-1})[2]. Pour décrire des gaz réels, l'expression (20) est modifiée en :

$$p = \rho_m RT(1 + B(T)\rho_m + C(T)\rho_m^2 + ...). \tag{23}$$

où B(T), C(T) sont les coefficients du *viriel* de la densité molaire. Ces coefficients peuvent être mesurés expérimentalement ou déterminés par des calculs *ab initio*. Pour les atomes multiélectroniques comme l'argon ($Z = 18$) ou le néon ($Z = 10$), la détermination des coefficients du *viriel* par voie expérimentale donne les incertitudes les plus faibles [32]. Pour l'hélium ($Z = 2$) cependant, la détermination des coefficients du *viriel* par des calculs *ab initio* donnent de meilleurs résultats.

[2]La constante des gaz parfaits a une valeur numérique exacte puisqu'elle est égale au produit de la constante d'Avogadro et de la constante de Boltzmann qui sont elles-mêmes des valeurs exactes par définition (*cf.* Introduction 1).

L'indice de réfraction du gaz peut être déduit de la densité molaire par les équations de Clausius-Mossotti pour la permittivité électrique et la perméabilité magnétique:

$$\frac{\epsilon_r - 1}{\epsilon_r + 2} = \rho_m A_\epsilon (1 + B_\epsilon(T)\rho_m + C_\epsilon(T)\rho_m^2 + ...) \tag{24}$$

$$\frac{\mu_r - 1}{\mu_r + 2} = \rho_m A_\mu (1 + ...) \tag{25}$$

où A_ϵ et A_μ sont les polarisabilités molaires du gaz (en $m^3.mol^{-1}$) associées à la permittivité électrique relative ϵ_r et la perméabilité magnétique relative μ_r. $B_\epsilon(T)$ et $C_\epsilon(T)$ sont les coefficients du viriel du diélectrique. Enfin, le carré de l'indice de réfraction n s'exprime à partir de la permittivité électrique relative ϵ_r et de la perméabilité magnétique relative μ_r par la relation:

$$n^2 = \epsilon_r \mu_r. \tag{26}$$

Le carré de l'indice de réfraction n mesuré par la cavité hyperfréquence a pour expression[37]:

$$\epsilon_r(p,T)\mu_r(p,T) = \left[\frac{< f_{ln}^{em} + \Delta f_{ln}^{em} >_0 \, [1 + \kappa_T(p/3)]}{< f_{ln}^{em} + \Delta f_{ln}^{em} >} \right]^2 \tag{27}$$

où $< f_{ln}^{em} + \Delta f_{ln}^{em} >_0$ est la valeur moyenne des fréquences de résonance[3] mesurée sous vide, $< f_{ln}^{em} + \Delta f_{ln}^{em} >$ est la moyenne des fréquences de résonance mesurée sous pression et κ_T est la compressibilité isotherme du résonateur. L'ordre de grandeur de $\kappa_T(p/3)$ est très petit comparé à 1 dans la gamme de pression étudiée (avec $\kappa_T \approx 7 \times 10^{-12}$ Pa^{-1}).

A partir des mesures de fréquence de résonance sous vide et sous pression, la pression du gaz peut être déduite au moyen des expressions 27 à 23.

[3]Le résonateur quasi-sphérique utilisé pour les expérimentations présente trois fréquences de résonance pour chaque mode.

2.2 Résolution en fréquence

La résolution en fréquence de la cavité hyperfréquence en présence de bruit blanc s'exprime par la relation suivante [35]:

$$\frac{\Delta f}{f} = \frac{1}{A}\frac{1}{Q}\frac{1}{SNR}\sqrt{\frac{\tau}{t}} \tag{28}$$

où A est une constante sans dimension d'ordre de l'unité, Q est le facteur de qualité de la cavité, SNR est le rapport signal sur bruit, τ est le temps pour une mesure et t le temps d'intégration. Cette relation montre que plus le facteur de qualité est élevé, meilleure est la résolution. En réduisant les pertes sur les parois, l'utilisation d'une cavité supraconductrice permet donc d'améliorer la résolution.

3 Materiel et méthodes

Les montages expérimentaux pour l'hélium et l'argon étant très proches, seront décrits conjointement.

3.1 Résonateurs hyperfréquences

Pour l'hélium:

La Figure 1 présente le résonateur supraconducteur réalisé en collaboration avec l'INRiM et l'INSTM (Consorzio Interuniversitario Nazionale per la Scienza e Tecnologia dei Materiali) de Padoue. Il est constitué de cuivre recouvert d'une couche de niobium d'épaisseur 3 μm dans sa cavité. Cette dernière est de forme ellipsoïde triaxiale de diamètre moyen 50 mm.

Pour l'argon:

Le résonateur est entièrement en cuivre. Il a été fabriqué en Chine sous la supervision de Mme Gao Bo, directrice adjointe du laboratoire commun TIPC-LNE Cnam. Ce résonateur, de masse 0.545(1) kg, a les mêmes dimensions que celui utilisé pour l'hélium.

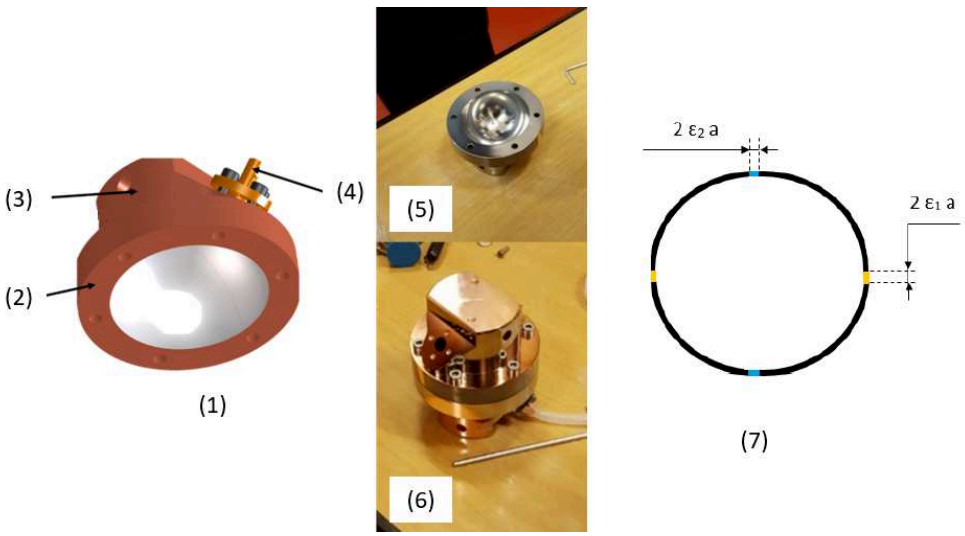

Figure 1: Cavité supracondutrice de diamètre intérieur 50 mm (1) Demi Cavité, (2) Corps en cuivre, (3) Logement pour un thermomètre, (4) Insert pour une antenne hyperfréquence, (5) Revêtement en niobium (d'apparence argentée), (6) Résonateur hyperfréquence fermé, (7) Schéma représentant la déformation d'une sphère de rayon a pour obtenir une quasi-sphère. L'ordre de grandeur des coefficients ϵ_1 et ϵ_2 est de 10^{-3}. Cette déformation permet de distinguer les fréquences de résonance de chaque mode en les éloignant les unes des autres [11].

Fréquence de résonance:

Pour chaque mode, il existe un triplet de fréquence de résonance. La forme quasi-sphérique de la cavité permet de les distinguer en éloignant leur valeur les unes des autres. Il est possible d'avoir une bonne estimation des fréquences de résonance à partir d'une cavité sphérique idéale aux parois parfaitement conductrices [96]. Pour une cavité sphérique de rayon a, les fréquences de résonance ont pour expression [37]:

$$f_{ln}^{\sigma} = \frac{c\,\xi_{ln}^{\sigma}}{2\pi a} \tag{29}$$

où f_{ln}^{σ} sont les fréquences propres, c est la vitesse de l'onde électromagnétique dans le gaz remplissant la cavité et ξ_{ln}^{σ} est la valeur propre de la n-ième racine de la fonction de Bessel sphérique $j_l(\xi) = 0$. L'exposant σ distingue les modes TM et TE. Le tableau 2 répertorie les valeurs propres et les fréquences inférieures des triplets de fréquence calculées pour $a = 25$ mm.

Table 2: Estimation des valeurs propres et des fréquences les plus basses des triplets selon les modes électromagnétiques pour une cavité sphérique sous vide de rayon $a = 25$ mm.

Mode	ξ_{ln}^{σ}	f_{ln}^{σ} (GHz)
TM_{11}	2.743 707 2	5.24
TE_{11}	4.493 409 4	8.58
TM_{12}	6.116 764 2	11.67
TE_{12}	7.725 251 8	14.74

3.2 Antennes

Les antennes utilisées sont de type filaire pour l'hélium et de type helicoïdale pour l'argon. Ces dernières permettent d'exciter les modes TM et TE de la cavité contrairement aux premières qui n'excitent que le mode TM.

3.3 Cryostats

Les pièces mécaniques constituant les cryostats sont en acier inoxydable sauf lorsque cela est précisé. Chronologiquement, trois versions de cryostat sont utilisées (*cf. 1.2*). La Figure 2 donne un aperçu des deux premières versions. Tous les cryostats ont été dimensionnés afin de réutiliser des vases Dewar déjà existants dans le laboratoire.

3.4 Le montage expérimental

La Figure 3 illustre le principe de l'expérimentation et la Figure 4 en donne un aperçu pratique.

L'enceinte de pression contenant le résonateur hyperfréquence est tiré au vide à température ambiante à l'aide d'une pompe turbomoléculaire. Le résonateur est équipé de deux antennes micro-ondes, de thermomètres et de résistances chauffantes. Les antennes hyperfréquences (émettrice et réceptrice) sont connectées à un analyseur de réseau vectoriel. Celui-ci est commandé à distance par un logiciel développé en LabVIEW^{TM} (langage de programmation graphique de National Instruments) pour mesurer le paramètre de dispersion S_{21} autour des fréquences de résonance dans un mode donné. Les fréquences de résonance f_{ln}^{σ} sont déterminées par ajustement en utilisant l'algorithme de Levenberg-Marquardt. La fonction

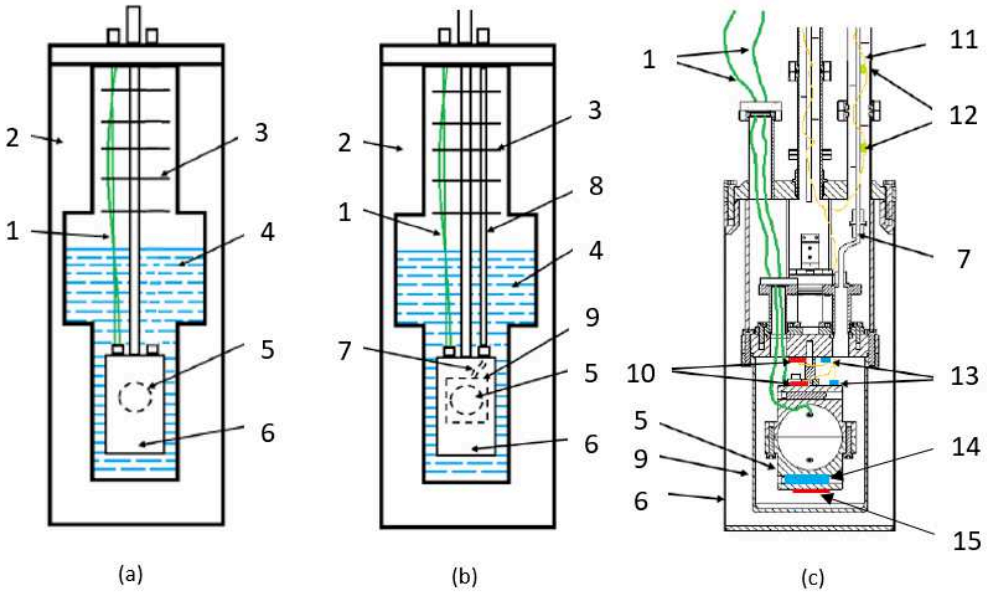

Figure 2: (a) Cryostat version I, (b) Cryostat version II, (c) Plan en coupe de la chambre à vide du cryostat II, (1) Câbles coaxiaux reliant un analyser de réseau vectoriel aux antennes du résonateur hyperfréquence, (2) Vase Dewar contenant le liquide cryogénique, (3) Ecrans en cuivre réduisant les pertes thermiques par rayonnement, (4) Liquide cryogénique ,(5) Résonateur hyperfréquence, (6) Enceinte à vide, (7) Conduit convoyant le gaz vers l'enceinte de pression. (8) Ligne de vide contenant la ligne de pression, (9) Enceinte de pression en cuivre, (10) Résistances chauffantes utilisées pour la régulation en température (11) Coupe de la ligne de vide contenant la ligne de pression garnie d'écran anti-rayonnement et de thermomètres, (12) Thermomètres mesurant la température du gaz le long de la ligne de pression, (13) Thermomètres de type Cernox^{TM} RTD utilisés pour la régulation de température pour l'expérimentation à l'hélium, (14) Thermomètre à résistance de platine de type Pt25 utilisé pour la régulation de température lors de l'expérimentation à l'argon, (15) Résistance chauffante utilisée pour la régulation de température.

modèle a pour expression:

$$S_{21}(f) = \frac{A_p f}{f^2 - (f_{lnp}^{\sigma} + i g_{lnp}^{\sigma})^2} + B + C(f - f_{lnp}^{\sigma}) + D(f - f_{lnp}^{\sigma})^2 \tag{30}$$

où A_p, B, C et D sont des constantes complexes, f_{lnp}^{σ} sont les fréquences de résonance et g_{lnp}^{σ} sont les demi-largeurs à mi-hauteur du triplet.

Un multimètre (Keithley 2002) permet de mesurer la résistance du thermomètre. Des sources de courant (Yokogawa GS200) alimentent les résistances chauffantes. Cette dernière n'est activée que dans la phase de régulation de température. Le schéma de la figure 3 présente

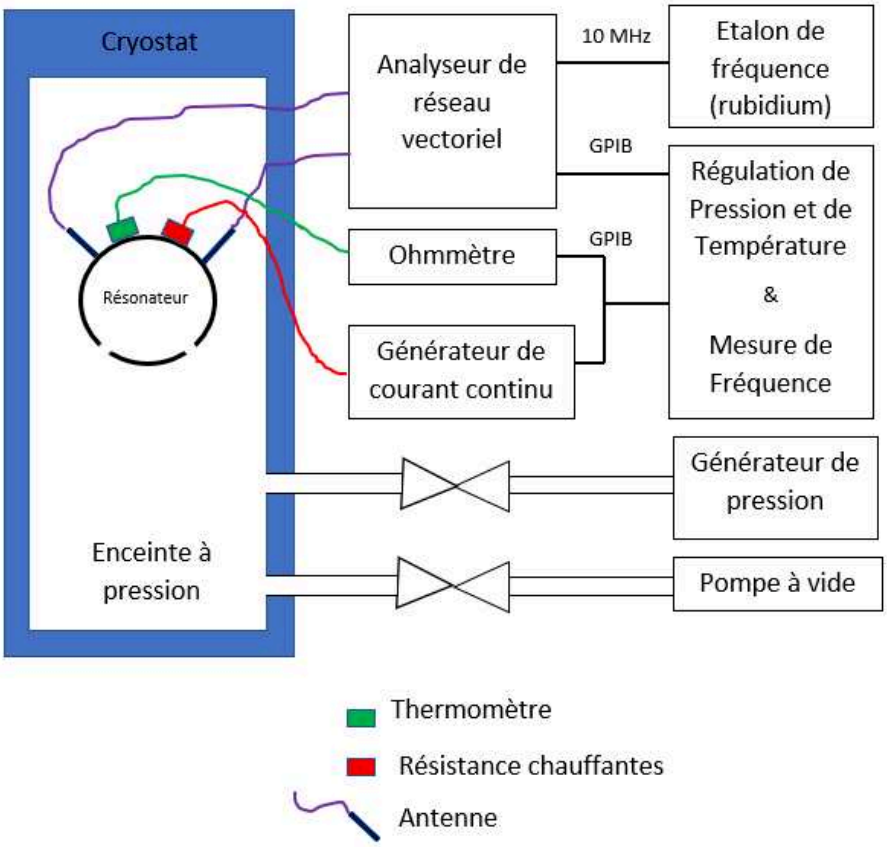

Figure 3: Schéma de principe de l'expérimentation

le schéma de principe de l'expérimentation. Trois appareils de mesure de pression sont connectés à la ligne de pression du résonateur. Cinq thermomètres mesurant la température de la ligne de pression dans le cryostat sont connectés à des ohmmètres. Au début de l'expérimentation, le résonateur reste sous vide à température ambiante pendant au moins 48 heures puis est refroidi à sa température de fonctionnement (5.4 K pour l'hélium et 90.4 K pour l'argon).

Une fois le résonateur thermiquement stabilisé, une première mesure de fréquence de résonance est réalisée sous vide. Cette mesure effectuée, le gaz est introduit dans la cavité afin de mesurer de nouvelles fréquences de résonance et de déterminer les valeurs de pression correspondantes par calcul itératif (*cf.* 2.1).

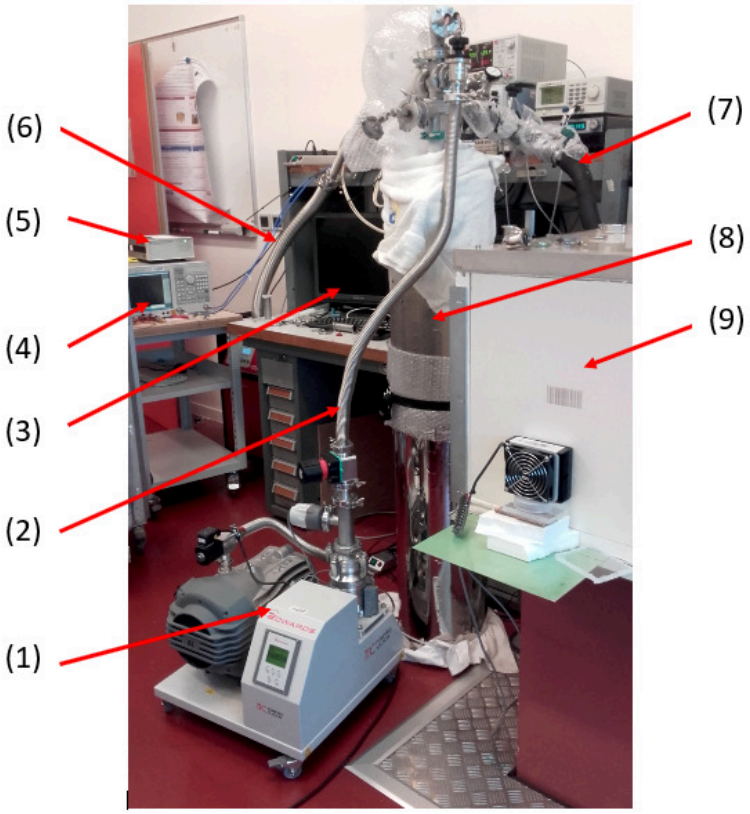

Figure 4: Montage expérimental pendant le run 5 (juin-juillet 2019): (1) Pompe turbomoléculaire avec une pompe rotative sèche, (2) Tube reliant le cryostat à une pompe turbomoléculaire et permettant d'évacuer le gaz de la chambre à vide, (3) Ordinateurs, (4) Analyseur de réseau vectoriel connecté au résonateur hyperfréquence, (5) Etalon de fréquence (Rubidium), (6) Tube reliant une seconde pompe turbomoléculaire au résonateur hyperfréquence, (7) Tube reliant le générateur de pression à l'enceinte à vide, (8) Vase Dewar, (9) Générateur de pression.

3.5 Le générateur de pression

Le générateur de pression, dont le principe est montré sur la figure 5, est protégé des variations de température ambiante par une enceinte thermique (B-box). Le gaz provenant des bouteilles est fourni (avec un niveau de pureté supérieur à $99,9999$ % mol) à une pression de 200 bar. Un détendeur réduit cette pression à un niveau proche de la pression atmosphérique. Le gaz traverse ensuite un régulateur de débit massique réglé à une valeur constante selon les pressions (allant de 0.4 sccm à 20 sccm pour des pressions de 500 Pa à 20 kPa). La régulation de pression proprement dite est réalisée par un second régulateur (ou une électrovanne) connecté à une pompe thermomoléculaire. Deux volumes situés de part et d'autre du régulateur de

débit massique d'entrée permettent de stabiliser la pression et de lisser les pics de pression. La pression est mesurée par deux capteurs de pression à quartz (DIGIQUARTZ® modèle 745). L'un d'eux est utilisé dans la boucle de régulation de pression, l'autre sert de référence. Un troisième capteur de pression (baratron AD06A12TRC de mks instruments) assure une redondance sur la mesure de pression jusqu'à 13 kPa.

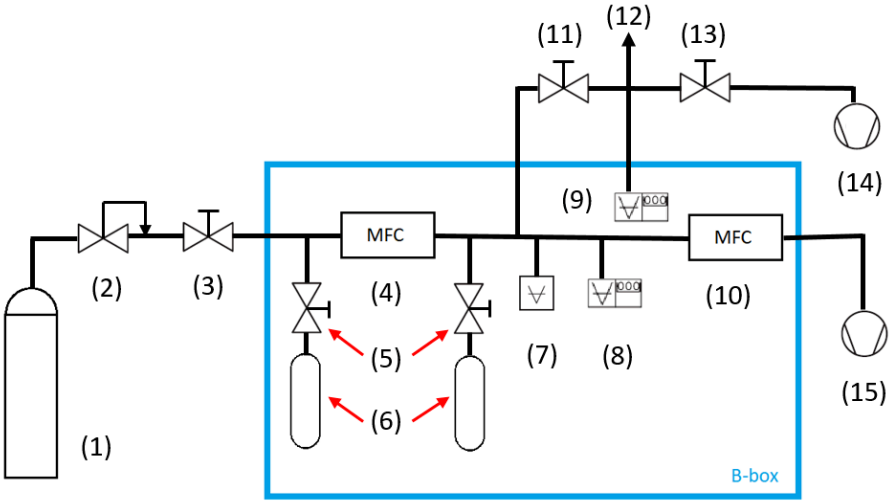

Figure 5: Schéma de principe du générateur de pression: (1) Alimentation en gaz, (2) Détendeur, (3) Vanne manuelle,(4) Régulateur de débit massique,(5) Vannes, (6) Volumes, (7) Capteur de pression (Baratron), (8) Capteur de pression (DIGIQUARTZ®) utilisé pour la régulation de pression, (9) Capteur de pression (DIGIQUARTZ®) utilisé comme référence, (10) régulateur de débit massique, (11) Vanne permettant d'alimenter le résonateur hyperfréquence en gaz, (12) Partie connectée à l'enceinte de pression et au résonateur hyperfréquence dans le cryostat, (13) Vanne d'évacuation du gaz, (14) Pompe turbomoléculaire, (15) Pompe turbomoléculaire.

4 Résultats et discussion

4.1 Experimentations à l'hélium

4.1.1 Transition supraconductrice

La Figure 6 présente la réponse en fréquence du paramètre $|S_{21}|$ autour d'une fréquence de résonance du mode TM_{12} et à différentes températures. Il apparaît qu'aux températures inférieures à la température critique du niobium (9.2 K), le coefficient de qualité Q du résonateur s'accroit jusqu'à atteindre une valeur de 3.8 millions à 5.4 K.

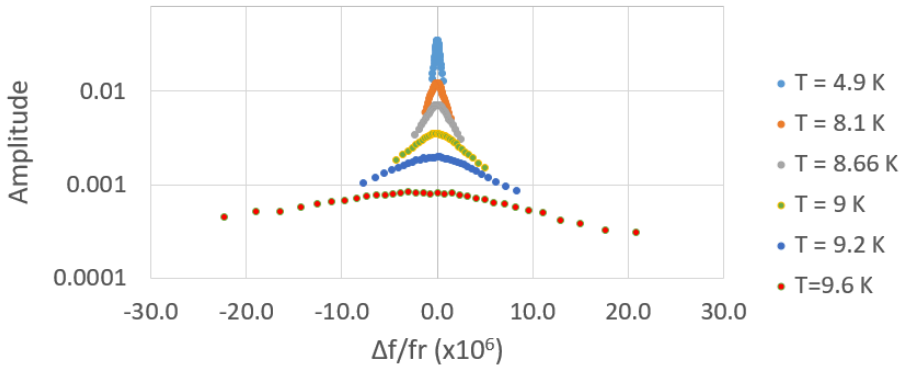

Figure 6: Spectre du paramètre de transmission $|S_{21}|$ autour de la fréquence de résonance f_{12} du mode TM_{12} pour différentes valeurs de température. Les centres des résonances sont alignés pour plus de clarté (source He-run 1).

4.1.2 Effet de la transition supraconductrice sur l'incertitude en fréquence

La figure 7 présente l'effet de la transition supraconductrice du niobium sur l'incertitude de détermination de la fréquence de résonance. Celle-ci se trouve réduite d'environ de trois ordres de grandeur.

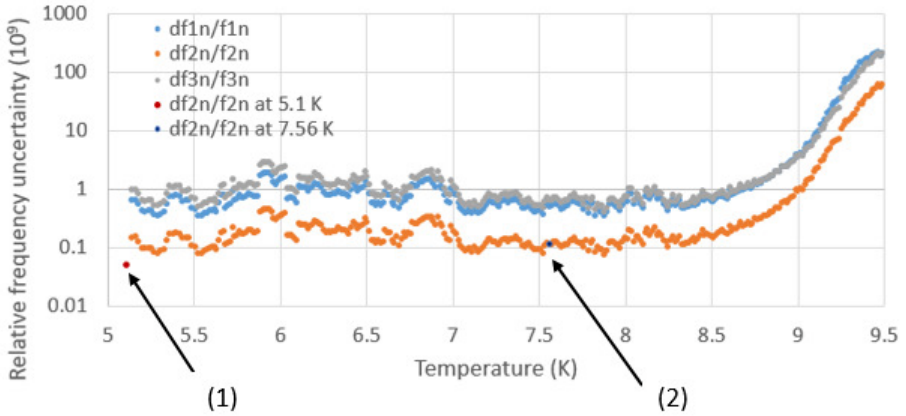

Figure 7: Incertitude en fréquence des composantes du triplet du mode TM_{11} en fonction de la température. Puissance micro-onde -28 dBm. (1) Mesure statique à 5.1 K.(2) Mesure statique à 7.56 K (source He-run 2).

4.1.3 Tests en pression

Le résolution en pression a été estimée à 3 mPa pour une variation de 20 Pa. La Figure 8 montre un cycle de mesure composé de paliers de pression allant de 20 kPa à 500 Pa. La température du résonateur est régulée à 5.4 kPa.

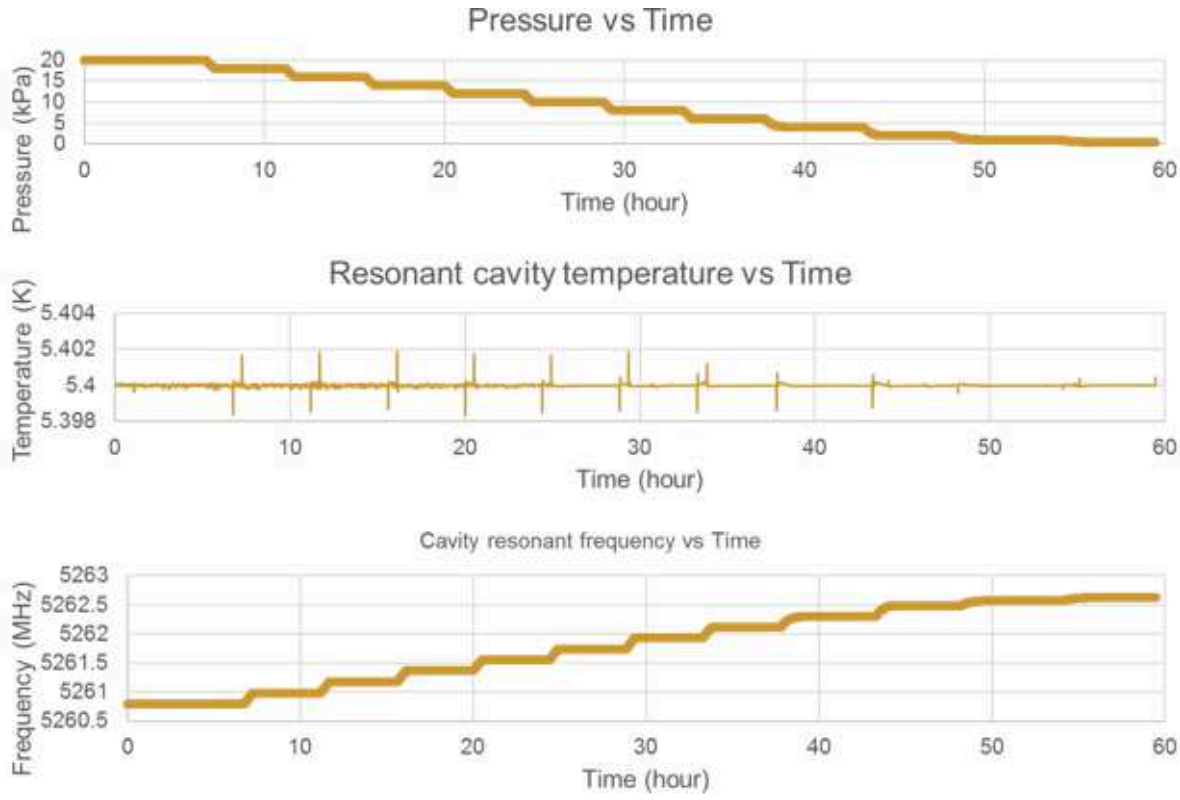

Figure 8: Evolution simultanée de la pression à mesurer, de la température du résonateur et de la fréquence de résonance au cours d'un cycle de pression. La température moyenne du résonateur est égale à 5.4 K (source He-run 7).

4.2 Expérimentations à l'argon

Les mesures en pression ont mis en évidence des instabilités liées au montage. Celles-ci font l'objet d'une recherche de cause afin d'y remédier.

4.3 Cyles de pression de l'hélium et de l'argon

La Figure 9 présente des écarts de mesure relatifs à l'hélium et à l'argon de l'étalon étudié par rapport à des étalons de référence du laboratoire. La divergence à faible pression peut provenir d'une mauvaise correction de l'effet thermo-moléculaire bien que celui-ci ne devrait théoriquement pas être aussi important à ces pressions. L'utilisation du nouveau cryostat (version III) qui par son tube de pression, d'un diamètre $6,3$ fois plus grand que le précédent, doit permettre de réduire d'environ 40 fois l'effet thermomoléculaire. A l'heure où ces lignes sont écrites, l'origine de l'écart quasi-constant entre les étalons de référence et l'étalon étudié n'a pas encore été identifié.

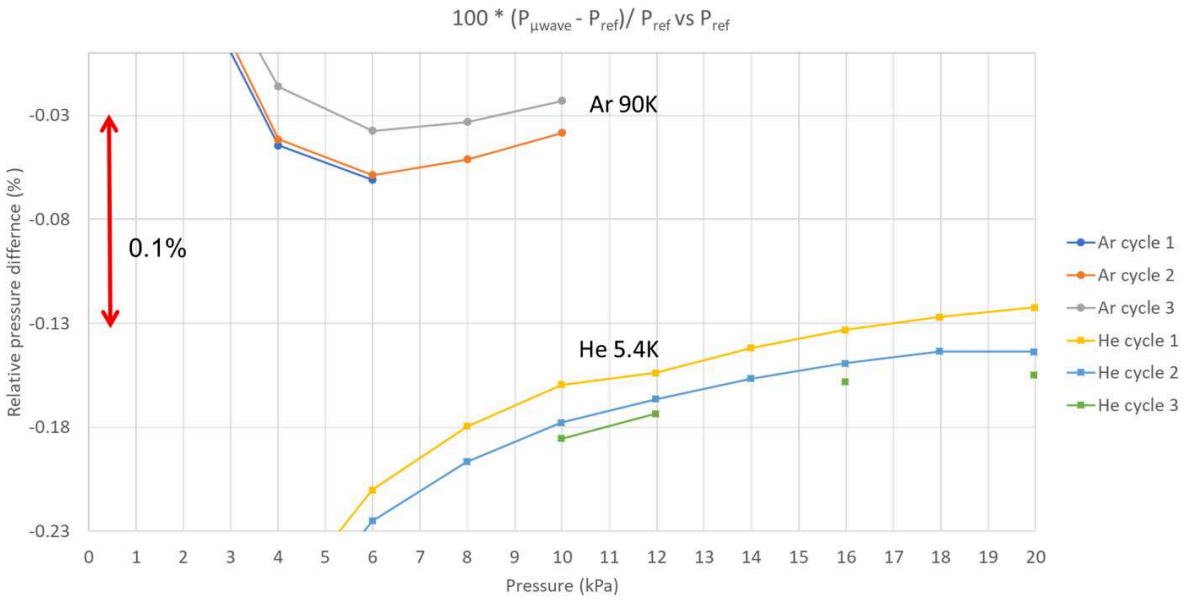

Figure 9: Résultat préliminaire : différence relative entre les étalons de pression et la mesure primaire de pression obtenue avec les deux résonateurs, le supraconducteur avec de l'hélium à 5.4 K et le non supraconducteur avec de l'argon à 90.4 K

4.4 Budget d'incertitude provisoire de l'hélium

Le Tableau 3 présente un premier bilan d'incertitude pour la mesure de l'hélium avec une cavité supraconductrice. Il apparaît que la composante d'incertitude prédominante est celle de la température.

Table 3: Bilan d'incertitude provisoire pour l'hélium aux pressions 200 Pa et 20 kPa mesurées à l'aide de la cavité supraconductrice à 5.4 K. Avec P pression ; κ_T compressibilité isotherme ; T temperature thermodynamique ; A_μ polarisabilité magnétique molaire ; A_ϵ polarisabilité magnétique molaire ; B_ϵ second coefficient diélectrique du viriel ; B_2, C_2, D_2 coefficients du viriel de la densité ; f_m fréquence mesurée. (Les composantes d'incertitude inférieures à 20 μPa sont omises et remplacées par le symbole "–").

Pression de travail Unité d'incertitude	200 Pa (mPa)	20 kPa (mPa)
P composantes d'incertitude, Type B		
κ_T	0.028	2.5
T étalonnage	3.9	545
impuretés du gaz	–	–
A_μ [62]	0.065	6.4
A_ϵ [62]	0.039	3.7
B_ϵ [62]	0.018	3.7
B_2 [81]	0.005	47
C_2 [81]	–	4
D_2 [81]	–	0.6
P composantes d'incertitude, Type A		
T regulation	1.2	252
f_m mesure et corrections	0.89	0.84
p incertitudes combinées	4.18	602

5 Conclusion

Ce document décrit le développement d'un nouvel étalon de pression absolue de gaz dans la gamme 200 Pa à 20 kPa. La méthode utilisée repose sur la mesure de l'indice de réfraction d'un gaz (hélium-4 ou argon) à l'aide d'un résonateur hyperfréquence. L'indice est déterminé par le rapport des fréquences de résonance à vide et sous pression mesurées à température constante. Pour l'hélium-4, les mesures ont été effectuées à une température de 5.4 K à l'aide d'une cavité supraconductrice en cuivre recouverte de niobium, permettant d'améliorer la résolution du système. La détermination de la pression bénéficie des très faibles incertitudes

des coefficients du viriel des propriétés thermo-physiques de l'hélium-4 obtenus par calculs *ab initio*. Les mesures à l'argon ont été effectuées à une température de 90.4 K avec un résonateur en cuivre (non supraconducteur). A cette température, l'expérimentation est moins exigeante en terme de cryogénie et est susceptible d'être largement généralisée. Des mesures de stabilité, de résolution et des cycles de pressions ont été réalisées. Des bilans d'incertitude provisoires ont également été présentés.

le cnam

Pascal GAMBETTE

Vers un étalon quantique pour des mesures absolues de pression

HESAM UNIVERSITÉ

Résumé :
Ce document décrit le développement d'un nouvel étalon de pression absolue de gaz dans la gamme 200 Pa à 20 kPa. La méthode utilisée repose sur la mesure de l'indice de réfraction du gaz (hélium-4 ou argon) à l'aide d'un résonateur hyperfréquence. L'indice est déterminé par le rapport des fréquences de résonance à vide et sous pression mesurées à température constante. Pour l'hélium-4, les mesures ont été effectuées à $5,4$ K à l'aide d'une cavité quasi-sphérique en cuivre recouverte d'une couche supraconductrice de niobium, permettant d'améliorer la résolution du système. La détermination de la pression bénéficie des très faibles incertitudes des coefficients du viriel des propriétés thermo-physiques de l'hélium-4 obtenu par calculs *ab initio*. Les mesures à l'argon ont été effectuées à $90,4$ K avec un résonateur en cuivre (sans revêtement supraconducteur interne). A cette température, le dispositif est moins exigeant en terme de cryogénie et donc plus susceptible d'être dupliqué.

Mots clés : Calculs *ab initio*, Etalon, Métrologie, Manométrie, Thermométrie, Cavité hyperfréquence, Supraconductivité, Indice de réfraction, Coefficient du viriel, Hélium, Argon.

Abstract :
The present dissertation describes the development of a novel absolute pressure standard in the range 200 Pa to 20 kPa (0.002 atm to 0.2 atm). The method used is based on measuring the refractive index of a noble gas (helium-4 or argon) using a microwave resonator. The index is determined via the ratio of the resonant frequencies under vacuum and under pressure measured at a constant temperature. For helium-4, to improve frequency resolution, measurements were made at a temperature of 5.4 K using a superconducting niobium coating sputtered onto a quasi-spherical copper cavity. The pressure determination benefits from the very low uncertainties of the virial coefficients of the thermophysical properties of helium-4 obtained by *ab initio* calculations. Measurements on argon were performed at 90.4 K with an uncoated copper resonator. At this temperature, the experiment is less demanding in terms of cryogenics than its helium counterpart and is more likely to be widely generalized.

Keywords : *Ab initio* calculation, Standard, Metrology, Manometry, Thermometry, Microwave cavity, Superconductivity, Refractive index, Virial coefficient, Helium, Argon.